SANDIA REPORT
SAND2019-10713
Printed September, 2019

Sandia National Laboratories

Prediction and Inference of Multi-scale Electrical Properties of Geomaterials

Chester J. Weiss, Güngör Didem Beşkardeş, and Bart G. van Bloemen Waanders

Prepared by
Sandia National Laboratories
Albuquerque, New Mexico 87185
Livermore, California 94550

Issued by Sandia National Laboratories, operated for the United States Department of Energy by National Technology & Engineering Solutions of Sandia, LLC.

Available to DOE and DOE contractors from

U.S. Department of Energy
Office of Scientific and Technical Information
P.O. Box 62
Oak Ridge, TN 37831

Telephone: (865) 576-8401
Facsimile: (865) 576-5728
E-Mail: reports@osti.gov
Online ordering: http://www.osti.gov/scitech

Available to the public from

U.S. Department of Commerce
National Technical Information Service
5301 Shawnee Road
Alexandria, VA 22312

Telephone: (800) 553-6847
Facsimile: (703) 605-6900
E-Mail: orders@ntis.gov
Online order: https://classic.ntis.gov/help/order-methods

ABSTRACT

Motivated by the need for improved forward modeling and inversion capabilities of geophysical response in geologic settings whose fine–scale features demand accountability, this project describes two novel approaches which advance the current state of the art. First is a hierarchical material properties representation for finite element analysis whereby material properties can be perscribed on volumetric elements, in addition to their facets and edges. Hence, thin or fine–scaled features can be economically represented by small numbers of connected edges or facets, rather than 10's of millions of very small volumetric elements. Examples of this approach are drawn from oilfield and near–surface geophysics where, for example, electrostatic response of metallic infastructure or fracture swarms is easily calculable on a laptop computer with an estimated reduction in resource allocation by 4 orders of magnitude over traditional methods. Second is a first-ever solution method for the space–fractional Helmholtz equation in geophysical electromagnetics, accompanied by newly–found magnetotelluric evidence supporting a fractional calculus representation of multi-scale geomaterials. Whereas these two achievements are significant in themselves, a clear understanding the intermediate length scale where these two endmember viewpoints must converge remains unresolved and is a natural direction for future research. Additionally, an explicit mapping from a known multi-scale geomaterial model to its equivalent fractional calculus representation proved beyond the scope of the present research and, similarly, remains fertile ground for future exploration.

ACKNOWLEDGMENT

This interdisciplinary, collaborative work is supported by Sandia National Laboratories LDRD program. Special thanks are extended to our external collaborators Dr. Mark Everett (Texas A&M University) with whom (PI) Weiss initially conceived many of the founding principles and observations for the hierarchical finite element concept of electromagnetic induction, Dr. Glenn Wilson (Halliburton Energy Services) who inspired application of the fractional calculus concept to oilfield awareness, and Dr. Harbir Antil (George Mason University), whose expertise in the mathematics of fractional calculus (supported by NSF grants DMS-1521590 and DMS-1818772, and Air Force Office of Scientific Research under Award NO: FA9550-19-1-0036) proved invaluable. Internal collaborators Dr. Christian Glusa and Marta D'Elia are also recognized for their valuable insights on the further development of the algorithms and mathematics for meaningful and efficient implementation of the fractional calculus.

The finite element work herein could not have been done without Sandia's Cubit software, where developer Trevor Hensley has earned our deepest gratitude for his patience in sorting out troublesome issues with mesh generation and optimization.

CONTENTS

LIST OF FIGURES

This page intentionally left blank.

1. INTRODUCTION

1.1. PROJECT MOTIVATION

Our purpose in this project was to develop subsurface imaging and predictive modeling under conditions where the usual assumptions of petrophysics no longer apply. Whereas geophysical measurements of rock properties are the only viable approach for reconnaissance and monitoring of the subsurface and its changing state, these properties (mass density, seismic wavespeed, electrical conductivity, etc) are often a proxy for other properties of greater interest (e.g. permeability, fracture density and orientation, mineralogy). The challenge in geophysics is thus twofold: proper accounting of these properties of interest in the petrophysics of predictive "forward" simulations; and, accurate extraction of these properties from gross, bulk-averaged maps ("inversion" solutions) of the geophysical proxies. In particular, the bulk electrical properties of rocks – much like their hydrologic properties – are driven strongly by small-scale features that can both "shunt" and "short" the underlying transport physics. In other words, for these problems what matters are the details and how the details connect across orders of magnitude in length scale. Prior to this LDRD, computational modeling capabilities could capture, to limited extent, an atomistic "brute force" response of such a detailed, spatially-correlated geologic medium, however little has been published from this perspective on the relationship between the geologic texture and macroscopic observable response. Alternatively, field observations are also consistent with a modified form of the Maxwell equations which result in fractional-order power law diffusion of induced electromagnetic fields. Our hypothesis going into this project was that these two views of observational data are mutually consistent and we thus proposed to indentify the limit and conditions where they converge.

The research herein is an advanced development of innovative concepts for modelling electromagnetic fields in realistic geologic materials. Modeling anomalous diffusion using the power-law formulation for Maxwell's equations is novel in the electromagnetic geophysics community and impacts the broader research question of transport processes in multi-scaled systems – a persistent and enigmatic problem in the geosciences.

1.2. PROJECT APPROACH

There is observational evidence for anomalous electromagnetic diffusion in near-surface geophysical exploration that is consistent with a detailed, spatially-correlated geologic medium. To date, the inference of multi-scale geologic correlation is drawn from two independent methods

of data analysis. The first of which is analogous to seismic move-out, where the arrival time of an electromagnetic pulse is plotted as function of transmitter/receiver separation (Weiss and Everett, 2007; Kazlauskas, 2010). The "anomalous" diffusion is evident by the fractional-order power law behavior of these arrival times, with an exponent value between 1 (pure diffusion) and 2 (lossless wave propagation). The second line of evidence comes from spectral analysis of small-scale fluctuations in electromagnetic profile data which cannot be explained in terms of instrument, user or random error (Everett and Weiss, 2002a; Bahr et al., 2002; Weymer et al., 2015). Rather, the power-law behavior of the spectral content of these signals (i.e. power versus wavenumber) and their increments reveals them to lie in a class of signals with correlations over multiple length scales, a class of signals known formally fractional Brownian motion (Mandelbrot and Ness, 1968). Numerical results over simulated geology with correlated electrical texture – representative of, for example, fractures, sedimentary bedding or metamorphic lineation – are consistent with the (albeit limited, but growing) observational data, suggesting a possible mechanism and modeling approach for a more realistic geology (Ge et al., 2012, 2015; Beskardes et al., 2016). Furthermore, we had shown how similar simulated results can arise from a modeling approach where geologic texture is economically captured by a modified diffusion equation containing exotic, but manageable, fractional derivatives (Oldham and Spanier, 1974). These derivatives arise physically from the generalized, convolutional form for the electromagnetic constitutive laws (Jackson, 1975) and thus have merit beyond mere mathematical convenience (Weiss and Everett, 2007; Tarasov, 2005, 2008).

There are two principal components to the proposed research. The first of which is multi-scale forward modeling of electromagnetic induction in geomaterials. Preliminary work by the PI in this area (Weiss and Everett, 2007) innovated a fractional calculus representation of diffusive electromagnetic transport on hierarchical media – that is, charge/fluid transport over pathways nested within pathways nested within pathways and so on. Such a structure is analogous to thin sedimentary bedding and fracture morphology, either naturally occurring or induced through engineered stressors. The nested hierarchy of the material can be captured through fractional order derivatives in the governing physics rather than an exhaustive (and Quixotic!) discretization of every minutia of heterogeneity. Preliminary results appeared in the journal *Geophysics* (Ge et al., 2012, 2015), but there was still much remaining unanswered. Among them is the length scale at which the fractional-derivative breaks down and how this relates to the interrogation frequency of the incident electromagnetic signal. This was coupled with poor undestanding of the transition and physical response between simple layered/fracturing and their fractional representation. These are some of the fundamental research questions which motivated the present work.

In doing so, our aim was to build on a related branch of prior work where computational models of increasing electrical complexity were analyzed to understand their asymptotic response in the fractional-calculus limit. Work (Beskardes et al., 2016) had been done on simplistic models of stochastic, spatially correlated conductivity distributions, but the models were relatively crude and not fully representative of "realistic" geologic materials likely to be found in exploration or engineering scenarios. Construction and evaluation of realistic models was known a priori to be computationally burdensome, requiring far greater computational resources than are available in the academic/commercial sector. Our initial plan was to further exploit previous work by the PI (Weiss, 2013, 2014) using mixed vector/scalar potentials and solve the Maxwell equations on

nested computational grids – not to be confused with "multi-grid", but rather a fine grid embedded within another – which are then "stitched" together through interpolation (e.g. Berger and Oliger, 1984; Weiss, 2014). This idea was superceded by an unforeseen breakthrough in Q1 of the first project year where, instead of nested grids, a hierarchical finite element framework was devised in which fine scale features could be economically represented in a discretized geomodel. This (truely transformative) breakthrough enabled a series of previously unobtainable results in oilfield/infrastructure/fracture modeling and eased the initial project objective of exploring the intermediate length scale from two converging directions: a zooming down of the macroscopic (fractional derivative) view; and, a heuristic homogenization of the atomistic (brute force discretization) view.

It's fair to point out that we are not the only ones in the computational electromagnetics community who strive toward accurate accounting of geologic detail, however existing work in this area is focused chiefly on accurate bathymetry/topography representation and adaptive mesh refinement for mitigating numerical error. While we initially believed that the stochastic models in Beskardes et al. (2016) could best be improved upon in the nested, but structured, grid environment on which the Weiss (2013) solver was been developed, the hierarchical finite element framework (Weiss, 2017), instead, turned out to be the primary computational workhorse.

The second major technical thrust to the research was envisioned as development of an inversion/imaging algorithm suitable for likely scenarios in Sandia's mission space such as underground facility characterization, situation awareness and energy/resource research. Thus, we anticipated leveraging the existing Trilinos framework for application-optimized imaging using traditional gradient-based methods with uncertainty estimates. The inversion/optimization effort for the proposed research would differ from present "state-of-the-art" in electromagnetic imaging (e.g. Haber et al., 2007; Um et al., 2014) in that we aimed to recover not only a conductivity model, but more importantly, the fractional order of the time derivative and/or the correlation statistics of the geologic conductivity model. Estimating these parameters would propel the interpretation of electromagnetic data out of a model space defined by crude, blocky conductivity structures and into one where realistic geologic structure is better represented and quantified. This effort, however, was de-prioritized in year 2 of the project for two reasons: excitement and accelerated commercial opportunities from the Weiss (2017) hierarchical breakthrough; and, techincal challenges implementing the fractional Helmholz solver with the Rapid Optimization Library.

To our knowledge, there are no other researchers in the US who are pursuing the concept of fractional diffusion models for electromagnetic prospecting, largely – we suspect – because of the greatly diminished size of the domestic EM research population. Elsewhere, others have made tentative progress with these concepts (e.g. Bahr et al., 2002; Skinner and Heinson, 2004), but they remain mostly fertile ground for research. The analogy between fluid and charge transport in rocks motivated much of our early thinking and we believe that the success of fractional, anomalous transport theory in hydrology (e.g. Berkowitz and Scher, 2005) can be paralleled or even surpassed in the applied geophysics community. At the project onset, we were aware of no existing IP in this technology space, and the expectation of the project was to generate meaningful IP in modeling, inversion and analysis as they arise from the pursuit of the project's technical goals.

The overarching science goal for the project is to pioneer a "new science" of transport physics on multi-scale, textured geomaterials, with an initial emphasis on electromagnetic current and charge transport. In particular we seek to better understand the effects of multi-scale geologic texture on electromagnetic interrogation by pushing the computational limits in modeling correlated, cell-by-cell variations in electrical conductivity and determining under what conditions of experimental setup, geology and instrumentation, these results converge with the provocative, but economical, use of fractional derivatives for bulk-scale modeling of sub-grid geologic texture. In doing so, we seek to harmonize the atomistic (brute force discretization) view with the macroscopic (fractional derivative) view of proper accounting for complex geologic texture. This should have immediate application underground facility characterization, fracture mapping, global nuclear assurance and security, and mineral/energy/resource science. As documented in the following subsection, that IP landscape has now changed considerably and as a direct result of LDRD funding.

1.3. STRUCTURE OF THIS REPORT

As will be demonstrated shortly, this project has generated a significant number of contributions to the scientific literature with corresponding intellectual property instruments for Sandia National Laboratories. Chapters 2 through 8 of this report are drawn directly from this published bibliographic record and modified here for formatting compliant with the requirements of a SAND report. For brevity, these chapters represent only the major findings of this LDRD: the hierarchical finite element concept; its application to oilfield, infrastructure and fracture characterization, wellbore modeling; and, a novel solution to the fractional Helmholtz equation. These chapters are intentionally self-contained and correspond to their published manuscripts in the following way:

Chapter 2: Weiss CJ, Finite element analysis for model parameters distributed on a hierarchy of geometric simplices, *Geophysics*, **82**, E155 (2017).

Chapter 3: Weiss CJ and BG van Bloemen Waanders, On the convergence of Neumann series for electrostatic fracture response, *Geophysics*, **84**, E47–55, (2019).

Chapter 4: Weiss CJ, Hierarchical material properties in finite element modeling: An example in 3D DC resistivity modeling of infrastructure, 3DEM-6, 6th International Symposium on Three-Dimensional Electromagnetics, Berkeley CA, 4pp, (2017).

Chapter 5: Weiss CJ and G Wilson, A new hierarchical finite element method for compact representation of oilfield infrastructure, *SEG Annual Meeting, Expanded Abstracts*, 5pp, (2017).

Chapter 6: Beskardes GD and CJ Weiss, Modeling DC responses of 3D complex fracture networks, *Geophysical Journal International*, **214**, 1901–12 (2018).

Chapter 7: Beskardes GD and CJ Weiss, Electrical signatures of fractures near energized geometrically-complex, steel-cased wells, *Geophysics*, (in revision, 2019).

Chapter 8: Weiss CJ, BG van Bloemen Waanders and H Antil, Fractional operators applied to geophysical electromagnetics, *Geophysical Journal International*, (in revision, 2019).

1.4. INTELLECTUAL PROPERTY SUPPORTED BY THE ACCOMPLISHMENTS OF THIS LDRD

1.4.1. Software Copyright Assertions

[1] **SCR #2238, HFEM3D, v1.0**

FORTRAN90 software for computing the solution to the Poisson equation in three dimensions using the hierarchical material properties framework for finite elements described in Weiss (Geophysics, 2017). *Licence agreement to CARBO Ceramics executed in 2018*

[2] **SCR #2322, FLUXNET, v1.0**

Finite element solution to the Poisson equation over segments of a 2D network of nodes connected by straight line segments (a.k.a. "graph").

[3] **SCR #TBD, FRACHELM, v1.0**

Solution of the fractional Helmholtz equation using linear finite elements and the spectral representation of the fractional Laplacian operator described in Weiss et al. (GJI, 2019).

[4] **SCR # TBD, HFEM3D-PARFRAC, v1.0**

A toolkit of FORTRAN90 and PYTHON routines to automate calculation of electrostatic response of fracture networks in geomaterials, specifically designed for distributed memory compute clusters. Software integrates pre-processing of Cubit–generated meshes with calculations from HFEM3D and post–processing for aggregate data analysis.

1.4.2. Technical Advances

[5] **SD # 14129, Borehole logging with transient electromagnetics**

Investigation of the physics of electromagnetic pulse propagation in the Earth from an uncased borehole antenna. Analysis restricted to a three-layer earth model — one central layer of electrical conductivity σ_1, bounded by semi-infinite halfspaces, each of conductivity σ_2. Borehole antenna envisioned as an axisymmetric loop energized with an instantaneous step-on current.

[6] **SD # 14680, Hierarchical Representations for Computer Analysis of Metamaterials**

TA extends the concept of hierarchical material properties representation described in non-provisionsal patent application SD14294 for geoscience applications to applications at the micron scale relevant to the design and analysis of metamaterials for photonics and photovoltaics.

[7] **SD # 14294, Hierarchical Material Properties in Finite Element Modeling**

A mathematical structure is proposed and tested for material properties associated with volumes, facets and edges of a tetrahedral finite element mesh. This structure allows for efficient representation of infinitely thin surfaces and lineaments without excessive discretization by may small volumetric elements. Simulation results from the proposed structure have been benchmarked against independent reference solutions for the problem of strongly conducting sheets and cylinders embedded in an electrically conducting medium in the zero frequency limit. Favorable agreement has been found. Reduction in computation resources and run times from traditional volume-discretization is shown to be on the order of a 2-3 orders of magnitude.

1.4.3. Patent Applications

[8] **US15/871,282 (pending, filed Jan 15, 2018)**

Title: Methods and devices for preventing computationally explosive calculations in a computer for model parameters distributed on a hierarchy of geometric simplices

Inventor: Chester J Weiss

Abstract: A computer-implemented method of preventing computationally explosive calculations. The method includes obtaining, by a processor of the computer, measured data of one of a physical process or a physical object; performing hierarchical numerical modeling of a physical process inclusive of an Earth model containing at least one of (a) infrastructure in the ground and (b) a formation feature in the ground, wherein predicted data is generated; comparing the measured data to the predicted data to calculate an estimated error; analyzing the estimated error via an inversion process to update the at least one of the Earth model and infrastructure model so as to reduce the estimated error and to determine a final composite Earth model of at least one of the infrastructure and the feature; and using the final composite Earth model to characterize at least one of the process and the physical object.

1.5. PUBLISHED WORK SUPPORTED BY THE ACCOMPLISHMENTS OF THIS LDRD

1.5.1. Peer–Reviewed Publications

[1] Swidinsky A and CJ Weiss, On coincident loop transient electromagnetic induction logging, *Geophysics*, **82**, E211 (2017).

[2] Weiss CJ, Finite element analysis for model parameters distributed on a hierarchy of geometric simplices, *Geophysics*, **82**, E155 (2017).

[3] Wilt M, E Um C Weiss, D Vasco, P Petrov, G Newman and Y Wu, Wellbore Integrity assessment with casing–based advanced sensing, *Proceedings of 43 Workshop on Geothermal Reservoir Engineering* 1–7 (2018).

[4] Beskardes GD and CJ Weiss, Modeling DC responses of 3D complex fracture networks, *Geophysical Journal International*, **214**, 1901–12 (2018).

[5] Weiss CJ and BG van Bloemen Waanders, On the convergence of Neumann series for electrostatic fracture response, *Geophysics*, **84**, E47–55, (2019).

[6] Downs C, CJ Weiss and S Kruse, Forward models to guide interpretations of EMI data in highly conductive environments, *Geophysics* (in revision, 2019).

[7] Um, E, Wilt M, CJ Weiss, G Nieuwenhuis and K MacLennan, Casing integrity mapping using top-casing electrodes and surface based electromagnetic fields, *Geophysics* (accepted, 2019).

[8] Beskardes GD, WA McAliley, M Ahmadian, DT Chapman, CJ Weiss and JE Heath, Power density distribution in subsurface fractures due to an energized steel well-casing source, *Journal of Environmental and Engineering Geophysics*, **24**, 285–297 (2019).

[9] Weiss CJ, BG van Bloemen Waanders and H Antil, Fractional operators applied to geophysical electromagnetics, *Geophysical Journal International*, (in revision, 2019).

[10] Beskardes GD and CJ Weiss, Electrical signatures of fractures near energized geometrically-complex, steel-cased wells, *Geophysics*, (in revision, 2019).

[11] Antil H, M D'Elia, C Glusa, B van Bloemen Waanders and C J Weiss, A fast solver for the fractional Helmholtz equation, *SIAM Journal of Scientific Computing*, (to be submitted, September, 2019).

[12] Beskardes GD, E Um, M Wilt and CJ Weiss, The effects of well casing corrosion and completion design on geo–electrical response in mature wellbore environments, *Geophysics*, (to be submitted, September 2019).

1.5.2. Peer–Reviewed Extended Abstracts with Conference Presentation

[13] Weiss CJ, Hierarchical material properties in finite element modeling: An example in 3D DC resistivity modeling of infrastructure, 3DEM-6, 6th International Symposium on Three-Dimensional Electromagnetics, Berkeley CA, 4pp, (2017).

[14] Weiss CJ and G Wilson, A new hierarchical finite element method for compact representation of oilfield infrastructure, *SEG Annual Meeting, Expanded Abstracts*, 5pp, (2017).

[15] Weiss CJ, E Um and M Wilt, Effects of completion design on electrically stimulated casing and its 3D response, *SEG Annual Meeting, Expanded Abstracts*, 5pp, (2018).

[16] Beskardes GD and CJ Weiss, 3D DC resistivity modeling of complex fracture networks, *SEG Annual Meeting, Expanded Abstracts*, 5pp, (2018).

[17] Weiss CJ, GD Beskardes and BG van Bloemen Waanders, Hierarchical material property representation in finite element analysis: Convergence behavior and the electrostatic response of vertical fracture sets, *SEG Annual Meeting, Expanded Abstracts*, 5pp, (2018).

[18] Wilt M, E Um, K MacLennan, CJ Weiss, and GD Beskardes, Case histories applying top-casing electrodes and surface based EM fields for well integrity mapping, *SEG Annual Meeting, Expanded Abstracts* (2019).

1.5.3. Short Abstracts and Conference Presentations

[19] Weiss CJ, Electromagnetic modeling of geology cluttered with infrastructure and other thin conductors: a finite element method for hierarchical model parameters on volumes, faces and edges of an unstructured grid, *SIAM Conference on Math. and Comp. Issues in the Geosciences*, Erlangen Germany, 2017. (INVITED).

[20] Van Bloemen Waanders BG, H Antil, D Ridzal and CJ Weiss, Fractional differential operators to detect multi-scale geophysical features, *SIAM Conference on Math. and Comp. Issues in the Geosciences*, Erlangen Germany, 2017.

[21] Weiss CJ, Electromagnetic modeling of geology cluttered with infrastructure and other thin conductors: a finite element method for hierarchical model parameters on volumes, faces and edges of an unstructured grid, *Society of Professinal Well Log Analysts Resistivity Sig Fall 2017 Meeting*, Houston TX, 2017. (INVITED)

[22] Weiss CJ and GA Wilson, Hierarchical material properties in finite element analysis: The oilfield infrastructure problem, *AGU Fall Meeting, Near Surface Session*, New Orleans LA, 2017.

[23] Wu Y, M Wilt, E Um, D Vasco, P Petrov, G Newman, CJ Weiss, P Cook and T Wood, WISE CASING: **W**ellbore **I**ntetrity as**SE**ssment with **C**asing–based **A**dvanced Sen**SING**,*Stanford Geothermal Workshop 2018 Annual Meeting*, Stanford CA, 2018.

[24] van Bloemen Waanders BG, CJ Weiss and H Antil, Fractional Helmholtz to help detect fine scale features, *Presented at 24th Workshop on Electromagnetic Induction in the Earth*, Helsignør, Denmark, August 13–20, 2018.

[25] Beskardes GD and CJ Weiss, DC electrical responses of complex fracture networks in 3D conducting media, *Presented at 24th Workshop on Electromagnetic Induction in the Earth*, Helsignør, Denmark, August 13–20, 2018.

[26] CJ Weiss and GD Beskardes, Hierarchical material properties in the solution to Maxwell's equations: Theory and applications in applied geophysics, *Presented at 24th Workshop on Electromagnetic Induction in the Earth*, Helsignør, Denmark, August 13–20, 2018.

[27] Weiss CJ, GD Beskardes and B G van Bloemen Waanders, Brute force evaluation of Neumann series adequacy for electrically conductive fracture response in the presence of strong cultural artifacts, *AGU Fall Meeting, Near Surface Session*, Washington DC, 2018.

[28] Beskardes GD and CJ Weiss, 3D DC Electrical Responses of Complex Fractured Environments Modelled by Hierarchical Finite Element Method (Hi-FEM), *AGU Fall Meeting, Geo/Paleo/Electromag Session*, Washington DC, 2018.

[29] Antil H, CJ Weiss and BG van Bloemen Waanders, Fractional Helmholtz to help detect fine scale features, *AGU Fall Meeting, Geo/Paleo/Electromag Session*, Washington DC, 2018.

[30] Beskardes GD and CJ Weiss, The effects of well casing corrosion and completion design on geo–electrical response in mature wellbore environments, *AGU Fall Meeting, Geo/Paleo/Electromag Session*, San Francisco, CA, 2019.

[31] Weiss, CJ, GD Beskardes and C Downs, The unstructured APhiD: A finite element formulation of Maxwell's equations using Lorenz–gauged potentials, *AGU Fall Meeting, Geo/Paleo/Electromag Session*, San Francisco, CA, 2019.

2. A HIERARCHICAL FINITE ELEMENT FRAMEWORK

2.1. SUMMARY

A resurgence of interest in the problem of electrical or electromagnetic scattering from thin conductors, either on a line or in a plane, has been motivated in recent years by time–lapse fracture monitoring in the near surface, enhanced geothermal reservoirs and unconventional hydrocarbon plays. However, finite element modeling of small electrical features in large computational domains results in a disproportionately large number of elements concentrated in volumetrically insignificant fraction of the mesh, and focuses computational resources away from areas of interest elsewhere, such as receiver locations. In the work described here, a novel hierarchical electrical model is proposed for unstructured tetrahedral finite element meshes, where the usual volume–based conductivity on tetrahedra is augmented by facet– and edge–based conductivity on the infintesimally thin regions between elements. Doing so allows a slender borehole casing of arbitrary shape to be coarsely approximated by set of connected edges on which a conductivity–area product is explicitly defined. Similarly, conductive fractures are approximated by a small number of connected facets that, together, may warp and bend with the mesh topology at no added cost of localized mesh refinement. Benchmarking tests of the direct current (DC) resistivity problem show excellent agreement between the facet/edge representations and independent analytic solutions. Consistency tests are also favorable between facet/edge and volume representations. Building on prior work in DC modeling of a single horizontal well, a multilateral well casing and fracture set is simulated, yielding estimates of borehole casing voltage and surface electric fields measurable with existing sensor technology. Lastly, the implications on broadband electromagnetic simulation with the proposed hierarchical conductivity model are discussed – in particular, its utility for describing variations in both magnetic permeability and electrical conductivity.

2.2. INTRODUCTION

A common requirement in numerical modelling of geophysical experiments, especially in electrical and electromagnetic methods, is the need to effectively capture a broad range of length scales in a single simulation, from the field scale over which sensors are deployed and regional geologic trends are dominant, to the fine scale where anthropogenic clutter and geologic details such as fractures have the potential to broadcast a disproportionate response. For example, it's

well known that metallic clutter such as rails, pipes and borehole casings, while volumetrically insignificant over the field scale, can generate significant and fully coupled, secondary electric and magnetic fields whose magnitude is comparable, if not larger, to the signal of interest from a geologic target (Fitterman, 1989; Fitterman et al., 1990). The challenge, from a computational perspective, is how best to accurately and economically simulate the response of both the large and the small in a given model. Variable mesh resolution in a computational model is nothing new, and there is a mature literature devoted to mesh refinement schemes in finite element, difference and volume methods. Consider, however, discretization of steel borehole casing in a computation over a modest field scale – say, a 1×1 km patch of ground and extending 1 km deep into the earth. At 0.1 m outer radius for the steel casing and 0.025 m wall thickness, a regular tetrahedron with edge length 0.025 m occupies a volume $(0.025\,\mathrm{m})^3/(6\sqrt{2}) = 1.84 \times 10^{-6}$ m^3 and therefore 500 m of casing would require $(500\,\mathrm{m})\left((0.1\,\mathrm{m})^2 - (0.075\,\mathrm{m})^2\right)\pi/(1.84 \times 10^{-6}\,\mathrm{m}^3) = 3.7 \times 10^6$ tetrahedra at the coarsest discretization. Over a 1 km^3 simulation volume finely discretized at, say 10 m, roughly $3.7/(3.7+8.5) \times 100\% = 30\%$ of the tetrahedra in the mesh will be devoted to $6.9 \times 10^{-7}\%$ of the mesh volume. For longer casings, typical of a production well, these ratios become even more extreme, especially considering larger physical domains for the computation and coarse meshing away from areas of interest. Furthermore, although (with proper mesh design and problem formulation) the electromagnetic problem can be solved for over domains of this topological size and larger, the computational resources required to do so become significant, typically resulting in specialized algorithms designed for parallel compute architectures (Commer et al., 2015; Um et al., 2015; Haber et al., 2016).

Hence, there's been considerable effort spent on alternative solutions to the problem of computing electric and electromagnetic fields scattered from thin boreholes subject to excitation by external sources. Nearly all are for simplified geometries of straight conductors in a layered or uniform medium and rely on either analytic or integral equation methods (e.g. Wait, 1952; Hohmann, 1971; Parry and Ward, 1971; Howard, 1972; Wait, 1957; Wait and Williams, 1985; Williams and Wait, 1985; Johnson et al., 1987; Schenkel and Morrison, 1990; Patzer et al., 2017). Qian and Boerner (1995) is a notable exception in that it considers the response of a sinuous conductor in a layered medium through integral equation methods. Extension of any of the work just cited, in an analytic sense, to generalized three–dimensional (3D) geometries has not been forthcoming.

In addition to the brute force discretization approach, where the high cost of borehole meshing is paid in full through fine scale discretization and parallelization (Commer et al., 2015; Hoversten et al., 2015; Um et al., 2015), or reduced by considering a slightly larger casing (hence, fewer elements) at the cost of sacrificing true geometric conformity between the borehole/earth interface (Haber et al., 2016; Weiss et al., 2016), the equivalent resistor network approach has also received some attention (Yang et al., 2016). Based on cross borehole tomography, where the borehole casing is exploited as an electrode (Newmark et al., 1999; Daily et al., 2004), Yang et al. (2016) construct a Cartesian grid of conductive blocks and assign electrical conductivity values to the blocks, along with the faces and edges between the blocks. Thin conductors are economically represented by face and edge elements of the mesh and electric scalar potential at the mesh nodes is computed by solving the linear system of equations resulting from volume averaging of the two Kirchhoff circuit laws. Yang et al. (2016) recognize the similarity between the coefficient matrix

of this linear system of equations and the more general $\nabla \cdot \sigma \nabla$ operator describing direct current (DC) excitation of a conducting medium σ, and rightfully point out that "regular" DC resistivity modeling (presumably finite element, volume or difference) is done only with volume–based conductivity cells and therefore does not accommodate edge– and face–based conductivity elements.

In the work described here, the concept of a hierarchical electrical structure – one in which electrical properties of conducting media are associated with volumes, facets and edges – is developed for the 3D DC resistivity problem, and in particular, for finite element analysis on unstructured tetrahedral grids. In doing so, the connection is drawn between the (Yang et al., 2016) circuit model and continuum modelling of fully heterogeneous conductivity distributions where edges and facets are free to be arbitrarily oriented and not constrained to a Cartesian grid. To summarize the algorithmic consequences of the proposed hierarchical model, we find that the global stiffness matrix arising from the governing Poisson equation is modified to also include element stiffness matrices for two–dimensional facets and one–dimensional edges, thus explicitly keeping the face and edge conductivities "local" to their corresponding nodes rather than distributed over an entire 3D element. The remainder of the paper is organized as follows: a discussion of the theory behind the hierarchical model; benchmarking and consistency tests to exercise the edge, facet and volume representations; and, a simulated "field" example where the DC response is computed for a idealized multilateral well system in the presence of conducting fractures.

2.3. THEORY

For simplicity, consider the Poisson equation governing the distribution electric scalar potential u throughout a 3D anisotropic medium $\boldsymbol{\sigma}$, subject to a steady electric current density $\mathbf{J}_s$:

$$-\nabla \cdot (\boldsymbol{\sigma} \cdot \nabla u) = f \tag{2.1}$$

where f is given by $\nabla \cdot \mathbf{J}_s$ and $\boldsymbol{\sigma} = \text{diag}(\sigma_{11}, \sigma_{22}, \sigma_{33})$ is a piecewise–constant, rank–2 tensor in some local principal axes reference frame defined by orthogonal unit vectors $\hat{\mathbf{e}}_1$, $\hat{\mathbf{e}}_2$ and $\hat{\mathbf{e}}_3$. That is, the local principal axes reference frame is free to vary spatially throughout the medium. In formulating the variational problem based on Eq (2.1), we introduce a "test" function v and integrate over the model domain Ω, on whose bounding surface we impose either a homogeneous Dirichlet or Neumann boundary condition. Integration by parts, followed by application of Gauss's Theorem and the homogeneous boundary conditions just described results in

$$\int_\Omega \nabla v \cdot (\boldsymbol{\sigma} \cdot \nabla u)\ dx^3 = \int_\Omega v f\ dx^3. \tag{2.2}$$

Pause, for a moment, to consider how the integrand on the left hand side of Eq (2.2) is affected by variability in the principal conductivities σ_{11}, σ_{22} and σ_{33}. In the case where $\boldsymbol{\sigma} = \text{diag}(\sigma, \sigma, \sigma)$ the medium is by definition isotropic and, hence, it is simple to show that $\nabla v \cdot (\boldsymbol{\sigma} \cdot \nabla u) = \sigma \nabla v \cdot \nabla u$. If instead, $\boldsymbol{\sigma} = \text{diag}(0, \sigma, \sigma)$, one finds that $\nabla v \cdot (\boldsymbol{\sigma} \cdot \nabla u) = \sigma \nabla_{23} v \cdot \nabla_{23} u$ where ∇_{23} is the two-dimensional gradient operator in the $\hat{\mathbf{e}}_2$-$\hat{\mathbf{e}}_3$ plane of the principal axes

reference frame. Taking this one step further, the case where $\boldsymbol{\sigma} = \mathrm{diag}(\sigma, 0, 0)$ yields $\nabla v \cdot (\boldsymbol{\sigma} \cdot \nabla u) = \sigma \nabla_1 v \cdot \nabla_1 u$ with ∇_1 being the spatial derivative in the $\hat{\mathbf{e}}_1$ direction.

At this point we've done nothing more that understand how the integrand on the left side of Eq (2.2) collapses to a simpler form under particular symmetries in $\boldsymbol{\sigma}$. This is a necessary, but insufficient condition for the problem of defining electrical conductivity over a hierarchy of geometric simplices such as volumes, facets and edges of a finite element mesh. To complete the development, let's articulate further the details of the electrical conductivity function $\boldsymbol{\sigma}$ and define it by the composite function:

$$\boldsymbol{\sigma}(\boldsymbol{x}) = \sum_{e=1}^{N_V} \sigma_e \boldsymbol{\psi}_e^V(\boldsymbol{x}) \; + \; \sum_{e=1}^{N_F} s_e \boldsymbol{\psi}_e^F(\boldsymbol{x}) \; + \; \sum_{e=1}^{N_E} t_e \boldsymbol{\psi}_e^E(\boldsymbol{x}), \tag{2.3}$$

with hierarchical, rank–2 basis functions

$$\boldsymbol{\psi}_e^V(\boldsymbol{x}) = \mathrm{diag}(1,1,1) \begin{cases} 1 & \text{if } \boldsymbol{x} \in \text{volume } e \\ 0 & \text{otherwise} \end{cases}, \tag{2.4}$$

$$\boldsymbol{\psi}_e^F(\boldsymbol{x}) = \mathrm{diag}(0,1,1)_e \begin{cases} 1 & \text{if } \boldsymbol{x} \in \text{facet } e \\ 0 & \text{otherwise} \end{cases}, \tag{2.5}$$

and

$$\boldsymbol{\psi}_e^E(\boldsymbol{x}) = \mathrm{diag}(1,0,0)_e \begin{cases} 1 & \text{if } \boldsymbol{x} \in \text{edge } e \\ 0 & \text{otherwise} \end{cases}. \tag{2.6}$$

For clarity, the number of volumes, facets and edges are denoted by N_V, N_F, and N_E, respectively. In Eq (2.5,2.6), the diagonal rank–2 tensor is subscripted by e to indicate representation in the local $\hat{\mathbf{e}}_1$-$\hat{\mathbf{e}}_2$-$\hat{\mathbf{e}}_3$ frame (Figure 2-1). For facets, we take the $\hat{\mathbf{e}}_2$ and $\hat{\mathbf{e}}_3$ directions to lie in the plane of the eth facet, where for edges, we take the $\hat{\mathbf{e}}_1$ direction to lie parallel to the eth edge. Note that volume integration of Eq (2.3) with the definitions laid out in Eq (2.4 through 2.6) takes on the SI units [S·m^2]. Hence, the SI units of coefficients s_e and t_e must be [S] and [S·m], respectively. That is, s_e represents the conductivity–thickness product of facet e, and t_e represents the product of conductivity and cross-sectional area for edge e.

Continuing from the integral form in Eq (2.3), completion of the variational problem statement – from which derives the finite element system of equations – proceeds along the usual way of defining the vector spaces on which v and u reside. This has been covered many times before in the literature (e.g. Rücker et al., 2006; Wang et al., 2013; Weiss et al., 2016) and omitted in the present discussion assuming familiarity by the reader. Defining the set of piecewise continuous, linear basis functions $\{\phi_i(\boldsymbol{x})\}_{i=1}^N$ over N nodes of the tetrahedral mesh defining our computational domain Ω,

$$\phi_i(\boldsymbol{x}) = \begin{cases} 1 & \boldsymbol{x} = \boldsymbol{x}_i \\ 0 & \boldsymbol{x} = \boldsymbol{x}_{j \neq i} \\ \text{pcws linear} & \text{otherwise} \end{cases} \tag{2.7}$$

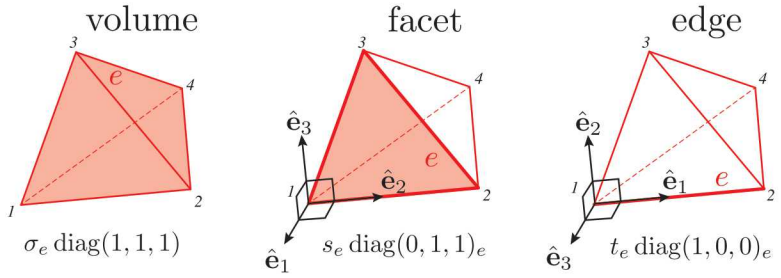

Figure 2-1. Hierarchy of volumes (left), facets (middle) and edges (right) on which the conductivity model Eq (2-3) is defined. Note that for facets and edges, the $\hat{\mathbf{e}}_1$ direction in the local principal axis references frame oriented normal to the facet and along the edge, respectively.

we can write the finite element solution $u = \sum_{i=1}^{N} u_i \, \phi_i(\boldsymbol{x})$ and test functions $v = \sum_{i=1}^{N} v_i \, \phi_i(\boldsymbol{x})$. Substituting these series expansions into the Eq (2.2) and evaluating the volume integrals results in a $N \times N$ system of linear equations

$$\mathbf{K}\mathbf{u} = \mathbf{b}, \tag{2.8}$$

where elements of $\mathbf{K}$ are integrals of $\nabla\phi_i \cdot \boldsymbol{\sigma} \cdot \nabla\phi_j$, the vector $\mathbf{u}$ contains the coefficients $u_1, u_2, \ldots$, and $\mathbf{b}$ is the vector of inner products (ϕ_i, f). Observe that the linear system is independent of the coefficients $v_1, v_2, \ldots$, and hence, its solution $\mathbf{u}$ is independent of v, as required.

The novelty of the preceding finite element formulation Eq (2.8) lies in the structure of $\mathbf{K}$ as a consequence of the conductivity model in Eq (2.3), as will soon be made apparent. Focusing on the first of the three summations in Eq (2.3), taken over the N_V tetrahedra within the domain Ω, we may write

$$\int_\Omega \nabla v \cdot \left[\sum_{e=1}^{N_V} \sigma_e \boldsymbol{\psi}_e^V(\boldsymbol{x}) \right] \nabla u \, dx^3 = \sum_{e=1}^{N_V} \sigma_e \int_{V_e} \nabla v \cdot \nabla u \, dx^3, \tag{2.9}$$

where V_e is the volume described by the eth tetrahedron in the model domain Ω. Substitution of the basis functions Eq (2.7) into Eq (2.9) leads to the well–known, three–dimensional "element stiffness matrices" $\mathbf{K}_e^4$, given in local node enumeration (Figure 2-1, left) as

$$\sum_{e=1}^{N_V} \sigma_e \int_{V_e} \nabla v \cdot \nabla u \, dx^3, = \sum_{e=1}^{N_V} \sigma_e \, \mathbf{v}_e^{\mathrm{T}} \mathbf{K}_e^4 \mathbf{u}_e, \tag{2.10}$$

with $\mathbf{K}_e^4 = \left\{ \int_{V_e} \nabla\phi_i \cdot \nabla\phi_j \, dx^3 \right\}_{i,j=1}^4$ and coefficients $\mathbf{v}_e = (v_1, \ldots, v_4)_e^{\mathrm{T}}$, $\mathbf{u}_e = (u_1, \ldots, u_4)_e^{\mathrm{T}}$. Observe, now, the consequences of defining the "transverse conductance" s_e as done in the second summation in Eq (2.3) over the N_F facets of the unstructured tetrahedral mesh:

$$\int_\Omega \nabla v \cdot \left[\sum_{e=1}^{N_F} s_e \boldsymbol{\psi}_e^F(\boldsymbol{x}) \right] \nabla u \, dx^3 = \sum_{e=1}^{N_F} s_e \int_{F_e} \nabla_{23} v \cdot \nabla_{23} u \, dx^2, \tag{2.11}$$

where F_e is the area of the eth facet and ∇_{23} is the two–dimensional gradient in the plane of the

facet. As a result, the right hand side of Eq (2.11) reduces to the two–dimensional element stiffness matrices $\mathbf{K}_e^3$ coupling only those three basis functions on one facet of a given tetrahedron:

$$\sum_{e=1}^{N_F} s_e \int_{F_e} \nabla_{23} v \cdot \nabla_{23} u \, dx^2, = \sum_{e=1}^{N_F} s_e \, \mathbf{v}_e^{\mathrm{T}} \mathbf{K}_e^3 \mathbf{u}_e. \tag{2.12}$$

In keeping with the local enumeration (Figure 2-1) of Eq (2.10), $\mathbf{K}_e^3 = \left\{ \int_{F_e} \nabla_{23} \phi_i \cdot \nabla_{23} \phi_j \, dx^2 \right\}_{i,j=1}^{3}$, $\mathbf{v}_e = (v_1, v_2, v_3)_e^{\mathrm{T}}$ and $\mathbf{u}_e = (u_1, u_2, u_3)_e^{\mathrm{T}}$. Evaluation third term in Eq (2.3), containing conductivity–area products t_e defined on mesh edges (Figure 2-1) proceeds in a similar way, revealing the underlying presence of the 1D element stiffness matrices $\mathbf{K}_e^2 = \left\{ \int_{E_e} \nabla_1 \phi_i \cdot \nabla_1 \phi_j \, dx \right\}_{i,j=1}^{2}$. Thus, we find that the composite global matrix $\mathbf{K}$ in the finite element system of equations is constructed by a sum of one–, two– and three–dimensional element stiffness matrices

$$\mathbf{K} = \sum_{e=1}^{N_V} \sigma_e \mathbf{K}_e^4 + \sum_{e=1}^{N_F} s_e \mathbf{K}_e^3 + \sum_{e=1}^{N_E} t_e \mathbf{K}_e^2 \tag{2.13}$$

capturing the electrical properties localized in a hierarchy over volumes, facets and edges of the finite element mesh.

Observe that the construction in Eq (2.13) arises from two key steps. First, through use of the rank–2 tensors $s_e \, \mathrm{diag}(0,1,1)_e$ and $t_e \, \mathrm{diag}(1,0,0)_e$, we restrict the coupling between neighboring nodes be consistent with facets and edges, respectively. Second, by defining the material property basis functions $\boldsymbol{\psi}_e^F$ and $\boldsymbol{\psi}_e^E$ in Eq (2.5 and 2.6) as non–zero only on facets and edges, the effect on u of s_e and t_e variations in the model is weighted by facet area and edge length, respectively, rather than tetrahedral volume. Hence, there is consistency between two meshes which share a common localized s or t distribution, but differ in how these facets and edges are connected to the rest of the mesh. It's also relevant to point out that although Eq (2.13) is built using the simple case of linear nodal elements, the same construction applies to nodal elements of higher polynomial order. Details on constructing $\mathbf{K}_e^3$ and $\mathbf{K}_e^2$ for linear nodal elements are found in Appendix A.

It's interesting to note that although we've only considered the scalar DC resistivity problem, an analogous construction is relevant to 3D finite element solutions of the frequency–domain electromagnetic induction problem where terms such as $\mathbf{v} \cdot (\boldsymbol{\sigma} \cdot \mathbf{u})$ appear in "mass" term of the governing second–order equation (e.g. Everett et al., 2001; Mukherjee and Everett, 2011; Schwarzbach et al., 2011; Um et al., 2015). In these cases it's clear that instead of a summation of element stiffness matrices Eq (2.13), the global system of equations would be constructed by a sum of element mass matrices.

2.4. BENCHMARKING AND CONSISTENCY CHECKING

To test the validity of the conductivity model Eq (2.3) and its manifestation in the finite element stiffness matrix Eq (2.13), finite element solutions are compared against the independent analytic solutions for simplified geometries. Here, the effects of facet– and edge–based conductivity are computed by modification — specifically, inclusion of the second and third summations in Eq

(2.13) — of the finite element software previously benchmarked in Weiss et al. (2016) for classical tet/volume based conductivity. In Weiss et al. (2016), the finite element solution was computed for a thin, conducting cylinder oriented vertically in a uniform halfspace and excited by point current source on the boundary of the halfspace, some distance laterally from top of the cylinder which is coincident with the halfspace boundary (Figure 2-2, inset). This problem geometry admits an analytic solution (Johnson et al., 1987) for perfectly conducting cylinders, which was favorably compared against multiple finite element solutions for a 10^5 S/m cylinder in a 0.001 S/m halfspace.

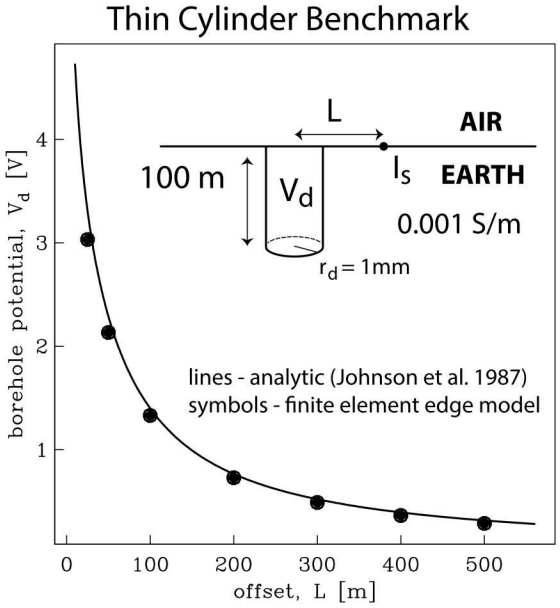

Figure 2-2. Comparison between finite element (symbols) and analytic (line) solutions for buried, thin and perfectly conducting cylinder (see inset for geometry). Plotted is the electric scalar potential V_d on the cylinder due to a 1 A point current source located a distance L away from the top end of the conductor. Analytic solutions are given for cylinder radius of 0.001 m, a dimension well within the asymptotic limit for an infinitesimally thin conductor.

For the first benchmark test here, the (Johnson et al., 1987) buried cylinder solution is compared against a finite element solution using only edge based conductivities – the last term in Eq (2.3) – for a range of cylinder/source offsets. Analytic solutions were computed in the asymptotic limit of an infinitely thin, perfect conductor with radius 0.001 m, a value taken practically to be several orders of magnitude smaller than the geophysical field scale. Finite element solutions were computed assuming a value $t = 10^4$ S·m for those edges coincident with the central axis of the cylinder. Elsewhere, t was set to zero, and hence the summation in the last term of Eq (2.13) is limited to only those edges representing the cylinder. Assuming a 0.001 m radius, this value of t is equivalent to conductivity value $\sim 3.3 \times 10^9$ S/m, a value well in excess of that for metals and even graphene. Volume conductivity was set to 0.001 S/m for all tetrahedra in the domain,

including those sharing an edge with a non–zero t value. There is strong agreement between the finite element and analytic solutions (Figure 2-2), with errors on the order of a few percent - a number consistent with the previous Weiss et al. (2016) benchmark and, in general, with total–field finite element results reported in the geophysical literature.

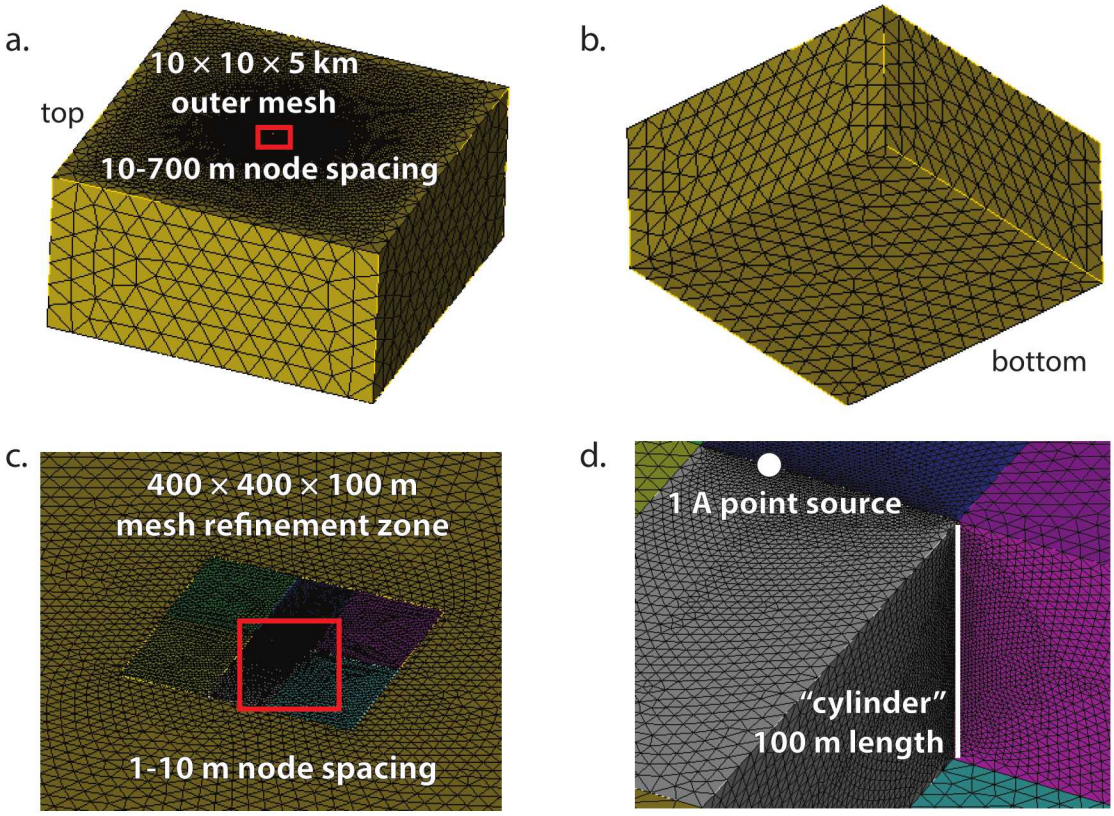

Figure 2-3. Top (a) and bottom (b) oblique views of the finite element mesh used for the benchmark exercise in Figure 2-2. Air region is assume to lie above the top surface in (a) and is excluded from the computational domain by application of a homogeneous Neumann boundary condition on the air/earth interface. In (c) a zoomed in view of the refinement zone highlighted by the red square in (a). In (d), further zooming on the red square in (c) with a cutaway showing the set of vertical edges representing the infinitesimally thin vertical cylinder in Figure 2-2.

Recall that a principal advantage of using edge–based conductivities is that thin conductors (or, potentially, resistors) such as that described above needn't be explicitly discretized in the computational grid. Rather, if their dimensions are small enough with respect to other features of interest, they may instead be represented as a set of infinitesimally thin edges, each connecting two nodes within the grid. Hence, the grid used in the benchmark just described contains no features attempting to replicate the interface between the cylinder and the halfspace in which it's embedded. Instead, the "cylinder" is approximated in the finite element mesh by a set of

continuous vertical edges (or line) with 1 m uniform node spacing, extending from the air/earth interface to a depth of 100 m. Node spacing between the 1 A surface point source and the cylinder is 1 m for source/cylinder separation less than 100 m, 10 m for separation values 100–250 m, and 30 m for separations beyond that, out to 500 m (Figure 2-3).

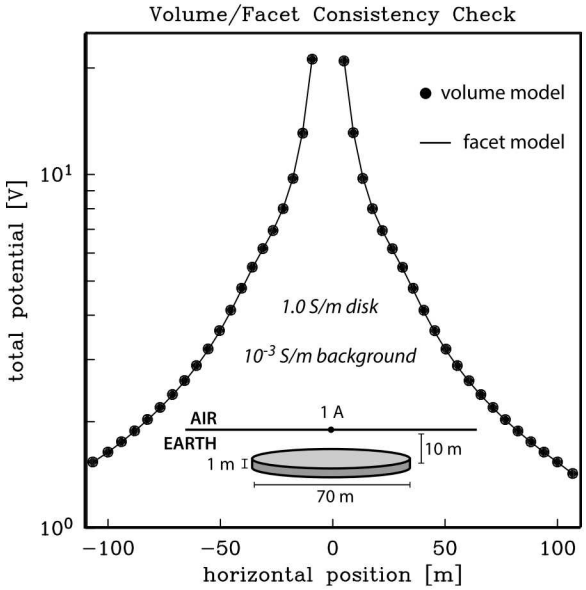

Figure 2-4. Comparison between finite element solutions of total electric potential for a moderately conductive, horizontal disk buried in a resistive halfspace subject to a 1 A point source on the air/earth interface (see inset). Shown by the circles are finite element solutions along the air/earth interface, centered over the disk, for the case where the disk is finite thickness and described by a conductivity value prescribed to tetrahedra within the disk volume. Shown by the dots are solutions where the disk is infinitely thin, with anomalous conductivity represented by an equivalent vertical conductance assigned to facets on the disk's top side.

Having demonstrated agreement between the volume–based conductivity model and analytic solutions (Weiss et al., 2016), and now between the infinitesimally thin edge–based conductivity model and analytic solutions (this study), we turn our attention to consistency between the facet– and volume–based conductivity models. In doing so, we complete the logical syllogism of benchmarking the hierarchical model concept in Eq (2.3). As an example calculation, take a 1 m thick disk of radius 35 m, lying horizontally at a depth of 10 m and excited by a unit amplitude point source centered above the disk (inset, Figure 2-4). Choosing a disk conductivity of 1.0 S/m and a background conductivity of 0.001 S/m, the computed values of the electric potential on the air/earth interface for a volume–based model, where the disk is represented by tetrahedra with edge lengths approximately 1.4 m and conductivity 1 S/m, are in strong agreement with computed values where the disk is represented by facets at a depth 10 m with conductance $s = 1$ S/m $\times 1$ m $= 1$ S (Figure 2-4). That is, for each model there are the same number of nodes ($N = 200,902$)

and tetrahedra ($N_V = 1,177,757$), of which $28,747$ were constrained to the volume of the thin disk. In the facet model, this subset of tetrahedra were assigned the background conductivity value, and instead, the $N_F = 8624$ triangles on the top side of the disk were assigned $s = 1$. Note that $N_F << N_V$ for the facet model, and therefore the added cost of computing the second summation in Eq (2-13) is minimal, especially when considering that there are 16 elements in each element matrix $\mathbf{K}_3^4$ versus only 9 in $\mathbf{K}_e^3$. Further calculations where disk conductivity is varied between 0.01 and 10 S/m show similar agreement for the smaller, and more sensitive, scattered potentials (Figure 2-5).

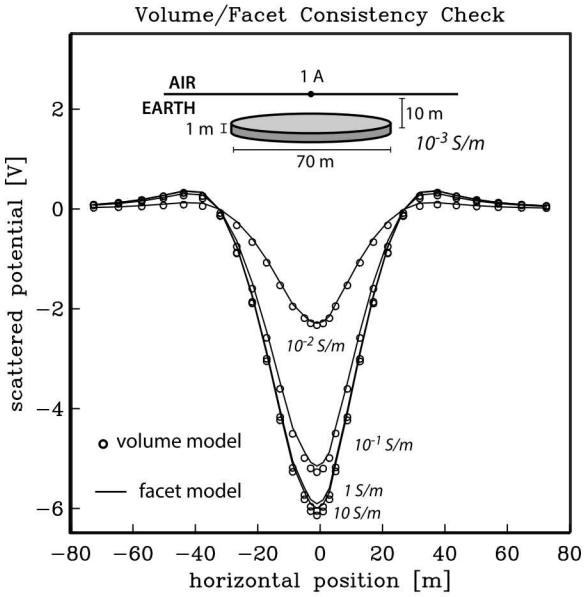

Figure 2-5. Comparison of finite element solutions of the scattered electric potential for a series of (0.01, 0.1, 1.0 and 10 S/m) conductive thin disks embedded in a 0.001 S/m halfspace, subject to a 1 A point source on the air/earth interface directly over disk center (see inset).

Examination of the cross section of electric field in a vertical plane through the center of the disk gives some indication of why the facet model is an appropriate representation for conductive features. Because the disk is conductive, one finds that the magnitude of the vertical gradient in the potential in the disk is far less than the magnitude in the horizontal direction (Figure 2-6). Hence, in the limit of very thin, but finitely conducting disk, the potential is reasonably approximated by a continuous, two-dimensional function along the disk face. In the limit of an infinitely conducting disk this function is, of course, a constant. In contrast, when the disk is resistive the potential is discontinuous in the vertical direction in the limit of an infinitely thin disk (Figure 2-7). The conductivity model Eq (2.3) is not invalidated in such a case – rather, the finite element basis itself must be modified to admit tears (discontinuities) in the solution. The mesh is modified such that a surface across which a discontinuity is to be enforced is twice discretized, with one set of nodes for facets corresponding to elements on one side of the mesh, and another set of nodes for facets of elements on the opposite side (Figure 2-8). Imposing a homogeneous Neumann boundary condition on the tear – quite easy to do – implies that the resistor is both

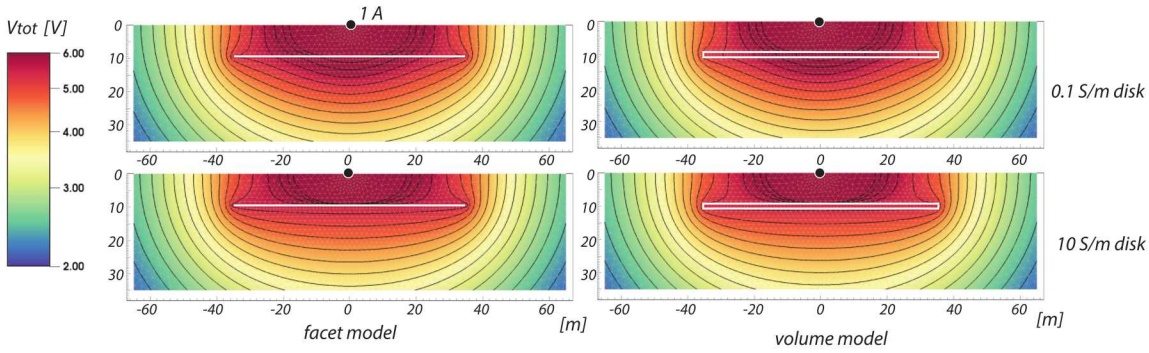

Figure 2-6. Vertical cross section of electric potential through the center of the disk in Figure 2-5 (left: fact model, right: volume model, top: 0.1 S/m disk, bottom 10 S/m disk).

infinitely thin and infinitely resistive. Algorithmically efficient means of accommodating an infinitely thin, but resistive, disk using the mesh tearing method are not immediately obvious at this time, but neither are they the focus of the current study. Further study of this tangential sub–topic is deferred to a future publication.

2.5. MULTI–LATERAL WELL SIMULATION

To demonstrate the flexibility of the proposed model representation, Eq (2.3), a set of numerical experiments have been devised which simulate the DC response of a multi-lateral well configuration, where the geology is described by conductivity σ on tetrahedral elements, the borehole is described by conductivity–area products t on tetrahedral edges and fractures are described by conductance s on tetrahedral facets. Thus, only the path of the borehole need be discretized, rather than actual borehole diameter and wall thickness. Similarly, only the fracture planes need discretization, and not some thin, but finite, slab populated by many small elements – a common, but computationally cumbersome approach (c.f. Commer et al., 2015; Um et al., 2015; Haber et al., 2016; Weiss et al., 2016). For the simulation results that follow, a multi–lateral well configuration is considered, consisting of a vertical borehole from which a set of 5 horizontal wells extending 1000 in length are located at 1000 m depth (Figure 2-9, right). With lateral separation of 200 m, these wells cover an area ~ 1 km^2. To minimize the effects of a complicated geology (e.g. Weiss et al., 2016), layering and heterogeneity are neglected and, instead, the wells reside in a uniform 0.001 S/m halfspace. Following the example in Weiss et al. (2016), the well system is energized by a 1 A source located in the heel of the central well. The well casing is discretized by a set of connected tetrahedral edges, geometrically conformal to the well bore path and with 20 m node spacing – equivalent to roughly 2 sections of standard well casing.

Recognizing that casing conductivity affects the DC electrical response, end member values 1×10^5 and 5×10^5 S·m of the conductivity–area product t in Eq (2.3) are considered. Assuming a 0.1 m radius well and with 0.025 m wall thickness, these t values correspond to casing

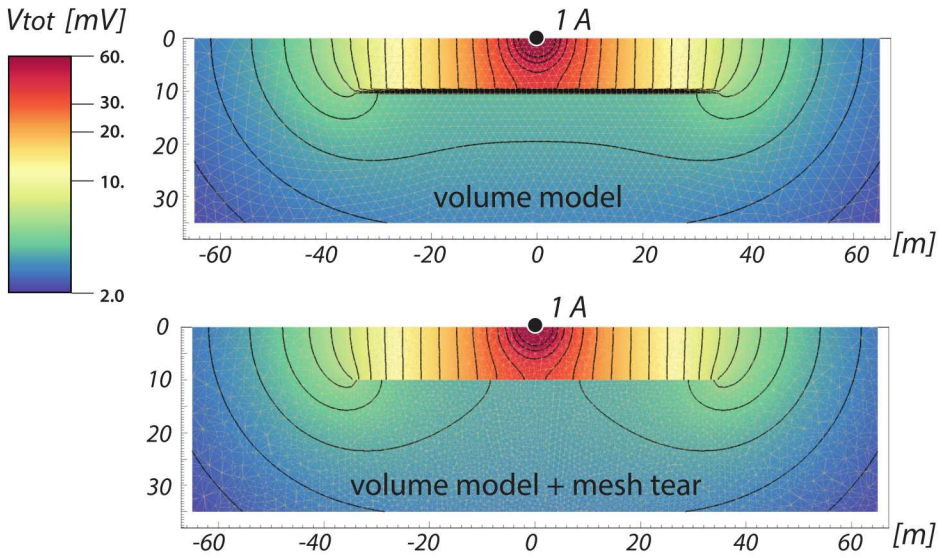

Figure 2-7. Vertical cross section of electric potential through the center of a resistive disk in a 1.0 S/m background, with geometry the same as shown in Figure 2-5. Top: Resistive disk is represented using a volume model with disk conductivity 0.001 S/m and thickness 1.0 m. Bottom: Finite thickness disk replaced with a circular tear in the finite element mesh coincident with the top surface of the disk, on which is imposed a homogeneous Neumann boundary condition, thus implying an infinitely thin and resistive disk.

conductivity 7.3×10^5 and 3.6×10^6 S/m, respectively. Although the well fluid inside the casing does constitute $\sim 56\%$ of the cross sectional area of the fluid–casing system under this geometry, its conductivity is so small (even with a generous upper bound for hypersaline brines at 10 S/m) that it contributes little to the overall t value. Under these assumptions, we find that the voltage drop along the horizontal well casings of a multi–lateral have magnitudes on the order of 10 mV for resistive casing and 1 mV for conductive casing (Figure 2-9, left). Inspection of the voltage gradients shows the direction taken by the casing current (not the leakage current) along the multi–lateral circuit, demonstrating agreement with Kirchhoff's current law, even though it is not explicitly imposed on the system. When considering the big picture of casing voltages and those distributed throughout the surrounding geology, one finds that the variation along the casing is small in comparison, and that the multi-lateral system energizes the formation between the wells to a voltage between 200 and 300 mV, outside of which there is a rapid decay to a few 10s of mV (Figure 2-10).

Fractures are introduced into the model as a set of four parallel ellipses, 100 m wide and 40 m tall, centered on the middle well of the multi–lateral, 200 m from the heel with 10 m spacing (Figure 2-11). Taking a high end–member estimate of $s = 1$ S total fracture conductance, the ellipses are discretized via triangular facets with 3 m edge length so that the elliptical shape is approximated to first order. As was shown in Weiss et al. (2016), the effect of the fractures is to

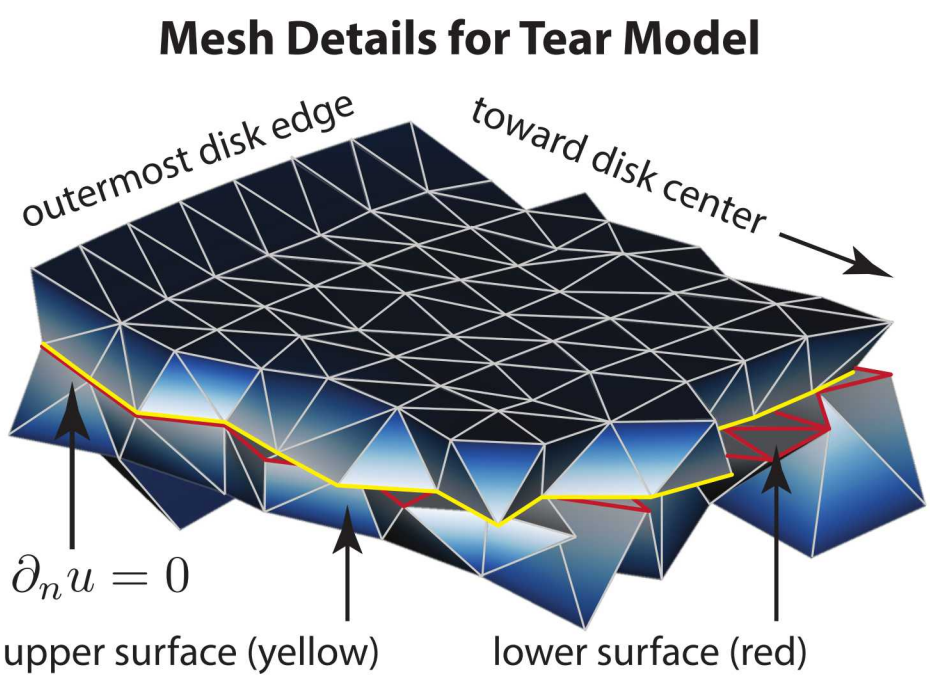

Figure 2-8. Close up of finite element mesh used for calculation of electric potential in Figure 2-7 (bottom), where a tear in the mesh – along with a homogeneous Neumann boundary condition – is imposed to represent an infinitely thin and infinitely resistive circular disk. Mesh edges corresponding to the upper (yellow) and lower (red) surfaces of the zero–thickness disk show that nodes on either side of the tear do not require a one–to-one spatial correspondence. Rather, each side may be discretized independently except on the perimeter where they must match. For scale, element edges are roughly 1 m in length in this figure.

lower the overall potential of the connected casing system (Figure 2-12). And whereas there is demonstrable leakage current in each of the modeling scenarios (fractures present and absent), the difference in casing potential between the two shows comparatively little along–casing variability, with the notable exception of the fracture location itself (Figure 2-13). This observation is consistent the the results in Weiss et al. (2016) where the voltage difference due to a fracture system can be reasonably approximated by uniform line charge along the casing plus a point charge of opposite sign at the fracture location.

As a final set of numerical experiments, the multi–lateral system is modified such that horizontal segments are interleaved from two, independent, downgoing wells but still offer the same coverage at 1000 m depth (Figure 2-14). In this design, the center and outermost wells are electrically connected through one vertical well, whereas the two intermediate wells are electrically isolated from the other three and connected instead by another vertical well. This scenario allows for testing of the passive coupling between isolated, but nearby, wells and

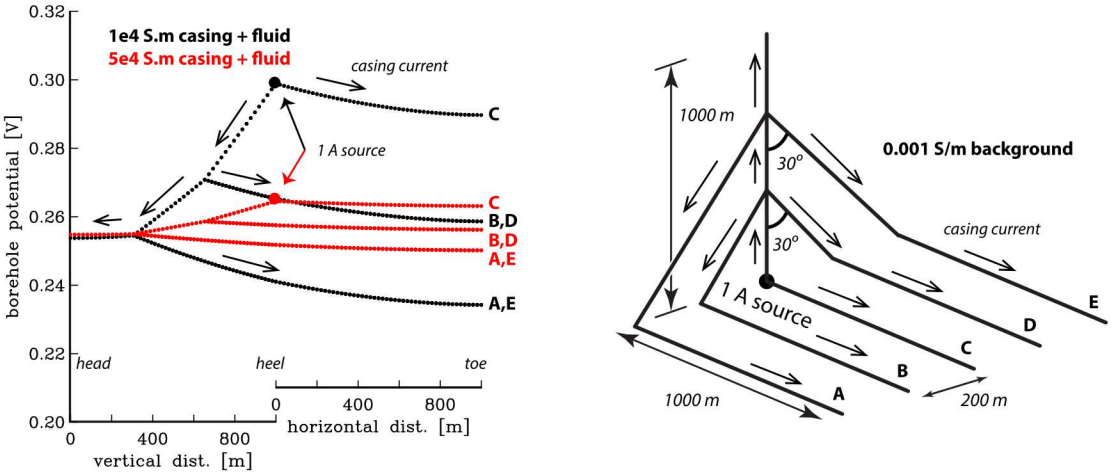

Figure 2-9. Casing voltage (left) for multi-lateral well geometry (right) in a 0.001 S/m formation. Assuming a 0.2 m diameter borehole casing with .025 m wall thickness, effect of casing conductivities 7.3×10^5 and 3.6×10^6 S/m are shown by the black and red curves, respectively. Averaged over the cross sectional area of the borehole, the fluid conductivity has negligible contribution to the total conductivity of the total conductivity–area product of the combined fluid–borehole system. Also shown (open arrows) is the direction of casing current given by the gradient of the casing potential.

addresses the question of fracture mapping by adjacent wells. As in the previous example, we see that among the connected wells, the effect of the fractures is to reduce the overall casing potential as energy is leaked into formation by the fractures. In response, the two coupled wells each realize an increase in electric potential as they effectively capture the energy lost through the fracture (Figure 2-15). Thus, the effect on the coupled wells is a voltage anomaly of opposite sign to that of the primary, fully connected wells. We also see that the casing current in horizontal section of the three primary wells is in the same direction as that in the two coupled wells (heel to toe in the primary is the same direction as toe to heel in the coupled). Voltage differences between the fracture/no–fracture case similar to that seen before, with the unsurprising observation that the voltage differences in the two coupled wells are much smaller than that in the three primary wells (Figure 2-16).

Estimates of the change in electric field due on the air/earth interface due the presence of fractures in these models show a considerable dependence on the well geometry (Figure 2-17). In particular, we find that the overall magnitude in the difference signal is significantly reduced in the case of the multi–lateral system when compared to the case of a single well – an observation consistent with comparatively less leakage current in the single well system. Additionally, there is a low amplitude anomaly over the toe of the fully connected multi–lateral system not seen in the single well example (Figure 2-17, middle). When a multi–lateral configuration is distributed between two vertical wells (Figure 2-17, bottom), the second vertical well connecting the two

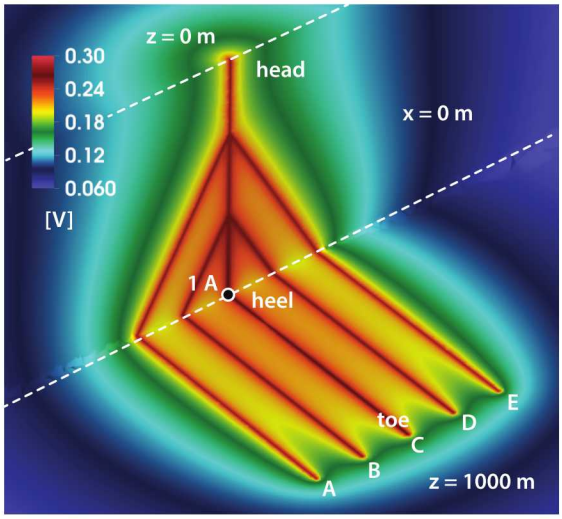

Figure 2-10. Example calculation of a multi-lateral casing excitation (cutaway view, units V) where the well casing is represented by an infinitesimally thin, edge-based conductivity model (middle term, Eq 2-3). Point 1 A source is located at the heel of the center well, C. Wells are 1000 m deep and extend 1000 m horizontally with a lateral separation of 200 m. Formation conductivity is 0.001 S/m; well casing + fluid represented by a line distribution of $t = 5 \times 10^4$ S.m (.1 m radius casing, 0.025 m wall thickness, conductivity 3.6×10^6 S/m).

interleaved horizontal sections acts as a current sink, thus increasing the potential gradient along a line connecting the two well heads. This effective "source" and "sink" is consistent with the (vertical) gradient in difference voltage seen at well head (Figure 2-16).

2.6. DISCUSSION

A few remarks are first offered to address the computational burden of modeling the fractures and borehole in the preceding examples. A set of 4 elliptical fractures with minor and major axes 20 and 50 m, respectively, have a combined surface area of $\pi \times 20$ m $\times 50$ m $=\sim 3142$ m^2. Discretized by (quasi) regular facets with edge length 3 m, the fractures require $N_F = 2616$ facets for their summation in Eq (2.3). Furthermore, with borehole discretization on 20 m node spacing, the coupled multi–lateral well system requires $N_E = 457$ edges in third summation of Eq (2.3). Following Weiss (2001) and Weiss et al. (2016), the finite element linear system of equations is solved iteratively, where at each iteration the action of the coefficient matrix is computed on the fly by summing over elements – of which, there are $N_V \sim 3$M tetrahedra (490k nodes) in the multi–lateral models. Hence, the number of additional floating point operations required for including the fractures well casing is small and results in a statistically insignificant increase in runtime for these models. In contrast, the effect of high casing and fracture conductivity is to

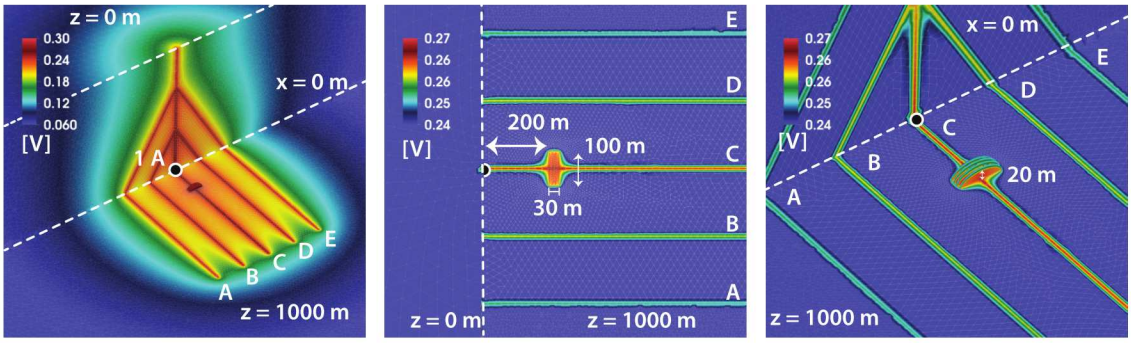

Figure 2-11. Total electric potential for the multi–lateral system in Figures 2-9 and 2-10, with the addition of a fracture system located 200 m downhole from the heel in well C. Fractures are modeled as a set of 4 infinitesimally thin ellipses, 60 m tall and 100 m wide, with 10 m separation, oriented normal to the well bore. For each, fracture conductance, s, is 1 S. (left: oblique view, full color scale; middle: plan view, compressed color scale; right, zoomed oblique view, compressed color scale).

increase the condition number of the finite element coefficient matrix, thus reducing the rate at which a Jacobi–preconditioned conjugate gradient solver converges (Figure 2-18) – an observation familiar to finite element practitioners. Run times for these models are on the order of a couple minutes, thoroughly unoptimized, on a MacBook Pro equipped with 16 GB memory and a dual–core 3 GHz Intel i7 CPU chip.

Geologic settings with elevated fracture conductivity, like that in the previous examples, can result from either natural causes such as secondary mineralization or engineered experiments where the fracture is filled with brine, a tracer fluid, or conductive proppant. With regard to the latter, production and completion of unconventionals typically requires proper accounting of the anisotropic effects of shales. Although the first term in Eq (2.3) – where the volume/tet based conductivity term resides – is written as isotropic conductivity (the product of a scalar σ_e with the rank 2 identity tensor), it's not clear that this is a necessary restriction. Rather, we are free to define the volume conductivity by a generalized, symmetric, rank 2 tensor in the (x, y, z) reference frame of the model domain. Doing so would allow for modelling transverse isotropic shales, of which there are only four degrees of freedom: two Euler angles describing the orientation of the bedding plane; and, two conductivity values representing the plane–parallel and plane–normal conductivities.

The benchmarking examples shown here demonstrate that hierarchical conductivity model Eq (2.3) is both self consistent and generates results that agree with independent reference solutions when the facets and edges are relatively conductive with respect to the volume elements. However, it's also been shown that the jump discontinuity in electric potential across the face of thin resistive disk requires more of the finite element formulation than the modified model Eq (2.3). When used in the context of DC resistivity simulations, the conductivity model must be accompanied by a suitable finite element discretization – one which admits step discontinuities –

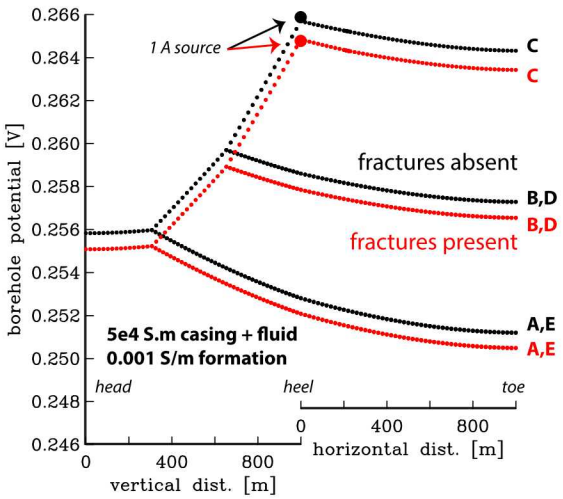

Figure 2-12. Effect of fractures on casing voltage of well bores A–E for the model shown in Figures 2-10 and 2-11.

for the evaluation of arbitrary conductivity structure. Extending the concept of the hierarchical material properties model to three–dimensional, time–dependent electromagnetics (either frequency domain or generalized time domain) is an open question best pursued, for several reasons, in future research. For example, the frequency domain problem has been cast is all varieties of magnetic–, electric– and potential–field formulations, and it remains to be understood how the facet– and edge–based conductivities may frustrate the numerical solution, as resistors do in DC, without additional mesh modification. In the context of exploration geophysics, the borehole examples presented here suggest investigating whether magnetic permeability can also be distributed by an analogous hierarchical model, thereby allowing for economical modeling of highly conductive and permeable steel casing. In principle, it appears that the mathematical structure of Eq (2.3) would admit such an idea, but at first blush, its implementation is problematic. That is, in the frequency domain electric field formulation, the governing equation in a source–free region is

$$\nabla \times \left[\boldsymbol{\mu}^{-1} \cdot (\nabla \times \mathbf{E})\right] + \mathrm{i}\omega\,(\boldsymbol{\sigma} \cdot \mathbf{E}) = 0,$$

and it's clear that although high–conductivity facets and edges are well represented by their corresponding s_e and t_e coefficients in $\boldsymbol{\sigma}$, a high–permeability edge or facet in $\boldsymbol{\mu}^{-1}$ results in analogous coefficients that, in the limit of infinite permeability, are zero and hence safely ignored. Recasting the governing Maxwell equations in terms of a second–order magnetic field formulation does not resolve the conflict, but rather shifts the problem from the $\boldsymbol{\mu}^{-1}$ term to the corresponding $\boldsymbol{\sigma}^{-1}$ term nested between $\nabla\times$. One possible workaround is to admit s_e and t_e coefficients with negative values, thus making a weighted sum (for unit consistency) of σ_e, s_e and t_e representative of the facet and edge conductance. However, doing so would still require compatibility with the underlying discretization, which in the case of DC resistivity, necessitated the introduction of tears in the finite element mesh. Lastly, it's conceivable that use of the hierarchical model, Eq (2.3), for conductivity, permeability, or both, may require re-evaluation of the time–stepping requirements for transient calculations since the facet and edge structures contained in the model are infinitesimally thin. Of course, such considerations could be avoided

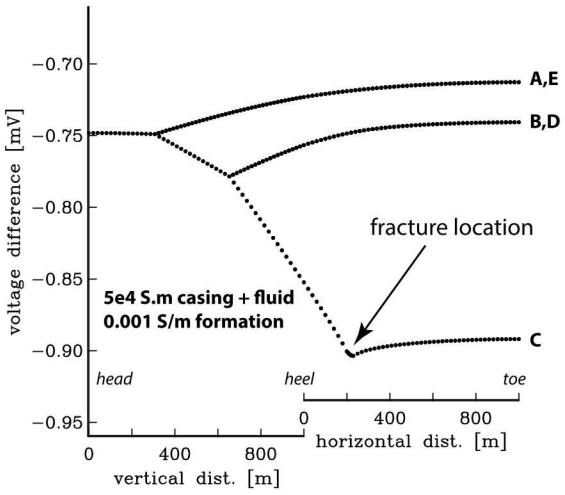

Figure 2-13. Difference in casing voltage on well bores A–E for the fracture/no-fracture results in Figure 2-12.

(or at least, deferred to a later time) by working first in the frequency domain, followed by Fourier transform.

The infinitely thin facets and edges pose some interesting opportunities regarding inversion and recovery of sharp features in the resulting conductivity model. Historically, recovery of sharp features or jumps has be achieved by introducing tears (surfaces informed by supplementary geologic information) in the earth model, across which smoothness regularization is not enforced. Examples of this include fracture imaging (Robinson et al., 2013) and reservoir characterization (Hoversten et al., 2001). With the hierarchical conductivity model evaluated here, it's conceivable that an alternative inversion strategy may prove profitable: inverting for either s_e or t_e alone, perhaps with internal smoothing, to constrain the model to a specific subsurface region. Following the development of McGillivray et al. (1994) for adjoint sensitivities, it's straightforward to show that the Fréchet derivative of the potential difference between points A and B in the subsurface is given by $\int_{F_e} \nabla_{23}\tilde{u} \cdot \nabla_{23} u\, dx^2$ and $\int_{E_e} \nabla_1 \tilde{u} \cdot \nabla_1 u\, dx$, for the e'th facet and edge, respectively, where $\tilde{u}$ is the electric potential for adjoint source $\tilde{f} = \delta(\boldsymbol{x} - \boldsymbol{x}_B) - \delta(\boldsymbol{x} - \boldsymbol{x}_A)$. These functions for the Fréchet derivatives are entirely analagous to the expressions required for 3D sensitivity calculation, and therefore pose little additional burden for their use in some previously developed inversion algorithm.

2.7. CONCLUSIONS

A novel and computationally economical model for hierarchical electrical conductivity has been introduced and exercised in the context of finite element analysis of the DC resistivity problem on an unstructured tetrahedral mesh. Electrical properties are assigned to, not only, volume–based tetrahedra, but also to infinitesimally thin facet– and edge–based elements of the mesh, thus

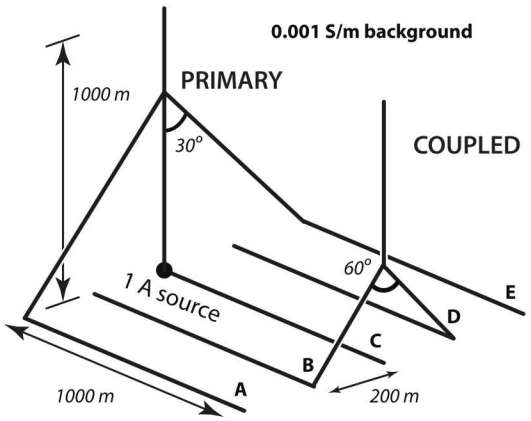

Figure 2-14. Modification of multi–lateral configuration (Figure 2-9) where wells B and D are galvanically coupled to wells A, C and E, rather than in direct electrical contact through connected segments of well casing.

allowing an approximate, but geometrically conformable, representation of thin, strong conductors such as fractures and well casing. Numerical experiments show agreement between numerical solutions and independent analytic reference solutions. Numerical experiments also show consistency in results between fine-scale discretization of thin structures and their surface– and edge–based counterparts. In the context of DC resistivity, the hierarchical model does not suitably capture the physics of infinitely thin resistors because of the intrinsic discontinuity in electric potential introduced therein. Rather, the physics of such resistive structures is shown to be reasonably captured through tears in the finite element mesh which admit discrete jumps across a surface in the computational domain. Using the edge–based conductivity elements, a series of numerical experiments on a hypothetical and idealized multi–lateral production well illustrate the effect of well casing geometry, including coupling from neighboring wells, on casing voltage, suggesting that actual casing conductivity should be accounted for in DC simulations of production/completion operations of an active oilfield. Furthermore, introduction of fractures through facet–based elements into the multi–lateral simulation is shown to be computationally economical and to confirm the physics seen in previous simulations where the borehole casing and fractures were explicitly discretized through extreme meshing of many very small volume elements. Predicted measurements of electric field on Earth's surface for single, multi–lateral and coupled multi–lateral configurations show distinct patterns of amplitude and direction such that neglecting a complete model of subsurface well casing out of computational convenience or limited computational resources may strongly compromise the predictive value of the simulation result.

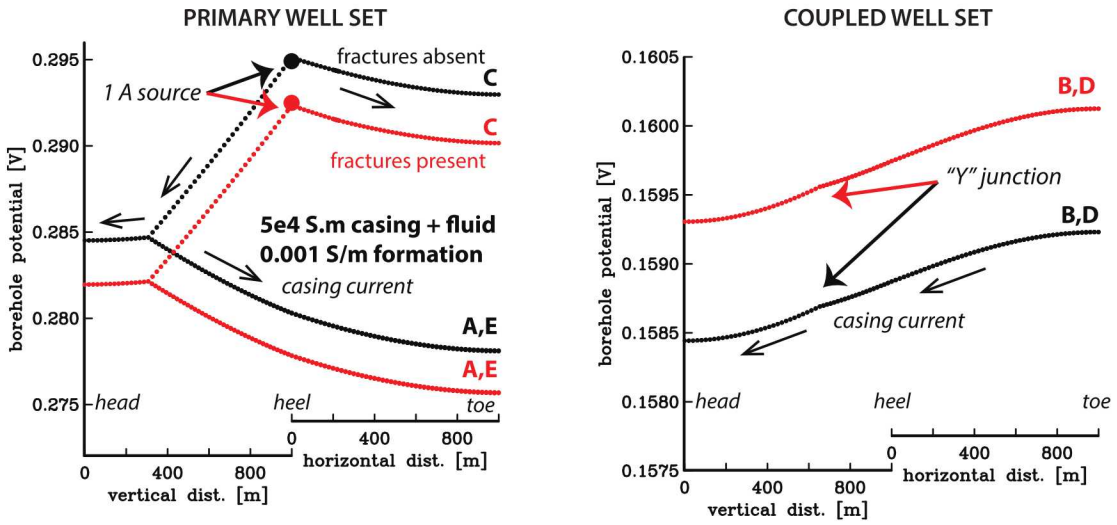

Figure 2-15. Effect on casing voltage for the galvanically coupled well system in Figure 2-14, where fractures are introduced 200 from the heel of the center well C (Figure 11). conductivity of the total conductivity–area product of the combined fluid–borehole system. Also shown (open arrows) is the direction of casing current given by the gradient of the casing potential.

2.8. APPENDIX: DERIVATION OF THE ELEMENT STIFFNESS MATRICES

Recall from Eq (2.12) and the discussion that follows, that element stiffness matrix $\mathbf{K}_e^3$ is formed by integration of $\nabla_{23}\phi_i(\boldsymbol{x}) \cdot \nabla_{23}\phi_j(\boldsymbol{x})$ for $i, j = 1, 2, 3$ over the triangular facet e. Gradients are taken in plane of the facet, denoted locally by the orthogonal direction vectors $\hat{\mathbf{e}}_2$ and $\hat{\mathbf{e}}_3$ (Figure 2-19). Whereas computing such gradients in two dimensions is relatively straightforward and covered in most elementary texts on finite element analysis, the situation faced here, where facets are arbitrarily oriented in (x, y, z), is less common, and, therefore, merits some attention. Letting x_2 and x_3 be the local coordinates in the $\hat{\mathbf{e}}_2$ and $\hat{\mathbf{e}}_3$ directions, respectively, our goal is to evaluate

$$\int_{F_e} \nabla_{23}\phi_i \cdot \nabla_{23}\phi_j \, dx^2 \quad = \quad \int_{F_e} \left(\frac{\partial \phi_i}{\partial x_2}\frac{\partial \phi_j}{\partial x_2} + \frac{\partial \phi_i}{\partial x_3}\frac{\partial \phi_j}{\partial x_3} \right) dx_2 \, dx_3 \tag{2.14}$$

over the triangular facet F_e. Values of this integral constitute the ijth element of the 3×3 matrix $\mathbf{K}_e^3$. By choosing $\hat{\mathbf{e}}_2$ parallel with the facet edge connecting nodes 1 and 2, we see from Figure 2-19 that all derivatives with respect to x_2 are simple to compute and given by

$$\frac{\partial \phi_1}{\partial x_2} = \frac{-1}{|\boldsymbol{r}_{21}|}, \qquad \frac{\partial \phi_2}{\partial x_2} = \frac{+1}{|\boldsymbol{r}_{21}|} \qquad \text{and} \qquad \frac{\partial \phi_3}{\partial x_2} = 0, \tag{2.15}$$

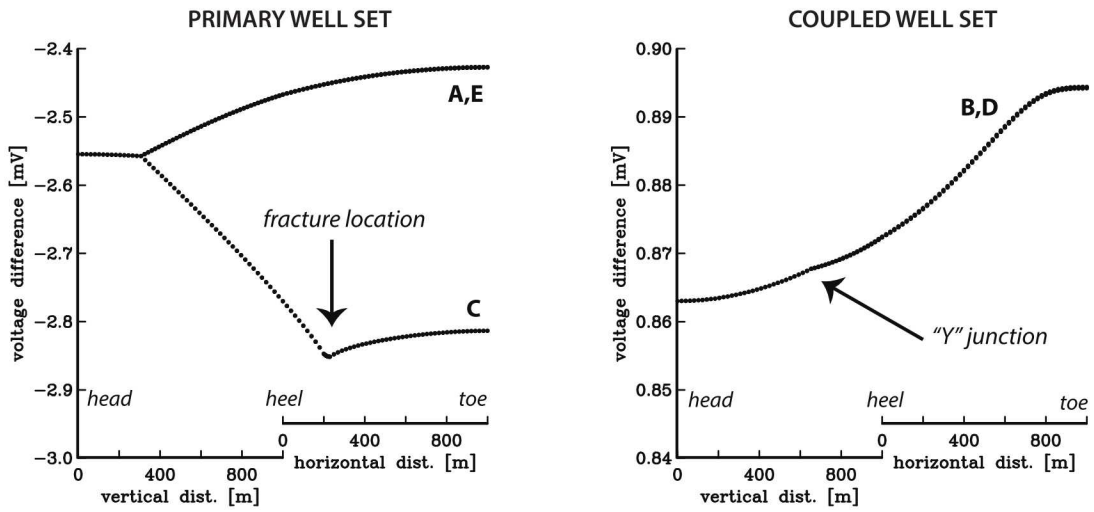

Figure 2-16. Difference in casing voltage due to fractures in the galvanically coupled well system in Figure 2-14. Note that whereas there is a notable fracture signature on well C (left), there is no obvious signature on the neighboring wells B and D.

where $\boldsymbol{r}_{ji} = \boldsymbol{r}_j - \boldsymbol{r}_i$ is the vector pointing from node i to node j. Note that these vectors needn't be specified in the local (x_2, x_3) coordinate system, but rather may conveniently remain in some global (x, y, z) reference frame since norms, dot and cross products are invariant under coordinate transformation. Calculation of the derivatives with respect to x_3 is slightly more involved, so let's start by observing that the distance between node 3 and the line connecting nodes 1 and 2 is $|\boldsymbol{r}_{31}| \sin\theta = |\boldsymbol{r}_{21} \times \boldsymbol{r}_{31}| / |\boldsymbol{r}_{21}|$, whereupon it's clear that

$$\frac{\partial \phi_3}{\partial x_3} = \frac{|\boldsymbol{r}_{21}|}{|\boldsymbol{r}_{21} \times \boldsymbol{r}_{31}|}. \tag{2.16}$$

To determine derivatives of ϕ_1, refer to Figure 2-19 and observe that $|\boldsymbol{r}_{31}| \cos\theta = \boldsymbol{r}_{21} \cdot \boldsymbol{r}_{31} / |\boldsymbol{r}_{21}|$ takes on values of 0 to $|\boldsymbol{r}_{21}|$ as point p varies between nodes 1 and 2. Therefore the quantity

$$1 - \frac{\boldsymbol{r}_{21} \cdot \boldsymbol{r}_{31}}{|\boldsymbol{r}_{21}|^2}$$

describes a linear function of position along the line connecting nodes 1 and 2, whose value is unity at node 1 and zero at node 2. We can now immediately write the remaining derivatives in Eq (2.14):

$$\frac{\partial \phi_1}{\partial x_3} = \left(\frac{\boldsymbol{r}_{21} \cdot \boldsymbol{r}_{31}}{|\boldsymbol{r}_{21}|^2} - 1 \right) \left(\frac{|\boldsymbol{r}_{21}|}{|\boldsymbol{r}_{21} \times \boldsymbol{r}_{31}|} \right) \quad \text{and} \quad \frac{\partial \phi_2}{\partial x_3} = -\frac{\boldsymbol{r}_{21} \cdot \boldsymbol{r}_{31}}{|\boldsymbol{r}_{21}|^2} \left(\frac{|\boldsymbol{r}_{21}|}{|\boldsymbol{r}_{21} \times \boldsymbol{r}_{31}|} \right). \tag{2.17}$$

To simplify notation, let

$$a = \frac{-1}{|\boldsymbol{r}_{21}|}, \qquad b = \frac{\boldsymbol{r}_{21} \cdot \boldsymbol{r}_{31}}{|\boldsymbol{r}_{21}|^2} \qquad \text{and} \qquad c = \frac{|\boldsymbol{r}_{21}|}{|\boldsymbol{r}_{21} \times \boldsymbol{r}_{31}|}, \tag{2.18}$$

and denote the area of the facet by $\Delta = \frac{1}{2}|\boldsymbol{r}_{21} \times \boldsymbol{r}_{31}|$. The element stiffness matrix for a given facet e in Eq (2.13) is

$$\mathbf{K}_e^3 = \Delta \begin{pmatrix} a^2+(b-1)^2c^2 & -a^2-(b-1)bc^2 & (b-1)c^2 \\ -a^2-(b-1)bc^2 & a^2+b^2c^2 & -bc^2 \\ (b-1)c^2 & -bc^2 & c^2 \end{pmatrix} \tag{2.19}$$

.

Derivation of edge–based the element stiffness matrix $\mathbf{K}_e^2$ in Eq (2.13) is far less involved than for the facet–based case Eq (2.19). Referring back to Figure (2-1) where $\hat{\mathbf{e}}_1$ is parallel to the edge connecting nodes 1 and 2, one sees that $\nabla_1\phi_1 = \partial_{x_1}\phi_1 = -1/|\mathbf{r}_{21}|$, and $\nabla_1\phi_2 = \partial_{x_1}\phi_2 = 1/|\mathbf{r}_{21}|$. Therefore, evaluation of

$$\int_{E_e} \nabla_1\phi_i \cdot \nabla_1\phi_j \, dx \quad = \quad \int_{E_e} \frac{\partial\phi_i}{\partial x_1}\frac{\partial\phi_j}{\partial x_1} \, dx_1 \tag{2.20}$$

over the eth edge is trivial and we find

$$\mathbf{K}_e^2 = \frac{1}{|\boldsymbol{r}_{21}|}\begin{pmatrix} 1 & -1 \\ -1 & 1 \end{pmatrix}. \tag{2.21}$$

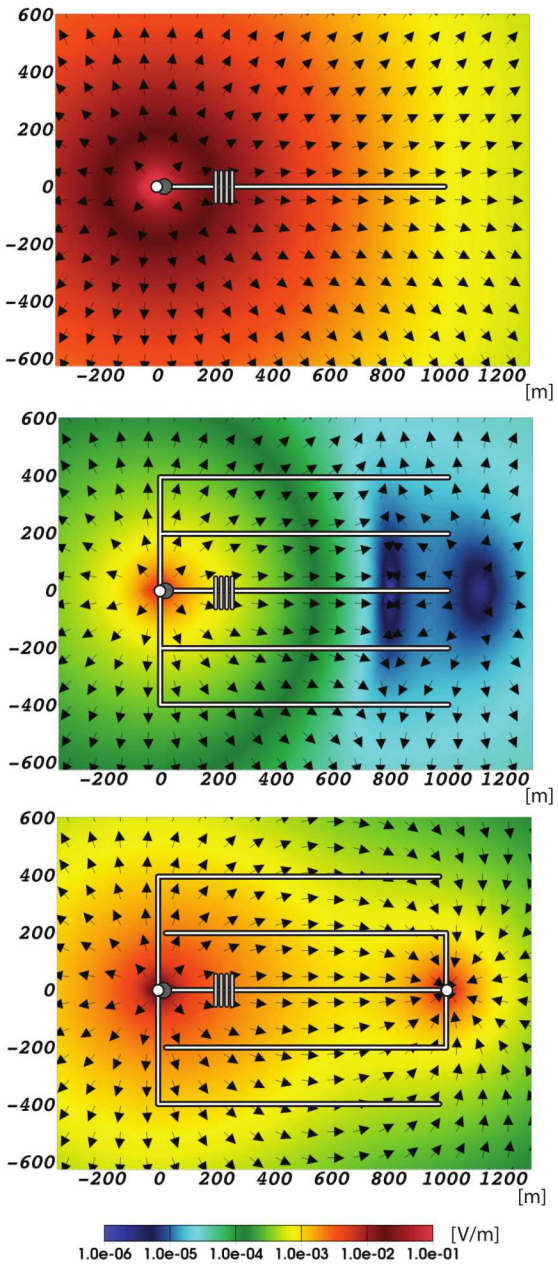

Figure 2-17. Plan view of difference in electric field on the air/earth interface due to the presence of fractures for three different well systems: single well (top); multi–lateral (middle); and coupled multi–lateral (bottom). Well geometry is the same as in Figures 2-9 and 2-14.

.

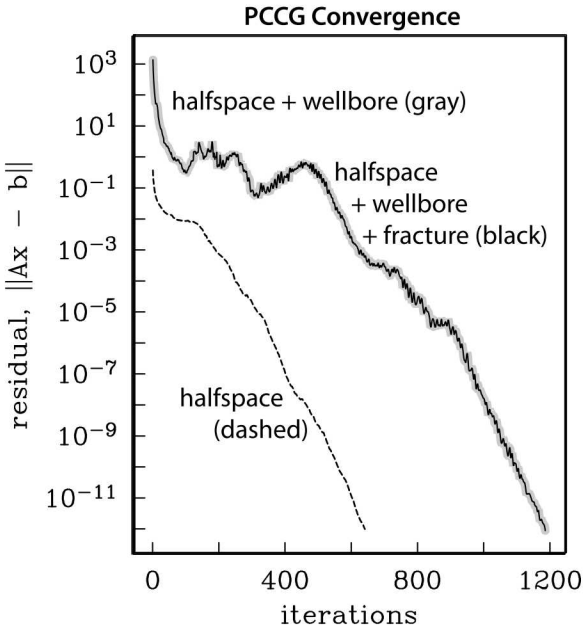

Figure 2-18. Convergence of the preconditioned conjugate gradient (PCCG) linear solver for discretization of the coupled multi–lateral model in Figure 2-14. Not including the well and fractures in the conductivity model, Eq (2-3), results in rapid convergence (dashed) to a target residual norm 1×10^{-12}. Including the high–conductivity well roughly doubles the number of iterations necessary to reach the same target residual (gray) and further inclusion of fractures has no appreciable effect (black).

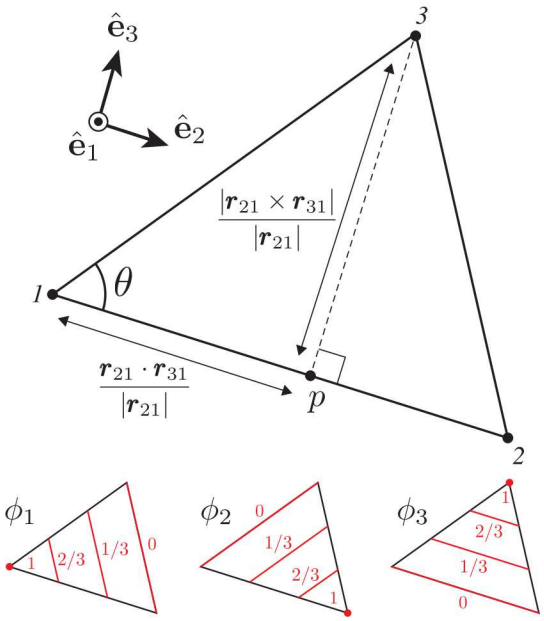

Figure 2-19. Sketch of a facet (top) and contours (red) of its corresponding nodal basis functions (bottom) in local enumeration. Length of the edge between nodes 1 and 3 projected in the $\hat{\mathbf{e}}_2$ and $\hat{\mathbf{e}}_3$ directions is annotated in the top figure in terms of operations on $\boldsymbol{r}_{ji} = \boldsymbol{r}_j - \boldsymbol{r}_i$, the vector pointing from node i to node j.

3. NEUMANN SERIES ANALYSIS OF WELLBORE RESPONSE

3.1. SUMMARY

The feasibility of Neumann series expansion of Maxwell's equations in the electrostatic limit is investigated for potentially rapid and approximate subsurface imaging of geologic features proximal to metallic infrastructure in an oilfield environment. While generally useful for efficient modeling of mild conductivity perturbations in uncluttered settings, we raise the question of its suitability for situations, such as oilfield, where metallic artifacts are pervasive, and in some cases, in direct electrical contact with the conductivity perturbation on which the Neumann series is computed. Convergence of the Neumann series and its residual error are computed using the hierarchical finite element framework for a canonical oilfield model consisting of an "L" shaped, steel–cased well, energized by a steady state electrode, and penetrating a small set of mildly conducting fractures near the heel of the well. For a given node spacing h in the finite element mesh, we find that the Neumann series is ultimately convergent if the conductivity is small enough – a result consistent with previous presumptions on the necessity of small conductivity perturbations. However, we also demonstrate that the spectral radius of the Neumann series operator grows as $\sim 1/h$, thus suggesting that in the limit of the continuous problem $h \to 0$, the Neumann series is intrinsically divergent for all conductivity perturbation, regardless of their smallness. The hierarchical finite element methodology itself is critically analyzed and shown to possess the h^2 error convergence of traditional linear finite elements, thereby supporting the conclusion of an inescapably divergent Neumann series for this benchmark example. Application of the Neumann series to oilfield problems with metallic clutter should therefore be done with careful consideration to the coupling between infrastructure and geology. The methods used here are demonstrably useful in such circumstances.

3.2. INTRODUCTION

A problem of long–standing interest to the geophysical community is the characterization of either naturally–occurring or engineered fracture systems where the fracture is impregnated with material, a contrast agent, which generates a data signature distinctive from that of the surrounding geology when subjected to geophysical interrogation. In particular, application of the electrical and electromagnetic methods through the combined exploitation of existing metallic infrastructure and electrically conductive or magnetically permeable contrast agents has been the

subject of a recent body of literature in oilfield geophysics (e.g. Yang et al., 2016; Zeng et al., 2017; Zhang et al., 2017; Jannin et al., 2017; Hickey et al., 2017; Couchman and Everett, 2017, and references therein). One considerable challenge in the interpretation of these data is the computational burden of 3D forward modeling the widely disparate length scales on which the fractures, infrastructure and regional geology reside – a problem exacerbated by extreme range in electrical conductivity values spanning the geology (< 0.1 S/m), fractures (0.1 – 1.0 S/m) and steel (10^6 S/m). And while the steel well casing is volumetrically insignificant when compared to rock over the field scale, it's widely recognized that electromagnetic scattering from long, strong conductors can pollute survey data with a spatially extensive footprint that can overwhelm the subtle signatures of the geologic features of interest. Explicit modeling of the casing with volumetric simplices is problematic because of the requirement that simplices be roughly equidimensional and that hundreds of millions of them are therefore required to represent a few kilometers of casing. As a corollary, brute force discretization of fractures a few millimeters in thickness, but meters in lateral extent, is also computationally explosive unless an alternative, approximate method can be employed.

One such method is the generalized Neumann series (Zhdanov and Fang, 1996). The attractiveness of the Neumann series as a solution method lies in its simplicity and speed: the anomalous field arising from a conductivity anomaly is computed as the product of the incident, unperturbed, electric (or magnetic) field and a polynomial in the fundamental linear operator representing integration of Green's function and conductivity contrast over the anomalous region. In choosing the Green's function to be that of the full, anomaly–bearing earth model, the series is exact in just one term. For complicated earth models, the Green's function is typically unavailable except through numerical methods and, instead, the Green's function is computed for a model absent any troublesome features – in the oilfield case, for example, steel casing and/or fractures. Doing so thus requires consideration of the full polynomial expansion for a target solution accuracy, and herein lies the problem. Convergence of the Neumann series only holds for holds for weak conductivity perturbations, although clever modifications (e.g. Habashy et al., 1993; Zhdanov and Fang, 1996; Christensen, 1996; Avdeev et al., 1997) can extend its range of usefulness considerably.

For oilfield scenarios where an electrically conductive fracture system is near (or in contact with) the strongly conductive steel casing, forward modeling in the electrostatic limit the response of weakly conducting fracture perturbations ($\sim 1:3$ contrast red with respect to background), 1 km depth, adjacent to the borehole) reveals that the dominant anomalous electric field arises from the borehole casing itself. This anomalous field radiates out from the well head to distances of several km with a second–order azimuthal dependence arising from the lateral section of wellbore casing at depth (c.f. Weiss, 2017, and references therein). A third–order effect is the scattering field from the fractures themselves, but this is localized to the vicinity of the fractures and does not measurably propagate to the Earth's surface. Hence, there is numerical evidence demonstrating that it is the coupling between the fracture perturbation and steel casing which is important, not the magnitude of the perturbation alone. This raises the question: in cases where small conductivity perturbations are near (or in contact) with a strongly conducting subsurface feature such as metallic infrastructure, can the Neumann series be used to approximate the anomalous electromagnetic response? If so, then at least one need only worry about modeling (via the convolution kernel) the infrastructure itself, rather than the more burdensome and coupled

perturbation/infrastructure system. To address this question, we employ hierarchical material properties in finite element analysis (Weiss, 2017) to construct a finite–dimensional Neumann series matrix operator and examine the series convergence explicitly.

Recall that in the hierarchical material model concept for tetrahedral finite element modeling, the electrical conductivity σ is represented as a summation of conductivities σ_e associated with tetrahedral elements, transverse conductances s_e associated with triangular facets, and conductivity·area products t_e associated with the remaining edges. As such, one may use the method to straightforwardly and efficiently evaluate the coupled fracture/casing problem in a single forward calculation (Weiss, 2017), no Neumann series required. Note that adoption of the Weiss (or any other) generalized 3D algorithm in an industrial workflow where Neumann series analysis is the norm could be seen as disruptive or even cost prohibitive. Hence, there is merit in asking whether Neumann series can do the job, if needed. In the present study, the borehole casing is represented in the Neumann series matrix operator through the edge–based variables t_e, and the fractures through the facet–based variables s_e, leading instead to a forward modeling method that allows us to test the convergence of a Neumann series expansion built directly on infinitesimally thin fracture perturbations s_e alone. This method, where the Neumann series is based on the discrete form of the Maxwell equations, complements the more common approach where the linear operator derives, ultimately, from repeated application of Green's theorem (e.g. Habashy et al., 1993; Avdeev et al., 1997).

Although the unstructured tetrahedral mesh of the hierarchical finite elements (Weiss, 2017) permits almost arbitrary complexity in the representation of oilfield infrastructure (Weiss and Wilson, 2017), we restrict the present analysis to a rectilinear geometry – a simple, 'L' shaped well with vertical fractures near the well heel embedded in a uniform geology (Figure 3-1) – so that results may most easily be built upon by others and contrasted with forward modeling schemes restricted (in practice) to Cartesian geometries such as finite differences or their variants (e.g. Yang et al., 2016). With the hierarchical finite element analysis, we also avoid questions about the suitability of other forward modeling approaches in which the electrically charged borehole casing is replaced by an approximate distributed source, derived perhaps from transmission line theory (Kaufman and Wightman, 1993) or other, hybrid methods (e.g. Nieuwenhuis et al., 2015; Tang et al., 2015) in an attempt to minimize the computational burden of its direct calculation.

Our analysis strategy is relatively straightforward. A Neumann series expansion is computed for the electrostatic response over the canonical model described above using the (Weiss, 2017) algorithm for fractures whose conductivity contrasts range from mild to moderate. We examine the convergence rate of the Neumann series and its residual as a function of truncation order in the polynomial series. We then confirm this convergence behavior through an eigenvalue analysis, and extend this analysis to determine the effect of mesh discretization on the spectral radius of the linear operator on which the Neumann series is built. Lastly, we expand the already presented benchmarking exercise (Weiss, 2017) to now include a set of verification and validation results which address any bias our numerical method may have introduced into the convergence behavior we observe with the Neumann series expansion.

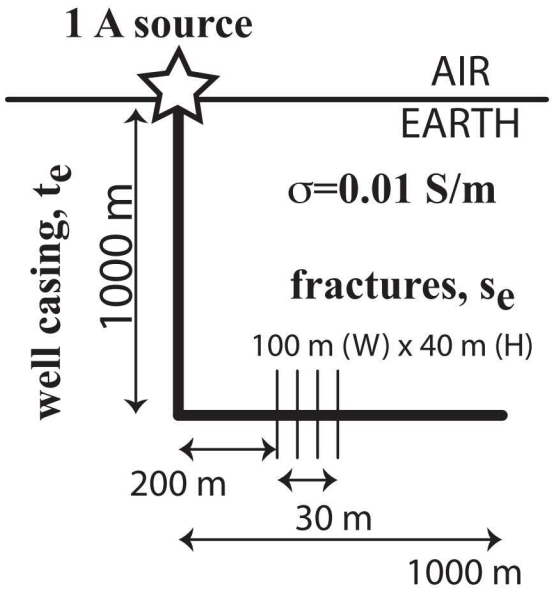

Figure 3-1. Sketch of the horizontal well geometry and fractures. Steel borehole casing of conductivity $\sigma = 5 \times 10^6$ S/m with outer diameter 0.2 m and 0.02 m wall thickness is assumed, resulting in a conductivity·area product $t_e \sim 5 \times 10^4$ S · m. Fractures are equally spaced, vertically oriented ellipses centered on the borehole whose width (W), height (H) and location are noted on the figure. Fracture conductance s_e ranges from 0.01 to 1.0 S for the models evaluated herein.

3.3. THEORY

Throughout an electrically conductive medium σ subject to an imposed electric current density $\mathbf{J}_s$, invariant in time, the static electric field $\mathbf{E} = \nabla\phi$ derives from Maxwell's equations as the solution the well–known Poisson equation,

$$-\nabla \cdot \sigma \nabla \phi = \nabla \cdot \mathbf{J}_s. \tag{3.1}$$

As an auxiliary problem, define a "reference" medium σ_0, with $\phi = \phi_0 + \phi^{(1)}$ and ϕ_0 solving the equation $-\nabla \cdot \sigma_0 \nabla \phi_0 = \nabla \cdot \mathbf{J}_s$. As a consequence, $\phi^{(1)}$ solves equation $-\nabla \cdot \sigma \nabla \phi^{(1)} = \nabla \cdot (\sigma - \sigma_0) \nabla \phi_0$, and the sum $\phi_0 + \phi^{(1)}$ is exactly equal to ϕ. Note the use of sub– and super–script i on ϕ: the former referring to the ith term in a sequence of ϕ values; and, the latter being the truncation error from only considering i terms of the sequence. Consider, however, when for whatever reason, the effort required in solving for $\phi^{(1)}$, as manifest in the material property σ, is significantly greater than the case when σ is simply the reference medium σ_0. In other words, we can let $\phi^{(1)} = \phi_1 + \phi^{(2)}$ and prefer to solve $-\nabla \cdot \sigma_0 \nabla \phi_1 = \nabla \cdot (\sigma - \sigma_0) \nabla \phi_0$. If $\phi^{(2)}$ is sufficiently small, then $\phi \sim \phi_0 + \phi_1$ is an acceptable approximation. Evaluation of the "smallness" of $\phi^{(2)}$ is found, therefore, by solving $-\nabla \cdot \sigma \nabla \phi^{(2)} = \nabla \cdot (\sigma - \sigma_0) \nabla \phi_1$. A principal question to address is determining the conditions under which this first order approximation

applies. Secondly, one may recursively extend this line of reasoning, letting $\phi^{(2)} = \phi_2 + \phi^{(3)}$ solving $-\nabla \cdot \sigma_0 \nabla \phi_2 = \nabla \cdot (\sigma - \sigma_0) \nabla \phi_1$. The approximation $\phi \sim \phi_0 + \phi_1 + \phi_2$ is therefore adequate when $\phi^{(3)}$, the solution to $-\nabla \cdot \sigma \nabla \phi^{(3)} = \nabla \cdot (\sigma - \sigma_0) \nabla \phi_2$, is sufficiently small.

We can generalize this recursive sequence of operations to N terms in the following way. Define the total solution

$$\phi = \sum_{i=0}^{N} \phi_i + \phi^{(N+1)} \tag{3.2}$$

such that

$$-\nabla \cdot \sigma_0 \nabla \phi_i = \nabla \cdot (\sigma - \sigma_0) \nabla \phi_{i-1} \quad \forall \quad i = 1, 2, \ldots \tag{3.3}$$

and

$$-\nabla \cdot \sigma \nabla \phi^{(N+1)} = \nabla \cdot (\sigma - \sigma_0) \nabla \phi_N. \tag{3.4}$$

To initiate the sequence at $i = 0$, the function ϕ_0 is defined as above. It's relevant to note that if the difference in electric potential $\phi - \phi_0$ is due to a time–lapse change of state from σ_0 to σ, we have

$$\phi - \phi_0 = \sum_{i=1}^{N} \phi_i + \phi^{(N+1)}. \tag{3.5}$$

Consider now that the continuous Poisson equation(s) previously discussed are solved by some numerical method yielding, as the solution to linear system of equations, a finite–dimensional solution vector with the analogous notation of sub– and superscripts,

$$\mathbf{x} = \sum_{i=0}^{N} \mathbf{x}_i + \mathbf{x}^{(N+1)}. \tag{3.6}$$

Define vector $\mathbf{b}$ as the discrete representation of the current density term $\nabla \cdot \mathbf{J}_s$ in our numerical method, matrix $\mathbf{K}$ for the discrete form of $\nabla \cdot \sigma \nabla$ and $\mathbf{K}_0$ for $\nabla \cdot \sigma_0 \nabla$. For example, when using finite elements, the matrices $\mathbf{K}$ and $\mathbf{K}_0$ are the global stiffness matrices for media σ and σ_0, respectively. Regardless of the specific numerical method, in full generality we may write

$$\mathbf{K}\mathbf{x} = \mathbf{b} \tag{3.7}$$

with

$$\mathbf{K}_0 \mathbf{x}_0 = \mathbf{b} \quad \text{and} \quad \mathbf{K}\mathbf{x}^{(1)} = \delta\mathbf{K}\,\mathbf{x}_0, \tag{3.8}$$

where $\mathbf{x} = \mathbf{x}_0 + \mathbf{x}^{(1)}$ and $\delta\mathbf{K} = \mathbf{K} - \mathbf{K}_0$. And in following through with the recursion described above, only now for the discrete case, we find,

$$\mathbf{x}_i = \left(\mathbf{K}_0^{-1}\,\delta\mathbf{K}\right)\mathbf{x}_{i-1} = \left(\mathbf{K}_0^{-1}\,\delta\mathbf{K}\right)^i \mathbf{x}_0 \quad \text{and} \quad \mathbf{x}^{(i)} = \left(\mathbf{K}^{-1}\,\delta\mathbf{K}\right)\mathbf{x}_{i-1}, = \left(\mathbf{K}^{-1}\,\delta\mathbf{K}\right)^i \mathbf{x}_0, \tag{3.9}$$

where the superscript $()^i$ represents i successive actions of matrix operator within the parenthesis. Substituting Eq (3.9) into Eq (3.6), it's now evident that the total (discrete) solution $\mathbf{x}$ is the sum of reference solution $\mathbf{x}_0$, an N–term Neumann series and a residual $\mathbf{x}^{(N+1)}$

$$\mathbf{x} = \mathbf{x}_0 + \left(\mathbf{T}_0 + \mathbf{T}_0^2 + \cdots + \mathbf{T}_0^N\right)\mathbf{x}_0 + \mathbf{x}^{(N+1)}, \tag{3.10}$$

where $\mathbf{T}_0 = \mathbf{K}_0^{-1}\,\delta\mathbf{K}$. Similarly, we observe that the residual is itself a Neumann series in terms of $\mathbf{T} = \mathbf{K}^{-1}\,\delta\mathbf{K}$ such that $\mathbf{x}^{(N+1)} = \left(\mathbf{T} + \mathbf{T}^2 + \cdots + \mathbf{T}^{N+1}\right)\mathbf{x}_0$. And in closing, the change of state from σ_0 to σ results, numerically, in the difference

$$\mathbf{x} - \mathbf{x}_0 = \left(\mathbf{T}_0 + \mathbf{T}_0^2 + \cdots + \mathbf{T}_0^N\right)\mathbf{x}_0 + \mathbf{x}^{(N+1)}, \tag{3.11}$$

representing the change in the electric scalar potential.

3.4. RESULTS

Although much of the prior work in Neumann series expansion for electromagnetic response has taken place in the context of integral equation forward solvers (e.g. Avdeev et al., 1997; Zhdanov and Fang, 1997; Avdeev et al., 2002) for fast computation, the present study uses the hierarchical finite element method developed in Weiss (2017) to study the Neumann series properties because it is both fast and able to handle directly the important, but volumetrically small, subsurface features around which our Neumann series is constructed. Specifically, we evaluate the electrostatic fields on and surrounding a horizontal well (Figure 3-1), on which lies a compact set of vertical fractures with anomalous electrical conductivity from that of a uniform background earth. Following Weiss (2017), the earth, fractures and edges are represented by material properties associated with tetrahedra, their facets and edges, respectively, of an underlying finite element discretization (Figure 3-2) on a linear nodal basis. Because the vanishingly thin fractures are defined by their equivalent conductance and casing by the product of conductivity and cross–sectional area, the method avoids the computationally explosive problem of volumetric discretization millions of small, regular tetrahedron where over each a conductivity value is defined. This hierarchical representation of material properties results in reduction of computational burden (time and storage resource) in comparison to strictly volume–based discretizations by several orders of magnitude.

For the examples presented here, the tetrahedral mesh covers a physical domain $10 \times 10 \times 5$ km in size representing only the earth region of study area, a region simply defined as a 0.01 S/m halfspace. Homogenous Dirichlet boundary conditions are applied to the lateral sides and bottom of the mesh out of convenience and to enforce decay of the potentials away from the source location at the center of the top side of the mesh, the air/earth interface. On the top side of the mesh a homogeneous Neumann boundary condition is (weakly) enforced through the variational form of the governing Poisson equation, thus representing the interface between a conducting earth and a perfectly resistive, overlying air layer. A few details on the mesh are as follows. The region of interest is a roughly 2 km^3 volume containing the horizontal well and fractures. Node spacing in this region is between 5 and 20 m, with 5 m spacing on the "fracture" ellipses (see Figures 3-1 and 3-2), 20 m spacing on the "borehole" and 10 m spacing on the air/earth interface. Outside of this region, the node spacing grows smoothly toward the outer mesh boundaries where node spacing is roughly 150 m. In total there are 514,728 mesh nodes and 3,085,751 tetrahedra, on which 105 edges are given values $t_e = 5 \times 10^4$ S·m to represent the borehole and 2616 facets are given values $s_e = 0.01, 0.1, 1.0$ S for each of the three models evaluated. Recall from Weiss (2017) that t_e is the product of cross–sectional area of borehole times the electrical conductivity.

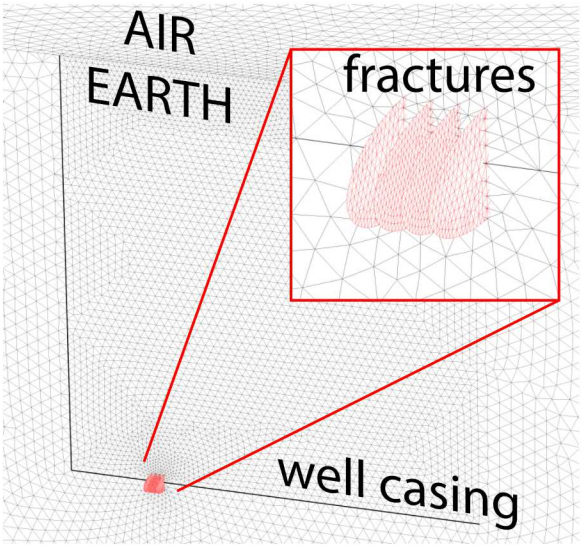

Figure 3-2. Vertical slice of finite element mesh through the borehole path (heavy line) and showing the set of 4 elliptical fractures (red). Node spacing along the borehole is 10 m and node spacing within the fracture planes is 3 m.

This value for t_e is consistent with a borehole casing model where steel conductivity is 5×10^6 S/m, 0.1 m borehole casing radius and 0.02 m thickness. Contributions to t_e from the casing fluid are ignored because of their comparatively low conductivity and minimal contribution to the overall t_e value. Similarly, s_e is the equivalent conductance of a thin sheet of conductivity σ_e and thickness h such that $s_e = \sigma_e h$. Assuming $h = 0.01$, the values $s_e = 0.01, 0.1, 1.0$ S represent "fracture" conductivity values 1.0, 10.0 and 100.0 S/m, equivalent on par with conductive fluids and contrast agents used for subsurface imaging (Robinson et al., 2013). For all models evaluated, the hierarchical finite element system of equations (Weiss, 2017) on this discretization is solved iteratively with Jacobi–preconditioned conjugate gradients (Hestenes and Stiefel, 1952) and updates (Polak and Ribière, 1969), showing generally monotonic convergence of the ℓ_2 residual with iteration count (Figure 3-3).

Choosing a reference earth conductivity model σ_0 consisting of a uniform earth plus the conductivity·area product, t_e associated with the steel casing, the Neumann series is thereby built around the conductivity perturbation due to the fractures. The $\sigma - \sigma_0$ term in Eq (3.3 and 3.4) is non–zero only on the fractures, and more specifically, by the values s_e. As demonstrated earlier, one effect of introducing electrically conductive fractures on the borehole is to lower the electrostatic potential on the borehole casing (Weiss, 2017), this same result is confirmed here under similar exploration conditions (Figure 3-4 through 3-6) and variable fracture conductivity. In each of the examples that follow, a 1 A source is positioned at the wellhead, driving current down the steel casing into the formation. A return electrode is not considered here, thus making the Earth model sourced by a "single pole". Because surface measurements of electrostatic scalar potential differences are known to be dominated by the response of the steel casing – regardless of whether those data are "total field" measurements or some time–lapse difference (a "scattered field") – we focus our attention on the casing potential, from which the longitudinal casing

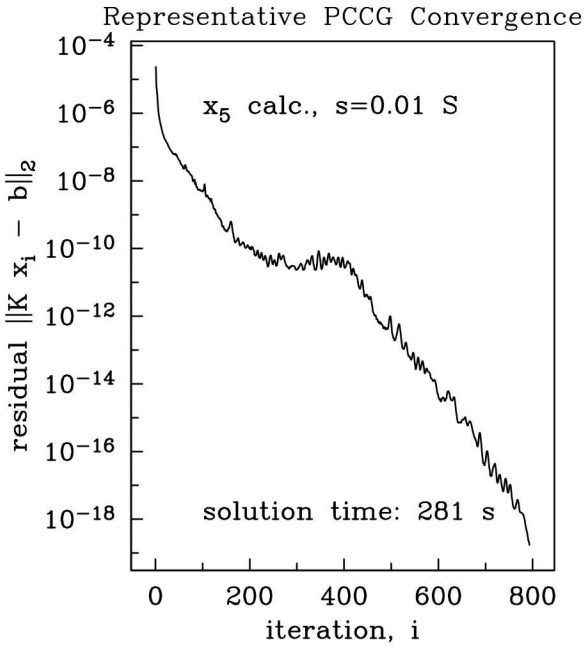

Figure 3-3. Representative convergence of the Jacobi preconditioned conjugate gradient solver – specifically, for facet conductance $s_e = 0.1$ S and solving the system $\mathbf{K}_0\mathbf{x}_6 = \delta\mathbf{K}\mathbf{x}_5$ from Eq (9) for the 6th order term $\mathbf{x}_6$ in the Neumann series.

current can be derived by differentiation, and the radially directed leakage current, by differentiation again.

The range of fracture conductances 0.01 to 1.0 S is sufficient to demonstrate the convergence behaviors of the Neumann series. The 'exact' solution is that from the full (Earth + borehole + fracture) model computed using the Weiss (2017) algorithm. In the case of mild fracture perturbation $s_e = 0.01$ S, superposed on the background conductivity 0.01 S/m, the Neumann series converges rapidly after 2 terms and remains stable in its high-accuracy approximation of the true (scattered) potential when extra terms in the series are added (Figure 3-4). Relative error of the $N = 1$ Neumann series is on the order of 1-2% for this example, with higher order terms driving that figure down by a factor of 40. When, however, the fracture conductance is increased to 0.1 S, the Neumann series converges initially for $N = 1, 2, 3$, but then begins to oscillate and rapidly diverge with increasing N (Figure 3-5). The best Neumann series approximations ($N = 2, 3$) in this initial convergence sequence have relative error of 5% with the known solution. Lastly, for a high contrast model $s_e = 1.0$ S, the Neumann series has, at best, a relative error $1.2/0.95 \times 100\% = 130\%$ at $N = 1$ and significantly diverges away from the known solution with the addition of each successive term (Figure 3-6). Computation of the residual $\mathbf{x}^{(i)}$ by solving Eq (3.9) yields results that are consistent with direct residual calculation and leads to values for the reconstructed potential $\sum_{i=1}^{N} \mathbf{x}_i + \mathbf{x}^{(N+1)}$ that are visually indiscernible from direct calculation of $\mathbf{x} - \mathbf{x}_0$ under the eyeball norm.

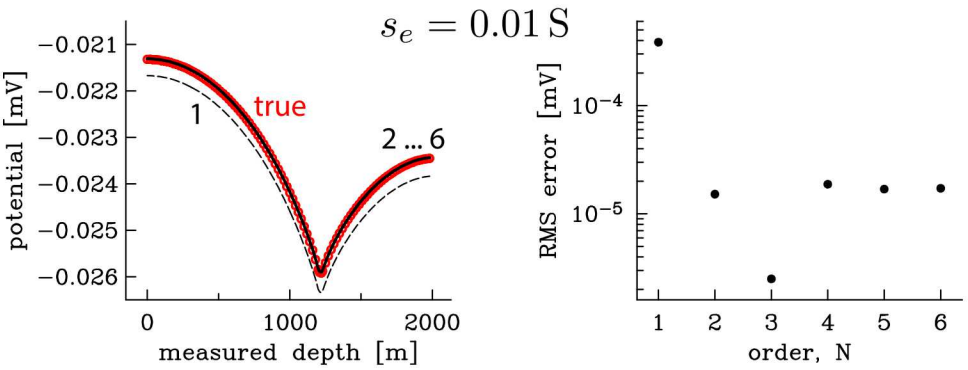

Figure 3-4. True scattered potential computed by direct differencing $\mathbf{x} - \mathbf{x}_0$ (red, left panel) and Neumann series expansions of orders 1 through 6 (left panel) for a fracture set with conductance $s_e = 0.01$ S at measured depth 1200 m and excited by a 1 A source at the well head. Root mean square of the residual between the Nth order series and true solution (right panel) showing rapid convergence and stability in series accuracy for terms 4 through 6. Here, 'measured depth' is the the total along–casing distance as measured from the well head.

3.5. DISCUSISON

The poor convergence of the Neumann series for high contrasts in fracture conductivity can be understood quantitatively in terms of an eigenvalue analysis. We expect the series Eq (3.11) to converge if its spectral radius – the absolute value of the maximum eigenvalue – is less than unity. Calculation of the full eigenspectrum for matrix operator $\mathbf{T}_0$, is computationally expensive because it is both dense and large (dimension 500k $\times$ 500k). Furthermore, we solve the finite element problem in the matrix–free framework (Weiss, 2001) to explicitly avoid excessive storage costs for the matrices $\mathbf{K}$ and $\delta\mathbf{K}$. Calculation of the maximum eigenvalue, however, can be done matrix–free by using the power method (Saad, 2011), in which the eigenvector $\mathbf{v}$ associated with the maximum eigenvalue is approximated by successive k-iterates

$$\mathbf{v}_{k+1} = \frac{\mathbf{T}_0 \mathbf{v}_k}{\|\mathbf{T}_0 \mathbf{v}_k\|_2} \tag{3.12}$$

until convergence where $\mathbf{v} \sim \mathbf{v}_{k+1}$. At each iteration of this sequence, the corresponding estimate for the maximum eigenvalue $\lambda_{\max}^{(k)}$ is therefore given in a least squares sense by

$$\lambda_{\max}^{(k)} \sim \frac{\mathbf{v}_k^T \mathbf{T}_0 \mathbf{v}_k}{\mathbf{v}_k^T \mathbf{v}_k}. \tag{3.13}$$

These iterates are computed matrix–free in two steps by first contracting the matrix $\delta\mathbf{K}$ with vector $\mathbf{v}_k$, followed by a conjugate gradient solve of the linear system $\mathbf{K}_0 \mathbf{v}_{k+1} = \delta\mathbf{K}\mathbf{v}_k$ as described in Eq (3.10). The sequence is seeded at $\mathbf{v}_0$ with random numbers uniformly distributed

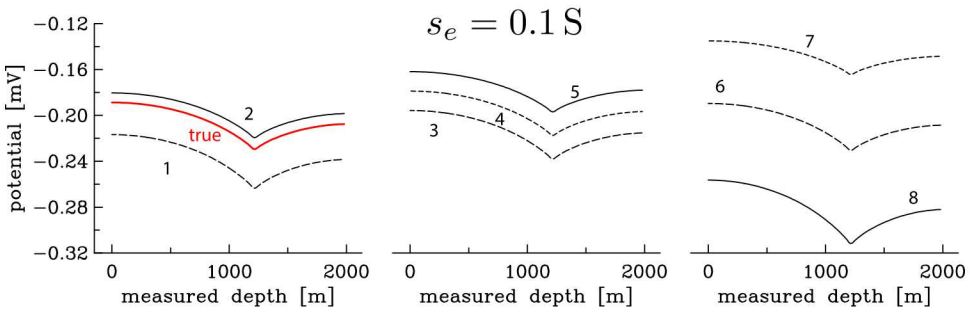

Figure 3-5. True scattered potential computed by direct differencing $\mathbf{x} - \mathbf{x}_0$ (red, left panel), Neumann series expansions of orders 1 and 2 (left panel), orders 3–5 (middle panel) and orders 6–8 (right panel), for a fracture set with conductance $s_e = 0.1$ S at measured depth 1200 m and excited by a 1 A source at the well head.

on $(0,1)$ at terminates when the ℓ_2 of the residual, $\|\mathbf{v}_{k+1} - \mathbf{v}_k\|_2$, stops decreasing.

For the three fracture conductances 0.01, 0.1 and 1.0 S, (Figure 3.4 through 3-6, respectively), the maximum eigenvalues estimated by Eq (3.13) are consistent with the convergence behavior we find with their corresponding Neumann series (Figure 3-7). For the case of low fracture conductance, 0.01 S, the maximum eigenvalue is roughly 0.4, a value less than the radius of convergence of the Neumann series. For the other two cases, where maximum eigenvalue is greater than the radius of convergence, the Neumann series is demonstrably divergent (Figure 3-5 and 3-6).

Further inspection of the maximum eigenvalue estimates for the three cases reveals an additional consistency check. Referring back to Eq (3.4) and its corresponding finite element linear system of equations, Eq (3.9), one sees that the difference in conductivity $\sigma - \sigma_0$ is zero outside the fracture and constant within. Therefore, the $\delta\sigma = \sigma - \sigma_0$ term is a constant prefactor in the matrix $\delta\mathbf{K} = \delta\sigma\mathbf{K}_L$ where $\mathbf{K}_L$ is the finite–element discretization of the Laplacian operator. Eigenvalues of $\mathbf{T}_0 = \mathbf{K}_0^{-1}\delta\mathbf{K} = \delta\sigma \cdot \mathbf{K}_0^{-1}\mathbf{K}_L$ thereby scale linearly as $\delta\sigma$ and we may infer from the results of the 1.0 S conductance model that the maximum eigenvalue of the matrix $\mathbf{K}_0^{-1}\mathbf{K}_L$ for this fracture/borehole model is approximately 41.1. This suggests that the maximum conductance contrast for which a Neumann series approximation will converge is less than $1/41.1 \sim 0.02$ S. For a brine–filled fracture ($\sigma \sim 2$ S/m), this upper bound on the fracture conductance results in a maximum fracture thickness of 0.01 m for a convergent Neumann series. For fractures permeated with higher conductivity materials, the maximum thickness decreases accordingly. Furthermore, we note that convergence of the Neumann series Eq (3.11) *will* require many terms if the spectral radius is close to unity and thus a simple one-term approximation $N = 1$ is likely to be numerically adequate under only the most subtle of conductivity perturbations. The problem is, evidently, a direct consequence of the strong borehole casing signature in this dominant eigenmode (Figure 3-8).

The severe restrictions posed above on the maximum conductance perturbation for a convergent Neumann series are further exacerbated under a more careful analysis on the effect of mesh

discretization. Prior results (Figure 3-4 through 3-7) were computed using a mesh discretization where the node spacing h within the plane containing the fracture ellipses was fixed at 3 m (Figure 3-2). In considering h values on the range 2–6 m, the maximum eigenvalue scales approximately as $1/h$ (Figure 3-9). Therefore, in the limit $h \to 0$ that the discrete finite element problem better approximates the infinite–dimensional (vector space) problem, the maximum eigenvalue approaches infinity. In such cases, under no condition is the Neumann series convergent – a conclusion that has serious consequences for analyses based on the presumption of Neumann series adequacy.

One might question at this point whether the terminal conclusion of the preceding analysis reflects some limitation of the hierarchical finite elements in the limit of $h \to 0$ rather than electrostatic coupling between the conducting fractures and steel borehole casing. Previous benchmarking exercises (Weiss, 2017) demonstrated agreement between the finite element solutions and independent reference solutions, as well as internal consistency between edge, facet and volume discretizations. However, for our main conclusion on Neumann series convergence to hold, we must also demonstrate that our (linear, nodal) finite element solver converges as h^2 in accordance with theory. To do so we adopt the verification and validation strategies known as the "method of manufactured solutions" (MMS) and "method of exact solutions" (MES) to analyze the convergence behavior (Salar and Knupp, 2000; Roache, 1998).

In the general MMS, an exact solution ϕ^* is defined *a priori* for the governing differential equation – in our case, Eq (3.1) – and a right–hand–side "source" is computed analytically. The analytic source function is then used in the construction of the finite–dimensional right–hand–side resulting from the numerical approach under consideration, which presently is the vector $\mathbf{b}$ in Eq (3.7) arising from linear, nodal finite elements on a tetrahedral mesh with node spacing h. The numerical solution $\mathbf{x}$ is then computed and compared with the exact solution evaluated the mesh nodes $\mathbf{x}^{EXACT}$, thus providing an error estimate as a function of h. The exercise is repeated over a range of h to determine the convergence rate of the numerical solution and verify that it agrees with theoretical estimates.

For the MMS problem we choose the exact solution $\phi^* = \exp\left[-(r/a)^2\right]$ with $\sigma = 1$ S/m because it is easily differentiable and smooth, with no singularities or discontinuities. Thus, this MMS solution tests whether the tetrahedral discretization of Weiss (2017) finite element solver is working as designed. The resulting (distributed) source function $\frac{1}{a^4}\left(6a^2 - 4r^2\right)\exp\left[-r/a\right]$ is substituted for $\nabla \cdot \mathbf{J}_s$ and the exact solution ϕ^* is imposed as a Dirichlet boundary condition over the model domain $-50 < x, y, z < 50$ m, with the constant a equal to 20 m. An advancing front method is used to discretize the model domain with (roughly) equidimensional tetrahedral elements of edge length h. Numerical experiments with h refinement over the range 2 to 10 m demonstrate a h^2 convergence rate in the residual error in accordance with theoretical estimates for linear finite elements (Figure 3-10).

Whereas the MMS result just described lends additional confidence to the results of the our finite element solver in the limit of decreasing h, the distributed source term is not representative of actual sources deployed in geophysical surveys. Hence, we also seek a convergence/verification test using an exact solution derived from a more geophysically relevant source. This is the MES method: Define the source term $\nabla \cdot \mathbf{J}_s$ and solve Eq (3.1) for the exact solution ϕ^{EXACT} under some relevant/convenient boundary conditions, then compare – as before – the numerical solution

to the exact solution over a range of h values. To keep things simple in the first of our MES analyses (MES1), $\nabla \cdot \mathbf{J}_s$ is a Dirac delta function located at the origin (thus representing the grounded end of an insulated wire carrying an implied 1 A current) and $\sigma = 1$ S/m everywhere. That is, the exact solution $1/4\pi r$ is that for unit–amplitude source electrode buried deep within the earth, sufficiently far away from the air/earth interface that the interface can be safely ignored, where r is the distance to the source electrode. Numerically, the MES1 problem is solved over the same $100 \times 100 \times 100$ m domain as the MMS problem described above with the exact solution imposed as a Dirichlet boundary condition. Discretization of the domain is done in two steps to ensure that a mesh node resides at the origin and some degree of mesh symmetry persists as h is refined. First, the domain is sliced along the $x, y, z = 0$ planes. Second, each of the resulting 8 subdomains are populated with tetrahedra having edge length h, sharing nodes, edges and faces across the subdomain boundaries. Although an algebraically simple analytic solution, the singularity at the origin and our insistence of putting a mesh node there guarantees that the norm of residual vector between numerical and exact solutions will always be infinite. Hence, we compute residual norms on $2 < h < 10$ as before, but only for those nodes greater than 10 m from the origin. At the coarsest discretization $h = 10$ m, this guarantees that the singularity and the error in its immediate vicinity does not affect the overall residual error estimate. As in the MMS case above, h^2 convergence of the residual norm is observed, demonstrating that the quixotic efforts our finite element solver to replicate singularities in the exact solution are spatially localized over a distance of a few h's (Figure 3-10).

Lastly, we construct a second exact solution test (MES2) to analyze how the hierarchical material representation (Weiss, 2017) affects the convergence of the global error estimate under h refinement. After all, we use the hierarchical representation to explicitly examine the Neumann series expansion described earlier in the Theory section, and the $1/h$ dependence on the maximum eigenvalue estimate (Figure 3-9) has serious consequences for the usefulness of Neumann series expansions in geophysical exploration settings like that considered here. Through the MMS and MES1 analyses, we've demonstrated that $h \to 0$ mesh refinement yields the expected theoretical convergence h^2 for smooth solutions over linear tetrahedral elements, even when in cases when the exact solution is singular. As a final test, consider a model of a vertically oriented, thin, conducting sheet, embedded in a less conducting halfspace. Geologically, this could represent a vertical fault plane or perhaps a thin dike. The electrostatic potential in the Earth region for a 1 A Dirac delta source located at the origin (on the air/earth interface) and an outcropping, semi–infinite vertical slab with boundaries $x = s > 0$ and $x = s + b > s$ can be "tediously" derived by the method of images (Telford et al., 1990). Letting the earth and slab conductivity be given by σ_1 and σ_2, respectively, the solution in region $-\infty < x < s$ is given as:

$$\phi(x,y,z) = \frac{1}{2\pi\sigma_1}\left[\frac{1}{R_1} + \frac{k}{R_2} + A\sum_{m=0}^{\infty}\frac{k^{2m}}{R_3}\right]; \tag{3.14}$$

in $s < x < s + b$ as,

$$\phi(x,y,z) = \frac{1}{2\pi\sigma_1}\left[B\sum_{m=0}^{\infty}\frac{k^{2m}}{R_3} + C\sum_{m=0}^{\infty}\frac{k^{2m}}{R_4}\right]; \tag{3.15}$$

and in region $x > s+b$ as,

$$\phi(x,y,z) = \frac{1}{2\pi\sigma_1}\left[D\sum_{m=0}^{\infty}\frac{k^{2m}}{R_4}\right], \tag{3.16}$$

with constants

$$A = -k(1-k^2), \quad B = -k(1+k), \quad C = 1+k, \quad \text{and} \quad D = 1-k^2 \tag{3.17}$$

reflection coefficient $k^2 = (\sigma_1 - \sigma_2)/(\sigma_1 + \sigma_2)$ and radial distances

$$\begin{aligned} R_1 &= \sqrt{x^2+y^2+z^2}, \\ R_2 &= \sqrt{(2s-x)^2+y^2+z^2}, \\ R_3 &= \sqrt{\big(2(m+1)b+2s-x\big)^2+y^2+z^2}, \quad \text{and} \\ R_4 &= \sqrt{(2mb+x)^2+y^2+z^2}. \end{aligned} \tag{3.18}$$

Note that while there is an inverse–distance term ($1/R_2$, $1/R_3$ and $1/R_4$) present for each of the image points in Eq (3.14 through 3.16), those image points, respectively, lie outside the domain where the potential is computed and thus do not introduce additional singularities beyond that due to source – the $1/R_1$ term.

Recall that under the hierarchical material property representation (Weiss, 2017), a thin sheet is assigned a finite conductance (anomalous conductivity $\times$ thickness product) whose value is assigned to the infinitely thin facets of the tetrahedral finite element mesh. In the present MES2 example, that value is taken arbitrarily to be 10 S, with a background "host rock" conductivity $\sigma_1 = 0.01$ S/m. Over a model domain $-100 < x,y < 100$ m and $-100 < z < 0$ m representing the earth region alone, the hierarchical finite element solution is compared to the exact solution Eq (3.14 through 3.16) for the case of a very thin (but not zero) slab of thickness $b = 0.1$ m offset $s = 20$ m from the origin (Figure 3-11). As in the MES1 example, the model domain sliced in the $x,y = 0$ planes, but now with an additional slice at $x = 20$ m so that a vertical plane of contiguous triangular facets is present for representing the conducting sheet. Because the model domain only encompasses the earth region, Eq (3.14 through 3.16) are imposed as a Dirichlet boundary condition on $x,y,z = -100$ m and $x,y = 100$ m sides of the computational domain while a homogeneous Neumann condition is applied to the air/earth interface, $z = 0$ m, to ensure current continuity between the air and earth regions.

Numerical experiments where the norm of the residual between the (hierarchical) finite element and the exact, Eq (3.14 through 3.16), solution is computed over the range $2 < h < 10$ m show agreement with the theoretical h^2 convergence rate for linear finite element methods and volume-based material representation (Figure 3-10). Hence, we see no evidence that the $1/h$ dependence on the maximum eigenvalue (Figure 3-9) is attributable to some unforeseen and pathological convergence behavior introduced by the hierarchical material model.

Given these findings, what are the possible paths forward for electric field modeling of mature, developed oilfields? Clearly, there remains the question of how other series approximations perform under circumstances similar to that considered here. These may include, for example, the Rytov series or one of the many Neumann series variants such as extended Born approximation.

Included in this is cross–analysis by competing 3D forward solvers and the consideration of alternative subsurface models with varying degrees of complexity. To that end, the chapter is not fully closed on series approximations for complicated subsurface models rich in anthropogenic clutter, despite the discouraging results just shown for the case of a simple, single–well oilfield model.

3.6. CONCLUSIONS

We have demonstrated through the unique capabilities of hierarchical finite element analysis the convergence of a Neumann series expansion of the electrostatic field in an idealized oilfield setting consisting of a modest set of mildly conducting fractures surrounding an idealized steel casing. The Neumann series is computed about these mild fracture perturbations alone, with the strong conductivity of the steel casing embedded in the linear operator on which the Neumann series is built. As a complementary approach to prior work where this linear operator is derived from integral equation methods, we derive a linear operator from the differential form of the governing Maxwell equations and show that its spectral radius varies as the inverse of mesh size $\sim 1/h$, suggesting that the Neumann series is intrinsically divergent for all perturbation in fracture conductivity in continuous limit $h \to 0$. The hierarchical finite element method upon which this analysis would otherwise not have been possible is shown to possess h^2 convergence in solution accuracy, consistent with theoretical estimates for traditional nodal final finite elements, and thus ruled out as an unwelcome agent to the Neumann series' inescapable divergence. In the case of oilfield characterization in the presence of steel infrastructure, fracture diagnoses methods reliant on Neumann series analysis or some abbreviated version therein are thereby suspect owing to the strong galvanic coupling between the fracture and infrastructure. Conditions under which there is sufficient decoupling between the fracture and infrastructure are surely complex and depending upon fracture/infrastructure separation and geometrical constraints, and it is yet to be determined whether useful "rules of thumb" are ultimately available. Until that time, analysis such as that presented here – convergence studies, eigenspectrum estimation, verification & validation – are useful tools for determining whether a particular manifestation of the Neumann series approach is numerically defensible.

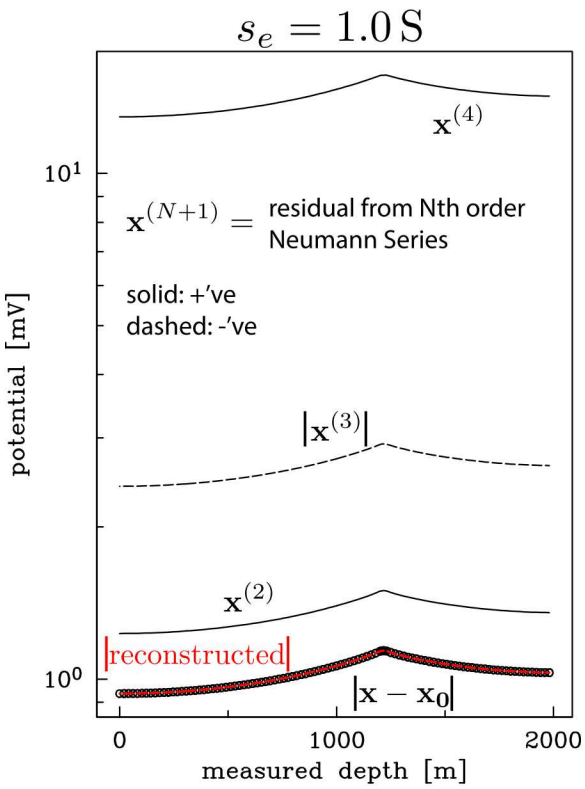

Figure 3-6. True scattered potential computed by direct differencing $\mathbf{x} - \mathbf{x}_0$ (black circles) and by reconstruction $\sum_{i=1}^{N} \mathbf{x}_i + \mathbf{x}^{(N+1)}, N = 0, 1, 2, 3$ (red) for fractures with total conductance $s_e = 1.0$ S located at measured depth 1200 m and excited by a 1 A source at the well head. Residuals for Neumann series expansion of order $i - 1$ are shown by $\mathbf{x}^{(i)}$ and computed directly by Eq (9). Earth model is a 0.01 S/m halfspace, with a 5×10^4 S·m steel casing extending 1 km down from the well head and then 1 km horizontally (Weiss, 2017). In all cases, the relative error between the reconstructed solution and direct differencing is less than 0.006% along the borehole casing.

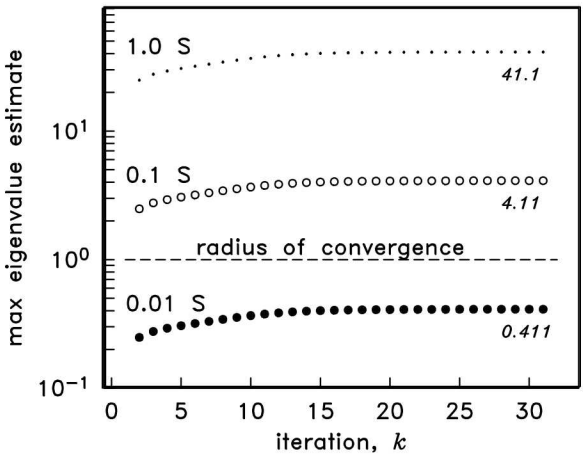

Figure 3-7. Convergence of maximum eigenvalue estimate as a function of iteration k for the three cases of conducting fractures considered in Figures 3-4 through 3-6, with conductances 0.01, 0.1 and 1.0 S, respectively. Shown by the dashed line is the radius of convergence 1.0 delineating the convergent Neumann series model (0.01 S) from the divergent others (0.1 and 1.0 S). Values of the maximum eigenvalue estimate (italics) annotate each of the three sequences at convergence.

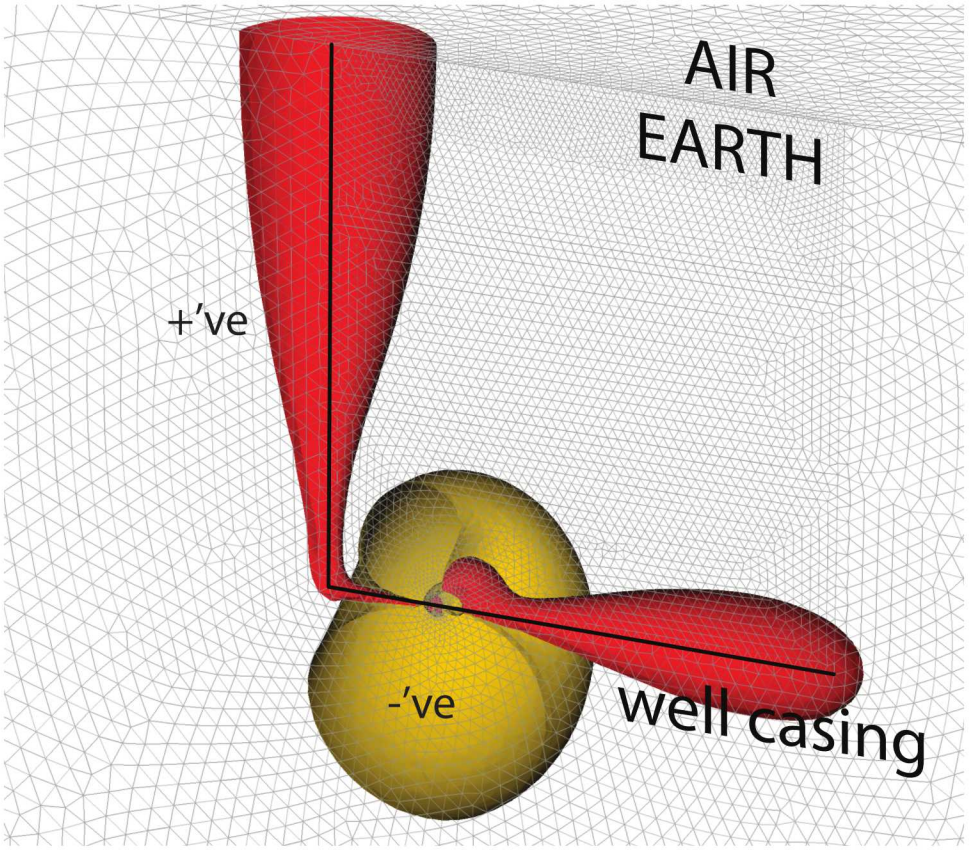

Figure 3-8. Following the cutaway view in Figure 3-2, representative isosurfaces (red, positive; amber, negative) for the eigenmode corresponding to the maximum eigenvalue for a Neumann series expansion around perturbations in fracture conductivity alone. Note the strong signature of the steel casing (red) which is not part of the conductivity perturbation in the fractures, but is nonetheless strongly coupled to it.

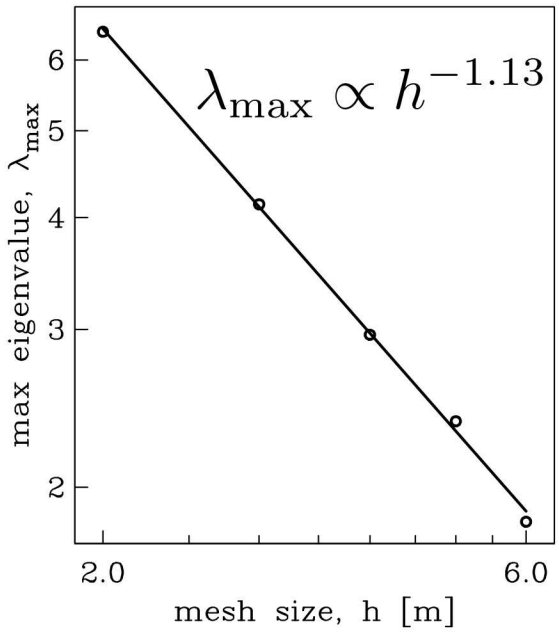

Figure 3-9. Effect of fracture discretization on maximum eigenvalue estimate. Keeping the fracture geometry constant, the maximum eigenvalue estimate is computed for five different fracture discretizations where the mesh size (node spacing) h ranges from 2 to 6 m. Empirically, we observe a roughly $1/h$ dependence for the maximum eigenvalue estimate.

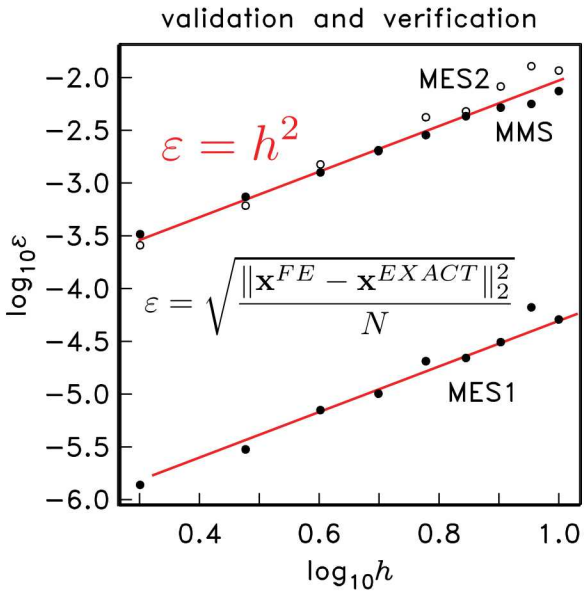

Figure 3-10. Verification of the second order error convergence of linear nodal finite elements for three independent solutions: one by the method of manufactured solutions (MMS) and two by the method of exact solutions (MES). Root mean squared error ε of the finite element solution increases as the square of the element size, h. See text for details on mesh design and MMS/MES problem statements.

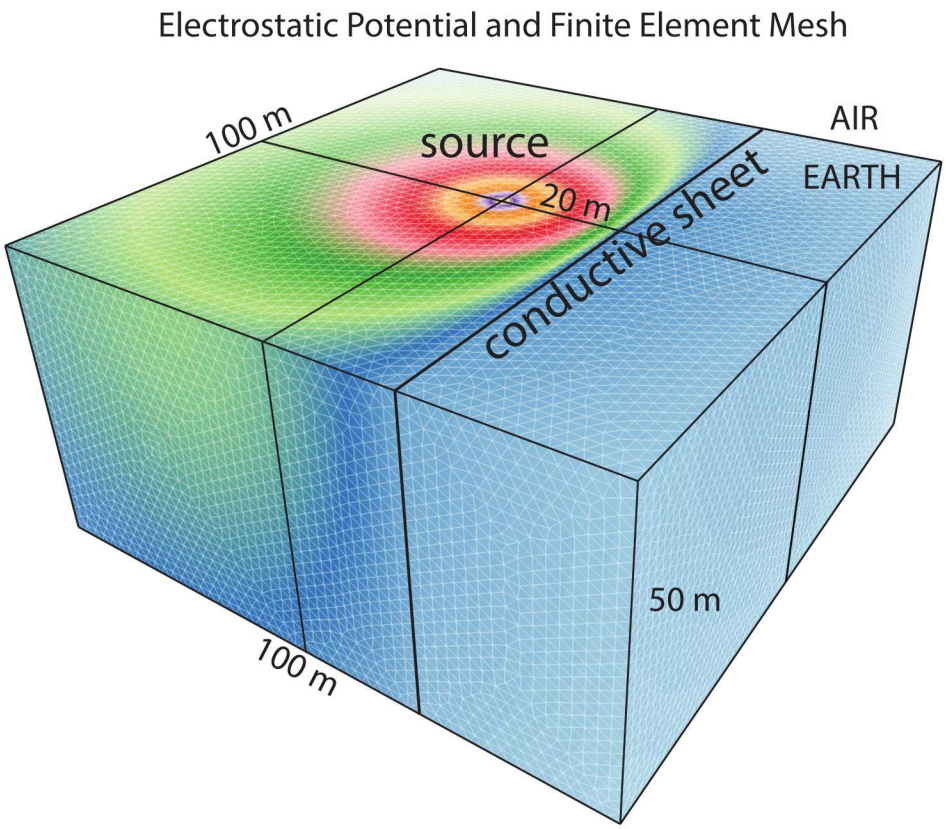

Figure 3-11. Finite element solution (color scale) and mesh for problem MES2, the electrostatic response due to a single pole on the air earth interface and adjacent to an infinitesimally thin vertical conducting sheet. Earth conductivity is 0.01 S/m and sheet conductance is 10 S. Exact solution is that from a 0.1 m sheet of 100 S/m conductivity, which yields the equivalent transverse conductance value 10 S. Heavy lines show block boundaries within the model domain, which themselves are discretized with uniform tetrahedra of edge length h.

4. APPLICATION OF EM METHODS FOR INFRASTRUCTURE EXPLOITATION

4.1. SUMMARY

A hierarchical model of material electrical properties representing volume–, face– and edge–based distributions is presented for the purpose of efficient representation of strong, but volumetrically insignificant, conductors in finite element modeling. The model is currently implemented in the context of three–dimensional (3D) DC resistivity simulations, but appears suitable for broadband electromagnetics as well. In contrast to the strategy of fine–scale discretization of thin or slender conductors by brute force with potentially millions of tiny tetrahedra, the hierarchical model collapses these small conductors onto infinitesimally thin faces and edges which reside on the interface between larger tetrahedra, thus avoiding excessive discretization and computational burden. The effect of this hierarchical model on the structure of the finite element formulation in the DC case is to augment the 3D stiffness matrix with the addition of a small set of 2D and and 1D element stiffness matrices corresponding to those facets and edges where the thin conductors reside. Thus, the added computational cost is minimal over that of the problem without the conductors. Benchmark solutions compare favorably with independent reference solutions and there is consistency between the volume–, face– and edge–based model parameters in the limit of extreme volume discretization. As an example application problem, results are presented on the DC response of an electrified underground railway line and show that the proposed model can reduce the resource footprint of the finite element calculation by several orders of magnitude.

4.2. INTRODUCTION

A widely recognized problem in electrical and electromagnetic studies of the subsurface is the efficient representation of anthropogenic clutter in numerical modeling. The need arises from a variety of exploration scenarios, ranging from ones where the clutter (e.g. pipes, landmines, unexploded ordnance) is the target of interest to cases where the scattered field from the clutter compromises the signal quality from some other target. Regardless, the numerical challenge in modeling strong conductors which are small in comparison to the scale of the geology or the geophysical survey arises from both the high conductivity contrast between the clutter and the

surrounding geology, and, the very fine discretization required to numerically capture their shape and size in a large computational domain. In the context of finite element modeling, small strong conductors of arbitrary shape can be reasonably approximated by many small tetrahedral elements - which, in the case of metal pipes, for example, may represent volumes on order of a cubic centimeter or less, which are then embedded in a mesh representing a volume of several cubic kilometers. Parallelized finite element, volume and difference methods have all been implemented in the limit of extreme discretization to reduce the computational cost of the broadband electromagnetic problem Commer et al. (2015); Um et al. (2015); Haber et al. (2016), resulting in run times on the order of several minutes to hours. Further reduction in runtime can be achieved by "upsizing" the conductive features to some length scale that is physically unrealistic, but whose adverse effects on numerical solution accuracy are acceptable Haber et al. (2016); Weiss et al. (2016).

The concept of a hierarchical material properties model for finite element analysis on an unstructured tetrahedral grid is motivated by the Cartesian resistor network of Yang et al. (2016), which, in turn, was based on the earlier work of Newmark et al. (1999) and Daily et al. (2004). In the resistor network concept, as cited here, a Cartesian lattice is defined with cell–by–cell variability in electrical conductivity. On each of the edges of the Cartesian grid, the two Kirchhoff circuit laws are enforced assuming a volume–averaged current surrounding the edge. This leads to a linear system of equations that can be solved for the electric potential on each node of the lattice. Yang et al. (2016) updated the resistor network to include face– and edge–based electrical properties on the Cartesian and recognize the similarity in mathematical form between the Kirchhoff linear system and that derived from discretization of the governing Poisson equation, but pointed out a key difference: face– and edge–based material properties could not be accommodated by the usual finite element method for the 3D DC resistivity problem. The hierarchical material properties model described here makes that previously unrecognized connection between finite element analysis and the resistor network formulation, with all the benefits of finite element analysis as a result – namely, a flexible discretization with elements geometrically conformable to complex conductivity distributions, including that of the thin and sinuous conductors lying at interstices between elements.

4.3. THEORY

The central concept of the hierarchical conductivity model is to associate electrical conductivity with three different geometric structures – volumes, facets and edges – in such a way that when used in a finite element discretization, the facet and edge conductivities remain local to facets and edges in the final global system of linear equations. Doing so addresses the central concern raised by Yang et al. (2016). Letting the electrical conductivity be represented by the rank–2 tensor $\boldsymbol{\sigma}$, one mathematical structure that achieves this goal is the following:

$$\boldsymbol{\sigma}(\boldsymbol{x}) = \sum_{e=1}^{N_V} \sigma_e \boldsymbol{\psi}_e^V(\boldsymbol{x}) + \sum_{e=1}^{N_F} s_e \boldsymbol{\psi}_e^F(\boldsymbol{x}) + \sum_{e=1}^{N_E} t_e \boldsymbol{\psi}_e^E(\boldsymbol{x}), \tag{4.1}$$

with hierarchical, rank–2 basis functions

$$\boldsymbol{\psi}_e^V(\boldsymbol{x}) = \mathrm{diag}(1,1,1)\begin{cases}1 & \text{if } \boldsymbol{x} \in \text{volume } e\\ 0 & \text{otherwise}\end{cases}, \tag{4.2}$$

$$\boldsymbol{\psi}_e^F(\boldsymbol{x}) = \mathrm{diag}(0,1,1)_e\begin{cases}1 & \text{if } \boldsymbol{x} \in \text{facet } e\\ 0 & \text{otherwise}\end{cases}, \tag{4.3}$$

and

$$\boldsymbol{\psi}_e^E(\boldsymbol{x}) = \mathrm{diag}(1,0,0)_e\begin{cases}1 & \text{if } \boldsymbol{x} \in \text{edge } e\\ 0 & \text{otherwise}\end{cases}. \tag{4.4}$$

In Eq (4.2-4.4) the diagonal rank–2 tensor is subscripted by e to indicate representation in the local $\hat{\mathbf{e}}_1$-$\hat{\mathbf{e}}_2$-$\hat{\mathbf{e}}_3$ frame (Figure 4-1). For facets, we take the $\hat{\mathbf{e}}_2$ and $\hat{\mathbf{e}}_3$ directions to lie in the plane of the eth facet, where for edges, we take the $\hat{\mathbf{e}}_1$ direction to lie parallel to the eth edge. Note that volume integration of Eq (4.1) with the definitions laid out in Eq (4.2-4.4) takes on the SI units [S·m^2]. Hence, the SI units of coefficients s_e and t_e must be [S] and [S·m], respectively. That is, s_e represents the conductivity–thickness product of facet e, and t_e represents the product of conductivity and cross-sectional area for edge e.

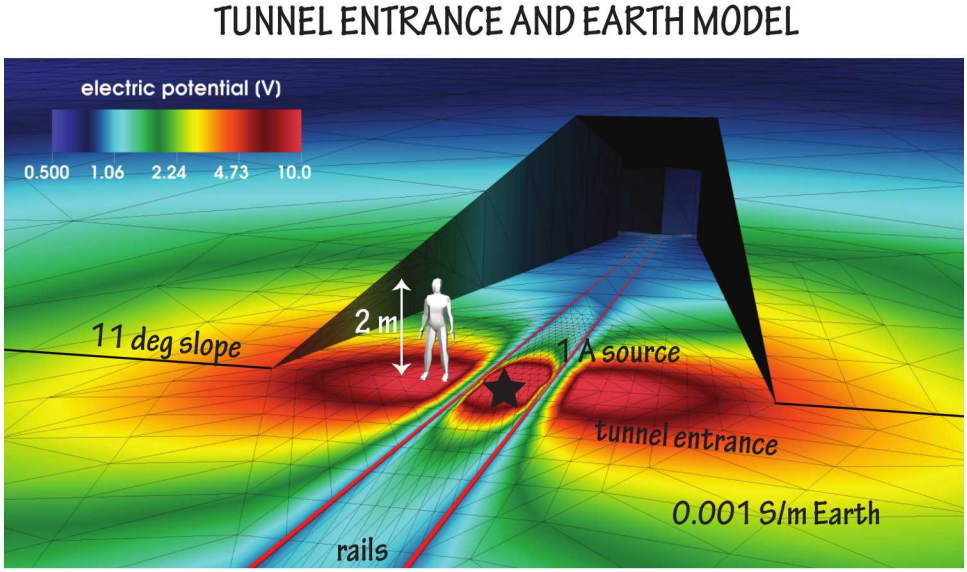

Figure 4-1. Entrance to an underground tunned complex into the side of an 11° slope. Rails (heavy lines) are energized at the entrance by a 1A point source.

Substitution of Eq (4.1) into the governing Poisson equation $\nabla\cdot(\boldsymbol{\sigma}\cdot\nabla u) = f$ leads to the weak variational form of the DC resistivity problem: find u such that $a(v,u) = (v,f)$ for all test functions v where

$$a(v,u) = \int_\Omega \nabla v\cdot(\boldsymbol{\sigma}\cdot\nabla u)\,dx^3. \tag{4.5}$$

It is clear that tensors $\text{diag}(0,1,1)_e$ and $\text{diag}(1,0,0)_e$ collapse the volume integration in Eq (4.5) into surface and line integrals. Hence, the resulting stiffness matrix $\mathbf{K}$ in the finite element system of linear equations

$$\mathbf{K}\mathbf{u} = \mathbf{b}, \tag{4.6}$$

is a sum of 3D, 2D and 1D element stiffness matrices

$$\mathbf{K} = \sum_{e=1}^{N_V} \sigma_e \mathbf{K}_e^4 + \sum_{e=1}^{N_F} s_e \mathbf{K}_e^3 + \sum_{e=1}^{N_E} t_e \mathbf{K}_e^2, \tag{4.7}$$

and the locality concerns raised by Yang et al. (2016) are now resolved.

4.4. BENCHMARKING AND EXAMPLE

Previous benchmarking of the Weiss et al. (2016) strictly volume–based DC resistivity modeling software showed favorable agreement with the Johnson et al. (1987) analytic solution for a finite vertical cylinder in a halfspace. Extending this benchmark exercise to now include edge–based conductivity elements in Eq (4.1), finite element solutions for an infinitely thin conductor with conductivity–area product $t = 10^4$ S·m are compared against analytic solutions for a conductor of radius 0.001 m and infinite conductivity (Figure 4-1, inset). In the finite element simulation, this t value is equivalent to conductivity value $\sim 3.3 \times 10^9$ S/m, a reasonable value in the asymptotic limit to infinite conductivity. In this limit, the electric potential on the borehole cylinder is nearly independent of position on the borehole itself. As such, the borehole potential is analyzed as function of source–borehole offset and excellent agreement is found between analytic and finite element solutions (Figure 4-1).

To complete the benchmarking exercise, results from the (previously validated) volume–based model representation are compared against those for facet–based conductivities, the middle term in Eq (4.1). Out of simplicity, the test model consists of a 35 m radius circular disk, 1 m thick, buried horizontally 10 beneath the air/Earth interface (Figure 4-2, inset). Discretizing the disk with small tetrahedra (edge length roughly 1 m), the volume–based finite element results are compared with those where the disk is simply represented by facets with transverse conductance $s_e = \sigma\,\text{S/m} \times 1\,\text{m}$. Again, the agreement is excellent (Figure 4-2) over a range of disk conductivities and thus, it would appear that the volume, facet and edge representations of electrical conductivity in Eq (4.1) are self consistent.

It's worth pointing out that benchmarking results shown here are for embedded conductors. This is encouraging for the metal clutter problem, but what about embedded resistors? This remains an open research question, but it's worth noting the following example in DC resistivity modelling. Replacing the conducting disk in Figure (4-2) with a perfectly resistive one results in equipotential lines normal to the disk face, with a strong potential gradient vertically through the disk. Hence, in the limit of an infinitely thin disk, the potential is discontinuous and thereby incompatible the vector space of continuous functions from which the finite element solution u is drawn. One possible workaround is to introduce a "tear" in the finite element mesh whereby a surface is twice discretized – once with facets for edges on one side of the tear, and again with

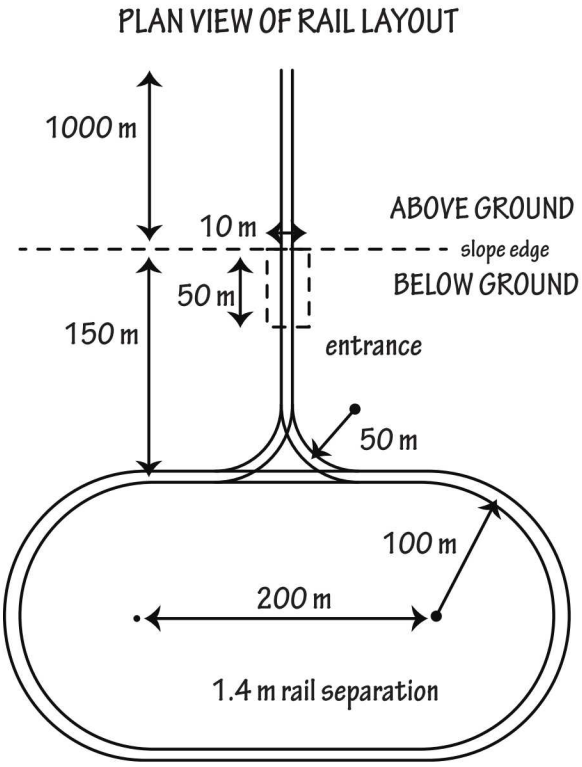

Figure 4-2. Plan view of tunnel complex and steel rails in Figure 4-1.

another set of facets for the other side – with homogeneous Neumann boundary conditions applied to each side. Such scheme has shown favorable results Weiss (2017).

As a final example, the DC response of an underground tunnel complex is presented, on the floor of which lies a pair of 2 km long railway rails energized by 1 A grounded source (Figure 4-1). Buried 1 km deep into the side of 11 degree slope, the tunnel complex presents an interesting challenge for modeling for several reasons. First is the fact standard light–freight rails have a cross sectional area of approximately 60 cm^2. A single rail 2 km in length thus occupies a volume 12 m^3 of steel, which would require roughly 100 million tetrahedra of 1 cm edge length to discretize for a finite element mesh. In the edge–based discretization, the rails are approximated by a set of edges, each 5 m in length, resulting in only $N_E = 800$ additional terms in the summation Eq (4.1). One small challenge presented by the use of edge–based elements is that it is no longer appropriate impose a homogeneous Neumann boundary condition on the air/Earth interface at those edges where the strong conductor lies. Because the conductor is zero thickness, such a boundary condition is in conflict continuity of current at the Earth/conductor interface. Hence, an air layer is added to the model, in this case roughly doubling the number of elements in the finite element mesh to approximately 300k, within which there are only 50k nodes. The finite element system of equations Eq (4.6) is solved iteratively using a Jacobi–scaled conjugate gradients in 32 s on a 3.1 GHz MacBook (Figure 4-3).

Oblique cutaway view of the electric potential in the 3D finite element simulation of the tunnel and rail complex described here. A vertical slice through the 3D Earth model is located on the

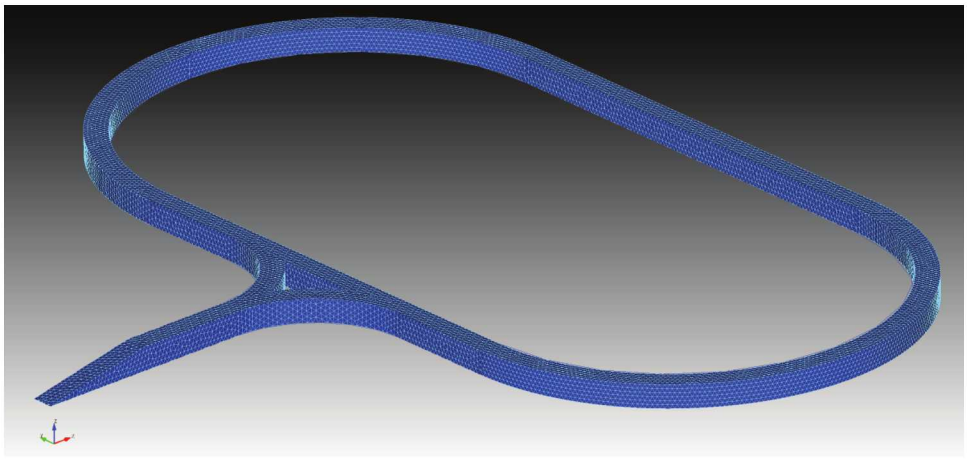

Figure 4-3. Discretized tunnels and rails in Figure 4-1. Rails are represented by finite element edges with 5 m nodal spacing, separated by 1.4 m and corresponding to light freight capacity (49.6 kg/m) with steel conductivity 7×10^6 S/m. Local mesh refinement near the tunnel entrance (adit) yields a mesh spacing of approximately 1 m.

left/right symmetry plane of the complex, on which the potential is shown (color scale) to illustrate how the potential on the rails manifests as a signal on Earth's surface. To the left of the vertical slice is the potential on the AIR/EARTH interface where pairs of surface electrodes can be deployed to measure potential differences as shown by variation in the color hue. To the right is the potential on a level surface cut into the slope on which the rail and tunnel complex lie. Whereas much of this area is inaccessible to direct measurement, except within the tunnel itself, it is useful to see the extent to which the rail is energized and how its elevated potential extends laterally within the subsurface.

4.5. CONCLUSIONS

The benchmarking examples shown here demonstrate that hierarchical conductivity model Eq (4.1) is both self–consistent and generates results that agree with independent reference solutions when the facets and edges are relatively conductive with respect to the volume elements. However, it's also been shown (Weiss, 2017) that the jump discontinuity in electric potential across the face of a thin resistive disk requires more of the finite element formulation than the modified model Eq (4.1). When used in the context of DC resistivity simulations, the conductivity model must be accompanied by a suitable finite element vector space– one which admits step discontinuities – for the evaluation of arbitrary conductivity structure. Extending the concept of the hierarchical material properties model to three–dimensional, time–dependent electromagnetics (either frequency domain or generalized time domain) is an open question best pursued, for several reasons, in future research. For example, the frequency domain problem has been cast is all varieties of magnetic–, electric– and potential–field formulations, and it remains to

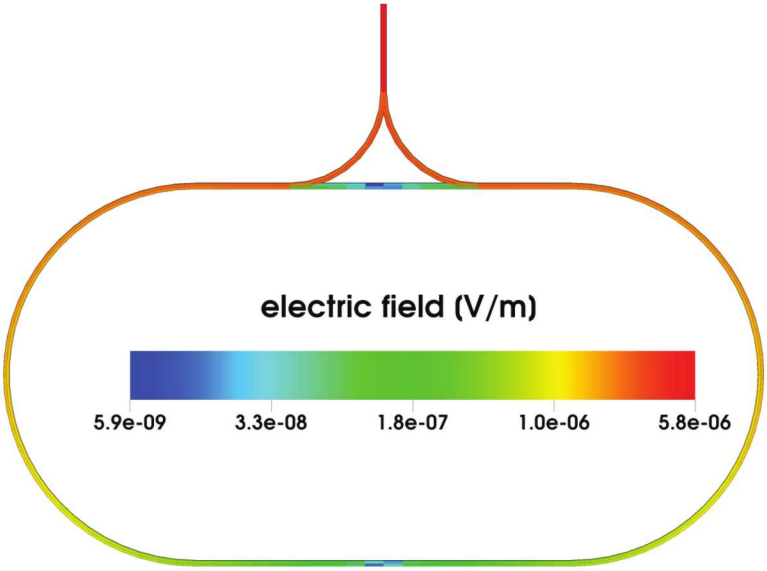

Figure 4-4. Electric field on the underground rails within the tunnel complex described in Figures 4-1 and 4-2. Source is a 1 A single pole electrode located at the tunnel entrance.

be understood how the facet– and edge–based conductivities may frustrate the numerical solution, as resistors do in DC, without additional mesh modification. In the context of near surface geophysics, the rail and tunnel example presented here suggests investigating whether magnetic permeability can also be distributed by an analogous hierarchical model, thereby allowing for economical modeling of highly conductive and permeable steel. In principle, it appears that the mathematical structure of Eq (4.1) would admit such an idea, but at first blush, its implementation is problematic. That is, in the frequency domain electric field formulation, the governing equation in a source–free region is

$$\nabla \times \left[\boldsymbol{\mu}^{-1} \cdot (\nabla \times \mathbf{E}) \right] + \mathrm{i}\omega (\boldsymbol{\sigma} \cdot \mathbf{E}) = 0 \tag{4.8}$$

and it's clear that although high–conductivity facets and edges are well represented by their corresponding s_e and t_e coefficients in $\boldsymbol{\sigma}$, a high–permeability edge or facet in $\boldsymbol{\mu}^{-1}$ results in analogous coefficients that, in the limit of infinite permeability, are zero and hence safely ignored. Recasting the governing Maxwell equations in terms of a second–order magnetic field formulation does not resolve the conflict, but rather shifts the problem from the $\boldsymbol{\mu}^{-1}$ term to the corresponding $\boldsymbol{\sigma}^{-1}$ term nested between $\nabla\times$ terms. One possible workaround is to admit s_e and t_e coefficients with negative values, thus making a weighted sum (for unit consistency) of σ_e, s_e and t_e representative of the facet and edge conductance. However, doing so would still require compatibility with the underlying discretization, which in the case of DC resistivity, necessitated the introduction of tears in the finite element mesh. Lastly, it's conceivable that use of the hierarchical model, Eq (4.1), for conductivity, permeability, or both, may require re–evaluation of the time–stepping requirements for transient calculations since the facet and edge structures contained in the model are infinitesimally thin. Of course, such considerations could be avoided (or at least deferred to a later time) by working first in the frequency domain, followed by Fourier transform.

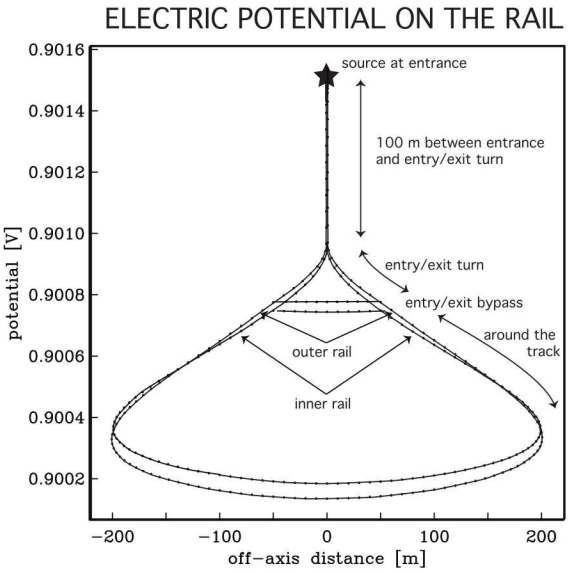

Figure 4-5. Electric potential (voltage) on the rails in the tunnel complex described in Figures 4-1 and 4-2. Source is a 1 A single pole electrode located at the tunnel entrance. Inspection of the potentials shows that there is continuity, as expected, at the junction points where the rails curve into the complex. Also evident is a measureable potential difference between rails in addition to the potential difference along the individual rails themselves. These effects are due to the finite conductivity of the rails and the current leakage from the rails into the surrounding geology.

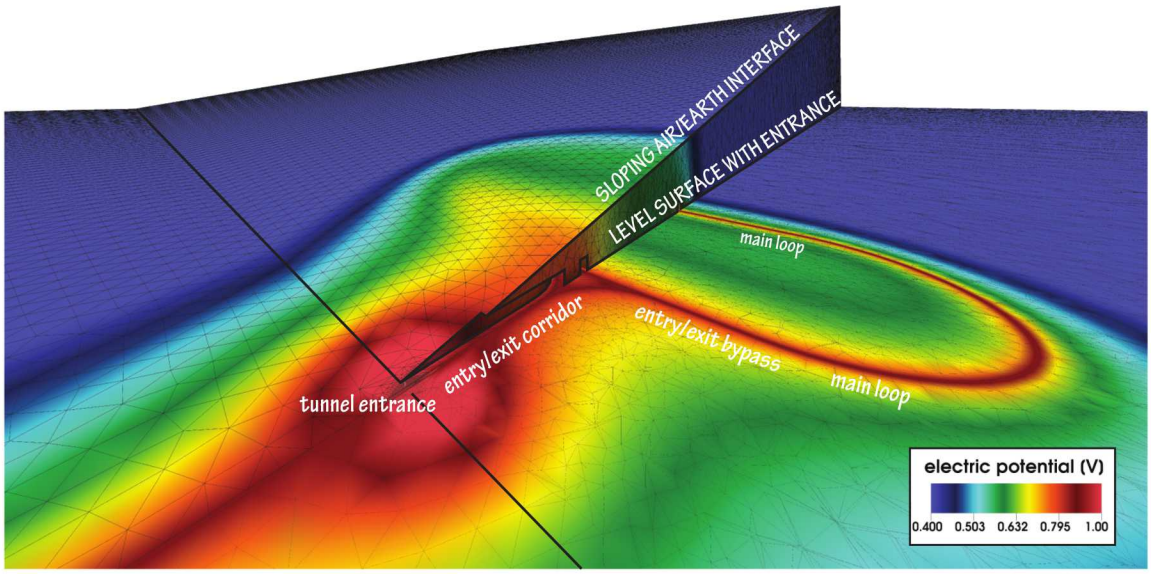

Figure 4-6. Partial cutaway view of the finite elemement mesh and electric potential for the tunnel and rail complex shown in Figures 4-1 and 4-2. Source is a 1 A single pole electrode located at the tunnel entrance. Mesh consists of 1.8M tetrahedral elements with 310k nodes. Rails were discretized with only 499 edge–based conductivity elements. Solution time was ~ 4 min with preconditioned conjugate gradients to an optimal solution with normalized target residual of 10^{-12}.

5. FINITE ELEMENT ANALYSIS FOR OILFIELD AWARENESS

5.1. SUMMARY

The recurring problem in electrical and electromagnetic modeling of anthropogenically impacted geologic settings is the need for efficient representation of strong, thin, arbitrarily oriented electrical conductors, such as metal pipes or conductive fractures. The difficulty arises from discretization with roughly equidimensional elements of the governing Maxwell equations over these volumetrically insignificant regions; which by virtue of conductors' thinness, can easily number in the 100's of millions for even simple models. To address this problem, a novel hierarchical electrical model is proposed for unstructured tetrahedral finite element meshes, where the usual volume–based conductivity in tetrahedra is augmented by facet– and edge–based conductivity on the infinitesimally thin regions between elements. This allows a slender borehole casing of arbitrary shape to be approximated by a set of connected edges within the mesh, and on which a conductivity–area product is explicitly defined. Benchmark testing of the direct current (DC) resistivity problem shows excellent agreement between the facet/edge representations and independent analytic solutions. As a practical case, the metallic infrastructure of a mature oilfield in the Kern River Formation is modeled. The oilfield comprises roughly 2 km of surface pipeline and 122 vertical, steel–cased wells, each extending to a depth of 300 m. Numerical results demonstrate strong coupling between surface and downhole conductors and reveal a complex circuit of current flow within the (finite conductivity) steel. This would be difficult to quantify using alternative, approximate methods for accommodating the approximately 30 km of steel casing and surface pipe combined.

5.2. INTRODUCTION

It has long been recognized in electromagnetic (EM) geophysics that over the field scale, volumetrically insignificant, but strongly conducting metallic features such as pipes, cables and rails can have a huge effect on measured signals, covering large distances and having magnitudes comparable to, if not larger than, those from geologic targets of interest (Fitterman, 1989; Fitterman et al., 1990). However, generalized discretization of such metal for numerical modeling is computationally burdensome if equidimensional elements – preferable for numerical tractability – are used because many small elements are necessary to fill the conductor volumetrically. For example, to discretize 500 m of standard well casing (0.1 m diameter, 0.025 m

wall thickness) would require roughly 3.7×10^6 equidimensional tetrahedra. Over a 1 km^3 volume discretized with 10 m edge length, the borehole would consume nearly 30% of the total tetrahedra, but only represent 7×10^{-7}% of the volume. This results in an extreme concentration of computational resources in a region potentially far from observation points, and also severely inflates the overall size of the numerical problem.

Presented with such a problem, one approach is to embrace the full computational burden of the problem and develop algorithms for massively parallel architectures (Commer et al., 2015; Um et al., 2015) or employ multigrid methods (Haber et al., 2016). Another approach is to employ analytic or integral equation methods for computing scattered electric and electromagnetic fields from some external source (Wait, 1952; Hohmann, 1971; Parry and Ward, 1971; Howard, 1972; Wait, 1957; Wait and Williams, 1985; Williams and Wait, 1985; Johnson et al., 1987; Schenkel and Morrison, 1990; Patzer et al., 2017) and use these fields as an equivalent sourcing term. However, with the exception of Qian and Boerner (1995), these formulae are typically for straight boreholes in uniform or layered earth.

Yet another approach is to expand the Cartesian resistor network model (Newmark et al., 1999; Daily et al., 2004) by including conductivity elements associated with the faces and edges of the Cartesian cells. Application of the Kirchhoff circuit laws at circuit junctions (nodes of Cartesian lattice) results in a linear system whose solution yields the electric scalar potential (Yang et al., 2016). Although the linear system bears some resemblance, in the matrix operator sense, to the governing equation for electrostatics, it was not recognized how the connection could be made. Weiss (2017) concieved the hierarchical volume–facet–edge conductivity concept, and generalized it to the finite element formulation of the electrostatics problem. Weiss demonstrated the aforementioned connection and provided framework for representing the facet and edge conductivities on an unstructured grid. The conducting facets and edges can be arbitrarily sized, connected and oriented, thereby allowing efficient representation undulating conductive sheets or circuitous, bending linear conductors.

In this study, the Weiss (2017) finite element formulation is applied to DC modeling in a mature oil field, where there is abundant surface pipeline and numerous, closely spaced wells. First, a brief review of the hierarchical finite elements is provided, along with one benchmark example from Weiss (2017). Next, analysis of a model based on the Kern River Formation near Bakersfield, California, is presented.

5.3. THEORY

The mathematical theory of DC resistivity modeling in geophysics is well established (Telford et al., 1990). Therefore, the theoretical development begins with the governing Poisson equation:

$$-\nabla \cdot (\boldsymbol{\sigma} \cdot \nabla u) = f, \tag{5.1}$$

where u is the electric scalar potential, f is the divergence of the electric current density source, and $\boldsymbol{\sigma}$ is the rank–2 tensor of electrical conductivity. By allowing the principal axes of the conductivity tensor to vary arbitrarily, element–by–element, the conductivity can be decomposed

into parts. These parts are associated with N_V tetrahedra (the usual method of discretization) plus two additional terms associated with some subset of N_F facets and N_E edges within the tetrahedral mesh (Weiss, 2017). That is:

$$\boldsymbol{\sigma}(\boldsymbol{x}) = \sum_{e=1}^{N_V} \sigma_e \boldsymbol{\psi}_e^V(\boldsymbol{x}) \; + \; \sum_{e=1}^{N_F} s_e \boldsymbol{\psi}_e^F(\boldsymbol{x}) \; + \; \sum_{e=1}^{N_E} t_e \boldsymbol{\psi}_e^E(\boldsymbol{x}), \tag{5.2}$$

with hierarchical, rank–2 basis functions.

$$\boldsymbol{\psi}_e^V(\boldsymbol{x}) = \mathrm{diag}(1,1,1) \begin{cases} 1 & \text{if } \boldsymbol{x} \in \text{volume } e \\ 0 & \text{otherwise} \end{cases}, \tag{5.3}$$

$$\boldsymbol{\psi}_e^F(\boldsymbol{x}) = \mathrm{diag}(0,1,1)_e \begin{cases} 1 & \text{if } \boldsymbol{x} \in \text{facet } e \\ 0 & \text{otherwise} \end{cases}, \tag{5.4}$$

and

$$\boldsymbol{\psi}_e^E(\boldsymbol{x}) = \mathrm{diag}(1,0,0)_e \begin{cases} 1 & \text{if } \boldsymbol{x} \in \text{edge } e \\ 0 & \text{otherwise} \end{cases}. \tag{5.5}$$

In Eq (5.2) through (5.4), the rank–2 tensor $\mathrm{diag}(\cdot)_e$ given in terms a local reference frame e for individual tetrahedra, facets, and edges (Figure 5-1). The result of this decomposition is the $N \times N$ finite element system of linear equations:

$$\mathbf{Ku} = \mathbf{b}, \tag{5.6}$$

is that the global stiffness matrix is a sum of element–based volume, facet and edge stiffness matrices

$$\mathbf{K} = \sum_{e=1}^{N_V} \sigma_e \mathbf{K}_e^4 + \sum_{e=1}^{N_F} s_e \mathbf{K}_e^3 + \sum_{e=1}^{N_E} t_e \mathbf{K}_e^2, \tag{5.7}$$

built by integration of $\nabla v \cdot (\boldsymbol{\sigma} \cdot \nabla u)$ over volumes, facets, and edges, respectively; where v is the test function introduced in solving the variation problem, which derives from Eq (5.1). N is the number of nodes in the discretization. Because the N_F facets and N_E edges in Eq (5.7) already reside inside the mesh of N_V tetrahedra, including the second and third summations in Eq (5.7) does not increase the size of the $N \times N$ coefficient matrix $\mathbf{K}$.

The linear system in Eq (5.6) is solved here using conjugate gradients with Jacobi (diagonal) preconditioning. Furthermore, the computational burden is minimized by computing the $\mathbf{K}$ matrix elements "on the fly" as necessary in each iteration of the conjugate gradient algorithm (Weiss, 2001), thus eliminating storage cost for $\mathbf{K}$. Out of conservatism, the iterative sequence is initiated with the zero vector and terminated once the residual ℓ_2 norm is decreased by a factor of 10^{-12} over its starting value.

Results of the hierarchical conductivity model, Eq (5.2), have been benchmarked against independent analytic solutions and checked for asymptotic agreement with thin conductors of finite thickness (Weiss, 2017). One such example is a comparison between analytic and

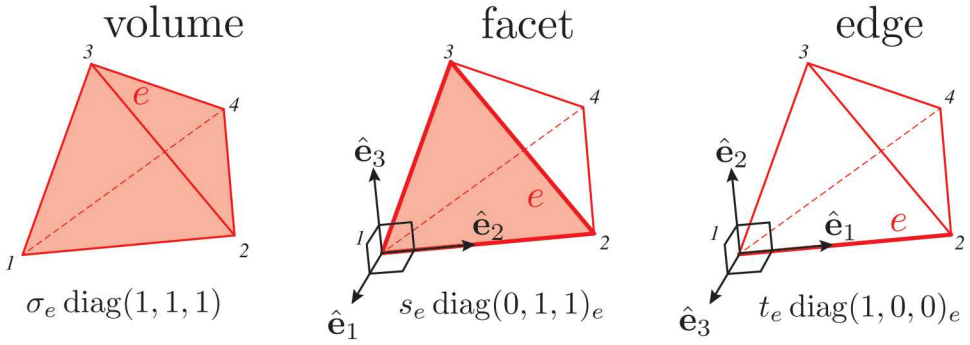

Figure 5-1. Hierarchy of volumes (left), facets (middle) and edges (right) on which the conductivity model in equation 3 is defined. For facets and edges, the $\hat{\mathbf{e}}_1$ direction in the local principal axis references frame oriented normal to the facet and along the edge, respectively.

edge-based finite element solutions of "casing voltage" for a perfectly conducting, thin (1 mm diameter) vertical cylindrical conductor (Figure 5-2). The potential on the surface of a perfect conductor is everywhere uniform, and it is this constant which is compared (see Figure 5-2, inset, for problem geometry). For the finite element calculation, a value of $t_e = 10^4$ S·m, was used, corresponding to a conductivity value $\sim 3.3 \times 10^9$ S/m, which is a reasonable approximation for a perfect conductor. Representing the cylinder by a set of continuous $(N_E = 100)$ 1 m segments yielded not only acceptable agreement with the (Johnson et al., 1987) solution, but also a considerable savings in mesh elements had we instead chosen to discretize the 100 m cylinder with tetrahedra 1 mm on a side.

5.4. OILFIELD EXAMPLE

As practical example, we examine a representative mature oilfield, taken here to be the Kern River Formation, north of Bakersfield, California. At this site, there is an abundance of metallic infrastructure that would frustrate traditional DC resistivity analysis of the subsurface (Figure 5-3). The particular model consists of nearly 2 km of surface pipeline and 122 steel cased wells. Public satellite imagery was hand digitized for well and surface pipe locations, with a resolution of approximately 0.1 m. For simplicity, clusters of adjacent, parallel surface pipelines were coalesced into a single conducting line. Absent specific information about the wells in the area, well depths are randomly distributed between 200 and 300 m into the subsurface. Topography and the the presence of four large storage tanks is ignored in this example.

A tetrahedral mesh was generated with the TriMesh algorithm in Cubit (cubit.sandia.gov) with mesh edges conformal to surface pipes and wellbore casings. Node spacing on wells is 10 m (one casing section), whereas it is 5 m for the surface pipes. Overall the oilfield infrastructure is embedded in a $10 \times 10 \times 10$ km block with air conductivity (upper half of the block) at 10^{-8} S/m and earth conductivity (lower half) 10^{-3} S/m, with node spacing on the order of 100 m away from the oilfield. Pipelines and well casings were assigned values $t_e = 5.5 \times 10^4$ S·m, which is

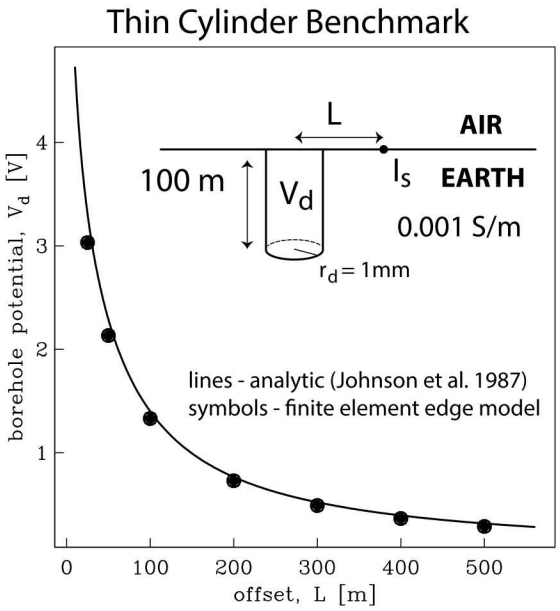

Figure 5-2. Comparison between finite element (symbols) and analytic (line) solutions for buried, thin, and perfectly conducting cylinder (see inset for geometry). Plotted is the electric scalar potential V_d on the cylinder due to a 1 A point current source located a distance L away from the top end of the conductor. Analytic solutions are given for a cylinder radius of 0.001 m; a dimension well within the asymptotic limit for an infinitesimally thin conductor.

consistent with 0.2 m diameter steel pipe with 0.025 m wall thickness. The overall mesh size is 356k nodes. A hypothetical 1 A single pole source is located in the lower right corner of the survey area (Figure 5-3).

Analysis of the complete oilfield infrastructure (pipes and boreholes) shows some interesting features. For example, the surface pipe's effects of on the current distribution in the well cases are severe. The absence of surface pipelines results in downgoing electric currents in all of the wells (Figure 5-4, bottom). However, the presence of surface pipelines not only affects the vertical current magnitude, but also affects its direction. As a result, many of the wells sustain a steady upgoing current (Figure 5-4, top), with a magnitude of several 10's of mA.

Furthermore, analysis of the surface pipeline (Figure 5-5) shows a complex distribution of electric current, originating from the lower right (near the source, but not on it) and winding its way through the various loops and branches present in the pipeline circuit. Notable features include current leakage into the geologic formation, along the peripheral spurs of the main circuit loop. Additionally, maximum current density is located away from the point nearest the actual current injection point in the lower right corner of the survey area. The effect of the well casings on surface pipes is mild, with small differences in amplitude and direction noticeable in the lower-middle section of the survey area.

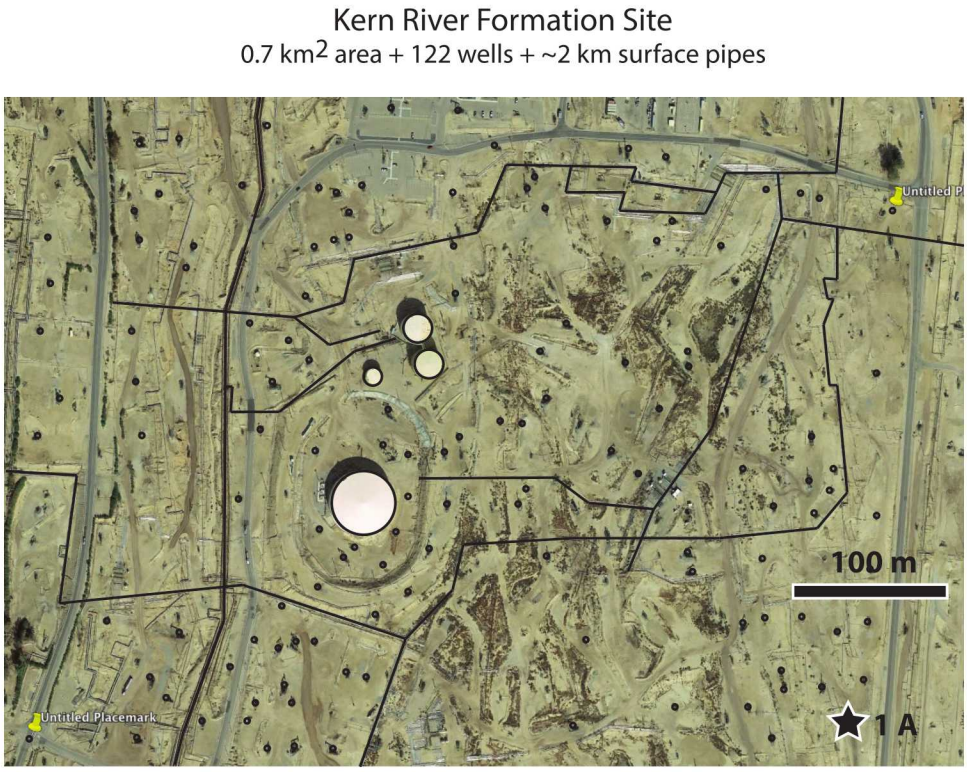

Figure 5-3. Aerial photo of a representative patch of the Kern River Formation oilfield north of Bakersfield, California, where metallic infrastructure in the form of well casings, surface delivery pipes and storage tanks are present. For simulation purposes, a 1 A single pole current source is located in the lower right corner of the region (star). Black lines represent surface pipes in the model; black dots represent the wells. The four storage tanks are not included.

Finally, electric field magnitudes are observed on the order of 0.1 – 1 mV/m over the survey area (Figure 5-6), with enhancement in overall amplitude over that expected by simple geometric spreading. The effect of individual wells and the elevated electric field in the earth region nearest the 1 A point current source (Figure 5-6, top) is clearly visible. Distribution of the electric field vector is expectedly complicated (Figure 5-6, bottom), with demonstrable current leakage both in to and out of the formation, normal to the sides of the surface pipes.

5.5. CONCLUSIONS

This work presents a novel finite element method for the economical representation of thin, finite conductors in solutions to the electrostatic DC resistivity problem. The method shows favorable agreement with independent benchmark solutions. It was applied to a realistic mature oilfield scenario consisting of multiple wells and surface pipeline. Results show that the fully coupled

system of strong conductors severely distort the electric field in ways difficult to predict otherwise.

Results demonstrate that the electric current density in the surface pipeline is not strongest in the region closest to the actual grounded source. Rather, the current density diverges in the pipeline at this location and becomes stronger further away along the pipeline circuit. The current density magnitude in the pipeline is on the order of 10s of mA/m^2, which is a measurable quantity that can be used for further validation.

It is possible the hierarchical finite element formulation in Eq (5.2) may also be applied to the electromagentic problem, thus enabling its use in either frequency– or time–domain analysis. Similarly, the magnetic permeability and electric permittivity (when appropriate) may also be defined on the same hierarchy, although further analysis is necessary to ensure compatibility between the finite element vector space and the fields generated by such features.

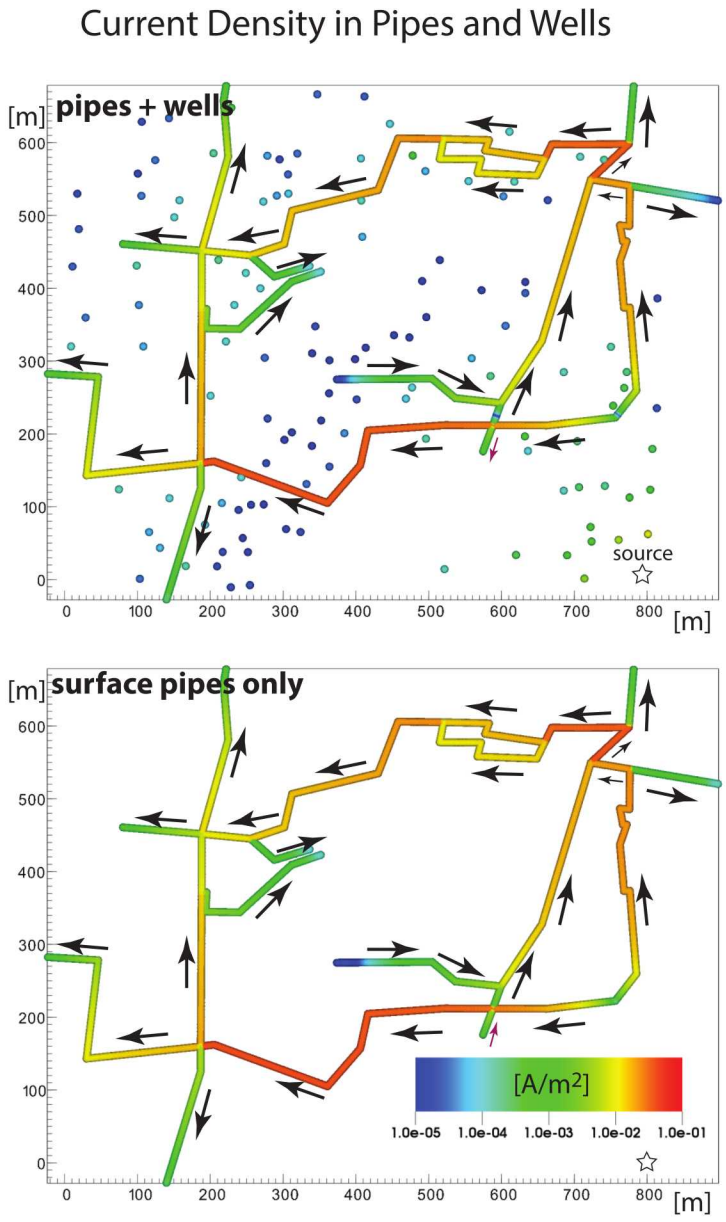

Figure 5-4. Magnitude (color) and direction (arrows) of electric current density in the surface pipes for the complete system of pipes and steel–cased wellbores (top) and the simplified system where well casing is ignored (bottom). Careful inspection of the scenarios reveals small differences in amplitude and direction, e.g., the regions at coordinates $(400, 300)$ **and** $(600, 200)$**.**

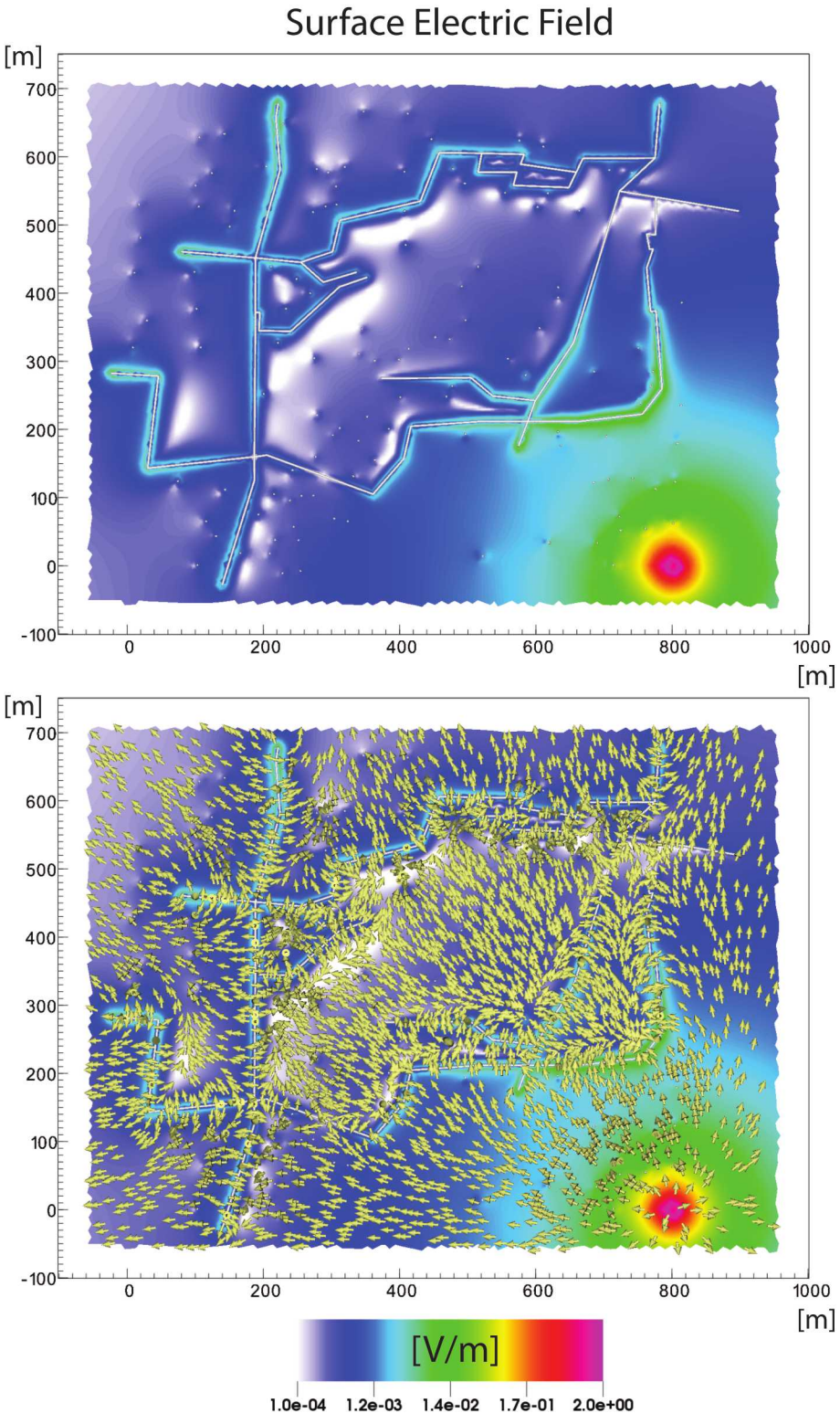

Figure 5-5. Magnitude (color) and direction (arrows) of the electric field on the Air/Earth interface from a 1 A single pole source located at coordinate (800,0).

6. THE ELECTROSTATIC RESPONSE OF FRACTURED MEDIA

6.1. SUMMARY

Determination of the geometrical properties of fractures plays a critical role in many engineering problems to assess the current hydrological and mechanical states of geological media and to predict their future states. However, numerical modeling of geoelectrical responses in realistic fractured media has been challenging due to the explosive computational cost imposed by the explicit discretizations of fractures at multiple length scales, which often brings about a tradeoff between computational efficiency and geologic realism. Here, we use the hierarchical finite element method (Weiss, 2017) to model the electrostatic response of realistically complex 3D conductive fracture networks with minimal computational cost. This finite element approach utilizes a novel parameterization of electrical conductivity in 3D conducting media that allows assignment of electrical properties at each hierarchical component of a finite volumetric element (1D edges, 2D facets and 3D tetrahedra) within an unstructured tetrahedra mesh. By employing this hierarchical material model concept in the finite element analysis, 3D fractures can be explicitly represented by connected facet elements or linear geologic features as well as infrastructures such as borehole casings, rails, pipes can be explicitly represented in form of connected edges in finite element mesh, and therefore the need of mesh refinement due to volumetrically insignificant structures can be drastically reduced. In this study, stochastically-generated, complex 3D fracture network models are considered to better understand the relationship between the heterogeneity of fracture network and the resulting DC resistivity responses. We mainly focus on the effects of fracture length and aperture distributions on the azimuthal variations in DC resistivity. Our numerical results indicate that conductive fracture networks with high network connectivity result in anomalously low apparent resistivity values with strong azimuthal dependence in comparison with networks with low network connectivity. Moreover, our results show that while the fracture size-aperture correlation has a strong influence on DC resistivity responses when the fracture network is well connected, the influence of aperture is marginal for fracture networks with poor network connectivity.

6.2. INTRODUCTION

Fractures are pathways where fluids migrate and transport, displaying scale-variant heterogeneity from fracture to network scale. The complex distribution and organization of fractures together

with hydraulic properties of the surrounding medium control the level of heterogeneity of flow patterns (Tsang and Neretnieks, 1998; de Dreuzy et al., 2001) as well as heterogeneity of stress fields (Pollard and Segall, 1987). Determining and monitoring the geometric properties of fractured media is critical information for rock mechanical and hydraulic behaviors in many engineering applications such as economic resource extraction, geologic isolation of nuclear wastes or dissolved CO_2 (Uchida et al., 1994; Tsang et al., 2015,?), geothermal reservoir enhancement (e.g. Legarth et al., 2005) and groundwater and solute management (Bear et al., 2012).

Many observational studies have demonstrated the direct current (DC) resistivity method as a useful geophysical tool to infer information regarding geometrical characteristics of fractured media (e.g. Robinson et al., 2015). Moreover, elongated resistivity anomalies over fractured media have been related to anisotropy and considered as an indicator of the strike direction of fractures (e.g. Taylor and HFleming, 1988; Lane et al., 1995; Busby, 2000). To clarify the relationship between electrical resistivity responses and fracture properties, numerous numerical approaches have been considered. While the electrical resistivity problem can be straightforwardly modeled for fracture media at the bulk anisotropic limit (e.g. Li and Spitzer, 2002; Shen et al., 2009); given a complex discrete fracture media, numerical modeling with classical finite methods (finite element, finite volume, finite difference) becomes computationally challenging. The challenge arises from the explosive computational cost caused by the explicit discretizations of the volumetrically insignificant structures that produce far-reaching responses (geologic details such as fractures) over the scale of volume of interest. The problem of how best to simulate models with multi-scale heterogeneity by considering the accuracy, the realism and the computational cost of a given model has become a focus for a long time in both electric and electromagnetic research. Proposed solutions to this problem include parallelizing the computations for the fine-scale mesh (Commer et al., 2015; Hoversten et al., 2015; Um et al., 2015) or exaggerating the size of structure (Haber et al., 2016). Also, the equivalent resistor network approach provides an economical way to represent conductive fractures by facet and edges in Cartesian meshes (Yang et al., 2016). Another proposed approach, called discontinuous Galerkin frequency-domain method, incorporates conductive fractures into modeling by considering subdomains and imposing impedance transition boundary condition at the surfaces that correspond to fractures (Sun et al., 2017).

The electrostatic problem we examine here is analogous to the steady state Darcy flow problem long studied by hydrogeophysicists, for which various numerical strategies have been also developed to make the multi-scale problem computationally tractable. One strategy is the "Discrete Fracture Network" method, whereby fluid flow is restricted to the connected channels within fracture network and fluid exchange is neglected between the fractures and the rock matrix based on the assumption of the impermeable host rock, thereby reducing the problem to discretization of the (connected) fractures alone (e.g. Long et al., 1982; Cacas et al., 1990; de Dreuzy et al., 2013; Zhang, 2015). This has the advantages of minimizing the size of the resulting linear system of equations to something reasonably manageable on a small computer since discretization of the rock matrix (and its inherent degrees of freedom) is not required. In doing so, it mitigates the problem of discretizing sub-parallel fractures by avoiding the creation of thin, flat discrete elements in the matrix along the edges defining the intersection of such fractures. If, however, fluid exchange is to be considered in the steady state flow solution, the

most popular approach is “Discrete Dual Porosity Model” (Lee et al., 2001; Li and Lee, 2008) in which an ad hoc flux distribution in imposed on the fracture faces. In each of these two major approaches, the fractures are considered to be infinitesimally thin (as they are in our model) however, the fracture/matrix flux is either neglected or approximated by equations supplementary to the main Poisson equation driving the system. Some progress has been made in flux–balanced finite volume methods (Mourzenko et al., 2011), also on infinitesimally thin fractures, whereby the support volume and nodal discretization for flux conservation is carefully designed to allow for discontinuities in pressure where present. We note that such double-discretization of resistive fractures was proposed independently in Weiss (2017) in the case of electrostatics, and with the additional observation (and demonstration) that the two discretizations needn’t be one-for-one in their node/element definition. In addition, the discrete-dual-porosity model has been modified to model DC resistivity responses of discrete, non-isolated fractures, which employs a semi-analytical formulation that accounts for the electric current flow exchange between fractures and surrounding media (Roubinet and Irving, 2014; Caballero-Sanz et al., 2017), and has been applied to 2D and 2.5D fractured media consisted of large number of connected fractures. To our knowledge, the electrical resistivity responses due to 3D complex discrete fracture networks embedded in a rock matrix consisting of hundreds of arbitrarily-oriented fractures with variable aperture have not yet been modeled.

Here, we use the recently developed hierarchical material model in finite element analysis to model the DC resistivity responses in 3D fracture media. The hierarchical finite element method (*Hi*-FEM) (Weiss, 2017) extends the Cartesian-grid-constrained circuit model of Yang et al. (2016) for unstructured tetrahedral meshes that allow to represent electrical conductivity distributions of complicated fracture network configurations. The *Hi*-FEM algorithm, within an unstructured tetrahedral mesh, embraces a hierarchy in the electrical properties of 3D conducting media, where not only tetrahedral elements but also triangle elements (2D, facets) and line elements (1D, edges) can locally contribute to the overall electrical conductivity of a model. The hierarchy provides a flexibility to represent very thin fractures as connected facets or linear features as connected edges without any mesh refinement and therefore drastically lessens the computational cost by reducing the degree of freedom for discretization.

In this study, we mainly focus on the behaviors of azimuthal resistivity responses over 3D stochastically-generated, complex fracture networks. First, we validate the hierarchical material model concept for both homogenized isotropic and anisotropic media as well as for “2D-like” random fracture networks. Then, we consider isolated, regularly-spaced, finite-sized fractures that present strong anisotropy to better understand the effect of the finiteness of fracture sizes on the azimuthal resistivity profiles. Further, we present numerical DC modeling results of complex fracture networks following certain statistical distributions. Particularly, the effects of fracture length and aperture distributions on azimuthal geoelectrical responses are investigated.

6.3. HIERARCHICAL FINITE ELEMENT METHOD (*Hi*FEM)

In the electrostatic limit, the electric field $\mathbf{E} = \nabla u$ throughout a 3D conducting media $\boldsymbol{\sigma}$, subject to a given steady electric current density $\mathbf{J}_s$ is governed by the well-known Poisson equation,

$$-\nabla \cdot (\boldsymbol{\sigma} \cdot \nabla u) = \nabla \cdot \mathbf{J}_s, \tag{6.1}$$

where u is the electric scalar potential and $\boldsymbol{\sigma}$ is the electrical conductivity function. Here, it is noted that the electric field $\mathbf{E}$ is intentionally considered as "∇u" instead of commonly-used "$-\nabla u$" to yield a more convenient variational form for the finite element solution.

The hierarchical material model concept incorporates the hierarchy over volumes, facets and edges of a finite element mesh into finite element analysis by introducing a composite definition of the electrical conductivity (Weiss, 2017):

$$\sigma(\mathbf{x}) = \sum_{e=1}^{N_V} \sigma_e \boldsymbol{\Psi}_e^V(\mathbf{x}) + \sum_{e=1}^{N_F} s_e \boldsymbol{\Psi}_e^F(\mathbf{x}) + \sum_{e=1}^{N_E} t_e \boldsymbol{\Psi}_e^E(\mathbf{x}), \tag{6.2}$$

where hierarchical, rank-2 basis functions are given by

$$\boldsymbol{\Psi}_e^V(\mathbf{x}) = \mathrm{diag}(1,1,1)_e \begin{cases} 1 & \text{if } \mathbf{x} \in \text{volume } e \\ 0 & \text{otherwise} \end{cases}, \tag{6.3}$$

$$\boldsymbol{\Psi}_e^F(\mathbf{x}) = \mathrm{diag}(0,1,1)_e \begin{cases} 1 & \text{if } \mathbf{x} \in \text{facet } e \\ 0 & \text{otherwise} \end{cases}, \tag{6.4}$$

and

$$\boldsymbol{\Psi}_e^E(\mathbf{x}) = \mathrm{diag}(1,0,0)_e \begin{cases} 1 & \text{if } \mathbf{x} \in \text{edge } e \\ 0 & \text{otherwise} \end{cases}. \tag{6.5}$$

Here, N_V, N_F and N_E denote the number of volumes, facets and edges in the finite element mesh, respectively. The subscript e of the diagonal rank-2 tensors denote the local principal axis reference frame defined by the orthogonal unit vectors $\hat{e}_1$, $\hat{e}_2$ and $\hat{e}_3$. The basis function for tetrahedra includes all orthogonal vector directions for a given volume element e (Eq (6.3)), whereas the basis function possesses only the $\hat{e}_2$ and the $\hat{e}_3$ directions for facets that lie in the plane of a given facet e (Eq (6.4)), and only $\hat{e}_1$ direction for edges that is parallel to the direction of a given edge e (Eq (6.5)). In this way, the electrical conductivities on facets and edges are

strictly local. The electrical conductivity function given in Eq (6.3) has the SI unit of S·m^2 which imposes s_e to be the conductivity-thickness product (S, conductance) of facet e and t_e to be the the product of conductivity and cross-sectional area (S·m) of edge e.

Consequently, the composite representation of the electrical conductivity function inherently result in a composite element-stiffness matrix in the finite element analysis that can be written as

$$\mathbf{K} = \sum_{e=1}^{N_V} \sigma_e \mathbf{K}_e^4 + \sum_{e=1}^{N_F} s_e \mathbf{K}_e^3 + \sum_{e=1}^{N_E} t_e \mathbf{K}_e^2 \tag{6.6}$$

where $\mathbf{K}_e^4$ is the 3D element-stiffness matrix (4×4) of eth tetrahedron, $\mathbf{K}_e^3$ is the 2D element-stiffness matrix (3×3) of eth facet and $\mathbf{K}_e^2$ is the 1D element-stiffness matrix (2×2) of eth edge.

The global form of the linear system of equations are then constructed for the model domain in the usual way of the classical finite element method and can be written as

$$\mathbf{Ku} = \mathbf{b}, \tag{6.7}$$

where $\mathbf{K}$ is the global composite element-stiffness matrix and $\mathbf{b}$ is the standard right-hand side vector consisting of the inner products of piecewise continuous, linear basis functions and $\nabla \cdot \mathbf{J}_s$. Here, the global finite-element system of equations (Eq (6.7)) is solved iteratively by using a Jacobi-preconditioned conjugate gradient (J-PCCG) solver (Weiss, 2001, 2017). For a mesh of N nodes, the global finite-element system of equations is $N \times N$, but its explicit storage is avoided by using J-PCCG which only requires computing the action of the matrix on some vector rather than explicit matrix storage (Weiss, 2001). The J-PCCG algorithm employs 6 working vectors, one the right-hand-side solution vector and one vector for the Jacobi scaling. Hence, the total storage cost is $N \times 8$ real double precision (8-byte) words. Storage of the model is $N_V + N_F$ double precision words with $N_V >> N_F$. The storage of nodes is $N \times 3$ double precision words (node coordinates). The Tetrahedra definition is $N_V \times 4$ whereas the definition of triangles is $N_F \times 3$ integer (4-byte) words. Therefore, for the models given in Figure 6-1, the minimum and the maximum total storage costs for a simulation are 43–105 MB. We iterate the solution on J-PCCG until the residual norm is 10^{-12}, a value determined through experience with these problems to yield high precision results. Example convergence plots of residual versus time and residual versus iteration are shown in Figure 6-1, showing generally monotonic convergence.

Whereas previous examples in fracture modeling with the *Hi*-FEM method (Weiss, 2017) dealt only with non-intersecting fractures in rock matrix, discretizing the 3D intersecting fracture network of interest here poses additional challenges. The computational mesh required for a medium with large amount of finite, arbitrarily-oriented fractures may impose very short intersection distances or low angles between fractures (Zhang et al., 2016). For such dense, complex fracture models, Delaunay-based (e.g. Bogdanov et al., 2003; Mustapha, 2011) and advancing-front methods (Koudina et al., 1998; Mourzenko et al., 2011) can not generate fine meshes that ensure the computational precision. One remedy for this problem for discrete fracture networks (without surrounding media) has been proposed as the projection of 3D staircase-like discretization of fracture borders and intersections onto each fracture plane (de Dreuzy et al.,

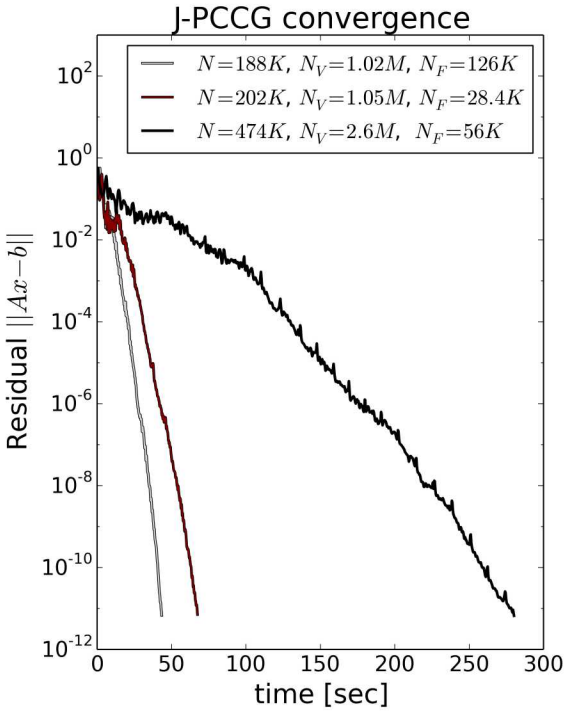

Figure 6-1. Convergence of the Jacobi-preconditioned conjugate gradient linear solver (Weiss, 2001) for discretization of the fracture models consisted of 100 fractures following power-law fracture length distribution, described in Section 4.2.1. The results show the elapsed times for a target residual norm 1×10^{-12}.

2013). We remark that there are many other methods that particularly focus on improving the efficiency of mesh generation for such models (e.g. Zhang, 2015; Zhang et al., 2016) and that the relative merits of meshing algorithms (efficiency, ease of use, time, accuracy, quality measures, etc) are an interesting, but tangential, topic to the primary topic of this paper. Furthermore, creation of a complex three–dimensional mesh is strongly dependent on the workflow of the mesh creator, as well as the underlying meshing algorithm. Hence, we offer here some general comments on mesh design for our problems with full recognition that more efficient methods or workflows may exist. Here, the mesh generation of fractured media is performed by using the meshing package "Cubit" (cubit.sandia.gov) following the execution of an external script that automatically generates the geometry of fractures for a given set of fracture parameters (e.g., size, orientation, aperture, etc. distributions). We employ the Delaunay triangulation/tetrahedralization to discretize the fractures for our models. We resist any "hand tuning of the mesh" due to intersecting sub-parallel fractures, and instead we reject the realization and substitute it with another one produced from a different random seed. As a reference, the meshes of the models given in Section 4.2.1. take on the order of $\sim$20 seconds for geometry definition and $\sim$40-60 seconds for full discretization on a 2017 MacBook Pro with 16GB main memory.

6.4. BENCKMARKING

6.4.1. Isotropic media

Previous benchmarking of the *Hi*-FEM algorithm described in the previous section was shown in Weiss (2017). Here, we extend the suite of benchmarking results by considering isotropic and anisotropic media consisting of thin conductive fractures. In addition, the benchmarks for "2D-like" random fracture networks are also considered in Appendix. As an analytical benchmark to validate the numerical solution of the *Hi*-FEM, we consider a vertical dike of anomalous resistivity in a uniform half-space. The dike reaches the surface with a constant thickness and extends to infinity in other two dimensions. The electric potentials due to this geoelectric structure can be obtained semi-analytically by calculating the summation series of the reflected electric current images from dike boundaries (Telford et al., 1990). The series in the analytic solution are very slow to converge for small dike thicknesses and require many thousands of terms to achieve an acceptable accuracy.

Here, we consider two vertical dike models with equivalent conductances to compare the volume- and facet-based finite-element solutions against the analytical solutions. For the test of the volume-based finite-element solution, a 5-m thick dike with a conductivity of 10^{-1} S/m is considered, which can be adequately discretized by using tetrahedral volume elements without imposing a high computational cost. In addition, to test the validity of the facet-based FE solution, a very thin dike (0.1 m) with the equivalent conductance of 0.5 S is considered, whose thickness is volumetrically very small with respect to the scale of computational volume. For both models, the dike is located in a 10^{-2} S/m half-space and 20 m away from the origin of the computational domain where a point current source is injected. The finite-element solutions are computed for a $10 \times 10 \times 5$ km volume. The Dirichlet boundary condition is imposed at the edges of the volume by using the analytical solution of a uniform 10^{-1}-S/m halfspace, except the air-Earth interface where the Neumann boundary condition is enforced. The volume-based finite-element solution over the 5-m dike is computed on an unstructured mesh consisting of $N = 231618$ nodes and $N_V = 1337472$ tetrahedra. The vertical dike itself is represented by 106367 tetrahedra. The facet-based solution for the 0.1-m dike with the equivalent conductance is computed on the same mesh without the need of any additional nodes for mesh refinement. The thin dike is defined by $N_F = 10048$ connected facet elements in the mesh and its 0.5-S conductance is assigned to these facets.

For the benchmarking tests, the numerical solutions of both models for a pole-pole array with a fixed source located at the origin, along and perpendicular to the dike are compared. Figure 6-2 shows the analytical and the numerical solutions for the 5-m and the 0.1-m dikes with the equivalent conductances of 0.5 S. The volume-based finite-element and the analytical solutions for the 5-m dike show a good agreement. The disagreement at short offsets is to be expected given the 1/r singularity in the exact solution at zero offset; however, this does not present significant far-ranging effects (Lowry et al., 1989).

The profiles also indicate a good agreement between the facet-based finite element and analytical solutions over the dike for the thickness 0.1 m with equivalent conductance. Moreover, the

agreement at dike for both numerical solutions are excellent. Overall, the comparison results demonstrate the validity of the *Hi*-FEM solutions.

In addition, given a very thin dike, the electrical response at the dike is negligible due to its insignificant thickness with respect to the scale of interest (0.1-m dike, Figure 6-2a). On the other hand, when the dike has a significant thickness, the response across the dike thickness becomes anomalous at the scale of interest (5-m dike, Figure 6-2a). This implies that the responses due to surface-like structures with significant thicknesses with respect to the scale of interest can not be approximated by the facet-based conductance representations, instead these structures must be explicitly discretized by volumetric elements with bulk electrical conductivity.

6.4.2. Anisotropic media

As yet another benchmarking exercise for the hierarchical representation of electrical conductivity, the consistency in electrostatic response between results from continuum–scale electrical anisotropy and those from a model composed of a discrete set of evenly–spaced conductive vertical fractures embedded in a homogeneous host medium is evaluated (Weiss et al., 2018). The model domain is defined as a $500 \times 500 \times 200$ m volume that is discretized with tetrahedra of conductivity σ. The conductive sheets embedded in the host domain are defined as vertical planes of contiguous triangular facets and set to be parallel with a spacing of $d = 5$ m (Figure 6-3). A conductance value s is assigned on the facets of these planes representing their anomalous conductivity $\Delta\sigma = \sigma' - \sigma$ and equivalent thickness ℓ (i.e. $s = \Delta\sigma\,\ell$). Equivalent values for the bed–parallel $\sigma_{||}$ and bed–perpendicular $\sigma_{\perp}$ elements of the (diagonal, in this case) conductivity tensor are therefore found in the limit $\sigma' \to \infty$, $\ell \to 0$ and $s = \delta\sigma\,\ell$ constant, taking the values $\sigma_{\perp} = \sigma$ and $\sigma_{||} = \sigma + s/d$. As in the previous examples, the air/earth interface is assigned a homogeneous Neumann boundary conduction, whereas the remaining sides of the model domain are assigned an inhomogeneous Dirichlet boundary condition in accordance with the known analytic solution for the potential u due to a unit magnitude point source:

$$u(x,y,z) = \left(2\pi \sqrt{\sigma_{\perp}\sigma_{||}\sigma_{||}} \sqrt{\frac{x^2}{\sigma_{\perp}} + \frac{y^2}{\sigma_{||}} + \frac{z^2}{\sigma_{||}}} \right)^{-1} \tag{6.8}$$

Agreement between the finite element and analytic solution is excellent in the isotropic limit ($s = 0$ S) for all source–receiver offsets in the mesh (Figure 6-4), whereas the agreement in the anisotropic case ($s = 0.1$ S) is evident at larger offsets $\sim 2-3\,d$ at where the length scale of measurement reaches an apparent homogenization limit. More extensive anisotropy examples and discussion can be found in Weiss et al. (2018).

6.5. DC ELECTRICAL RESPONSES OF DISCRETE FRACTURE NETWORKS

6.5.1. Regular Fractures

First, to investigate the effect of the fracture size on geoelectric responses, we consider numerical models made up of regularly-spaced, finite-size fractures. These fracture models present strong anisotropy; however, being different from a homogenized anisotropic medium, they comprise circular conductive fractures that implicitly impose some heterogeneity due to the fracture shape. To examine the impact of the anisotropy arising from the circular fractures on DC resistivity responses, three simple cases are considered: horizontal, vertically-oriented and 45°-dipping fractures in a uniform half-space (Figure 6-5). In addition, we also consider different fracture spacings ($d = 50$ m, 10 m and 5 m) for these models. The fracture domain is defined over a 100 $\times$100 $\times$100 m volume that is completely spanned by the circular fractures with 50-m radius. The conductivity of the host media is 10^{-2} S/m and the conductance of the fractures with constant aperture (thickness) is defined as 1 S.

Figure 6-6 shows the azimuthal resistivity profiles measured as by a pole-pole survey with a 20-m fixed offset. Figure 6-6a. indicates that the horizontal fractures produce uniform azimuthal resistivity profiles as in fully homogeneous media. While the fracture spacing increases, the resistivity slowly decreases implying that given a very dense fracture spacing, the resistivity will converge to an intermediate half-space's resistivity (Figure 6-6a). The vertical fractures produce ellipses not identical but very similar with the well-known resistivity ellipses of homogenized anisotropic media whose major axis coincides with the strike of the fractures. Figure 6-6c shows that the resistivity profiles of the 45°-dipping fractures are not symmetric but still are elongated in the strike direction of the fractures. In addition, we see that lower resistivity values indicate the updip direction. The resistivity ellipses of all models also indicate that the most dramatic decrease in resistivity respect to fracture spacing occur when the fractures are vertical (Figure 6-6). Further, only 45°-dipping fractures result in some distortions on resistivity ellipses (Figure 6-6c, especially $d = 10$) directly related to the fracture finiteness.

6.5.2. Complex Fracture Networks

Practically, the complete quantification of the complex topologies of fracture networks is not feasible due to their wide range of length scales and the lack of accurate field measurements (e.g. de Dreuzy et al., 2001; Xu and Dowd, 2010). In general, complex fracture networks are studied by stochastically representing the network geometrical properties (location, length, aperture, conductivity, etc.) by certain distributions where each fracture is defined explicitly as the so-called "Discrete Fracture Network (DFN)" (Long et al., 1982; Robinson, 1983; Andersson et al., 1984; Andersson and Dverstorp, 1987; Gutierrez and Youn, 2015; Lei et al., 2017). Here, benefiting from the *Hi*-FEM approach that enables to economically define fractures by connected facets, we model the DC resistivity responses due to stochastic complex fracture networks which possess strong heterogeneity in their geometric properties. Particularly, we consider DFN models

to examine the influences of the fracture length and aperture distributions on geoelectrical responses.

6.5.2.1. Length distribution

Fracture lengths exhibit a scaling character presenting long-range correlations at a broad range of length scales, which is commonly characterized by a power-law distribution (e.g. Davy, 1993; Bonnet et al., 2001). The power-law exponent a of the distribution controls the ratio of large and small fractures in fracture networks. While small power-law exponent values generate similar small size fractures, large exponent values correspond to fracture systems where the connectivity of fracture network is enabled at larger scales via large fractures. The range of exponent a for fracture networks has been observed to be between 1.3 and 3.5 (Bonnet et al., 2001). To examine the effect of the fracture length distribution on DC resistivity responses, we consider three complex fracture networks following a power-law length distribution with the power-law exponent a values of 1.5, 2.5 and 3.5. Moreover, to investigate the influence of the total number of the fractures in the network, the power-law length distributed models are also considered for the cases when the total number of fractures is 10, 50 and 100. The locations and orientations of the fractures are drawn from uniform distributions. For each statistical geometric property of fractures, a unique random seed is chosen and kept as the same for each model so that the behavior of geoelectric response only depends on the power-law exponent and the number of fractures.

The fracture network is defined in a $100 \times 100 \times 100$ m volume where each fracture is regarded as an ellipse. The conductivity of the host media is 10^{-4} S/m, a value consistent with granitic basement (relevant to geothermal) or brittle limestone where fractures can be either open or occluded by secondary mineralization. The fractures have a constant conductivity of 1 S/m with an aperture of 10^{-3} m and are defined as facets with a conductance of 1 S/m $\times$ 10^{-3} m $= 10^{-3}$ S. The power-law length distribution is truncated for all models with a radius interval of 5 m–80 m to allow network connectivity up to a degree. In addition, to better understand the relationship between the network connectivity and the resulting geoelectric responses, the backbone structure of each fracture network is also considered. The backbones are obtained by connecting the center of each fracture intersection with the center of the intersecting fracture. Figure 6-7 presents the connectivity of the fracture networks as a function of both power-law exponent and the number of the fractures. It can be seen that increasing number of fractures and dominance of large fractures in the system inherently improve the connectivity of fracture system.

We consider a pole-pole azimuthal survey with a fixed offset of 20 m to investigate the azimuthal behavior of the DC resistivity responses over these complex fracture media. The polar plots (Figure 6-8) show that the fracture network following the power-law distribution of $a = 1.5$ produces the lowest resistivity values in comparison with the other two fracture models, regardless of the total number of fractures in the system. The fracture network with the smallest power exponent ($a = 1.5$) results in a significant decrease in resistivity even when the number of fractures is small (Figure 6-8a) implying a strong influence from the presence of large fractures in the system.

When the number of fractures is small ($N_{fracture} = 10$), the resistivity profiles are almost uniform azimuthally and do not provide an indication regarding the location or orientation of fractures in the media (Figure 6-8). On the other hand, while the number of fractures increases, we see that the azimuthal resistivity profiles become distorted along with increasing heterogeneity of the fracture networks. The distorted resistivity profiles do not present resistivity ellipses with an obvious "major axis" that is commonly observed with anisotropic fracture sets or joints (e.g., Taylor and Fleming, 1998; Busby 2000). This is a consistent result due to the fact that the fracture networks are very complex rather than anisotropic and that the length scale of measurement is below the homogenization limit. Moreover, while the distortions on the resistivity profiles do not present a strong correlation with the network connectivity, we see that the most connected network produces the most distorted resistivity profile. The three cases with increasing fracture number can be considered as the evolution of a developing fracture network since we employ the same random seed for the distribution of fracture locations. In summary, the azimuthal resistivity profiles indicate that significant decreases in apparent resistivity and their direction-dependence is strongly controlled by the connectivity of the fracture networks.

6.5.2.2. Aperture

Fracture aperture is a crucial controlling parameter on fluid transport as well as electrical current flow. Laboratory experiments and field observations suggest that fracture aperture usually obeys a lognormal distribution (e.g. Snow, 1970; Long and Billaux, 1987; Tsang et al., 1996) and may be related to fracture size (e.g. Hatton et al., 1994; Bonnet et al., 2001). Many discrete fracture simulations employ lognormal aperture distribution to investigate the behavior of fluid flow in fracture media (e.g. Gong and Rossen, 2017). Here, we analyze the DC resistivity responses resulting from different fracture aperture distributions.

Particularly, we examine the effect of fracture aperture distribution by considering two fracture networks with highly differing connectivity. The well-connected fracture network is a model with 100 fractures that follows a power-law length distribution ($a = 1.5$, Figure 6-7a). By considering the same volume size ($100 \times 100 \times 100$ m), the second fracture network is generated from a uniform fracture size distribution with a upper limit of 20 m to obtain a narrow fracture length distribution that results in poor connectivity (Figure 6-9). The locations and the orientations are chosen as random and they are drawn from unique random seeds for each model. For the fracture apertures, we consider lognormal, normal and uniform distributions generated from different random seeds. The mean and standard deviation of the lognormal and normal distributions are 10^{-3} m and 0.5 m, respectively. The lognormal and normal distributions are truncated in the range 10^{-5} m to 10^{-2} m which is also the range of the uniform aperture distribution. In addition, we also consider the models for which fracture aperture is positively correlated with fracture size. To achieve the fracture size-aperture correlation, each aperture distribution already obtained for the case of independent correlation is sorted and subsequently the aperture values are assigned to each fracture according to fracture size. In our simulations, the conductivities of the host media and the fractures are defined as 10^{-4} S/m and 1 S/m, respectively.

Figure 6-10 shows the resistivity polar plots of the two fracture networks following different aperture distributions. The resistivity plots indicate that for all models with and without

size-aperture correlation, the normal aperture distribution results in the highest azimuthal resistivity values whereas the uniform aperture distribution results in the lowest azimuthal resistivity values. In addition, the plots also indicate that the difference in resistivity in the presence or absence of the fracture size-aperture correlation are much larger for the well-connected fracture network (Figure 6-10a). For the well-connected fracture network, the aperture distributions with correlation always result in lower resistivity values in azimuth in comparison to the ones with no correlation. On the other hand, the network with poor connectivity does not exhibit such a systematic trend; moreover, we see that the azimuthal resistivity values tend to be slightly larger in the absence of correlation and at some azimuths they remain unchanged. As a result, these results suggest that when a fracture network becomes more connected, the fracture size-aperture correlation has more control on the behavior of resistivity responses.

6.6. DISCUSSION

We further extend the previously published benchmarking of *Hi*-FEM algorithm (*not the algorithm itself*) by considering the comparisons with analytical solutions for both the vertical dike and the anisotropic media as well as "2D-like" random fracture networks. These results show excellent agreement between *Hi*-FEM and independent reference solutions. The numerical results of the regularly-spaced, circular fractures indicate that when fractures are much larger than the azimuthal survey profile, the azimuthal resistivity profiles still present resistivity ellipses with major axis coincident with the strike direction of fractures similar to the ones measured over homogenized anisotropic fracture media, and the influence of the fracture shape becomes significant only in case of dipping fractures.

The azimuthal resistivity profiles of fracture networks for which the lengths follow power-law distributions reveal that the DC resistivity responses are strongly controlled by the connectivity and the heterogeneity of the fracture network. On the other hand, the resistivity profiles of the complex fracture networks point out strong and complicated azimuthal variations in electrical responses in comparison with the resistivity ellipses of the regularly-spaced striking fractures, emphasizing the need of multiple current sources locations and various electrode offsets to study complex fracture networks. Further, the modeling results also indicate that the DC resistivity responses are very sensitive to fracture connectivity. This highlights the suitability of resistivity measurements for 4D (time lapse 3D) characterization and therefore the importance of efficient 3D inversion algorithms.

The aperture distribution in the presence and absence of the fracture size-aperture correlation has a strong influence on the geoelectric responses in case the fracture network is connected at large scales (such as in the model with the exponent $a = 1.5$). For the well-connected model, the aperture distributions with correlation systematically cause a decrease in resistivity. In contrast, in the case of a poorly-connected fracture network, the influence of the correlation becomes insignificant. These results show similarity with the modeling results of de Dreuzy et al. (2001) which point out that for power-law distributions for which the exponent $a < 3$, the aperture

correlation result in larger hydraulic permeabilities and different flow structures, when the correlation becomes irrelevant for narrow fracture length distributions.

The finite-element meshes for the fracture models considered here include ∼1-2 millions of tetrahedra, depending on fracture complexity. The elapsed times for the DC resistivity simulation of the models, excluding the elapsed time for meshing, are in the order of a couple of minutes, without parallel processing, on a MacBook Pro having 16 GB memory and a 3.5 GHz Intel Core i7 processor. These fast simulation times are possible only through the use of the hierarchical *Hi*-FEM algorithm. For a comparison, a single fracture 1-mm thick and 2-m in diameter would require ∼25 million tetrahedra to discretize, thus demonstrating that fracture simulations such as those shown here are beyond the capabilities of present day supercomputing facilities if standard finite element methods were to be considered.

Here, we modeled DC responses of 3D fractured media incorporating the network-scale heterogeneity into our finite-element analysis. Our results show that the depth and azimuthal position of fractures relative to the electric current source location strongly affect geoelectrical responses, and that how fractures interconnect (i.e., network backbone structure) substantially controls the distribution of resulting electric potentials. This strongly suggests the necessity of 3D considerations while the DC responses of fractured media are being studied. Further, we consider the homogeneity of background geology and the heterogeneity at network scale in our models. Our future studies will consider variable background geology to quantify stratigraphic coupling between fractures as well as fracture scale heterogeneity (such as variable fracture aperture).

6.7. CONCLUSIONS

Here, we demonstrated the relevance of the hierarchical finite element method on DC resistivity modeling of complex fracture networks. We presented demonstration calculations for a small set of realizations and intended to show possible DC responses of fractures. The representative fracture models considered herein reveal the complexity of the resulting DC resistivity responses due to the heterogeneity of fractured media as well as how the characteristic properties of fractured media (such as network connectivity, fracture aperture distribution and total number of fractures) control the complexity. This motivates the idea of retrieving the fracture properties from observed DC resistivity data. On the other hand, it also leads us to modify/improve data collection methods and develops specific inversion schemes to reveal geologic information at multiple length scales from resolution-limited data. Finally, we highlight the need of more numerical studies to better understand the signatures of fracture properties on DC resistivity responses as well as to further investigate the controls on the scale limit of representative elementary volume and the transition from homogenized anisotropy to multi-scale heterogeneity.

6.8. APPENDIX: RANDOM FRACTURE NETWORK BENCHMARKING

To supplement the benchmarking exercises previously described in Section 3, we describe here two additional exercises inspired by flow modeling in 3D fractured media (de Dreuzy et al., 2013). Both in the present manuscript and in Weiss (2017), finite element results from the hierarchical materials property representation were compared against various analytic solutions for simplified geometries containing either an isolated scattering anomaly (e.g. a buried pipe or a single fracture/dike) or regularly spaced, non–intersecting fractures to approximate macroscopic anisotropy. In this supplementary analysis, we consider a new class of benchmarking models – randomly distributed intersecting fracture planes – arranged in such a way, with appropriate boundary conditions, that the electric potential within is available either as an analytic solution or an easily–derived numerical solution from an equivalent 2D flux network.

A convenient simplifying assumption for benchmarking models of 3D fracture networks is to consider the case of conducting fractures embedded in a non–conducting host. In the case of fluid flow, we may speak of hydraulic conductivity, whereas in the case of Maxwell's equations we refer to the electrical conductivity. Regardless, the Poisson equation Eq (6.1) describes both steady state Darcy flow and electrostatics, and hence the "type" of conductivity under consideration may safely be assumed by the context of the governing physics. Given this assumption of a non–conducting host, we define the model domain of the benchmark as a rectangular box, on whose top and bottom sides we impose a potential difference through inhomogeneous Dirichlet boundary conditions, and lateral sides endowed with a homogeneous Neumann boundary condition (Figure 6-A1, left). When the box is populated with intersecting fractures, each orthogonal to opposite lateral faces of the box (e.g., faces parallel to the $x-z$ plane, assuming z is the vertical coordinate), the Neumann condition on those lateral faces, along with the Dirichlet condition on the box top and bottom, ensures that the fracture response is invariant in the lateral direction orthogonal to that plane (e.g., the y direction). The homogeneous Neumann condition on the remaining two lateral sides of the box is thus a "no flow" condition", restricting fluid/current to zero along those edges. And because the fractures are embedded in a perfectly non-conducting medium, all flow/current is restricted entirely to the fractures themselves, with none in the surrounding host medium. Hence, the 3D problem, with a fully discretized domain of planar fractures and volumetric host material, yields a response that is equivalent to that of a far–simplified 2D flux network where the fractures are only modeled in $(x-z)$ cross-section, which in some cases, offers a simple analytic solution.

Such a simple analytic solution is available when the fractures propagate from the top of the box to the bottom, and do not exit from the side of the box (Figure 6-A1). In this case it is well known that the potential at a point within some fracture is strictly a linear function of the vertical coordinate alone (e.g. de Dreuzy et al., 2013). We construct a benchmark model consisting of a $10 \times 10 \times 10$ m block impregnated by 21 randomly distributed fractures which adhere to aforementioned geometrical constraint. Fractures were uniformly assigned a conductance value $s = 1$ S whereas the "non–conducting" host medium is assigned conductivity 1×10^{-12} S/m, a value comparable to dry air at sea level (Seran et al., 2017). Three dimensional meshing of this structure is done in the Cubit meshing environment (commercially available through CSimSoft)

in two steps: definition of geometrical elements of the model, and their subsequent meshing. The geometry is constructed by first defining the 10 m box, after which the box is "sliced" top–to–bottom, by a sequence of 21 randomly defined planes. At the introduction of each fracture, the slicing algorithm determines which volumes are affected by slice, subdivides them accordingly, and renumbers the volume/face/edge accounting to reflect the new geometry so that, for example, adjacent faces of a just–sliced volume are defined by a single face rather than a pair of spatially coincident but uniquely numbered facets. Once the geometry specification is complete, the fracture surfaces are meshed, followed by an advancing front method for meshing tetrahedra in the remaining host medium. Node density of the discretization on the fractures is shown in Figure 6-A1. The resulting 3D model contains 23743 nodes, 123814 tetrahedra for the host medium and 25874 triangular facets for the fractures. Total meshing time is about 80 s. Solution time for the Jacobi–scaled conjugate gradient solver is 1.7 s over 211 iterations for a 10^{10} reduction in the ℓ_2 norm of the residual. At the intersections of the fractures, the root–mean–squared error between potentials from the 3D solution and the analytic solution ϕ^{exact} is approximately 1×10^{-8} V, thus demonstrating excellent agreement.

For the slightly more complex case where some of the fractures propagate from the top of the box to the side of the box, rather than the bottom, we see excellent agreement between solutions obtained by the 3D code and an independent 2D solution, with RMS values again on the order of 1×10^{-8} V at the fracture intersections (Figure 6-A2). In the hydrology literature, such problems are sometimes referred to as "2D–like fracture networks" (de Dreuzy et al., 2013) and serve an important role in both benchmarking and examining the role of fracture complexity on overall fracture system response. Because of the relative ease in doing so, we construct our own 2D fracture network simulator for comparison of results with those obtained by 3D code. In the 2D simulator, fracture segments are represented only by their endpoints (no nodes in between, as is the case with the 3D discretization) and a linear system of equations is constructed which enforces flux/current balance fracture intersections. Endpoints at the on the "top" and "bottom" of the network are assigned fixed values, equivalent to our Dirichlet condition for the 3D problem, and those on the "sides" are prescribed with a homogeneous Neumann condition, just as in the 3D case. The resulting linear system matrix can be assembled edge–wise and thus knowledge of the coordination number of each fracture intersection is not required for matrix assembly. Furthermore, the edge–wise matrix assembly means that we can solve 2D linear system of equations matrix–free (again, as we do in 3D) using conjugate gradients. For the 2D–like fracture network considered here, again there is a total of 21 ($s = 1$ S) randomly generated fractures slicing a $\sigma = 1 \times 10^{-12} S/m$ non–conducting domain over $10 \times 10 \times 10$ m. Ten of the 21 fractures span the top and bottom sides of the domain, whereas the remaining 11 crosscut horizontally. Meshing in 3D is done as before: sequential slicing of the domain by the introduction of each fracture; and, advancing front meshing of the fracture faces followed by interstitial volumes. Total number of nodes is 44741 over 241810 tetrahedra with 47267 triangular facets defining the fracture surfaces. Simulation time is 6.3 s over 386 conjugate gradient iterations for a reduction in ℓ_2 residual norm by a factor of 10^{10}. Empirical scaling of the conjugate gradient solver follows expectations: roughly twice the number of iterations and degrees of freedom in this second benchmark in comparison to the first results in a factor of 4x increase in runtime. For the 2D flux simulator, there are 293 fracture segments defined by a modest 178 nodes. Solution of the linear system by a 10^{10} reduction in ℓ_2 residual norm occurs over a svelte 3 ms and 117 iterations.

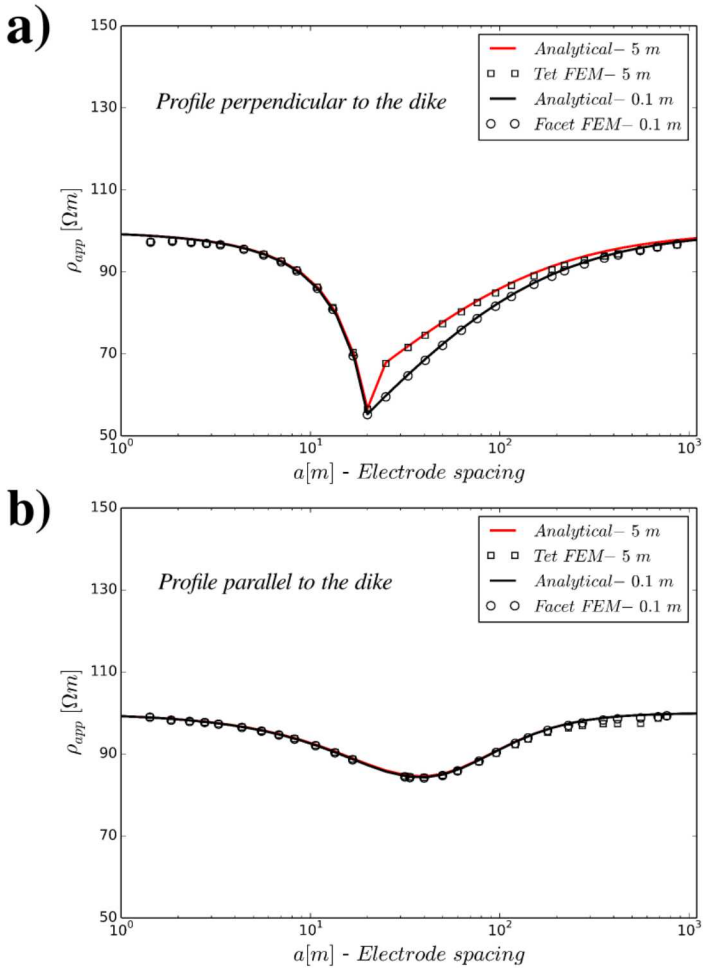

Figure 6-2. Comparison of analytical (lines) and *Hi*FEM (symbols) solutions for the vertical dike models. The DC apparent resistivity is plotted a) perpendicular and b) parallel to the dike as a function of distance from the point source. Black and red lines denote the analytical solutions of 0.1-m-thick and 5-m thick dike models, respectively.

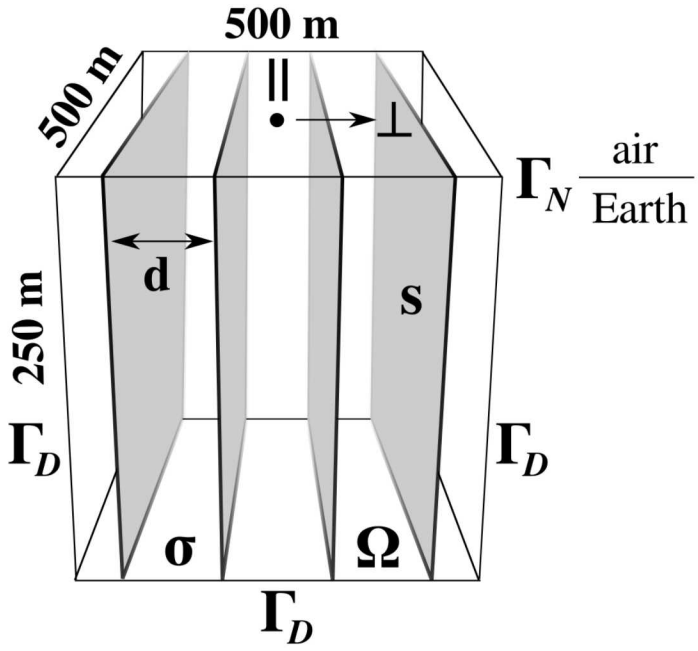

Figure 6-3. Schematic model of homogenized anisotropic medium consisted of regularly-spaced, vertical fractures. Fractures with a uniform conductance s are located in a homogeneous medium Ω with a conductivity of σ. Fracture separation is d. Point current source (black dot) is located in the center of model. Γ_D and Γ_N denote Dirichlet and Neumann boundary conditions, respectively.

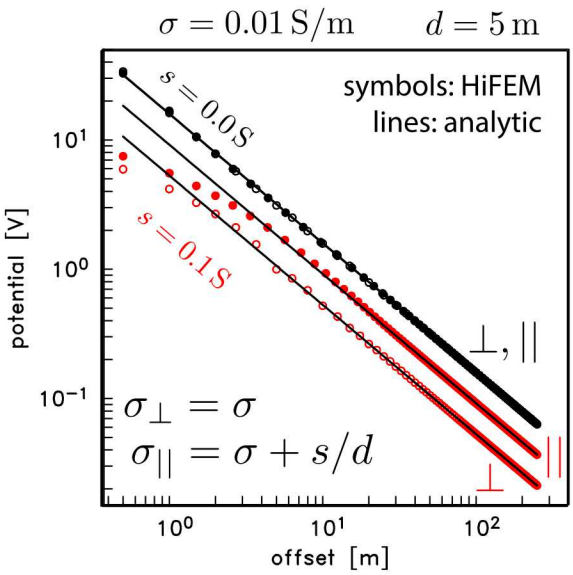

Figure 6-4. Electric potential from a 1 A point source on the air/earth interface, plotted as a function of lateral offset for two different Earth models: a $\sigma = 0.01$ S/m halfspace (black); and, when the σ halfspace is filled with infinitely thin vertical sheets with conductance $s = 0.1$ S and spacing $d = 5$ m (red). Offsets in the sheet–perpendicular and –parallel directions are annotated by $\perp$ and $||$, respectively.

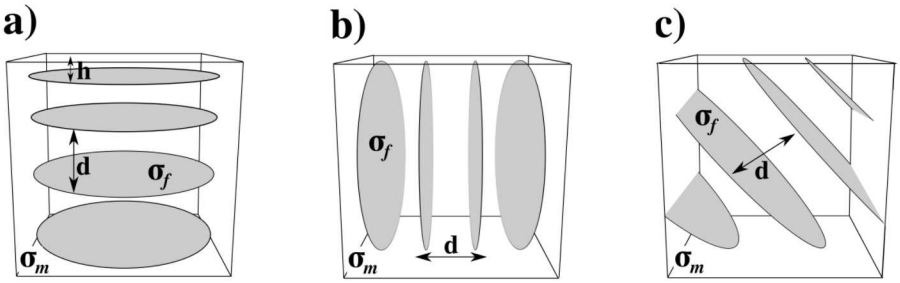

Figure 6-5. Schematic model of regularly-spaced circular fractures: a) horizontal, b) vertical, c) 45°-dipping fractures. σ_m and σ_f denote medium and fracture conductivity, respectively. d denotes fracture separation. h shown in model a denotes the depth of the first horizontal fracture from surface and is set to be 1 m.

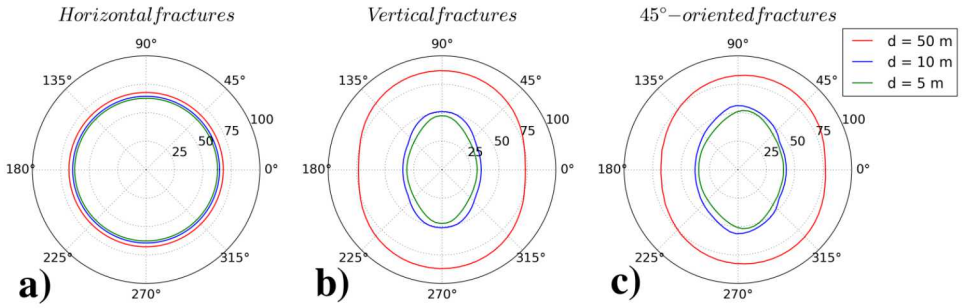

Figure 6-6. Azimuthal resistivity profiles of a) horizontal, b) vertical and c) 45°-dipping circular fractures (Figure 6-5). Resistivity is sampled along a 20-m radius survey path. The resistivity profiles of regular fractures with fracture densities of 50 m (red), 10 m (blue) and 5 m (green) are shown.

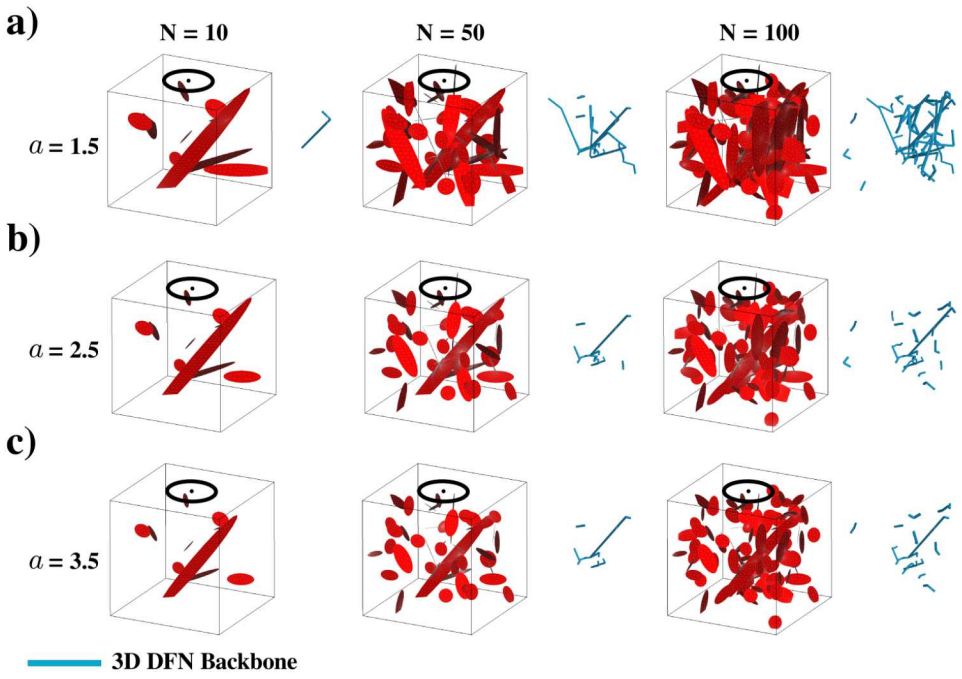

Figure 6-7. Fracture networks following power-law fracture length distribution with power-law exponents of a =1.5 (a), 2.5 (b) and 3.5 (c). The three development stages of fracture networks ($N_{fracture}$ =10, 50 and 100) are shown. The 3D backbone structures (pipes in blue) show connectivity of fracture networks. Fractures with random orientations are randomly distributed over a 100 ×100 ×100 m volume. The survey profile with 20-m radius (black circle) and the point current source (black dot) location are shown on each fracture model. The fracture aperture (10^{-3}m) is constant and uniform for each fracture. The conductivities of fractures and homogeneous half-space are 1 S/m and 10^{-4}S/m, respectively.

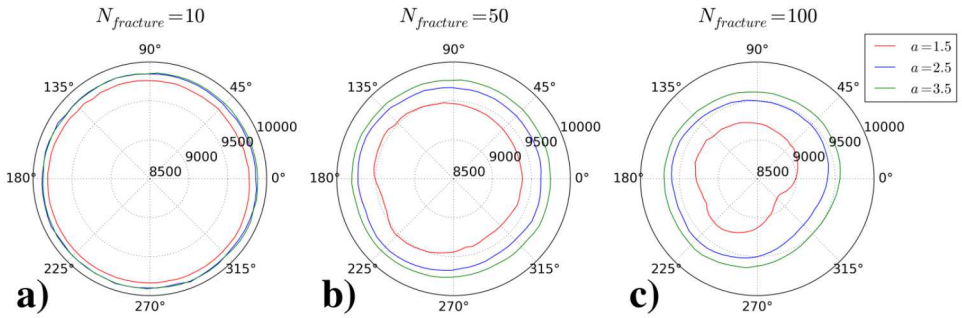

Figure 6-8. Azimuthal resistivity profiles of fracture models (Figure 6-7) consisted of a) 10, b) 50 and c) 100 fractures, following power-law fracture length distribution with power-law exponent of a =1.5 (red), 2.5 (blue) and 3.5 (green).

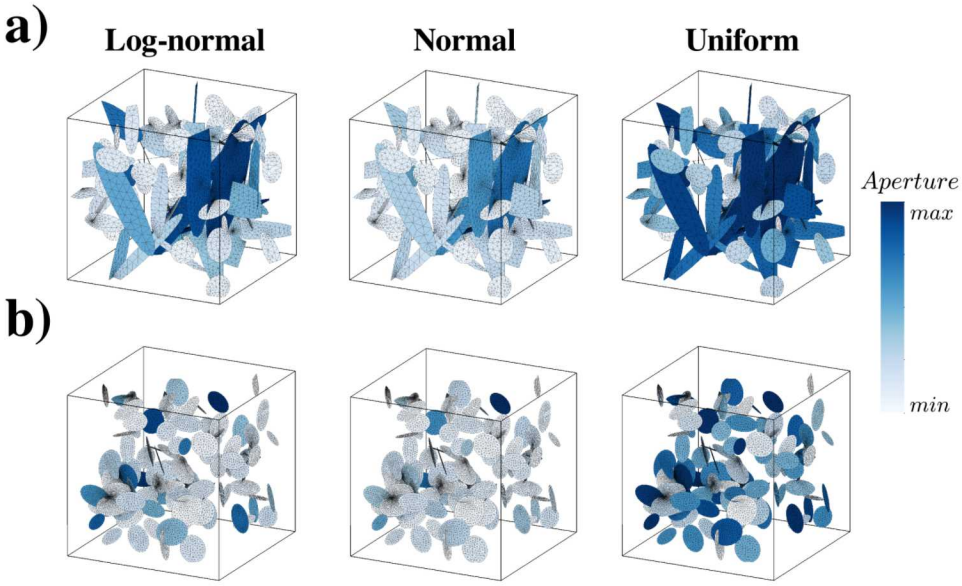

Figure 6-9. Fracture networks where fracture apertures are positively correlated to the fracture length, obeying lognormal, normal and uniform distributions. a) A well-connected fracture network shown in Figure 6-7a, b) a poor-connected fracture network following a narrow uniform length distribution. Both models consist of $N = 100$ fractures. Fractures are colored by their apertures and facet elements are shown on fractures. For visual clarity, three aperture distributions have different aperture limits. The apertures of the lognormal distribution take values between 3.60e-5–8.41e-3, the apertures of the normal distribution take values between 3.37e-5–8.90e-3, and the ones of the uniform distribution take values between 2.67e-4–9.83e-3.

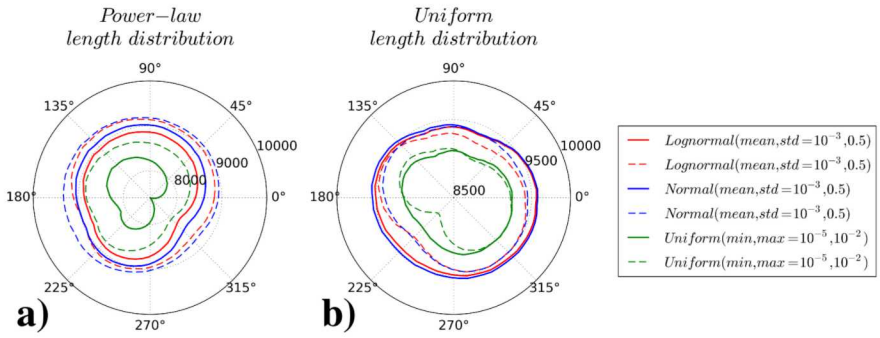

Figure 6-10. Azimuthal resistivity profiles of (a) well- and (b) poor-connected fracture networks shown in Figure 6-9 where fracture apertures obey lognormal (red), normal (blue) and uniform (green) distributions. The profiles are shown in presence (solid) and absence (dashed) of fracture length-aperture correlation. The mean value and standard deviation of lognormal and normal distributions, and the truncation limits of uniform distribution are given in the legend.

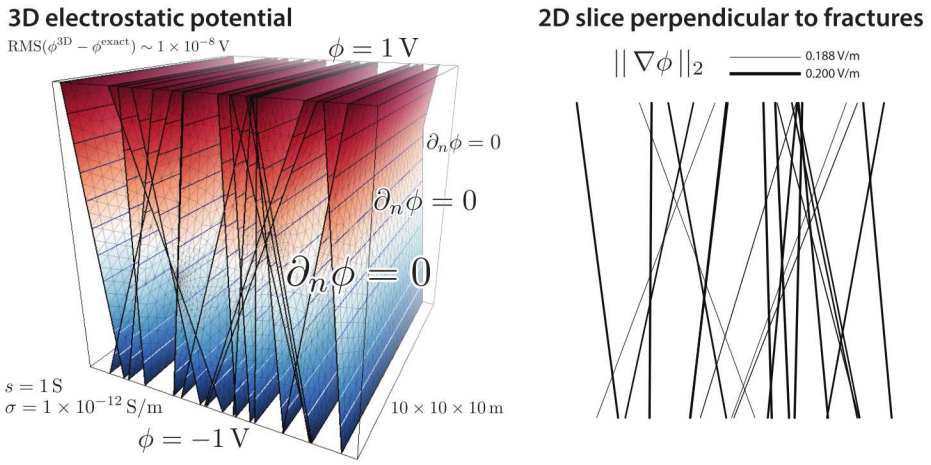

Figure 6-11. (left) Rendering and benchmark problem setup for an electrically conducting ($s = 1$ S) 3D fracture network in "air" ($\sigma = 1 \times 10^{-12}$ S/m) where the fractures only connect 4 of the 6 sides of the modeling domain and are spatially invariant one direction. For clarity, only the discretized fractures are shown, where the air region between fractures (not shown) is discretized by unstructured tetrahedral elements. See text for further details. Potentials within the fractures computed by the 3D HiFEM algorithm (color coded) show the expended linear dependence on the vertical coordinate and agree with the analytic solution to an RMS error of approximately 1×10^{-8} V. (right) Two-dimensional cross section through the middle of the volume shown on the left showing the magnitude of the potential gradient (electric field) within the fractures as calculated by the 3D HiFEM algorithm. As expected, for cases such as this where the fractures all have equal transverse conductance s, the electric field magnitude is uniform throughout each of the fractures and varies between fractures in proportion to the cosine of vertical deviation angle, resulting here in a maximum electric field magnitude of $(+1\,\mathrm{V} - (-1\,\mathrm{V}))/10\,\mathrm{m} = 0.2\,\mathrm{V/m}$.

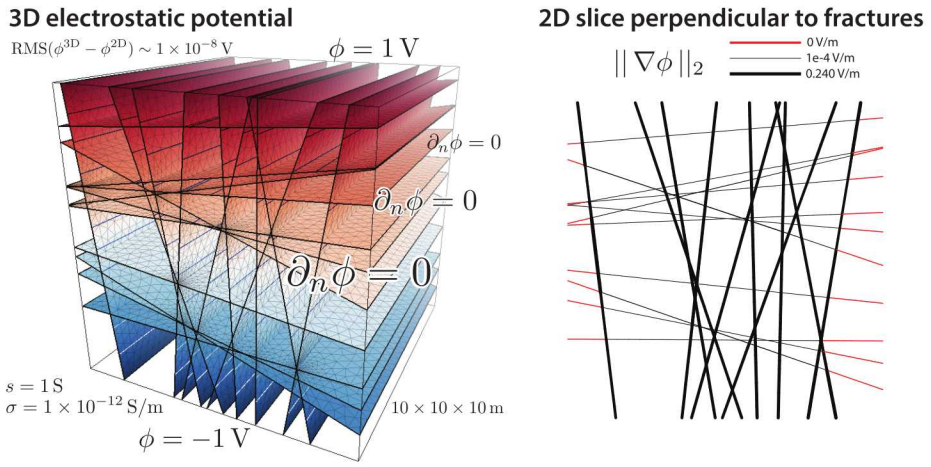

Figure 6-12. (left) Rendering and benchmark problem setup for second electrically conducting ($s = 1$ S) 3D fracture network in "air" ($\sigma = 1 \times 10^{-12}$ S/m) where the fractures fully connect all 6 sides of the modeling domain, retaining spatial invariance in one direction as was done in the previous example. Hence the fracture network can be reduced to a 2D problem. For clarity, only the discretized fractures are shown, where the air region between fractures (not shown) is discretized by unstructured tetrahedral elements. See text for further details. Potentials within the fractures computed by the 3D HiFEM algorithm (color coded) show a rough linear dependence on the vertical coordinate and agree with the 2D network solution to an RMS error of approximately 1×10^{-8} V. (right) Two-dimensional cross section through the middle of the volume shown on the left showing the magnitude of the potential gradient (electric field) within the fractures as calculated by the 3D HiFEM algorithm. In contrast to the previous benchmark, the presence of laterally connected fractures with "no–flow" boundary conditions results in a complex distribution of electric field where the magnitude within a given fracture is no longer necessarily uniform, but instead is uniform only along segments defined by fracture intersections. In some cases, this magnitude (0.24 V/m) can exceed that of the background vertical electric field 0.2 V/m. As expected, fractures segments connected to the lateral sides of the model domain are equipotential surfaces and thus have zero electric field in accordance with the imposed homogeneous Neumann boundary condition at their endpoints.

7. WELLBORE INTEGRITY MODELING WITH HIERARCHICAL FINITE ELEMENTS

7.1. ABSTRACT

Electrical responses in the vicinity of energized steel-cased well sources offer a great potential to monitor induced fractures. However, the high complexity of well-fracture-host models spanning multiple length scales compels analysts to simplify their numerical models due to explosive computational costs. This consequently limits our understanding regarding monitoring capabilities and the limitations of electrical measurements on realistic hydraulically-fracturing systems. Here, we utilize the hierarchical finite element approach to construct geoelectric models where geometrically-complex fractures and steel-cased wells are discretely represented in 3D conducting media without sacrificing the model realism and the computation efficiency. We present systematic numerical analyses of the electrical responses to evaluate the influences of borehole material conductivity and the source type as well as the effects of well geometry, conductivity contrast between fracture and host rock, source location, fracture growth and fracture propagation. The numerical results indicate that the borehole material property has a strong control on the electrical potentials along the production and monitoring wells. The monopole source located at a steel-cased well results in a current density distribution that decays away from the source location throughout the well length whereas the dipole source produces a current density that dominates mainly along the dipole length. Moreover, the conductivity contrast between the fractures and host does not change the overall pattern of the electrical potentials but varies its amplitude. The fracture models near different well systems indicate that the well geometry controls the entire distribution of potentials whereas the characteristics of the voltage difference profiles along the wells before and after fracturing are not sensitive to the well geometry as well as the well in which the source is located. Further, the hydraulic-fracturing models indicate that the voltage differences along the production well before and after fracturing have strong sensitivity to fracture growth and fracture set propagation.

7.2. INTRODUCTION

Hydraulic fracturing has been a primary approach for enhancing oil recovery in tight reservoirs and increasing thermal efficiency of geothermal resources. Monitoring fracture states and fluid

migrations is vital for all phases of fracturing to optimize injection operations. Electrical conductivity is an important geophysical metric to assess reservoir properties that is governed by porosity, power fluid type, and saturation (Revil and Glover, 1998; Slater and Lesmes, 2002; Lesmes and Friedman, 2005). Due to its sensitivity to hydraulic properties, electrical methods are often used to characterize and monitor time-varying hydraulic states of subsurface. Although traditional electrical surveys are practically limited to shallow investigation depths due to Ohmic losses of the injected electrical current, deep investigation depths have become feasible by using steel-cased boreholes as electrical sources, which channels the current into greater depths along well trajectory. The concept of using energized steel-cased infrastructure sources is not limited to reservoir assessment (e.g. Daily et al., 2004); has a broad spectrum of use including monitoring fluid flow in geothermal reservoirs (e.g. Ushijima et al., 1999), tracer movements (e.g. Ramirez et al., 1996), near-surface contamination (e.g. Rucker et al., 2011), saltwater intrusion (e.g. Ronczka et al., 2015), and CO_2 injection (e.g. Ramirez et al., 2003).

Highly conductive, buried metallic infrastructures (e.g., well casing, pipes, tanks) have strong electrical response interspersed with the signal of interest and often dominating over a large spatial footprint (Fitterman, 1989; Fitterman et al., 1990) which strongly requires to incorporate their geometric and electrical properties into modeling as realistic as possible for accurate model validations. To address the problem of how to simulate the electrical response of long electrodes in the DC limit, several approaches have been proposed. Rucker et al. (2010) approximates a metallic well casing as vertically stacked rectangular cells in conjunction with a surface point electrode; however, the numerical solution reportedly has inaccuracies when the contrast is large at the well boundary (e.g. You and Liu, 2005; Kafafy et al., 2005). Rücker and Günther (2011) introduced an electrode model that can accommodate the arbitrary (non-point) electrode shapes where the interior of the electrode is not discretized; on the other hand, the effects of metallic infrastructure not used as a source can not be incorporated into the overall solution. Further, long electrodes can be represented as connected nodes via the shunt electrode model where the corresponding nodes are connected with shunt conductances (Wang et al., 1999; Zhang et al., 1995, 2014; Ronczka et al., 2015). Alternatively, metallic infrastructures with known location and dimension can be represented as lines or surfaces in the model and their approximate effects can be removed during inversions by superimposing the partial solutions based on the assumption of infinite conductivity (Johnson and Wellman, 2015). These two latter approaches have advantages of reducing the mesh discretization for wellbores but are more problematic for discrete fractures in hydraulic-fracturing simulations.

Along with metallic infrastructures, induced fractures whose lengths are significant enough and not statistically homogenized over a representative volume element are needed to be discretely defined in modeling with their explicit sizes, apertures and orientations. Considering the insignificant length scales and the numbers of manmade infrastructures and fractures over the field of interest (such as basin scale), it is a challenging modeling task to represent them in a single model due to the computational cost raised from the need of dense mesh refinement. Several advances have been proposed by researchers to economically achieve a solution for such multi-scale models. One of them is the equivalent resistor network approach where thin conductors can be represented as edges and facets in Cartesian meshes (Yang et al., 2016); on the other hand, the solution is obtained by only volume-based conductivity cells. Another proposed approach, called discontinuous Galerkin frequency-domain method, consider thin conductors as

subdomains and treats the surface boundaries that correspond to fractures or boreholes by imposing impedance transition boundary condition (Sun et al., 2017). Nevertheless, none of the above approaches easily incorporate a high number of geometrically-complex fractures and wellbores simultaneously without special treatment at boundaries and without explosive mesh refinement and computational effort. In the work described here, "Hierarchical Finite Element Method" (*Hi*-FEM) is used to deal with highly-complex hydraulic-fracturing models (Weiss, 2017). The method reduces the insignificant dimensions of planar- and curvilinear-like model features by translating them into integrated conductivities; thereby allowing one to represent fractures and steel casings with facet- and edge-based electrical properties while still enabling cost-effective simulations and inherent solutions at conductive discontinuities without enforcing boundary conditions.

Using steel well casings as long electrodes provides is one way to monitor fractures without disturbing the injection operations. A solid monitoring strategy, capable of detecting and monitoring fractures, is therefore desirable. Unfortunately, due to the numerical challenges just discussed, the realism and complexity of "real-world" models are often compromised. Here, to better understand the capabilities of electrical responses on fracture monitoring, we evaluate using *Hi*-FEM the electrical signatures of fractures near energized well bores considering various realistic hydrofracturing models. First, we start with examining the effects of borehole material conductivity (steel casing vs. no casing) and the source type (dipole vs. monopole) on the distribution of electric potentials in a homogeneous medium. Then, three representative multi-well systems are considered to better understand the influence of well geometry on the electrical responses of fractures. Moreover, the scenarios with various parameters such as conductivity contrast, source location, fracture size and fracture propagation are evaluated regarding fracture detection and monitoring.

7.3. MODELING - *Hi*-FEM APPROACH

The *Hi*-FEM method is a finite element-based approach that recognizes the geometric hierarchy of a discrete unstructured computational domain and efficient representation of thin model features via translating them into their corresponding integrated material properties. The hierarchic concept renders flexibly the material properties to be defined on each dimensional component of an volumetric cell within a tetrahedral mesh (Figure 7-1a); thereby it drastically reduces the degree of freedom, mesh requirement and computational cost. For such complex multi-scale models that possess a high number of geometrically-complex thin fractures and collinear wells in a large scale heterogeneous medium, fractures and wells can be discretely represented as 2-D planes and 1-D lines in the 3-D host medium, and their electrical properties can be defined over a set of connected facets and a group of connected edges, respectively (Figure 7-1b).

Adopting the $+$'ve sign convention to simplify the finite element analysis that follows the electric field $\mathbf{E} = \nabla u$ in the electrostatic limit, within a conducting media $\boldsymbol{\sigma}$ due to a steady electric current density $\mathbf{J}_s$, is governed by the Poisson equation,

$$-\nabla \cdot (\boldsymbol{\sigma} \cdot \nabla u) = \nabla \cdot \mathbf{J}_s, \tag{7.1}$$

where u is the electric scalar potential and $\boldsymbol{\sigma}$ is the electrical conductivity function. To represent the material properties at each dimensional component of a finite volumetric element, the electrical conductivity is introduced as a composite function in the finite element analysis (Weiss, 2017)(Figure 7-1a):

$$\sigma(\mathbf{x}) = \sum_{e=1}^{N_V} \sigma_e \boldsymbol{\Psi}_e^V(\mathbf{x}) + \sum_{e=1}^{N_F} s_e \boldsymbol{\Psi}_e^F(\mathbf{x}) + \sum_{e=1}^{N_E} t_e \boldsymbol{\Psi}_e^E(\mathbf{x}), \tag{7.2}$$

where N_V, N_F and N_E denote the number of volumes, facets and edges in the finite element mesh, respectively. σ_e is the electrical conductivity of tetrahedron e (S/m), s_e is the conductivity-thickness product of facet e (S, conductance) and t_e is the the product of conductivity and cross-sectional area (S·m) of edge e (Figure 7-1a). The hierarchical, rank-2 basis functions in Eq (7.2) are given by

$$\boldsymbol{\Psi}_e^V(\mathbf{x}) = \mathrm{diag}(1,1,1)_e \begin{cases} 1 & \text{if } \mathbf{x} \in \text{volume } e \\ 0 & \text{otherwise} \end{cases}, \tag{7.3}$$

$$\boldsymbol{\Psi}_e^F(\mathbf{x}) = \mathrm{diag}(0,1,1)_e \begin{cases} 1 & \text{if } \mathbf{x} \in \text{facet } e \\ 0 & \text{otherwise} \end{cases}, \tag{7.4}$$

and

$$\boldsymbol{\Psi}_e^E(\mathbf{x}) = \mathrm{diag}(1,0,0)_e \begin{cases} 1 & \text{if } \mathbf{x} \in \text{edge } e \\ 0 & \text{otherwise} \end{cases}, \tag{7.5}$$

where the subscript e of the diagonal tensors denote the local principal axis reference frame defined by the orthogonal unit vectors. The unique definition of electrical conductivity via basis functions with proper orthogonal vector directions enables the conductivity to be strictly local without imposing any boundary condition at conductivity discontinuities. As a result, a composite element-stiffness matrix is obtained in the finite element analysis that can be written as

$$\mathbf{K} = \sum_{e=1}^{N_V} \sigma_e \mathbf{K}_e^4 + \sum_{e=1}^{N_F} s_e \mathbf{K}_e^3 + \sum_{e=1}^{N_E} t_e \mathbf{K}_e^2 \tag{7.6}$$

where $\mathbf{K}_e^4$ is the 3D element-stiffness matrix (4×4) of eth tetrahedron, $\mathbf{K}_e^3$ is the 2D element-stiffness matrix (3×3) of eth facet and $\mathbf{K}_e^2$ is the 1D element-stiffness matrix (2×2) of eth edge. Finally, the global form of the linear system of equations are then constructed as in the traditional finite element analysis and can be given as follows:

$$\mathbf{K}\mathbf{u} = \mathbf{b}. \tag{7.7}$$

The solution of the Eq (7.7) is obtained iteratively by using a Jacobi-preconditioned conjugate gradient (J-PCCG) solver (Weiss, 2001, 2017). Benchmarks, convergence behaviors and other applications of the *Hi*-FEM approach can be found in Weiss (2017); Weiss et al. (2018); Beskardes and Weiss (2018) and Beskardes et al. (2019).

7.4. THE EFFECTS OF WELL MATERIAL AND SOURCE DESIGN

We begin by examining the effects of steel casing and the influence of the source design on the current density leaked into the surrounding homogeneous medium. A 0.01 S/m homogenous medium with two vertical steel-cased wells is considered (Figure 7-2). Both wells extend 2 km and a dipole source with 50 m length is used to energize the wells. The well casing conductivity is 10^6 S/m. The radius of the well is 0.1 m and the wall thickness is 0.025 m which corresponds to casing conductance of 1.37×10^4 S. Note the absence of magnetic susceptibility in the governing electrostatic Eq (7.1), meaning that the time-invariant **E** field is independent of the magnetic properties of steel. Four combinations of steel-cased and noncased wells as well as three different source locations are considered. The resulting potential distributions (Figure 7-3) clearly indicate the dominating effect of steel casing displaying completely different patterns of potentials. The well material is particularly important for the well in that the source is located. On the other hand, both well material and source location controls the overall resulting potential pattern (Figures 7-3 and 7-4).

In addition, we also consider different source designs along a steel-cased well located in a homogenous medium. The conductivities of the well and the host are set to be the same with the model shown in Figure 7-2. The results in Figure 7-5 describe the borehole potential and the current density profiles due to a monopole source as well as dipole sources with different lengths. The longitudinal density along the casing is calculated as $t_e\mathbf{E}$. The monopole source distributes the current along the entire casing exhibiting a linear decay from the source location, whereas dipole source yields a higher strength of current density through the length of dipole source. The increasing length of dipole source decreases the strength of current along the length of dipole source. The results indicate that the use of dipole source is more suitable to deliver higher current into a specific zone of nearby formation and the length of the dipole is a control on the strength of current. In addition, the results suggest that there is no dependence of the current strength on the ratio between the length of dipole source and the length of well.

7.5. MONITORING FRACTURES VIA ENERGIZED WELL SOURCES

To examine the electrical signatures of fractures due to energized steel-cased wells, we consider scenarios with different conductivity contrasts, well geometries, source locations as well as fracture growth and fracture set propagation.

7.5.1. Conductivity contrast

The effect of conductivity contrast between surrounding rock and fractures is examined via a lateral well casing with five regularly-spaced fractures. The casing vertical length is 750 m and it

extends horizontally 1000 m in a 0.01 S/m host medium. The first fracture is located at 480 m and at 750 m depth, and the fracture separation is 10 m. The major and minor radii of the fracture ellipses are 50 m and 20 m, respectively. The well casing conductivity, radius and wall thickness are the same with the model in Figure 7-2.

To examine different conductivity contrasts, by keeping the well conductivity fixed, the composite conductivity function (Eq (7.2)) can be normalized by the host conductivity as follows:

$$\sigma = \mathbf{I}_{3\times 3} + \sum_{e=1}^{N_F} \eta h \boldsymbol{\Psi}^F + \sum_{e=1}^{N_E} \frac{t_e}{\sigma_{host}} \boldsymbol{\Psi}_e^E \quad \text{and} \quad \mathbf{J}_s \mapsto \mathbf{J}_s/\sigma_{host}, \tag{7.8}$$

where h is the fracture aperture and the conductivity contrast between fracture and host is $\eta = \Delta\sigma_e/\sigma_{host}$. Using Eq (7.8), the electrical potentials for the conductivity contrasts from 10^0 to 10^6 are simulated. Figures 7-6a and 7-6b shows the potential distributions when $\eta = 10^0$ and 10^3. The overall pattern of potential for both contrasts is quite similar except near the fractures. The higher contrast results in higher potential on the fractures. The results in Figure 7-6c, compare the voltage differences along the well casing before and after fracturing. The increase in conductivity contrast between the host and the fractures indicate higher voltage difference along the casing shifting the profiles up; however, the shift in amplitudes becomes gradually smaller while contrast increases.

The anomaly due to the fracture set (centered at 500 m at 750 m depth) can be seen as a higher potential difference on the borehole profile and is not significantly affected by the contrast level. The results indicate that the contrast between the host rock and the fractures controls the amplitude but not the shape of the potential distribution and its effects becomes less significant for very high contrast levels.

7.5.2. Well geometry and source location

Three representative multi-well geometries are considered: lateral, multi-lateral and multi-vertical wells (Figure 7-7). The well casing conductivity, radius and wall thickness are the same with the model in Figure 7-2. Each model has five equally-spaced discrete fractures with 10 m spacing. The conductance of the fracture planes is 1 S, and the major and minor radii of fracture ellipse are 50-m major and 20-m minor, respectively. The first fracture is located at 480 m in the horizontal direction at 750 m depth except the multi-vertical well model where the fractures are placed at 500 m depth. This distinction is done purposefully to examine whether the fractures located at the shallow arm of the multi-vertical well system has any influence on the current that flows towards the deeper arm. Besides, another important point to investigate is whether it is possible to detect fractures through a monitoring well. To examine the influence of the source location, we consider the cases when the source is located in the production well as well as the monitoring well (Figure 7-7).

Figure 7-8. compares the resulting potential distributions over different well geometries when the 100-m dipole source is located in the production well. The electrical potential decays away from the conductive wells. The results clearly indicate that the potential distribution is strongly

controlled by the well trajectory as well as where the dipole source is located along the well. In addition, the potentials tend to surround the highly-conductive monitoring well. Figure 7-9 shows the potential distributions for different well geometries in case the 100-m dipole source is located in the monitoring well. In this case, the significant difference is the anomalously high potentials along fracture planes regardless of the source location.

Figure 7-10 shows the voltage difference profiles along production and monitoring wells before and after fracturing. The voltage difference profiles along the production well for both source locations (Borehole A, black and red solid lines) and for all three well systems show the elevated values corresponding to the location of the fracture zone. This indicates that the shape of the electrical signature of fractures along the production well has no sensitivity to the geometry of wells as well as the source location. Their only effect is the change in the amplitudes. On the other hand, regardless of the source location, it is not possible to measure an indicative electrical response along the monitoring well corresponding to the fracture locations. Moreover, in case of parallel lateral wells, the voltage differences along the monitoring well for both source locations are different from those on multi-lateral and vertical wells (Figure 7-10a, black and red dashed lines). Rather than a smooth decay, the profiles first show a smooth decay and then an exponential increase; however, the locations of the zero voltage difference for both source locations does not correspond to the location of fracture zone (Figure 7-10a). In addition, in case of the multi-vertical wells, the voltage difference profiles along the monitoring well for both source locations indicate no characteristic difference suggesting that the depth of fractures relative to the monitoring well has no influence on the resulting voltage difference along the monitoring well (Figure 7-10c).

7.5.3. Fracture growth

The multi-lateral wells shown in Figure 7-7b are chosen to examine the effects of fracture growth. We consider the base fracture size as 50-m major and 20-m minor radii for comparisons. The cases where the fracture sizes are R, 2R, 4.5R and 5R where the fractures reach to the monitoring well, are examined. Figure 7-11 shows the casing voltage difference (post- and pre-fracturing) for different fracture sizes and for different source locations where the source is placed in the production well (a) and in the monitoring well (b).

Figure 7-11a indicates that while the fracture size increases perpendicular to the casing, the voltage difference gradually increases along the entire well system and the fracture zone is consistently significant with the elevated values along the production well profile for both source locations unless the fractures do not intersect with the monitoring well (except the case of fracture size 5R). Moreover, the monitoring well profiles due to different source locations tend to behave differently such that the source in the monitoring well results in the change in the decay rate of exponential decays of the voltage difference more rapid than those resulting from the source in the monitoring well, consequently resulting in coalescing the profiles roughly 400 m away and the indistinctive values at larger horizontal distances (such as Figure 7-11b, sizes 2R and 4.5R). Probably, this is because of the sensitivity of the source in the monitoring well to the approaching fractures.

When the fractures reach the monitoring well, the voltage difference profiles (in absolute value) along the production well for both source locations show an anomalous increase implying the location of the fracture zone higher than those for smaller fracture sizes (Figure 7-11, black solid lines). Besides this similarity, the profiles suggest two different behaviors for the different source locations. In case of the source in the production well, the potential difference along the vertical section of the well system is lower than that of the case with size 4.5R (Figure 7-11a, black solid line) whereas the vertical section has the lowest values in case of the source in the monitoring well (Figure 7-11b, black solid line). Furthermore, the voltage difference profile along the monitoring well in case of the source in the production well (Figure 7-11a, black dashed line) first indicates a rapid decay and subsequently an increase until where the fractures are located; on the other hand, the profile in case of the source in the monitoring well shows no decay and solely an increase at the location of fractures exhibiting a completely similar behavior with the production well profile (Figure 7-11b, black dashed line). This suggests that even though the profiles along the monitoring wells in case of different source locations show different behaviors and amplitudes, both signifies the fractures as an increase at the fractures location. Note that the potential distributions along the fracture ellipses due to different source locations are quite distinct resulting from different distances from the source to the center of the fractures (Figure 7-12). This may explain the reason of the different characteristics of the profiles (Figure 7-11, black dashed lines). The results suggest that the electrical anomaly of fractures is significant on the voltage difference profiles of the monitoring well only if the fractures are in contact with that well; in other words, for multi-lateral wells, monitoring fractures from a monitoring well can be only possible if fractures reach the monitoring well.

7.5.4. Fracture set propagation

The electrical indication of fracture set propagation is investigated via a multi-stage hydraulic-fracturing model in a homogeneous host rock (Figure 7-13). The properties of the multi-lateral wells are set to be the same with that shown in Figure 7-7b. A monopole source is located at 450 m horizontally. The fractures are circular with uniformly-distributed radii (20 m, 50 m) and the first fracture is located at 480 m. Four fracturing stages are considered; each stage has five additional fractures with a 10 m separation. The results described in Figure 7-13b indicate that the increase in the number of fractures perpendicular to the production well result in larger voltage differences along both wells. The monitoring well does not give an electrical indication regarding fracture locations except the increase in voltage difference along the entire well length; on the other hand, the voltage difference along the production well shows an anomalous increase in voltage difference with gradually increasing widths related to the propagating fractures. When the source is placed in the monitoring well, the same profiles are obtained with lower amplitudes; therefore, they were not herein presented.

7.6. CONCLUSION

We present the numerical modeling results of the electrical responses of fractures due to energized steel-cased well sources as a function of various well and fracture properties. The effects of the well material property (steel casing vs. no casing) and the source type (dipole vs. monopole) on the resulting electrical potentials have been first considered. The different wellbore materials result in significantly different patterns of potential distribution and thus different borehole potentials for the wells that host the electrical source as well as the wells that are used for monitoring. Whereas the monopole source distributes the current density that decays from the source location along the entire well length, the dipole source provides a focussed current density along the dipole source length. Moreover, the amplitude of elevated current density along the dipole source length is not directly proportional to the ratio between the source length and the entire well length. The conductivity contrast between the host medium and fractures does not affect the distribution of electrical potentials but controls the amplitude. While the contrast increases, the voltage difference before and after fracturing along the well casing increases in amplitude; however, this effect gets saturated at very high contrast levels. The results of different multi-well systems indicate that even though the overall potential pattern is directly controlled by the well geometry, the voltage differences before and after fracturing along both the production and monitoring wells are insensitive to the well layout. Moreover, the choice of well in which the source is located also does not cause any change in the characteristics of the borehole voltage difference. The models of different well geometry and source location suggest that it is not possible to monitor the electrical signatures of fractures from the monitoring well unless the fractures connect with that well. When fractures intersect the monitoring well, the electrical response corresponding to the fracture location is significant along both production and monitoring wells.

The electrical potentials along the production well casing due to regularly-spaced, non-elongated fractures show a smooth anomaly corresponding to the location of fractures. In addition, the electrical potentials along the production well show a high sensitivity to the extent of fractures perpendicular to the casing as well as the width extent of the fracture sets parallel to the casing, which suggests a fast through-casing fracture monitoring capability on multi-branch wells. On the other hand, monitoring through the well casing strongly depends on the health of wells. The effects of well completion design and corrosion on the resulting electrical potentials must be the next step of analyses to develop a complete understanding on the capabilities and limitations of through-casing monitoring as well as to inform future measurement strategies. Furthermore, the recoverability of these fracture properties from the smooth electrical measurements via inversion still remains as a valid question and must be investigated in detail via further numerical modeling studies and real data validations. Using the *Hi*-FEM approach, the simulations with complex multi-well geometries and discrete fractures have been achieved with the computational times in the order of a few minutes on a single processor. The fast forward solutions make the inversion feasible for such complicated models; on the other hand, the parametrization of hierarchical electrical properties and the choice of the initial mesh for the inversion process are still ongoing research problems.

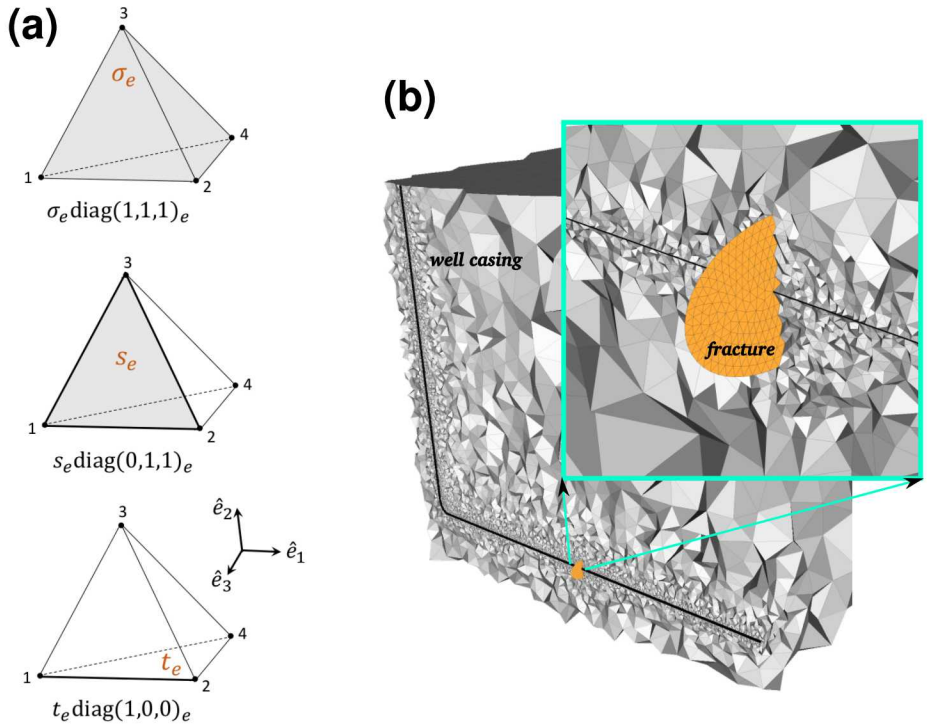

Figure 7-1. a) Hierarchical components of material property for a tetrahedral finite element. Volumetric electrical conductivity σ_e is defined over the tetrahedral element whereas the incorporation of the conductivity contrasts on facet and along edge is achieved via defining them as conductance s_e (S) and conductivity-are product t_e (S·m), respectively. b)Hierarchical representations of a lateral well and a single fracture in a basin-scale tetrahedra mesh volume. Black line indicates the lateral well that is represented as a set of connected edges, and the ellipse (in orange) indicates the fracture plane that is represented in forms of a set of connected facets in the mesh. The inset map shows a magnified view of the well and the fracture plane.

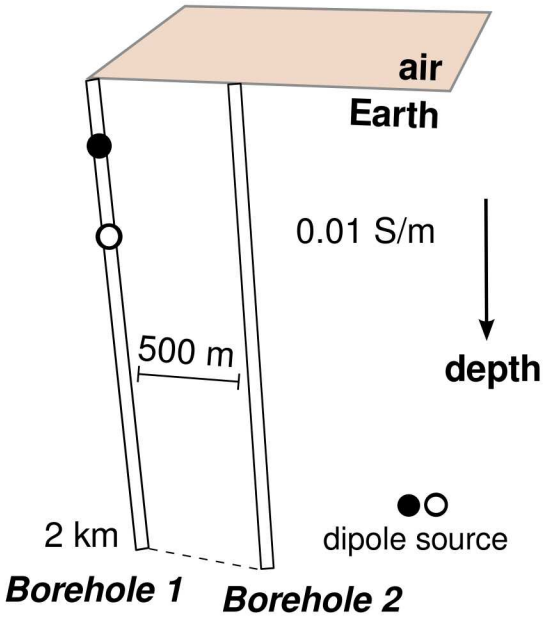

Figure 7-2. A subsurface model with two vertical wells. Equal-length wells are located 500 m apart in a 0.01-S/m homogeneous medium. The black and white circles denote a dipole source.

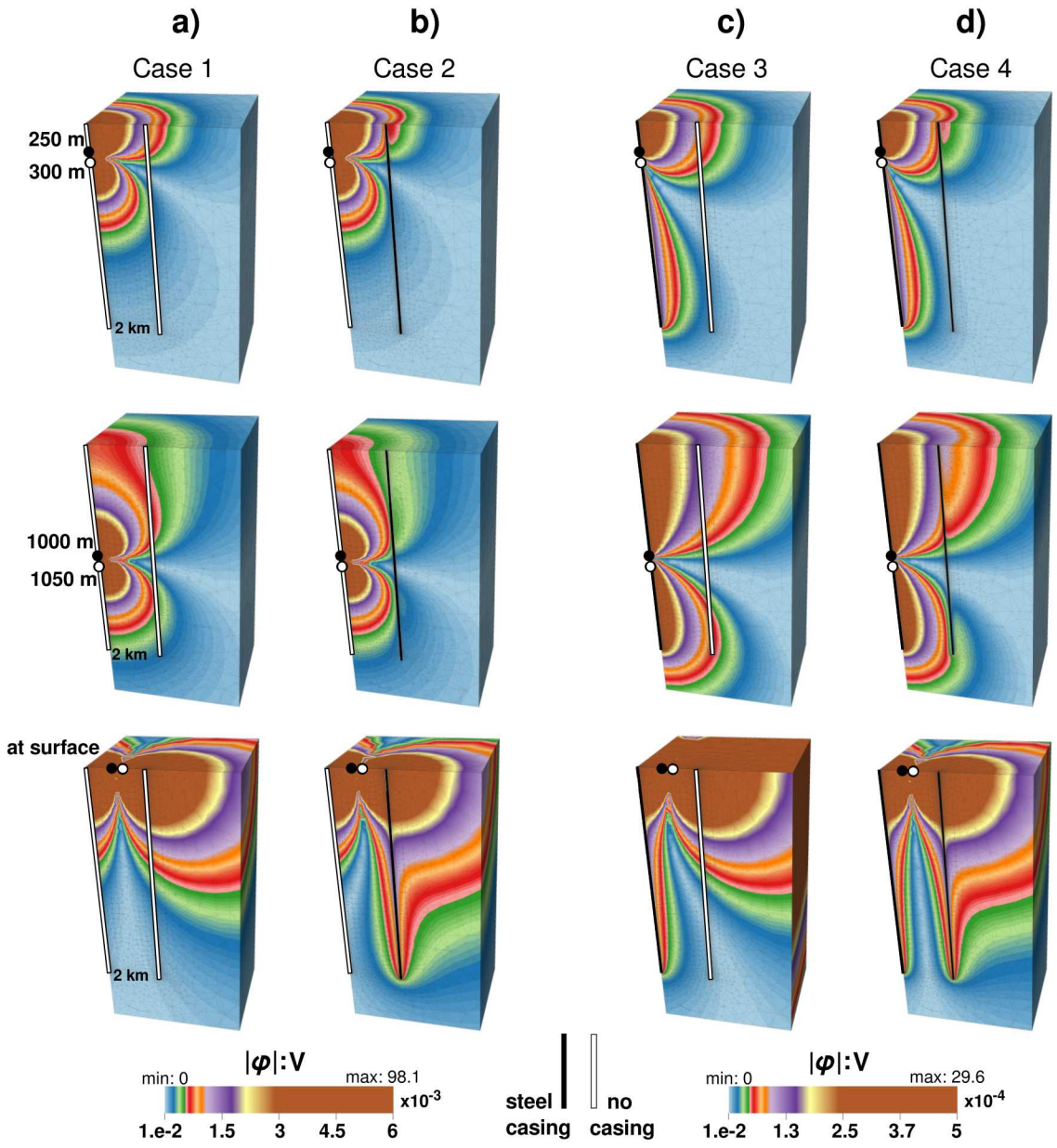

Figure 7-3. Electrical potential distributions near two vertical wells (Fig. 7-2) resulting from different source locations (rows) and different combinations of well material (steel vs. no steel, columns). Black and white circles denote a 50-m dipole source with 1 A and -1 A. Black wells have steel casing with a conductivity of 10^6 S/m and white wells have no steel casing.

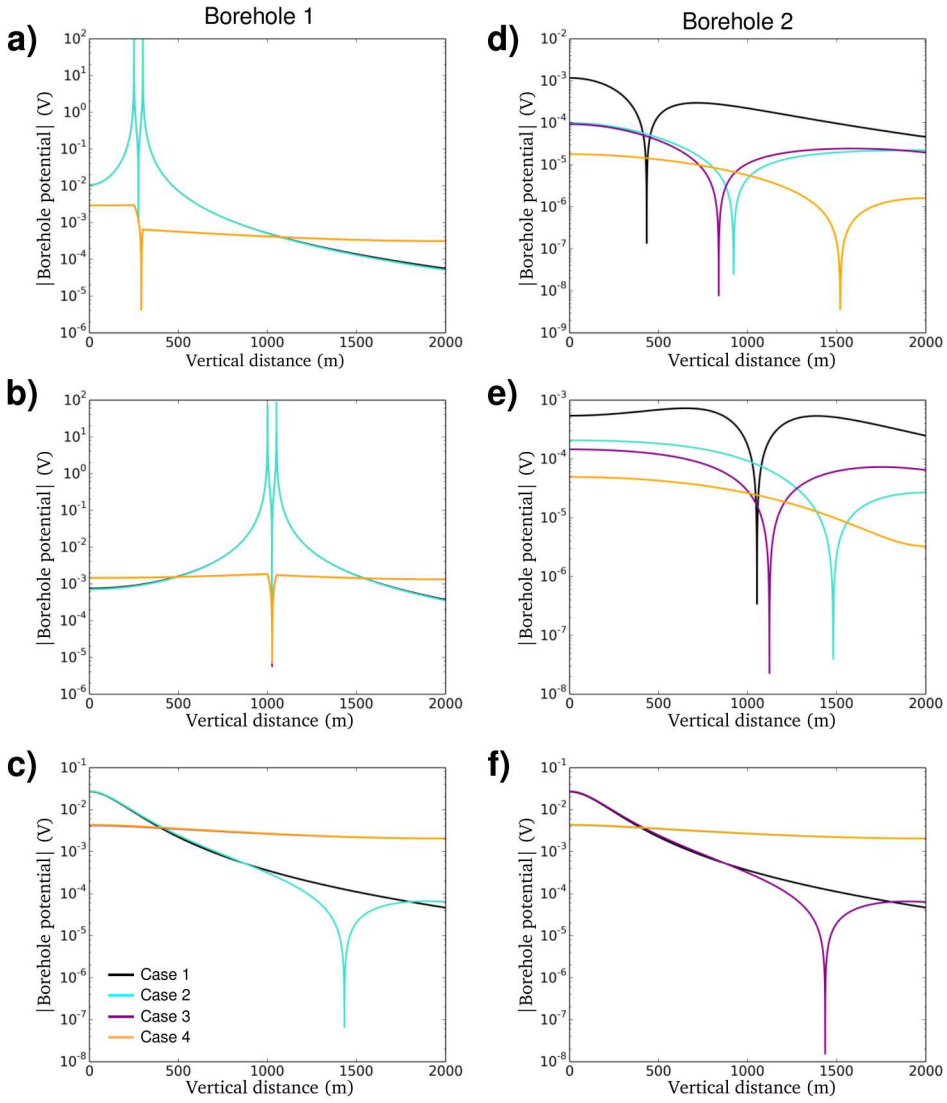

Figure 7-4. Profiles of the absolute values of the electrical potentials along Borehole 1 (first column) and along Borehole 2 (second column). Each row shows the borehole voltage due to a different source location (as shown in Fig. 7-3). Each color indicates a different combination of well material (Fig 3a-3d) as indicated in the legend of (c).

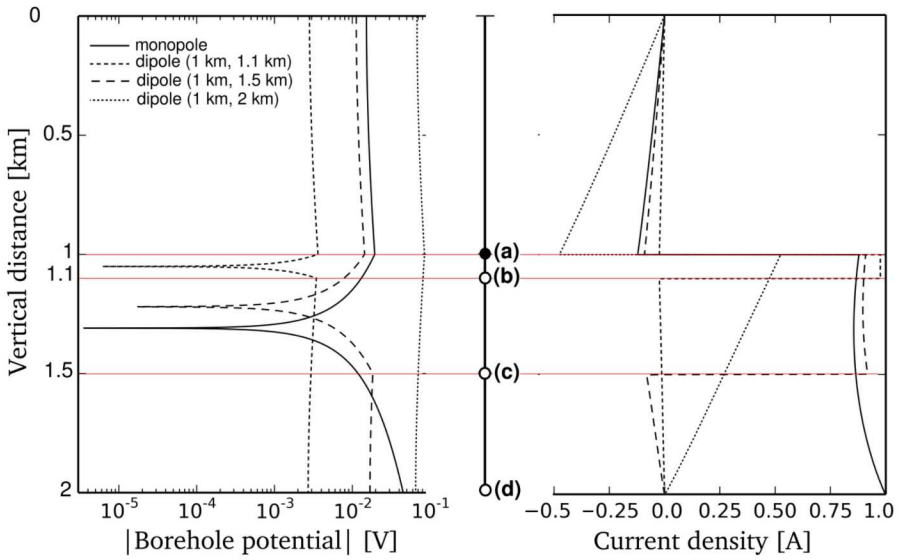

Figure 7-5. Borehole potential (in absolute value) and current density along a 2-km vertical well with a steel casing with a conductivity of 10^6 S/m due to a) a monopole source (1 A) located at 1 km depth, and a dipole source with b) 0.1 km, c) 0.5 km and d) 1 km length. For each dipole source, the positive point source (black circle, 1 A) is fixed to be located at 1 km and the negative point source (white circle, -1 A) is located at greater depth according to the dipole length.

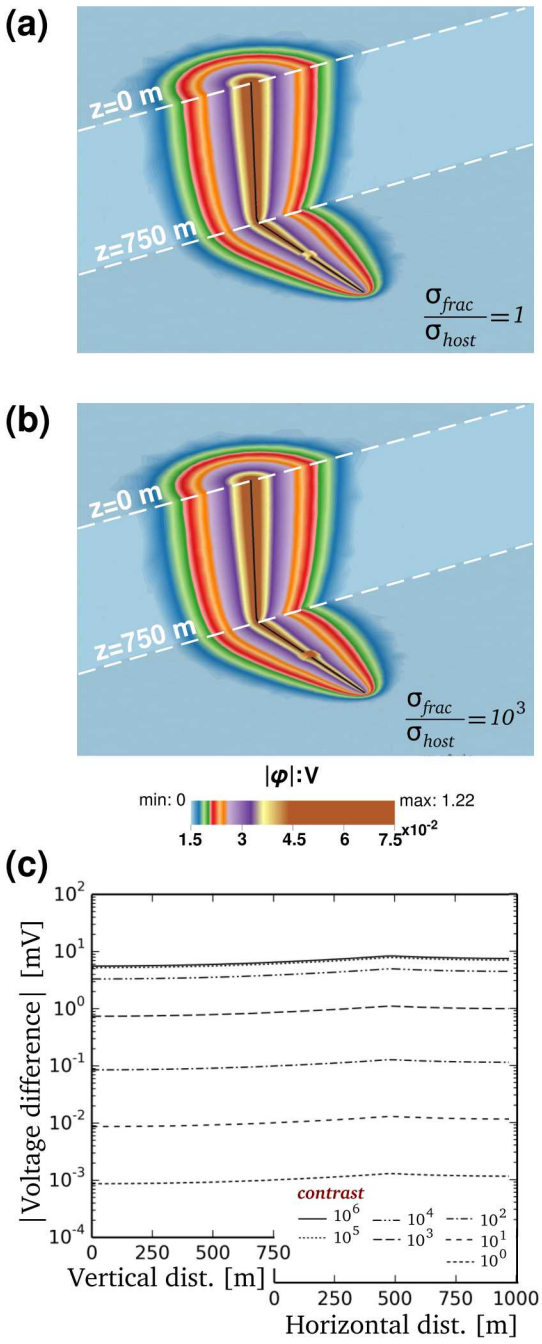

Figure 7-6. Oblique views of electrical potential distribution for a single lateral well with 5 fractures where the conductivity contrast between the fractures and the host is a) 1 and b) 10^3. The lateral well extends 750 m vertically and 1000 m horizontally (black line). The fractures with a 10 m separation are located at 480 m−520 m at 750 m depth. c) Profiles of the absolute values of the voltage differences along the steel-cased well before and after fracturing due to different conductivity contrasts.

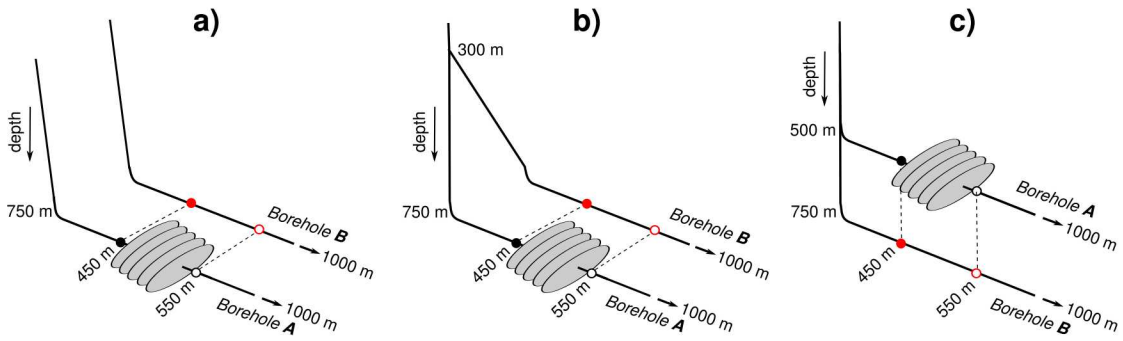

Figure 7-7. Three representative well models: a) lateral wells, b) multi-lateral wells, c) multi-vertical wells. Well systems are located in a 0.01-S/m host medium and extend 1 km horizontally. The separation of horizontal wells in (a) and (b), and the vertical separation in (c) is 250 m. Each well has steel well-casing with a conductivity of 10^6 S/m. Grey ellipses with 10-m spacing indicate fracture planes with a 1-S conductance. Each filled and open circle pair in the same color denote a dipole source with 1 A and -1 A. For each well model, two different source locations are considered; where the dipole source is located at 450 m and 550 m in Borehole A (in black) and in Borehole B (in red).

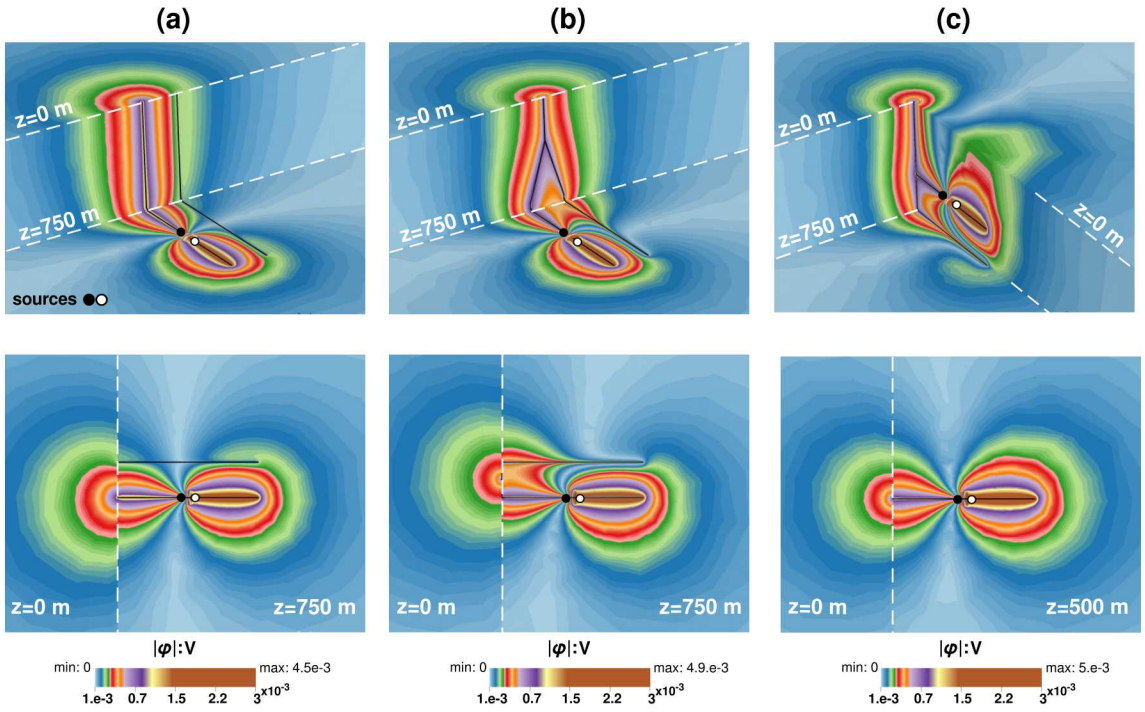

Figure 7-8. Electrical potential distributions for a) parallel lateral wells, b) multi-lateral wells, c) multi-vertical wells with regularly-spaced fractures (Fig. 7-7) due to a dipole source (black and white circle pair) that is located in the production well. First row shows the oblique views and second row displays the corresponding plan views. Black lines indicate the well geometry and fractures (on plan views only).

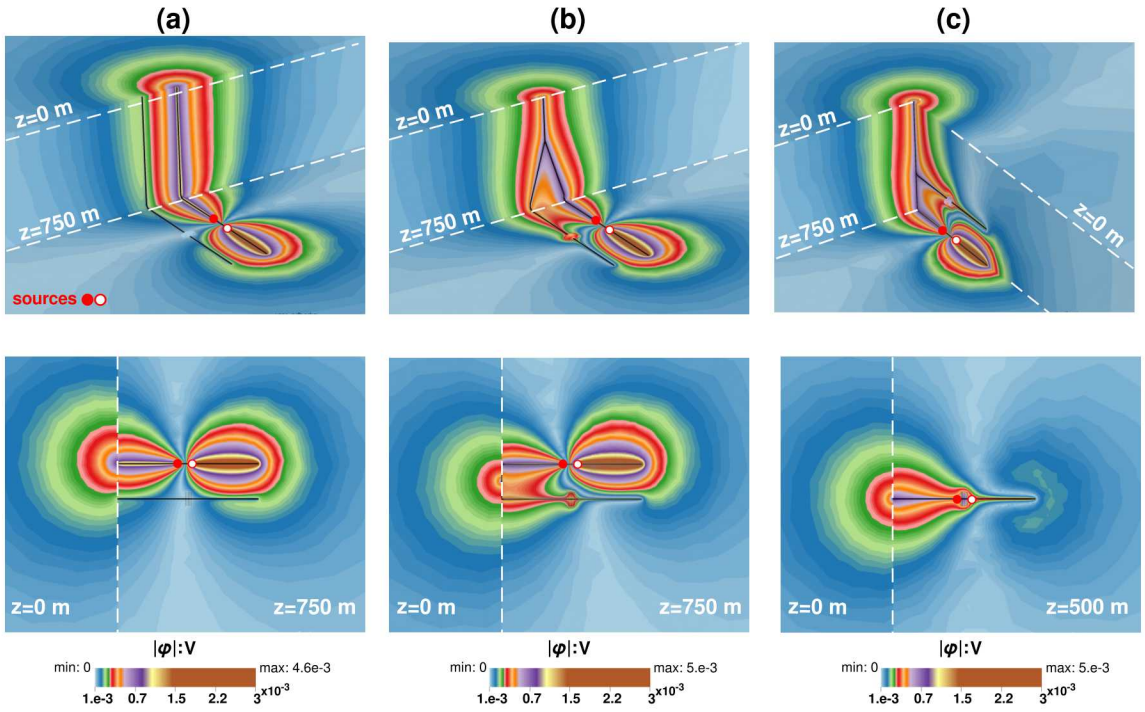

Figure 7-9. Electrical potential distributions for a) parallel lateral wells, b) multi-lateral wells, c) multi-vertical wells with regularly-spaced fractures (Fig. 7-7) due to a dipole source (red and white circle pair) that is located in the monitoring well. First row shows the oblique views and second row displays the corresponding plan views. Black lines indicate the well geometry and fractures (on plan views only).

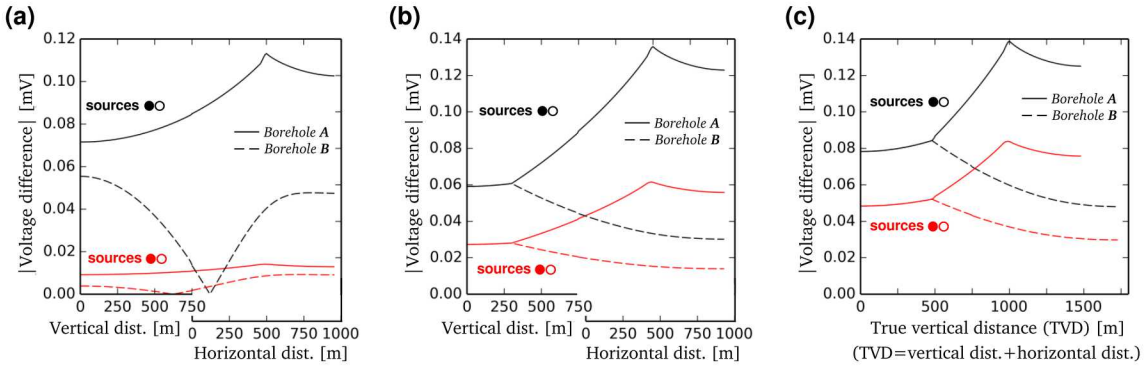

Figure 7-10. Profiles of the absolute values of the potential differences along a) parallel lateral wells, b) multi-lateral wells, c) multi-vertical wells before and after fracturing shown in Fig. 7-7. Solid lines indicate the production wells (Borehole A) where the fractures are located and dashed lines indicate the monitoring wells (Borehole B). The dipole source location is indicated with black (in the production well) and red (in the monitoring well). Note that from Fig. 7-7c, the heel of Borehole A is at TVD=500 m and the heel of Borehole B is at TVD=750 m. For clarity, the values in the red curves of Figure (a) have been multiplied by a factor of 30.

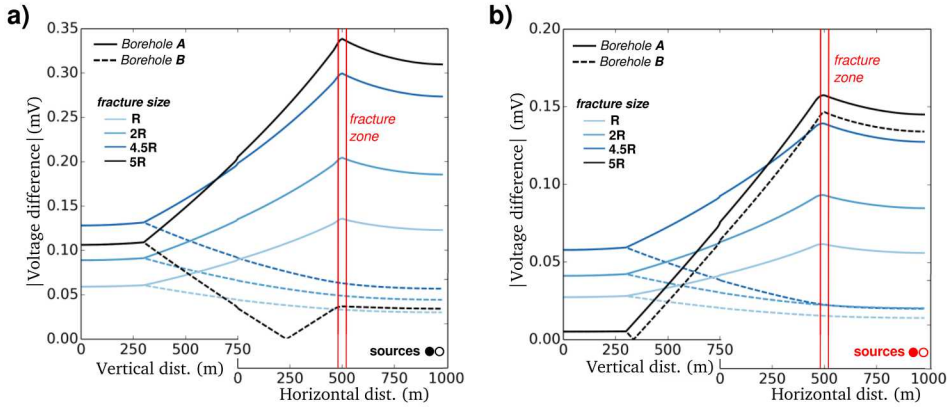

Figure 7-11. Absolute values of the voltage differences (before and after fracturing) along the multi-lateral wells (Fig. 7-7b) for different fracture sizes. R indicates a fracture with a 50-m major and 20-m minor radii. Fracture zone is bounded by red lines. Solid lines indicate the production wells (Borehole A) where the fractures are located and dashed lines indicate the monitoring wells (Borehole B).

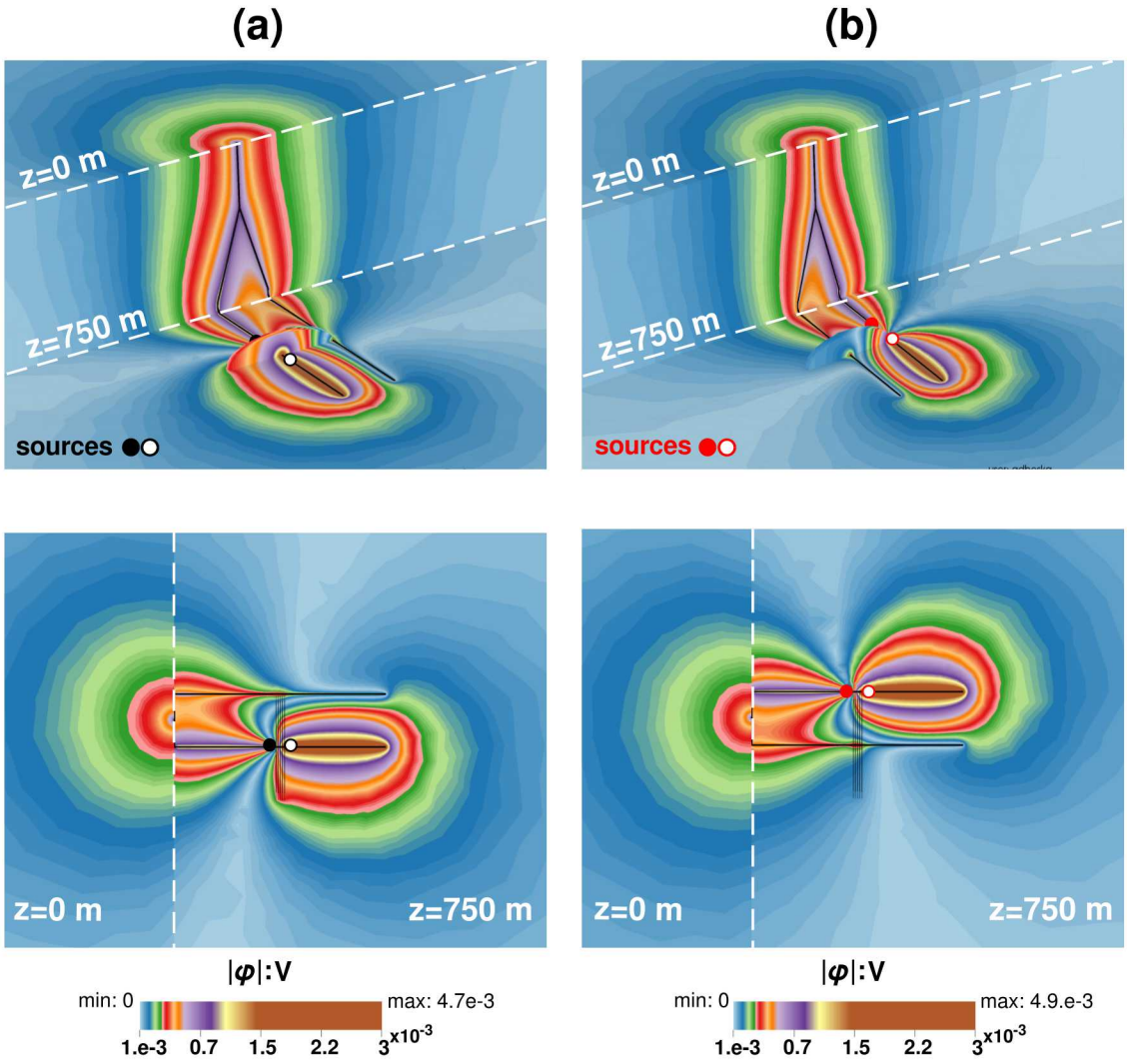

Figure 7-12. Electrical potential distributions of the multi-lateral wells (Fig. 7-7b) when the size of fractures is 5 R, for two different dipole source locations (a) in the production well, b) in the monitoring well). First row shows the oblique views and second row shows the corresponding plan views. Black lines indicate the well geometry and fractures (on plan views only).

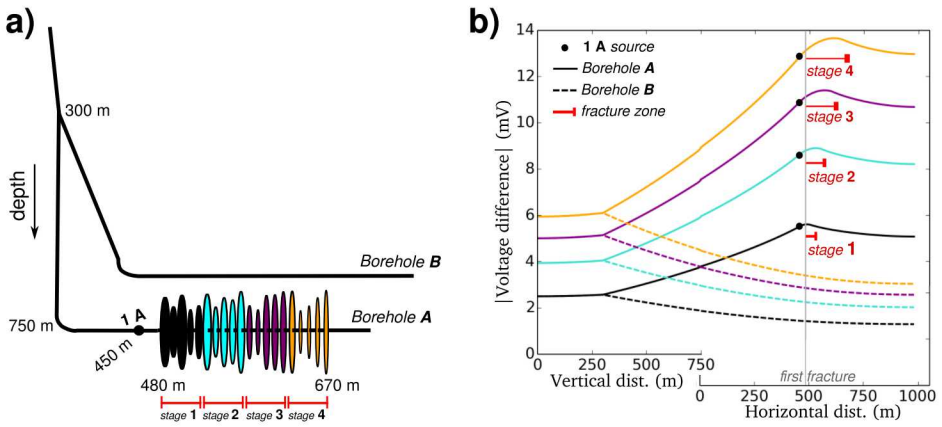

Figure 7-13. a) Fracture propagation model. The multi-lateral wells has the same geometry and physical properties with the model shown in Fig. 7-7b. The fractures are located along Borehole A, and the first fracture is located at 480 m in the horizontal direction. The fracture set propagation is considered as four stages. Each stage has additional 5 fractures with 10 m spacing. The fractures are circular with radii populated from a uniform distribution (20 m, 50 m). Black dot denotes a 1-A monopole source. b) The voltage difference profiles (in absolute value) along borehole A and B for different stages of fracture set propagation. Black dots indicate the source location. The zone of the fracture set after each fracturing episode is shown with red bars.

8. A FRACTIONAL CALCULUS SOLUTION TO THE HELMHOLTZ EQUATION

8.1. SUMMARY

A growing body of applied mathematics literature in recent years has focused on the application of fractional calculus to problems of anomalous transport. In these analyses, the anomalous transport (of charge, tracers, fluid, etc.) is presumed attributable to long–range correlations of material properties within an inherently complex, and in some cases self-similar, conducting medium. Rather than considering an exquisitely discretized (and computationally intractable) representation of the medium, the complex and spatially correlated heterogeneity is represented through reformulation of the governing equation for the relevant transport physics such that its coefficients are, instead, smooth but paired with fractional–order space derivatives. Here we apply these concepts to the scalar Helmholtz equation and its use in electromagnetic interrogation of Earth's interior through the magnetotelluric method. We outline a practical algorithm for solving the Helmholtz equation using spectral methods coupled with finite element discretization. Execution of this algorithm for the magnetotelluric problem reveals several interesting features observable in field data: long–range correlation of the predicted electromagnetic fields; a power–law relationship between the squared impedance amplitude and squared wavenumber whose slope is a function of the fractional exponent within the governing Helmholtz equation; and, a non–constant apparent resistivity spectrum whose variability arises solely from the fractional exponent. In geologic settings characterized by self–similarity (e.g. fracture systems; thick and richly–textured sedimentary sequences, etc.) we posit that diagnostics are useful for geologic characterization of features far below the typical resolution limit of electromagnetic methods in geophysics.

8.2. INTRODUCTION

Anomalous diffusion has been at the heart of considerable research directed at understanding non-standard, or "anomalous", transport behavior where the mean squared displacement of random walk particles no longer adheres to a linear relationship with time. As a result, such systems reveal power laws indicative of sub– and super–diffusive behavior. Anomalous diffusion can be described through random walks endowed by heavy tail distributions and can be captured

through non-integer exponents on time and space derivatives. Fractional derivatives in space model super-diffusion and are related to long power–law particle jumps, whereas fractional time derivatives model sub–diffusion and reflect long waiting times between particle jumps. Such behavior has been observed in many applications including reaction-diffusion, quantum kinetics, flow through porous media, plasma transport, magnetic fields, molecular collisions, and geophysics applications. We refer the reader to Metzler and Klafter (2000) for a detailed description of anomalous diffusion, including a comprehensive list of applications. The underlying cause for anomalous behavior in these applications is the presence of complex structures or mechanisms that either promote sub-diffusion or super-diffusion. For instance, in fluid flow through porous media, complex permeability fields cause sub-diffusive transport through trapping mechanisms or solid/liquid surface-chemistry kinetics, ultimately inducing a memory–type effect (Caputo, 2000; Deseri and Zingales, 2015). Super-diffusive responses have been experimentally observed in diffusion-reaction system where the variance of a chemical wave exceeds a linear temporal relationship (von Kameke et al., 2010). This is interpreted to be a result of non–local interactions over distances beyond that to the nearest neighbors. In the diffusion–reaction case, vortices in a chaotic velocity field introduce flow paths that exceed standard diffusion rates.

A range of natural phenomena can be described as processes in which a physical quantity is constantly undergoing small, random fluctuations. Such Brownian motion can be interpreted as a random walk that, according to the central limit theorem, approaches a normal distribution as the number of steps increases. A macroscopic manifestation of Brownian motion is defined as diffusion whereby a collection of microscopic quantities tends to spread steadily from regions of high concentration to regions of lower concentration. Through Fick's first and second laws, macroscopic particle movement can be captured by the familiar diffusion equation, the solution of which is a normal distribution corresponding to the random walk probability density. These well known concepts provide the underpinning to investigate phenomena that violate the standard diffusive regime. An application space which has received relatively little attention but is poised for further exploration is low-frequency electromagnetic imaging and interrogation of Earth's subsurface, a classic geophysical exploration technique premised on diffusive physics, through the mobility of solid-state defects in crystalline materials and free electrons in metals, and electrolytic conduction in fluids (Karato and Wang, 2013).

Capturing anomalous diffusion in partial differential equations (PDEs) poses considerable mathematical and numerical challenges, particularly in the area of 1) imposing non-zero boundary conditions, 2) validating fractional behavior for different physics, and 3) achieving computational efficiency to realize scalable performance. In representing the fractional Laplacian operator, an integral or a spectral definition can be considered. The choice of method however remains an open question, especially in the presence of non-zero boundary conditions. In this paper we consider the spectral definition and justify this choice based on the authors' previous developments. Validating fractional PDEs against field observations, laboratory measurement, or analytic solutions is difficult, in part, because fractional calculus development has been somewhat isolated from engineering and science applications community. In this paper, we offer results to help bridge that gap between the observational science and mathematics communities. In particular, fractional concepts are applied to geophysical electromagnetics to better characterize the subsurface and subsequently validated through field observations, as well as geophysical insight.

A key challenge in simulating fractional PDEs is achieving computational efficiency. In our work we pursue an approach that leverages the Dunford–type integral representation, which in the case of the fractional Poisson equation, is computationally very attractive because the problem is easily tranformed into an uncoupled set of classical (integer order) Poisson solves that can be computed in parallel and then aggregated afterward for the fractional–order solution. This parallelism however does not map to our Helmholtz implementation because of coupling cross-terms, a fact which impacts our eventual desire to make use of adjoint-based optimization. Nonetheless, we begin with the solution strategy in Bonito and Pasciak (2015, 2017), with its resultant Helmholtz coupling, and augment it with the lifting (splitting) strategy of Antil et al. (2018b) for handling non-zero boundary conditions to arrive at a unique approach to solving the fractional Helmholtz equation, regardless of its particular application here in geophysical electromagnetics.

The aim of this paper is to explore anomalous diffusion in the context of geophysical electromagnetics and to derive mathematical and algorithmic strategies for practical simulation capabilities. Earth's subsurface is known to be ripe with complex geologic heterogeneity of hierarchical structures and self–similar geometries arising from its generative petrophysical processes and subsequent tectonic and physiochemical experiences. In many cases, low–frequency electromagnetic energy incident upon such media is well–known to produce a measured response incompatible with that of an "equivalent" homogeneous and isotropic medium, or even practical approximations of piecwise–constant material assemblages. For example, non-local electromagnetic effects due to fractures and stratigraphic layering have been analyzed, and in some cases observed, in the context of near-surface geotechnical engineering (Everett and Weiss, 2002b; Weiss and Everett, 2007; Ge et al., 2015) and (Vallianatos, 2017, 2018; Vallianatos et al., 2018). This perspective on electromagnetic data analysis was hugely influenced by speculative analogy with fluid flow in porous media and the fractional calculus framework developed therein (Caputo, 2000; Deseri and Zingales, 2015; Benson et al., 2000), and is bolstered by a growing body of observational evidence of electromagnetic phenomena elsewhere (e.g., the response of composite metamaterials in Elser et al., 2007). Ultimately, as geophysicists, we are interested in detecting small scale features in the geological subsurface (e.g. fine-scale stratigraphic laminations or regions permeated by fractures) that may aggregate into a hierarchical "meta-material", but our interest is tempered by practical necessity, to avoid the detailed and computationally explosive discretization required to represent each of them in a given numerical simulation. To mitigate this problem, we propose to dispense with the equisite discretization just described and replace it by a piecewise blocky medium endowed with a non–local response captured through a fractional space derivative in the material constitutive relation. This is similar to prior approaches for studying anomalous diffusion in hydrology (Caputo, 2000) and geophysical electromagnetics (Everett and Weiss, 2002b; Weiss and Everett, 2007; Ge et al., 2015), where, instead, a time–fractional derivative was considered. The challenge here is deriving a solution to the space–fractional Helmholtz equation, a task not obviously suited to the Fourier/Laplace spectral approach readily adaptable for its time–fractional counterpart (Everett, 2009; Ge et al., 2015).

Our main contributions consist of the following: 1) deriving fractional Helmholtz by introducing a fractional space derivative into Ohm's law to account for non-local conductivity and recognizing that the solution process for this fractional PDE requires a decomposition to separate boundary conditions on the fractional Laplacian operator; 2) implementing computationally efficient

methods through a combination of spectral characterization of the Laplacian, finite element discretization, and a Dunford–type integral representation, followed by a reformulation allowing for sparse, scaled Jacobians with much improved conditioning; and 3) validating EM behavior through exemplar problems in magnetotullerics. The remainder of the paper is organized by first deriving the fractional Helmholtz equation through a fractional gradient relationship between the magnetic field and the underlying electric conductivity. Next the fractional Helmholtz equation with non-zero boundary conditions is decomposed to separate non-zero right-hand side and non-zero boundary conditions. The separation provides a convenient solution strategy and leverages the Dunford–type integral approach to numerically solve one of the remaining equations with a fractional Laplacian. After the mathematical formulation, our finite element implementation is verified through the methods of manufactured solutions. Finally, our numerical capability is demonstrated on a relevant magnetotullerics application. Our numerical results are validated through field measurements and geophysical insight.

8.3. MATHEMATICAL FORMULATION

The formulation that follows consists of multiple steps. We start by motivating the fractional derivative operator in the context of geophysical electromagnetics and define Ohm's constitutive law in terms of a fractional space derivative, later moving that derivative to the Laplacian term of the Helmholtz PDE. Given a fractional Helmholtz equation with non-zero boundary conditions, a two-equation decomposition provides a grouping of boundary conditions, source terms, and fractional operators that allow for convenient solution strategies. One equation with non-homogeneous boundary conditions is transformed to non-fractional form by deriving the "very weak form" so that standard solution techniques can be applied. For the remaining equation with a fractional Laplacian and homogeneous boundary conditions, we appeal to a spectral representation and resolvent formalism whereby the fractional Laplacian is transformed to a summation of standard Laplacians using a Dunford–type integral with appropriate quadrature. The solution to the final system of equations is detailed in section (8.4, Mathematical Formulation) in which a finite element discretization of both equations results in a large and dense coefficient matrix that requires further manipulation to achieve efficient solution performance.

We start with Faraday's law in the frequency domain with the Fourier convention of time derivatives ∂_t mapping to the frequency domain ω as $\partial_t \mapsto \mathrm{i}\omega$ and assuming constant magnetic permeability $\mu_0 = 4\pi \times 10^{-7}$ H/m:

$$\nabla \times \mathbf{E} = -\mathrm{i}\omega\mu_0\mathbf{H}, \tag{8.1}$$

relating the curl of electric field $\mathbf{E}$ to time variations in magnetic field $\mathbf{H}$. Paired with this is Ampère's Law, $\nabla \times \mathbf{H} = \mathbf{J}$, where $\mathbf{J}$ is the total electric current density – the sum of Ohmic currents, Maxwell's displacement current $\mathrm{i}\omega\varepsilon\mathbf{E}$, and, any impressed external currents due to natural sources or engineered antennas. Typically, for simple linear, isotropic materials the Ohmic currents are described by the product of electrical conductivity σ and electric field and at suffiently low frequencies $\sigma >> \omega\varepsilon$ Maxwell's displacement current can safely be ignored. In a similar fashion as Caputo (2000), where he replaced the permeability in Darcy's equation with a

time–fractional derivative, we replace the simple conductivity/field product in Ohm's law with a space–fractional derivative. Preserving the symmetry of both positive and negative power law jumps in the z direction for a two–sided stable diffusion process requires both positive and negative fractional derivatives (Meerschaert and Sikorskii, 2012, p15) $\mathscr{D}_z^\alpha = \frac{1}{2\cos\left(\frac{1}{2}\pi\alpha\right)}\left(\frac{\partial^\alpha}{\partial z^\alpha} + \frac{\partial^\alpha}{\partial(-z)^\alpha}\right)$ which we normalize by the factor $\cos\left(\frac{1}{2}\pi\alpha\right)$ to preserve magnitude invariance under α. As a consequence, the space–Fourier transform for this operator maps to the wavenumber ν domain as $D_z^\alpha \mapsto |\nu|^\alpha$. Note that had a one–sided derivative with Fourier mapping $(\pm \mathrm{i}\nu)^\alpha$ been used, the unit–magnitude prefactor $(\pm\mathrm{i})^\alpha$ could be interpreted as rotating the electrical conductivity into the complex plane, effectively reintroducing the Maxwell displacement current and turning the Maxwell derivation into a mixed diffusion/wave propagation problem rather than a strictly diffusive one. Unlike Caputo's attempt to emulate memory effects in permeability, our hypothesis is that certain non-local conductivity properties create superdiffusive behavior and can be represented by a spatial fractional derivative. With this fractional Ohm's law in the low–frequency limit (and no external sources) inserted into Ampère's law, the curl of Eq (8.1) is thereby:

$$\nabla \times \nabla \times \mathbf{E} = -\mathrm{i}\omega\mu_0 \mathscr{D}_z^\alpha \left[\sigma_{\alpha,z}\mathbf{E}\right], \tag{8.2}$$

where $\mathscr{D}_z^\alpha$ is the α–order fractional derivative in the z direction and $\sigma_{\alpha,z}$ is the electrical conductivity in units of S/m$^{1-\alpha}$. For an Earth model whose conductivity varies only as a function of vertical coordinate z, subject to a vertically incident electric field oriented in the horizontal x direction, the electric fields in the Earth are everywhere horizontal such that $\mathbf{E} = \hat{x}\,u(z)$ is the primary state variable that needs further consideration. Furthermore, for dimensional consistency in the fractional calculus methodology described in the following section, we non–dimensionalize with respect to the z coordinate such that $z \mapsto \zeta = z/z^*$ to arrive at

$$-\frac{\mathrm{d}^2 u}{\mathrm{d}\zeta^2}\left(\frac{1}{z^*}\right)^2 + \mathrm{i}\omega\mu_0 \mathscr{D}_\zeta^\alpha \left[\sigma_{\alpha,\zeta}\, u(\zeta)\right] = 0 \tag{8.3}$$

which, after action by $\mathscr{D}_\zeta^{-\alpha}$ and generalization to 3D, becomes

$$\left(-\Delta_\zeta\right)^s u + \mathrm{i}\kappa^2 u(\zeta) = 0, \tag{8.4}$$

where $\left(-\Delta_\zeta\right)^s$ is the fractional–order Laplacian in dimensionless coordinate ζ, $s = 1 - \frac{1}{2}\alpha$ and κ^2 the dimensionless squared wavenumber $\omega\mu_0\sigma_{\alpha,\zeta}\,(z^*)^2$. Note that in Eq (8.3) the conductivity $\sigma_{\alpha,z}$ possesses fractional length dimensions to retain consistency with the fractional derivative operator $\mathscr{D}_z^\alpha$. However, through the non-dimensionalization process transforming Eq (8.3) to Eq (8.4) we see that the conductivity $\sigma_{\alpha,\zeta}$ reclaims its familiar, integer-ordered units of S/m, thus avoiding awkward, fractional–dimensioned conductivities reported elsewhere (Everett, 2009; Ge et al., 2015).

We observe that the fractional exponent is on the Laplacian term and in combination with the Helmholtz term motivate the challenge of a solution strategy. An additional complication is the need to incorporate non-trivial boundary conditions, such as special radiation or self-absorbing boundary conditions. We address these issues through the use of linear decomposition, a Dunford

type integral formulation and the very weak form for finite element discretizations. We write the generalized fractional–order Helmholtz equation as

$$\begin{aligned} (-\Delta)^s u - k^2 u &= f \quad \text{in } \Omega, \\ u &= g \quad \text{on } \Gamma, \end{aligned} \tag{8.5}$$

where $k^2 = -\mathrm{i}\kappa^2$ is introduced to simplify notation for our electromagnetic problem, but in fact, transcends this particular choice of physics, and $(-\Delta)^s$ is understood to be the spectral fractional Laplacian operator for non–zero Dirichlet boundary conditions

$$(-\Delta)^s u(\boldsymbol{x}) := \sum_{k=1}^{\infty} \left(\lambda_k^s \int_\Omega u\, \varphi_k \,\mathrm{d}\Omega + \lambda_k^{s-1} \int_\Gamma u\, \partial_n \varphi_k \,\mathrm{d}\Gamma \right) \varphi_k(\boldsymbol{x}), \tag{8.6}$$

where φ_k are the eigenfunctions of the Laplacian with corresponding eigenvalues λ_k (Antil et al., 2018b, Def. 2.3) and $\boldsymbol{x} \in \Omega$ is the coordinate of interest. Moreover, u is assumed to be sufficiently smooth. As it is customary in the PDE theory, we have stated this definition for smooth functions, however by standard density arguments it immediately extends to Sobolev spaces and we refer to Antil et al. (2018b) for details. In addition, we emphasize that when $u = 0$ on the boundary Γ, the definition above is simply the standard spectral fractional Laplacian $(-\Delta_0)^s$ with zero boundary conditions (i.e., no surface integral terms in Eq (8.6)). We will omit the subscript 0 when it is clear from the context.

Following this earlier work on fractional Poisson equation, we extend the basic approach to fractional Helmholtz and split u into two parts (a.k.a. "lift") thusly: Let v solve

$$\begin{aligned} (-\Delta)^s v - k^2 (v + w) &= f \quad \text{in } \Omega, \\ v &= 0 \quad \text{on } \Gamma, \end{aligned} \tag{8.7}$$

and let w solve

$$\begin{aligned} (-\Delta)^s w &= 0 \quad \text{in } \Omega, \\ w &= g \quad \text{on } \Gamma. \end{aligned} \tag{8.8}$$

Summing Eqs (8.7) and (8.8) it is evident that $u = v + w$. The presence of the homogeneous boundary condition on Eq (8.7) allows for a spectral representation of the Dirichlet fractional–power Laplacian operator. Furthermore, it has been shown Antil et al. (2018b) that solving Eq (8.8) is equivalent to solving the standard, integer–power Laplacian equation in the very–weak sense (c.f. Berggren, 2004; Lions and Magenes, 1972), which in the case of smooth g is simply the more–familiar weak sense. A simple algebraic manipulation of the spectral decomposition results in a Laplacian with integer exponents (see Theorem 4.1 and the subsequent proof in Antil et al. (2018b) for additional details). Hence, we may replace Eq (8.8) with the following:

$$\begin{aligned} (-\Delta) w &= 0 \quad \text{in } \Omega, \\ w &= g \quad \text{on } \Gamma, \end{aligned} \tag{8.9}$$

which, when solved simultaneously with Eq (8.7), yields the solution to the original Eq (8.5).

To solve Eq (8.7), we follow others (e.g. Bonito and Pasciak, 2015; Antil and Pfefferer, 2017) in

using spectral analysis of linear operators and resolvent formalism. Specifically, we start with the Kato (1960) definition of fractional powers for linear operators (Theorem 2 and supporting proof) and simplify by setting Kato's λ coefficient to zero. This definition due to Kato coincides with Eq (8.6) when the function values are zero on the boundary, as in this case the surface integral over Γ vanishes which is indeed the case in Eq (8.7). After a change of variable, the Kato definition results in a symmetric integral, which is approximated through quadrature as

$$\begin{aligned}(-\Delta)^{-s} &= \frac{\sin s\pi}{\pi}\int_{-\infty}^{\infty} e^{(1-s)y}\left(e^{y}-\Delta\right)^{-1}\,\mathrm{d}y,\\ &\approx \frac{\sin s\pi}{\pi} m \sum_{\ell=-N^-}^{N^+} e^{(1-s)y_\ell}\left(e^{y_\ell}-\Delta\right)^{-1},\end{aligned} \tag{8.10}$$

where the quadrature nodes are distributed uniformly as $y_l = m\ell$. Accuracy of the quadrature representation of this continuous integral is a function of the constants m, N^- and N^+ and has been shown to be exponentially convergent (Bonito and Pasciak, 2015). The constants are chosen such that the quadrature error is balanced with the error in the spatial discretization of Eq (8.7) (c.f. $w = 0$ case in Bonito and Pasciak, 2015). In the case of a finite element solution with linear nodal basis functions on the unit interval and node spacing h, they are

$$m = \frac{1}{\ln\frac{1}{h}}, \quad N^+ = \left\lceil \frac{\pi^2}{4sm^2} \right\rceil, \quad \text{and} \quad N^- = \left\lceil \frac{\pi^2}{4(1-s)m^2} \right\rceil. \tag{8.11}$$

The use of the "ceiling" operators $\lceil\cdot\rceil$ in Eq (8.11) ensure N^- N^+ are integer valued, as required.

We remark that in using Eq (8.10), we avoid the costly (and in many cases, inaccurate) precalculation of the eigenspectrum for the Laplacian over an arbitrary spatial domain Ω with Dirichlet condition $u|_\Gamma = g$. Even in cases where calculation of the eigenspectrum bears an acceptable computational cost, there still remains the outstanding question of just how much of the spectrum is required for computing the Laplacian by this method to acceptable accuracy. For these reasons, our Eq (8.10) is far more practical.

Rewriting Eq (8.7) as $v - (-\Delta)^{-s} k^2(v+w) = (-\Delta)^{-s} f$, we may write v as a Kato–style expansion

$$v = \frac{\sin s\pi}{\pi} m \sum_{\ell=-N^-}^{N^+} e^{(1-s)y_\ell} v_\ell \tag{8.12}$$

and equate each of the ℓ terms to arrive at the coupled equation

$$v_\ell - \left(e^{y_\ell}-\Delta\right)^{-1} k^2 (v+w) = \left(e^{y_\ell}-\Delta\right)^{-1} f, \tag{8.13}$$

or

$$\left(e^{y_\ell}-\Delta\right) v_\ell - k^2 (v+w) = f. \tag{8.14}$$

Observe that there are $N^- + N^+ + 1$ of these equations and that the ℓth equation fully couples the function v_ℓ into w and all remaining functions $v_{\ell'\neq\ell}$ of the expansion Eq (8.12). Enforcement of the modified boundary condition $v_\ell = 0$ guarantees enforcement of $v = 0$ via Eq (8.12). Hence,

with the inclusion of Eq (8.9), we have the complete differential problem statement consisting of a coupled system of $N^- + N^+ + 2$ equations with unknown functions $v_{N^-}, \ldots, v_{N^+}, w$ over the domain Ω.

8.4. NUMERICAL IMPLEMENTATION

The method of solution for Eqs (8.9) and (8.14) (including corresponding boundary conditions) is to first transform the differential problem statement into an equivalent variational problem statement for the appropriate infinite dimensional function spaces and then approximate its solution by the optimal one, in a Sobolev norm sense, taken from finite dimensional space of linear, nodal finite elements over some discretization. In doing so, we introduce the test function ξ_ℓ and construct the weak form of Eq (8.14) for all ℓ from $-N^-$ to N^+:

$$\int_\Omega \left(-\xi_\ell \Delta v_\ell + e^{y_\ell}\, \xi_\ell v_\ell - k^2\, \xi_\ell\, (v+w)\right) \mathrm{d}\Omega = \int_\Omega \xi_\ell f \,\mathrm{d}\Omega, \tag{8.15}$$

recalling that v is given by the expansion Eq (8.12). The test function ζ is used in the weak form of the Laplace equation (8.9) as,

$$\int_\Omega \nabla\zeta \cdot \nabla w \,\mathrm{d}\Omega = 0. \tag{8.16}$$

Combining the left hand sides of Eqs (8.15) and (8.16), the bilinear form $A(\cdot,\cdot)$ is therefore given as

$$\begin{aligned} A(\{\xi_\ell\}, \zeta; \{v_\ell\}, w) = \sum_{\ell=-N^-}^{N^+} \int_\Omega \left(\nabla\xi_\ell \cdot \nabla v_\ell + e^{y_\ell}\, \xi_\ell v_\ell - k^2\, \xi_\ell\, (v+w)\right) \mathrm{d}\Omega \\ + \int_\Omega \nabla\zeta \cdot \nabla w \,\mathrm{d}\Omega, \end{aligned} \tag{8.17}$$

the combined right hand sides are denoted as

$$F(\{\xi_\ell\}, \zeta) = \sum_{\ell=-N^-}^{N^+} \int_\Omega \xi_\ell f \,\mathrm{d}\Omega, \tag{8.18}$$

and v is understood to be expanded in terms of v_ℓ according to Eq (8.12). The variational problem statement equivalent to the differential problem statement in Eqs (8.9) and (8.14) is therefore: Find $\{v_\ell\} \in V_0; w \in V$, such that

$$A(\{\xi_\ell\}, \zeta; \{v_\ell\}, w) = F(\{\xi_\ell\}, \zeta) \quad \forall \{\xi_\ell\}, \zeta \in V_0, \tag{8.19}$$

where V is the space of L^2 functions on Ω with first order weak derivatives also in L^2 of Ω and inhomogeneous Dirichlet boundary conditions Eq (8.8), and $V_0 \subset V$ taking homogeneous boundary conditions as in Eq (8.7). The next step is to choose a finite–dimensional space $V_h \subset V$ from which the approximate solutions $v_h \approx v$ and $w_h \approx w$ will be drawn. To further simplify notation we will drop the h subscript and only re–introduce it as needed in relation to the true (weak) solutions v and w.

Let $\phi_1(\boldsymbol{x}), \phi_2(\boldsymbol{x}), \ldots, \phi_N(\boldsymbol{x})$ be the basis functions in V_h as a function of spatial coordinate $\boldsymbol{x}$, which in our implementation will be linear, nodal finite elements . We write in bold the column vector $\boldsymbol{\phi}$ of basis functions $(\phi_1, \phi_2, \ldots, \phi_N)^T$, and $\boldsymbol{v}_\ell = \left(v_\ell^1, v_\ell^2, \ldots, v_\ell^N\right)^T$. By construction, it follows that $v_\ell(\boldsymbol{x}) = \boldsymbol{\phi}^T \boldsymbol{v}_\ell = \sum_{i=1}^N \phi_i(\boldsymbol{x}) v_\ell^i$. Likewise, $\boldsymbol{\xi}_\ell = \left(\xi_\ell^1, \xi_\ell^2, \ldots, \xi_\ell^N\right)^T$ and $\boldsymbol{w} = (w_1, w_2, \ldots, w_N)^T$ yield $\xi_\ell = \boldsymbol{\xi}_\ell^T \boldsymbol{\phi}$ and $w = \boldsymbol{\phi}^T \boldsymbol{w}$, respectively. As such, construction of the linear system Eq (8.19) requires the following block matrices built by volume integration of the basis functions and their spatial derivatives:

$$\mathbf{K} = \int_\Omega (\nabla \boldsymbol{\phi})^T (\nabla \boldsymbol{\phi}) \, \mathrm{d}\Omega, \quad \mathbf{M}_1 = \int_\Omega \boldsymbol{\phi} \boldsymbol{\phi}^T \, \mathrm{d}\Omega, \quad \text{and} \quad \mathbf{M}_2 = -\int_\Omega k^2 \boldsymbol{\phi} \boldsymbol{\phi}^T \, \mathrm{d}\Omega \tag{8.20}$$

where the integrands are understood to be outer products, each yielding a symmetric matrix of dimension $N \times N$. To simplify notation, introduce the coefficients $c_\ell = e^{y_{\ell-N^-}}$ and $d_\ell = \frac{1}{\pi}(\sin s\pi)\, m\, e^{(1-s)y_{\ell-N^-}}$, matrix $\mathbf{A}_\ell = \mathbf{K} + c_\ell \mathbf{M}_1 + d_\ell \mathbf{M}_2$, and sum $L = N^- + N^+$ so that we may compactly write $A(\{\xi_\ell\}, \zeta; \{v_\ell\}, w)$ as

$$\left(\boldsymbol{\xi}_{-N^-}^T \cdots \boldsymbol{\xi}_{N^+}^T \, \boldsymbol{\zeta}^T\right) \begin{pmatrix} \mathbf{A}_0 & d_1\mathbf{M}_2 & d_2\mathbf{M}_2 & \cdots & d_L\mathbf{M}_2 & \mathbf{M}_2 \\ d_0\mathbf{M}_2 & \mathbf{A}_1 & d_2\mathbf{M}_2 & \cdots & d_L\mathbf{M}_2 & \mathbf{M}_2 \\ d_0\mathbf{M}_2 & d_1\mathbf{M}_2 & \mathbf{A}_2 & \cdots & d_L\mathbf{M}_2 & \mathbf{M}_2 \\ \vdots & \vdots & \vdots & \ddots & \vdots & \vdots \\ d_0\mathbf{M}_2 & d_1\mathbf{M}_2 & d_2\mathbf{M}_2 & \cdots & \mathbf{A}_L & \mathbf{M}_2 \\ \mathbf{0} & \mathbf{0} & \mathbf{0} & \cdots & \mathbf{0} & \mathbf{K} \end{pmatrix} \begin{pmatrix} \boldsymbol{v}_{-N^-} \\ \boldsymbol{v}_{1-N^-} \\ \boldsymbol{v}_{2-N^-} \\ \vdots \\ \boldsymbol{v}_{N^+} \\ \boldsymbol{w} \end{pmatrix}. \tag{8.21}$$

Lastly, the right hand side of Eq (8.19) follows as

$$\left(\boldsymbol{\xi}_{-N^-}^T \cdots \boldsymbol{\xi}_{N^+}^T \, \boldsymbol{\zeta}^T\right) \begin{pmatrix} \boldsymbol{f} \\ \boldsymbol{f} \\ \boldsymbol{f} \\ \vdots \\ \boldsymbol{f} \\ \mathbf{0} \end{pmatrix} \tag{8.22}$$

with column vector $\boldsymbol{f} = \int_\Omega \boldsymbol{\phi} f \, \mathrm{d}\Omega$. In equating Eq (8.21) with Eq (8.22) as required by the variational problem statement Eq (8.19), we see that the coefficient vector $\left(\boldsymbol{\xi}_{-N^-}^T \cdots \boldsymbol{\xi}_{N^+}^T \, \boldsymbol{\zeta}^T\right)$ is common to both the left and right hand sides, and may therefore be divided out, thus leaving a $N(L+2) \times N(L+2)$ system of linear equations for the unknown coefficients $\left(\boldsymbol{v}_{-N^-}^T \cdots \boldsymbol{v}_{N^+}^T \, \boldsymbol{w}^T\right)$ which holds for all functions $\{\xi_\ell\}, \zeta \in V_h$. Upon solution of the linear system, aggregation of the coefficient vectors $\boldsymbol{v}_\ell$ according to Eq (8.12) plus the vector $\boldsymbol{w}$ completes the sum $v + w$, which we recognize as the discrete, approximate solution to the original differential equation (8.5).

Because the matrix in Eq (8.21) is complex–valued, large and nonsymmetric, the solution strategy for the linear system equating Eq (8.21) and Eq (8.22) must be carefully chosen for scalability and economy of compute resources. As such, we solve this linear system using stabilized bi-conjugate gradients (van der Vorst, 1992): The algorithm is easily parallelizable; has a

minimum number of working vectors; and requires only two matrix–vector products per iterative step. The latter is especially important for reducing computational resource burdens because these products can be computed cheaply and quickly "on the fly" as needed and without explicit storage of entire system matrix. Notice, however, that the matrix in Eq (8.17) is block dense and a large number of floating point operations is required for a single matrix–vector multiply – operations which may significantly increase the time required to perform the multiplications. To remedy this, we modify the variational formulation Eq (8.19) to include the function v in addition to the vectors v_ℓ and w, and augment $A(\cdot)$ by weak enforcement of the compatibility expansion Eq (8.12) between vectors $\boldsymbol{v}_\ell$ and $\boldsymbol{v}$. That is, in addition to $\{v_\ell\}$ and w, we introduce the additional unknown v and find $\{v_\ell\}, w$ and v such that

$$\tilde{A}(\{\xi_\ell\},\zeta,\eta;\{v_\ell\},w,v) = \tilde{F}(\{\xi_\ell\},\zeta,\eta) \quad \forall \{\xi_\ell\},\zeta, \text{ and } \eta, \tag{8.23}$$

where

$$\begin{aligned}\tilde{A}(\{\xi_\ell\},\zeta,\eta;\{v_\ell\},w,v) = \\ \sum_{\ell=N^-}^{N^+} \int_\Omega \left(\nabla\xi_\ell\cdot\nabla v_\ell + e^{y_\ell}\,\xi_\ell v_\ell - k^2\,\xi_\ell\,(v+w) + \nabla\zeta\cdot\nabla w\right) \mathrm{d}\Omega \\ - \frac{\sin s\pi}{\pi} m \sum_{\ell=-N^-}^{N^+} e^{(1-s)y_\ell} \int_\Omega \eta\, v_\ell \,\mathrm{d}\Omega \quad + \quad \int_\Omega \eta\, v\,\mathrm{d}\Omega\end{aligned} \tag{8.24}$$

and

$$\tilde{F}(\{\xi_\ell\},\zeta,\eta) = \sum_{\ell=N^-}^{N^+} \int_\Omega \xi_\ell f \,\mathrm{d}\Omega. \tag{8.25}$$

The resulting sparse linear system is thus,

$$\begin{pmatrix} \tilde{\mathbf{A}}_0 & \mathbf{0} & \cdots & \cdots & \mathbf{0} & \mathbf{M}_2 & \mathbf{M}_2 \\ \mathbf{0} & \tilde{\mathbf{A}}_1 & \mathbf{0} & \cdots & \mathbf{0} & \mathbf{M}_2 & \mathbf{M}_2 \\ \vdots & & \ddots & & \vdots & \mathbf{M}_2 & \mathbf{M}_2 \\ \mathbf{0} & \cdots & \mathbf{0} & \tilde{\mathbf{A}}_{L-1} & \mathbf{0} & \mathbf{M}_2 & \mathbf{M}_2 \\ \mathbf{0} & \cdots & \cdots & \mathbf{0} & \tilde{\mathbf{A}}_L & \mathbf{M}_2 & \mathbf{M}_2 \\ \mathbf{0} & \cdots & \cdots & \cdots & \mathbf{0} & \mathbf{K} & \mathbf{0} \\ -d_0\mathbf{M}_1 & \cdots & \cdots & \cdots & -d_L\mathbf{M}_1 & \mathbf{0} & \mathbf{M}_1 \end{pmatrix} \begin{pmatrix} \boldsymbol{v}_{-N^-} \\ \boldsymbol{v}_{1-N^-} \\ \boldsymbol{v}_{2-N^-} \\ \vdots \\ \boldsymbol{v}_{N^+} \\ \boldsymbol{w} \\ \boldsymbol{v} \end{pmatrix} = \begin{pmatrix} \boldsymbol{f} \\ \boldsymbol{f} \\ \boldsymbol{f} \\ \vdots \\ \boldsymbol{f} \\ \mathbf{0} \\ \mathbf{0} \end{pmatrix} \tag{8.26}$$

with $\tilde{\mathbf{A}}_\ell = \mathbf{K} + c_\ell \mathbf{M}_1$. We refer to the sparsified system of linear equations in Eq (8.26) as the *v-formulation* for the discretized, variational form of original differential equation (8.5). Inspection of the prefactors d_ℓ from the Kato expansion, however, suggests that their exponential decay with respect to ℓ may lead to ill-conditioning of the coefficient matrix in Eq (8.26) by their

presence in the last block–row. As such, we recast Eq (8.26) as the *scaled v-formulation*:

$$\begin{pmatrix} \tilde{\mathbf{A}}'_0 & \mathbf{0} & \cdots & \cdots & \mathbf{0} & \mathbf{M}_2 & \mathbf{M}_2 \\ \mathbf{0} & \tilde{\mathbf{A}}'_1 & \mathbf{0} & \cdots & \mathbf{0} & \mathbf{M}_2 & \mathbf{M}_2 \\ \vdots & & \ddots & & \vdots & \mathbf{M}_2 & \mathbf{M}_2 \\ \mathbf{0} & \cdots & \mathbf{0} & \tilde{\mathbf{A}}'_{L-1} & \mathbf{0} & \mathbf{M}_2 & \mathbf{M}_2 \\ \mathbf{0} & \cdots & \cdots & \mathbf{0} & \tilde{\mathbf{A}}'_L & \mathbf{M}_2 & \mathbf{M}_2 \\ \mathbf{0} & \cdots & \cdots & \cdots & \mathbf{0} & \mathbf{K} & \mathbf{0} \\ -\mathbf{M}_1 & \cdots & \cdots & \cdots & -\mathbf{M}_1 & \mathbf{0} & \mathbf{M}_1 \end{pmatrix} \begin{pmatrix} \boldsymbol{v}'_{-N^-} \\ \boldsymbol{v}'_{1-N^-} \\ \boldsymbol{v}'_{2-N^-} \\ \vdots \\ \boldsymbol{v}'_{N^+} \\ \boldsymbol{w} \\ \boldsymbol{v} \end{pmatrix} = \begin{pmatrix} \boldsymbol{f} \\ \boldsymbol{f} \\ \boldsymbol{f} \\ \vdots \\ \boldsymbol{f} \\ \mathbf{0} \\ \mathbf{0} \end{pmatrix} \tag{8.27}$$

with $\tilde{\mathbf{A}}'_\ell = (\mathbf{K} + c_\ell \mathbf{M}_1)/d_\ell$ and $\boldsymbol{v}'_\ell = \boldsymbol{v}_\ell d_{\ell+N^-}$. In the scaled system Eq (8.27), the Kato scale factors d_ℓ are implicit in the unknown vectors $\boldsymbol{v}'_\ell$ and act within block diagonal matrices $\tilde{\boldsymbol{A}}'_\ell$ alone.

As a closing remark on the theory and algorithms just described, observe that in Eqs (8.9), (8.26) and (8.27) the solution of the scalar Laplacian equation for w is fully decoupled from the solution for v and v_ℓ. Hence, one option for solving the full system of equations is a two–step procedure, where first the solution for w is obtained, and then used as a sourcing term for the remaining v_ℓ equations. We have, instead, chosen to solve the full system simultaneously. This has some advantages. First, in looking ahead to the implementation of Robin boundary conditions (e.g. a Sommerfeld radiation condition), we anticipate that the Laplacian equations will couple directly into the v (or, equivalently, v_ℓ) equations, which would consequently eliminate the convenience of solving for w a priori. We wish this coupling to modify our existing algorithm/code structure as little as possible and therefore retain the Laplacian equation for w in the full system matrix. Second, including the Laplacian comes at an increased cost of only N degrees of freedom on top of the existing cost of LN for the v_ℓ equations. Because L is typically on the order of 100 or more for adequately refined meshes (Figure 8-1), this added cost is objectively minimal. Lastly, looking further ahead toward PDE constrained optimization where we might invert for s or $\sigma_{\alpha,\zeta}$, or for the design problem (e.g. optimal sensor sensor placement), it is more convenient to create and solve for the corresponding adjoint objects.

8.4.1. Non–locality of the fractional Laplacian operator

We next provide insight as to why equations (8.10), (8.6) are nonlocal operators. As pointed out in Song and Vondraček (2008); Caffarelli and Stinga (2016); Antil et al. (2017) and Antil and Warma (2019), the spectral fractional Laplacian with zero boundary conditions can be equivalently written as:

$$(-\Delta_0)^s u(\boldsymbol{x}) = \int_\Omega (u(\boldsymbol{x}) - u(\boldsymbol{x}'))\mathscr{K}_s(\boldsymbol{x},\boldsymbol{x}')\,\mathrm{d}\Omega' + u(\boldsymbol{x})B_s(\boldsymbol{x}) \tag{8.28}$$

where $\mathscr{K}_s$ and B_s are appropriate Kernel functions. One can see from the equivalent definition that, in order to evaluate $(-\Delta_0)^s u$ at a point $\boldsymbol{x} \in \Omega$, we need information about u on the entire domain Ω, thus making $(-\Delta_0)^s$ a nonlocal operator. Moreover, let $\mathscr{O}$ be an open set contained in

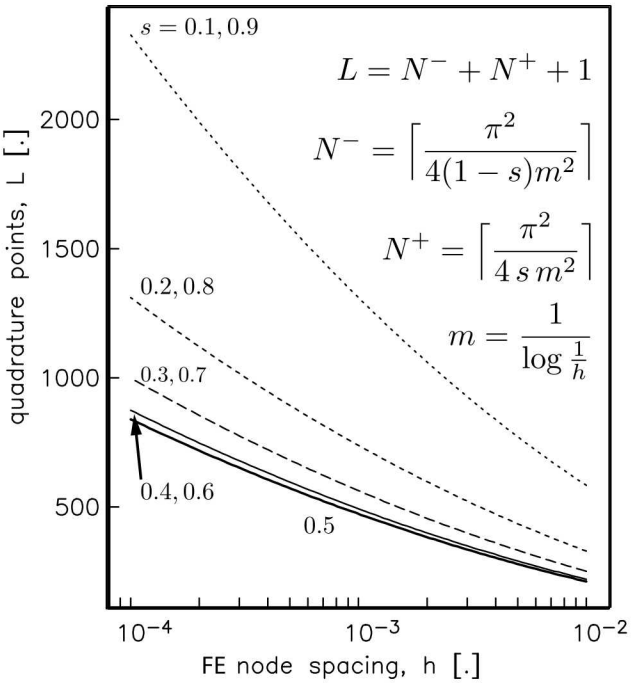

Figure 8-1. Total number of quadrature points L as a function of Laplacian exponent s and node spacing h. Sinc quadrature summation is over the range of indices $\ell = -N^-, \ldots, N^+$.

Ω such that $u \equiv 0$ on $\mathscr{O}$. Then a classical Laplacian implies $-\Delta u(\boldsymbol{x}) = 0$ for all $\boldsymbol{x} \in \Omega$. However, this is not the case when we deal with $(-\Delta_0)^s$. Indeed, let $\boldsymbol{x} \in \mathscr{O}$ and let use the equivalent definition Eq (8.28), since $u \equiv 0$ on $\mathscr{O}$, we obtain that

$$\begin{aligned}(-\Delta_0)^s u(\boldsymbol{x}) &= \int_\Omega \big(u(\boldsymbol{x}) - u(\boldsymbol{x}')\big)\, \mathscr{K}_s(\boldsymbol{x},\boldsymbol{x}')\mathrm{d}\Omega' \\ &= \int_{\mathscr{O}} \big(u(\boldsymbol{x}) - u(\boldsymbol{x}')\big)\, \mathscr{K}_s(\boldsymbol{x},\boldsymbol{x}')\,\mathrm{d}\Omega' + \int_{\Omega\setminus\mathscr{O}} \big(-u(\boldsymbol{x}')\big)\, \mathscr{K}_s(\boldsymbol{x},\boldsymbol{x}')\,\mathrm{d}\Omega' \\ &= \int_{\Omega\setminus\mathscr{O}} \big(-u(\boldsymbol{x}')\big)\, \mathscr{K}_s(\boldsymbol{x},\boldsymbol{x}')\,\mathrm{d}\Omega' \end{aligned} \tag{8.29}$$

which is not necessarily zero. This is unlike the local case.

8.5. NUMERICAL VERIFICATION

To verify the implementation of the fractional Helmholtz equations with inhomogeneous Dirichlet boundary conditions we adopt the Method of Manufactured Solutions (MMS) (Roache, 1998; Salar and Knupp, 2000). In the MMS method, a proposed solution is substituted into the governing differential equation, after which the corresponding boundary conditions and sourcing functions are derived. Upon discretization, the recovered numerical solution is then compared to the known analytical solution. The MMS solution used here over the interval $x \in [0,1]$ takes the

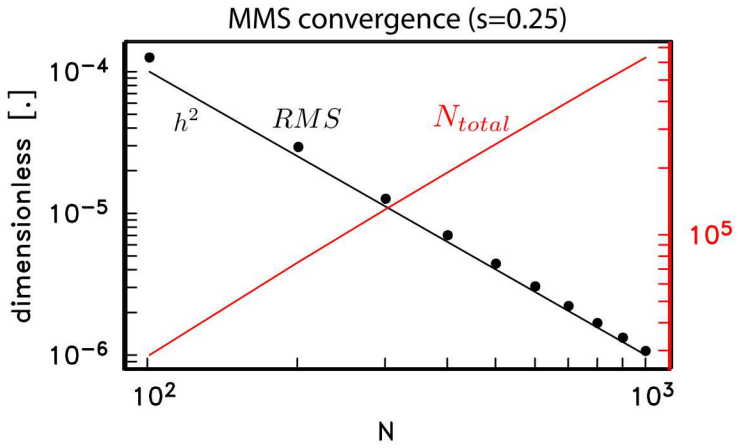

Figure 8-2. Convergence of MMS solution $u = \sin(2\pi x) + 1$ for $s = 0.25$ as a function of mesh size N with corresponding node spacing $(N-1)^{-1}$. In symbols is the RMS residual; black lines, the curve h^2; and in red, the total number of degrees of freedom in the discretized linear system (8.27). Linear system (8.27) is solved using BiCG-STAB to a tolerance of 10^{-16} in RHS-normalized residual.

following form: $v = \sin(2\pi x), w = 1 \mapsto u = 1 + \sin(2\pi x)$. Inspection of Eq (8.9) results in setting $g(0) = g(1) = 1$, whereas recognizing that $\sin(2\pi x)$ is an eigenfunction for homogeneous $(-\Delta)^s$ results in $f = \left((2\pi)^s - k^2\right)\sin(2\pi x) - k^2$ according to Eq (8.7). Hence, we have constructed for arbitrary s the requisite source terms and boundary conditions for our posited solution u solving an inhomogeneous fractional Helmholtz with non-zero Dirichlet boundary conditions. Note that MMS solution u is independent of both s and k and is thus powerful test of fractional Helmholtz algorithm.

Numerical evaluation of the MMS problem just described is done using linear, nodal finite elements with uniform node spacing for the case of $s = 0.25$ and k arbitrarily set to unity. Linear system Eq (8.27) is solved to high accuracy using the stabilized bi-conjugate gradient van der Vorst (1992) iterative scheme with simple Jacobi scaling to a tolerance of 10^{-16} reduction in normalized residual. Over the range of node spacing $0.001 \leq h \leq 0.01$ the MMS solution shows the expected h^2 convergence in error between the recovered finite element and known analytic solutions (Figure 8-2) in $L^2(\Omega)$-norm. For reference, the size N_{total} of the linear system Eq (8.27) grows roughly as $N^{1.4}$ over the corresponding range in h, resulting, for example, in $L = 629$ quadrature points for $N = 1001$ finite element nodes and a total of $N_{total} = 631631$ unknowns in the linear system Eq (8.27). Convergence of the bi–conjugate gradient residual error as a function of iteration count (Figure 8-3) is generally well behaved, with only minor localized excursions from monotonicity. Furthermore, the error in simultaneously solving each of the three sets of coupled equations – fractional Helmholtz for v_ℓ; Laplacian for w; and, compatibility between v and v_ℓ – decreases synchronously with iteration count, with error for the compatibility equation approximately a factor 100 less than the error for the remaining two.

Lastly, we confirm that the choice $m = 1/\log\frac{1}{h}$ for quadrature spacing (and by extension, the

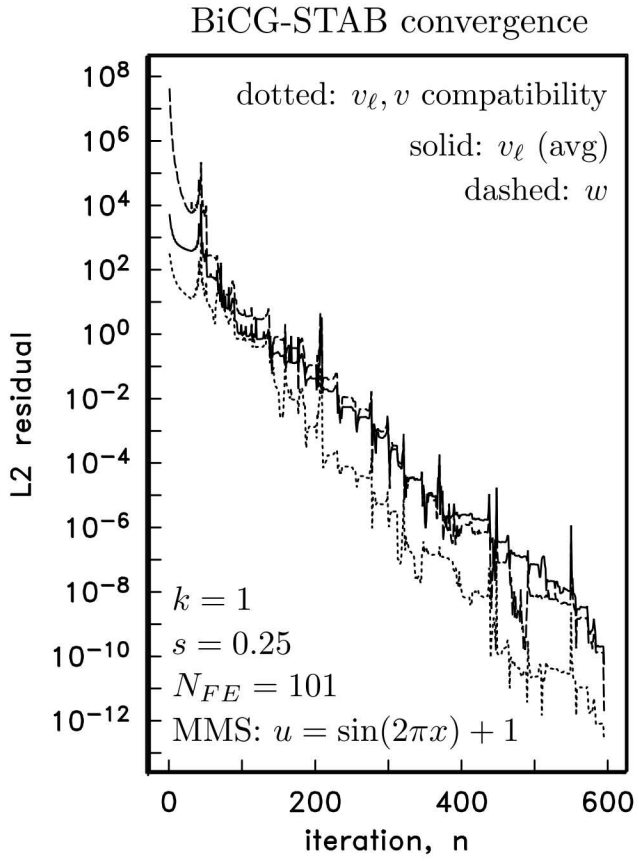

Figure 8-3. Convergence of BiCG-STAB algorithm with Jacobi preconditioning for the $N = 101$ MMS solution in Figure 1. In the solid line is the average residual for equations in blocks $0, \ldots, L$ in (8.27) corresponding to fractional Helmholtz equations on v_ℓ; dashed, the residual for equations in block $L+1$ corresponding to solution of the Laplace equation for w; and dotted, the residual for the final $(L+2)$ block of equations enforcing compatibility between v and v_ℓ.

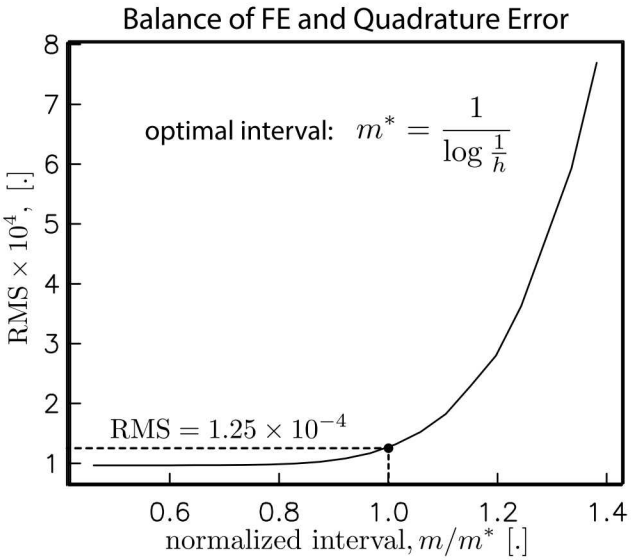

Figure 8-4. Convergence of RMS error as a function of quadrature spacing m for the MMS problem with $N = 101, h = 0.01$ finite element nodes (see Figure 2). Optimal quadrature interval m^* is given by (8.11) yields RMS $= 1.25 \times 10^{-4}$, a value close to the asymptotic limit when $m < m^*$. Note the rapidly increasing RMS error as $m^* < m$.

number L of v_ℓ equations) is nearly optimal by examining the effect on RMS of varying m. As a representative example, the $N = 101, s = 0.25$ discretization of the MMS problem is solved for a range of m values around $1/\log\frac{1}{h}$. In this example the asymptotic limit for minimum RMS value is achieved at m roughly 90% of its optimal value, where the asymptotic limit is driven by the error of the finite element discretization itself (Figure 8-4). In contrast, choices of m larger than the optimal value result in a rapidly increasing RMS, consistent with the exponential convergence of quadrature error reported elsewhere (Bonito and Pasciak, 2015).

8.6. NUMERICAL RESULTS

Our fractional Helmholtz system is numerically demonstrated in the context of magnetotellurics (MT). This is a geophysical surveying method that measures naturally occurring, time-varying magnetic and electric fields. Resistivity estimates of the subsurface can be inferred from the very near surface to hundreds of kilometers that are applied to subsurface characterization for myriad, broad–reaching geoscience applications such as hydrocarbon extraction, geothermal energy harvesting and carbon sequestration, as well as studies into Earth's deep tectonic history. The MT signal is caused by the interaction of the solar wind with the earth's magnetic field (lower frequencies less than 1 Hz) and world-wide thunderstorms, usually near the equator (higher frequencies greater than 1 Hz). Figure 8-5 provides a conceptual diagram of MT in which an idealized ionospheric "sheet current" is the electromagnetic source (see Section 2) for inducing

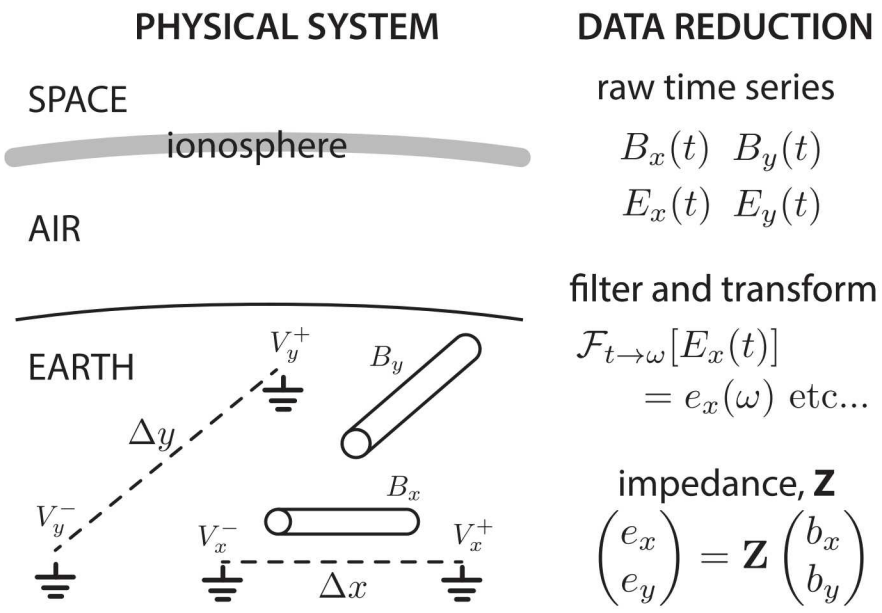

Figure 8-5. Overview of magnetotelluric experiment and data reduction. (left) Collocated time series of horizontal electric field, measured by pairs of grounded electrodes, and magnetic field, measured by induction coils or fluxgates, measure Earth's inductive response to ionspheric source currents. (right) Time series are windowed, filtered and transformed into the frequency domain, from which the impedance tensor is estimated, containing information on the distribution of electricical conductivity variations in Earth's subsurface (Chave and Jones, 2012). Because high–frequency fields decay more rapidly with depth than low frequency fields, frequency can loosely be interpreted as a proxy for depth, and hence an impedance spectrum is a coarse measure of the local, depth variations in electrical conductivity.

secondary electromagnet eddy currents in the subsurface. Because, in practice, the magnitude of this source current is unknown, the fundamental quantity for MT analysis is the impedance tensor mapping electric correlated electric and magentic fields. Computed in the frequency domain, the impedance tensor is an estimate of the Earth "filter" mapping magnetic to electric fields – in other words, it is an expression of Earth's conductivity distribution. Common in preliminary MT analysis is the assumption of locally 1D (depth dependent) electrical structure and excitation by a vertically incident plane wave, such as described in Section 2. We adopt these modest assumptions in our investigation of MT data – in particular, data collected by the decadal, trans–continental USArray/EarthScope project – and find examples where MT data are consistent with predicted impedances for a fractionally–diffusing electromagnetic Earth.

Because of the novelty in applying fractional derivative concepts to electromagnetic geophysics, the first question that draws our attention is simply: How does a fractionally diffusing field, as described by Eqs (8.3) and (8.4), compare to a field derived from the classical Helmholtz

equation? To address this question we solve (8.4) on the dimensionless unit interval $\zeta \in [0,1]$ with unit amplitude Dirichlet conditions $u(0) = \sqrt{2}\mathrm{i}$ and $u(1) = 0$ on the horizontal electric field and choose the dimensioned scaling factor $z^* = 1000$ m to represent the physical domain $z \in [0,1000]$ m. Choice of homogeneous Dirichlet condition at $\zeta = 1$ is commonly known as "perfectly conducting" boundary condition, representing the presence of an infinitely conductive region for $\zeta > 1$, but is used here strictly out of computational convenience. Scattering from this interface back to Earth's surface $\zeta = 0$ will be negligible as long as the frequency ω in Eq (8.4) is sufficiently high that the electric field at depth is essentially zero. The unit interval is discretized with 501 evenly distributed nodes, on which the electric field is drawn from the finite dimensional vector space of linear nodal finite elements. Hence, node spacing is $h = 0.002$, which, when $s = 0.7$ for example, leads to $N^- = 318$ and $N^+ = 137$ according to Eq (8.11) and a linear system Eq (8.27) with $501(3 + N^- + N^+) = 229458$ equations. Comparable to the error tolerances on the BiCG-STAB solver specified previously for the MMS problem, the iterative sequence is terminated once the normalized residual is reduced by 10^{-12} over its starting value.

The horizontal electric fields in Figure 8-6 show depth–dependent behavior that is clearly also s-dependent: increased curvature in the near–surface and decreased curvature at depth in comparison with their classical $s = 1.0$ counterpart. This suggests that the effect of the fractional Laplacian in Eqs (8.3) and (8.4) over a uniform $\sigma_{\alpha,\zeta}$ Earth model is, at first blush, in some ways similar to that of a classical Laplacian over a layered Earth which is conductive in the near surface and resistive at depth. However, closer inspection of the fractional response (see, for example the $s = 0.60$ curves) reveals that the damped oscillations, characteristic of classical Helmholtz, are simply not present as s decreases from unity, and instead then are replaced with a steady non–oscillatory decay with depth.

There is a dramatic manifestation of this fractional Helmholtz response in observable magnetotelluric data through calculation of the impedance spectrum (Figure 8-7). Amplitude of the impedance spectrum, reported here as the familiar apparent resistivity

$$\rho_a = \frac{1}{\omega\mu_0}\left|\frac{E_x}{H_y}\right|^2_{z=0} = \omega\mu_0(z^*)^2\left|\frac{u}{\partial_\zeta u}\right|^2_{\zeta=0} \tag{8.30}$$

and complex phase angle θ of the ratio $-u/\partial_\zeta u$, show a clear s–dependence at frequencies above 1 Hz (Figure 8-7). Decay of the apparent resistivity as frequency approaches zero can be understood as a consequence of the perfect electric conductor boundary condition at $z = z*$, where at these low frequencies the reciprocal wavenumber $\frac{1}{\kappa} >> z^*$ and hence the apparent resistivity approaches that of the perfect conductor, zero, in the region $z > z^*$. Furthermore, in the limit of zero frequency, the fractional Helmholtz equation asymptotes to the fractional Laplacian equation (analagous to Eq (8.8)) with inhomogeneous Dirichlet boundary conditions, whose solution has already been established Antil et al. (2018b) as equivalent to the classical Laplacian equation, leaving the ratio $-u/\partial_\zeta u = 1$, or equivalently $\theta = 0$.

The decrease in apparent resistivity at high frequencies when $s \neq 1$ can further be understood by examination of the electric field gradient at $z = 0$ (Figure 8-8). Although there is a slight decrease in the vertical gradient of the imaginary component of electric field when $s \neq 1$, the magnitude of the real component increases dramatically in comparison to the $s = 1$ case. This overall rise in

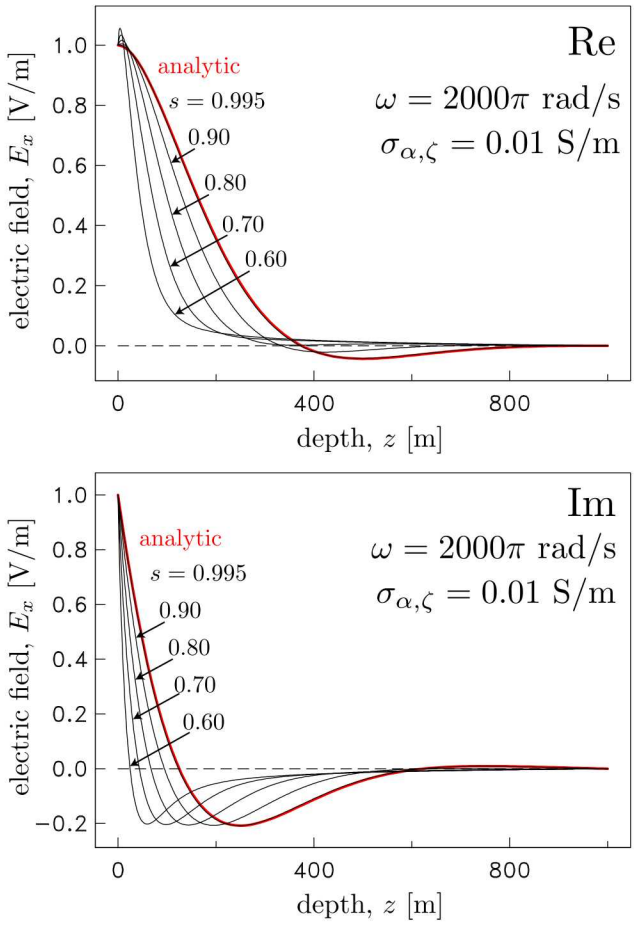

Figure 8-6. For a range of fractional exponent values $s = 0.6, 0.7, 0.8, 0.9, 0.995$, decay of unit–amplitude real (top) imaginary (bottom) components of horizontal electric field $E_x = u$ as a function of depth z into a uniform $\sigma_{\alpha,\zeta} = 0.01$ S/m medium at frequency $f = 1$ kHz, corresponding to dimensionless wavenumber $\kappa \approx 8.89$. In red is the analytic solution for the corresponding classical $s = 1$ Helmholtz. See text for additional details on boundary conditions and scaling to the physical domain from the dimensionless unit interval.

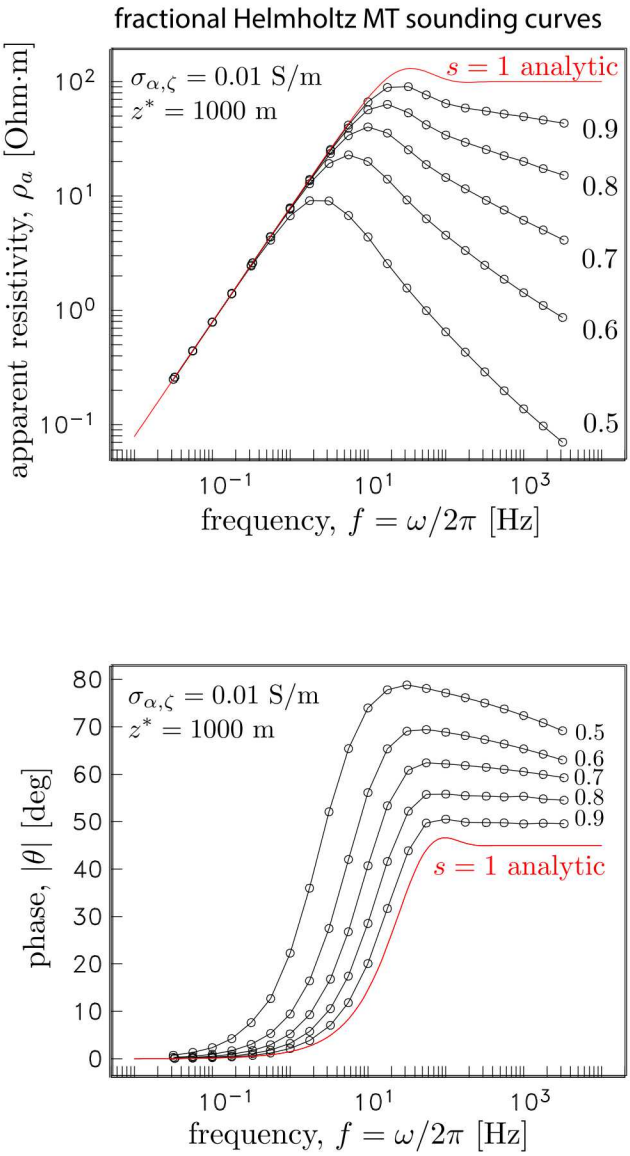

Figure 8-7. Magnetotelluric sounding curves for a uniform $\sigma_{\alpha,\zeta}$ Earth model over the depth domain $z \in [0, z^*]$ for a range of fractional exponent values $s = 0.5, \ldots, 1.0$ with a perfect conductor boundary condition at $z = z^*$. Apparent resistivity (top); complex phase (bottom). See text for description. In red are the classical $s = 1$ Helmholtz solutions, computed analytically.

vertical gradient at the air/earth interface for a fractional Earth model decreases the value of the quotient in Eq (8.30), thereby leading to a decreased estimate of the apparent resistivity at large frequencies.

8.6.1. Validation through USArray data

We have made progress towards validating our hypothesis of "fractional Helmholtz leading to new geophysical interpretation" though geophysical insight of numerical experiments. These numerical results suggest that a *uniform* subsurface subject to superdiffusing electromagnetic plane waves exhibits a high apparent conductivity in the near surface while appearing more resisistive at depth (Figure 8-7). This is consistent with actual field data observed in the mid–continent of the USArray footprint. In these data, apparent resistivity and phase angle spectra from USArray MT station for KSP34 located NW of Kansas City, KS, USA are consistent the non-local behavior as our numerical experiments (Figure 8-9). An in-depth study of the geology in the Kansas City region would futher endorse our observations but is beyond the scope of this paper. These field data correlations however provide further motivation to support additional algorithmic development for fractional electromagnetics.

8.6.2. Strategies for a spatially–variable fractional exponent

An initial assumption in problem statement Eq (8.5) is the spatial invariance of the fractional exponent s over the spatial domain Ω. However, if s is intepreted to represent via non–locality some degree of long–range correlation of underlying material properties (e.g. electrical conductivity), then it is relevant to consider how spatial variability in this correlation is accommodated in the architecture of the fractional calculus paradigm. In addition, variability in s enables us to truly capture the non-smooth effects such as fractures by prescribing variable degree of smoothness across the scales. A detailed analysis for variable s, where the authors have created a time-cylinder based approach, has been recently carried out in Antil and Rautenberg (2018). For a precise definition of the fractional Laplacian with variable s we refer to Antil et al. (2018a).

In the case of a piecewise constant s, a conceptually simple strategy is to decompose the domain Ω into subdomains on which s is constant and impose our Kato method over each of the subdomains. Note that the solution for w in Eq (8.8) is independent of s and may be obtained without any need for domain decomposition. Although differences in s among domains means that the number of functions $v_{\ell=0,\ldots,L}$ also varies among domains, the boundary condition $v = 0$ on each of the subdomains ensures continuity of v, and therefore continuity of $u = v + w$ throughout Ω. Observe that computation of $\{v_\ell\}$ in one subdomain is independent of its calculation in another, and hence, $\{v_\ell\}$ over each of the subdomains can computed in parallel with no message passing or interdomain communication required once w is solved for and shared globally throughout Ω. That said, several issues need to be resolved before this idea can be defensibly implemented. First, the suggestion of zero (subdomain) boundary conditions on $\{v_\ell\}$ needs to be physically justified. If found to be unsound, the embarrassingly parallel structure just described will instead require interdomain communication and potentially interpolation. Second,

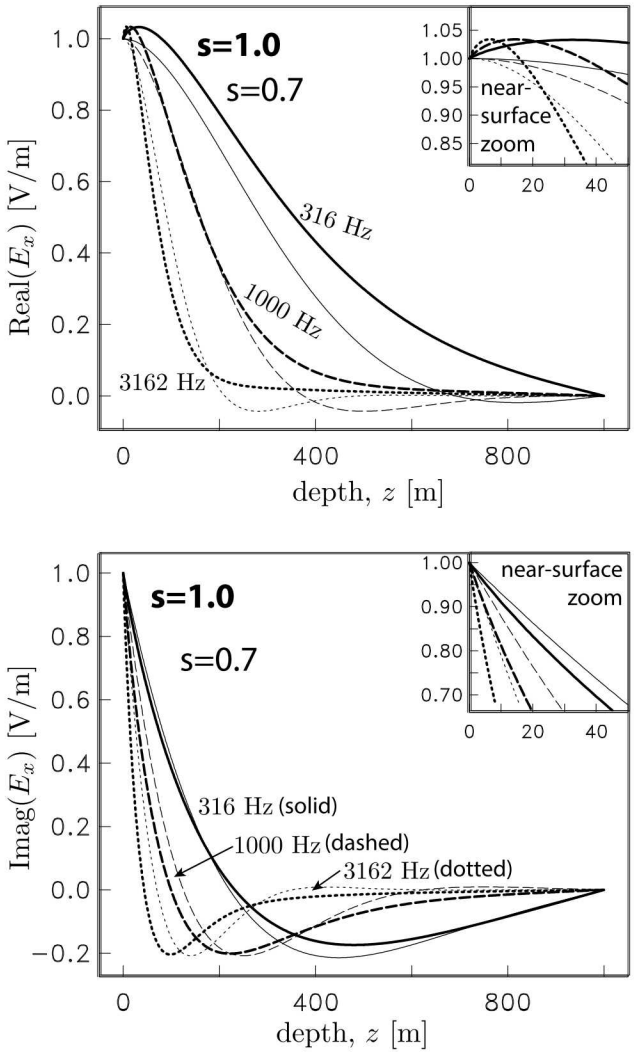

Figure 8-8. Real (top) and imaginary (bottom) components of horizontal electric field as a function of depth in a uniform 0.01 S/m Earth underlain by a perfect conductor for frequencies $f = 316, 1000$ and 3162 Hz, corresponding to the high–frequency region of the magnetotelluric apparent resistivity spectrum (Figure 6) with approximate s dependent power law behavior. Curves for classical $s = 1$ (heavy lines) and fractional $s = 0.7$ response (light lines) are shown. The decrease in apparent resistivity is evidently due to the strongly increased vertical gradient of Real component of electric field at the air/Earth interface $z = 0$ for fractional Helmholtz. Recall that from Eq (4.1) that the vertical gradient of electric fields resides in the denominator of the of the apparent resistivity estimator.

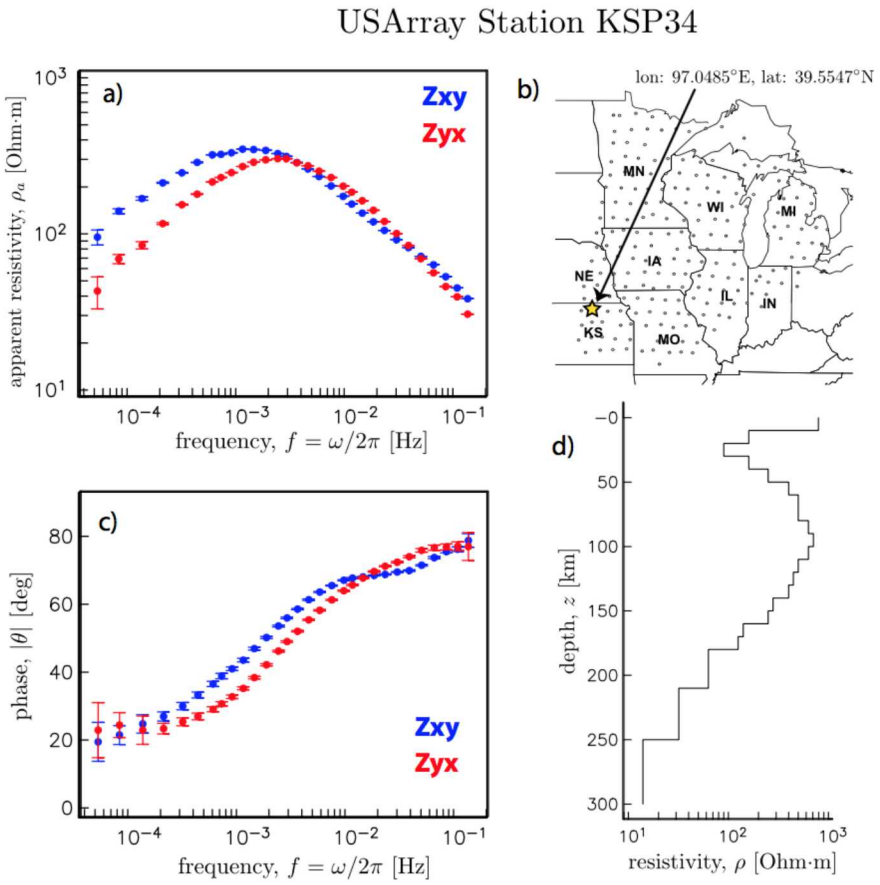

Figure 8-9. Apparent resistivity and phase angle data from US-Array MT station for KSP34 located NW of Kansas City, KS, USA from the US Array: a) Apparent resisistivity spectrum based on Zxy (blue) and Zyx (red) elements of the 2×2 impedance tensor $\mathbf{Z}$. The similarity in the curves, especially at high frequencies, is indicative a locally 1D conductivity profile beneath the observation point. b) Location map for USArray MT station KSP34. c) Complex phase angle of the ratios E_x/H_y (Zxy, blue) and E_y/H_x (Z_{yx}, red), again generally similar and indicating a locally 1D conductivity profile beneath the station. d) Depth profile of electrical resistivity beneath station KSP34 estimated by 3D inversion of all sites in sub-panel (b) (figure 3, sub-panel (a), Yang et al., EPSL 2015).

because the fractional Laplacian is inherently non–local, its support extends over the global domain Ω. Ensuring global extent of non–locality in the context of subdomains requires further analysis. Lastly, function and flux continuity for a given v_ℓ within a subdomain is guaranteed; the conditions for such guarantees, in a general sense, at subdomain boundaries have yet to be determined. Because of these complexities, further analysis of this domain decomposition concept is deferred to future publication.

8.6.3. Fractional time derivatives

Prior work in electromagnetic geophysics in contemplation of Ohm's constitutive law being represented in terms of fractional calculus have focused on fractional *time* derivatives, rather than the fractional space derivatives described here (Weiss and Everett, 2007; Everett, 2009; Ge et al., 2015). Such analyses are comparatively simple in that the fractional space derivatives D_z^α of (1.2) are replaced by time derivatives D_t^β, thus modifying the complex wavenumber as $k^2 = -(\mathrm{i}\omega)^{1-\beta}\mu_0\sigma$. Solutions to Eq (8.5) in layered media when $s = 1$ (equivalently, $\alpha = 0$ since $s = 1 - \frac{\alpha}{2}$) follow the usual method of posing characteristic solutions $\exp(\pm kz)$ in each of the layers, coefficients for which are determined through enforcement of boundary condition Eq (8.5) along with continuity of u and $\partial_z u$ at layer boundaries. Solving this time-fractional Helmholtz equation on the domain $\Omega : z \in [0, z^* = 1000]$ m with $u(0) = 1 + \mathrm{i}$, $u(z^*) = 0$ and $\sigma = 0.01$ S/m(rad/s)$^{-\beta}$ yields a characteristic magnetotelluric response (Figure 8-10) distinct from that obtained in the case of space–fractional derivatives $s \neq 1$ (Figure 8-7). As noted in Ge et al. (2015), imposing the time–fractional derivative in this way is equivalent to recasting real–valued electrical conductivity σ as a frequency–dependent, complex–valued conductivity $\sigma(\mathrm{i}\omega)^\beta$. The quasi–linear power–law behavior in apparent resistivity and phase angle (Figure 8-10) seen at high frequencies ($f > 100$ Hz) is objectively distinct from that computed for the space–fractional Helmholtz system (Figure 8-7) and offers an unambiguous diagnostic for discriminating between the two. These differences have their origin in the how anomalous power–law diffusion is captured by each. In the case of fractional time derivatives of order $1 - \beta$, as considered in this latest example, the system is considered subdiffusive and consistent with an anomalously high likelihood of long wait times between successive jumps of charge carriers in a continuous time random walk, analogous to that suggested for fluid transport in a porous medium (Metzler and Klafter, 2000). Instead, the space–fractional derivatives which occupy the primary focus of the present study capture long–range interactions (spatial nonlocality) of charge carriers as a superdiffusive system, perhaps through inductive coupling (a phenomena absent in the physics of fluid flow in porous media). This contrast – super- versus sub-diffusion – is the essence of the causative physics behind the different magnetotelluric responses predicted by (Figures 8-7 and 8-10).

8.7. CONCLUSIONS

We have presented a novel, practical solution to the fractional Helmholtz equation based on the Kato formulation of the fractional Laplacian operator, a lifting (splitting) strategy to handle

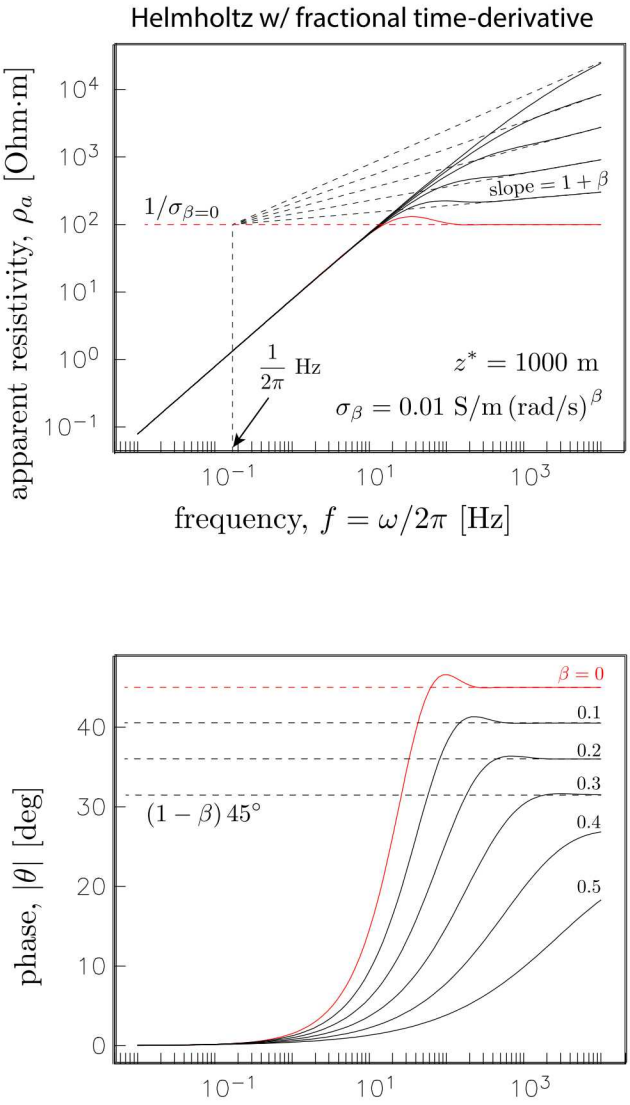

Figure 8-10. Apparent resistivity spectra for classical Helmholtz equation $s = 1$ with $\mathbf{i}\kappa^2 = (\mathbf{i}\omega)^{1-\beta}\mu_0\sigma$, where the β terms arise in the 1D magnetotelluric case from Ohm's law with a fractional, non–local time dependence attributable to sub-diffusion of electric charge following a continuous time random walk with a heavy–tailed distribution of waiting times. Compare to Figure 7 for the space–fractional case describing super–diffusion, where the heavy–tailed distribution of step length (a.k.a. Lévy flights) captures long–range interactions between charges.

non-zero Dirichlet boundary conditions, and finite element discretization of the spatial domain. This specific finite element discretization derives from our statement of the variational problem, from which alternative discretizations (orthogonal polynomials, wavelets, spectral functions, etc.) offer an interesting direction for future research. Whereas the analogous Kato/lifting strategy for solving the fractional Poisson equation leads to decoupled system of integer Laplace solves which can be done in parallel with no inter-solve communication, solution of the fractional Helmoltz admits no such decoupling. This leads to a large, block–dense system of linear equations upon discretization which significantly increases the resource requirements for obtaining a numerical solution. In response, we augment the variational problem by introducing an additional unknown which collapses the $L-1$ block coupling matrices in a given block–row into a single block matrix, at the expense of only one additional (dense) block–row in the linear system. For typical problems where with $L >> 100$, the added computational burden of this compatibility equation is inconsequential, yet the reduction in matrix storage is significant, going from L^2 to simply $2L$. Thus, a key feature of this augmented variational problem is the extreme block–sparsity of the resulting linear system of equations, a feature which is independent of the choice of discretization and important for efficient solution of large–scale systems. Validation of the algorithm for linear, nodal finite elements shows h^2 reduction in RMS error for an MMS test problem – demonstrating that our formulation of the fractional Helmholtz problem does not corrupt the convergence behavior expected from solution of integer-order Helmholtz.

We apply this formulation for fractional Helmholtz to the growing body of observational evidence of anomalous diffusion in nature – here, asking the question, "Does the Earth, with its incalculable geologic complexity, respond to electromagnetic stimulation in a way that is consistent with fractional diffusion and the non–locality that is central to the differential operators of the governing physics"? Whereas temporal non-locality of Maxwell's equations has previously been observed as sub–diffusive propagation, the fractional Helmholtz equation studied here describes super–diffusion by attributing fractional derivatives directly to the spatial distribution of material properties in Ohm's constitutive law. Earth electromagnetic response is computed in the context magnetotelluric (MT) analysis – a classic geophysical exploration technique dating back to to middle 20th century – and comparison with the EarthScope USArray database. We find qualitative agreement between the predicted fractional Helmholtz response functions and those observed at a middle North American measurement site. This congruence in electromagnetic response thereby offers an altenative interpretation of the MT data at the site, one where the classical interpretation of a layered Earth geology with deep resistive rocks overlain by a conductive overburden is contrasted with new interpretation suggesting complex, geologic texture consistent with the site's proximity significant deep crustal tectonic structure.

Outstanding issues for future research therefore lie in two fundamental areas: arriving at a clearer mapping between the value of a fractional exponent s and the material heterogeneity it's intended to represent; and, extension of the computational tools to higher dimension with parallel implementation, including spatially variable and/or anisotropic s values. The former may be informed, as we've done here, by reinterpretation of existing observational data through fractional calculus concepts, but augmented by detailed material analysis. The latter naturally feeds into ongoing efforts in PDE–constrained optimization for material property estimation, now augmented with the desire to recover s, too, as a measure of material complexity or sub–grid structure. Algorithmic advances in multi-level domain decomposition (decomposition over

physical domain in addition to decomposition over the functional blocks of global system matrix) will also be required for full exploration of fractional Helmholtz concepts on large, 3D domains.

8.8. ACKNOWLEDGEMENTS

This interdisciplinary, collaborative work is supported by Sandia National Laboratories LDRD program, NSF grants DMS-1521590 and DMS-1818772, and Air Force Office of Scientific Research under Award NO: FA9550-19-1-0036. Sandia National Laboratories is a multimission laboratory managed and operated by National Technology and Engineering Solutions of Sandia LLC, a wholly owned subsidiary of Honeywell International, Inc., for the U.S. Department of Energy's National Nuclear Security Administration under contract DE-NA-0003525. This paper describes objective technical results and analysis. Any subjective views or opinions that might be expressed in the paper do not necessarily represent the views of the U.S. Department of Energy or the United States Government.

8.9. APPENDIX

Faraday's law of induction equates the circulation of electric field $\mathbf{E}$ to the negative time rate of change of the magnetic induction $\mathbf{B}$,

$$\nabla \times \mathbf{E} = -\partial_t \mathbf{B}. \tag{8.31}$$

Assuming non-magnetic media where magnetic permeability μ is equal to that of free space $\mu = \mu_0 = 4\pi \times 10^{-7}$ H/m, the right hand side of Eq (8.31) can be written as $-\mu_0 \partial_t \mathbf{H}$, where $\mathbf{H}$ is the magnetic field. Similarly, Ampère's Law equates the circulation of magnetic field to the total electric current density, $\mathbf{J}_{\text{tot}}$,

$$\nabla \times \mathbf{H} = \mathbf{J}_{\text{tot}}, \tag{8.32}$$

which in the absence of prescribed source currents — naturally occuring or engineered — is given by Ohm's constitutive law, a convolution of the electrical conductivity σ and electric field over both space $\boldsymbol{r}$ and time t:

$$\mathbf{J}_{\text{tot}} = \sigma * \mathbf{E}. \tag{8.33}$$

The convolutional nature of the empirically–derived constitutive laws of electromagnetics reflects not only the linearity between the vector fields such as $\mathbf{J}$ and $\mathbf{E}$, but also the fact the effect of material properties may be non–local in time and/or space. The latter is representative of materials with "memory", whose behavior at a given time is dependent on the time–history of the material. This has been studied previously in the context of geophysical electromagnetics (Everett, 2009) and motivated by observational evidence of anomalous power–law scaling (Weiss and Everett, 2007) from an engineered loop antenna. Similar anomalous power laws have also been observed in the context of diffusive fluid transport in porous media (e.g. Benson et al.,

2000). In attributing the anomalous diffusion to memory effects alone, Everett (2009) defines the spatially uniform but temporally non–local Ohm's law as the convolution

$$(\sigma * \mathbf{E})(t) \equiv \frac{1}{\Gamma(\beta)} \int_0^t \frac{\sigma_\beta \mathbf{E}(t')}{(t-t')^{1-\beta}} \, \mathrm{d}t', \tag{8.34}$$

where $\Gamma(\cdot)$ is the Gamma function, σ_β is electrical conductivity (with fractional units for dimensional consistency) and β describes the anomalous power–law relationhip. The exact mapping between (piecewise?) constant σ_β and the presumed, causative "rough geologic medium" σ remains an open research question. Nonetheless, substituting Eq (8.32) into Eq (8.32) eliminates the magnetic field variable and introduces via Eqs (8.33) and (8.34) the term

$$\frac{\partial}{\partial t}(\sigma * \mathbf{E})(t) = \frac{\partial}{\partial t} \frac{1}{\Gamma(\beta)} \int_0^t \frac{\sigma_\beta \mathbf{E}(t')}{(t-t')^{1-\beta}} \, \mathrm{d}t'. \tag{8.35}$$

The term on the right is recognized as the Riemann–Liouville fractional derivative, in time, of order $1-\beta$, thusly motivated by a particular representation of Ohm's convolutional constitutive law for consistency with observations of anomalous, fractional power law in geophysical electromagnetics in which the governing diffusion equation posesses integer order derivatives in space coupled with fractional-order derivatives in time.

Alternatively, an anomalous power law can also be captured through a governing diffusion equation whose space derivatives are of fractional order and the time derivatives are integer order. Indeed, mixed fractional space–time derivatives are now an accepted element of the mathematical architecture for quantifying anomalous hydrologic diffusion (e.g. Benson et al., 2000; Meerschaert and Sikorskii, 2012). To motivate the proposed fractional space derivatives, we return to the fundamental definition of Ohm's constitutive law and write it as local in time, but non–local in space. For the sake of notational simplicity, consider non-locality in the z direction alone and write analagously to (8.34)

$$(\sigma * \mathbf{E})(z) \propto \frac{\partial}{\partial z} \frac{1}{\Gamma(1-\alpha)} \int_{-\infty}^{+\infty} \frac{\sigma_{\alpha,z}(z') \mathbf{E}(z') \mathrm{sgn}(z-z')}{|z-z'|^\alpha} \, \mathrm{d}z', \tag{8.36}$$

where the signum function, $\mathrm{sgn}(\cdot)$, is equal to ± 1, consistent with the sign of its real argument. A couple of differences between our space–convolution Eq (8.36) and the (Everett, 2009) time–convolution Eq (8.34) merit some comment. First, the limits of integration in Eq (8.36) extend from $\pm\infty$ and in practice would be truncated at the bounds of some model domain Ω under consideration, whereas the limits on the time–convolution are truncated at time t to enforce causality. Because of this we may further decompose the convolution into an integration over two domains, one with $z' < z$ and the other with $z' > z$:

$$(\sigma * \mathbf{E})(z) \propto \frac{\partial}{\partial z} \frac{1}{\Gamma(1-\alpha)} \left[\int_{-\infty}^{z} \frac{\sigma_{\alpha,z}(z') \mathbf{E}(z')}{(z-z')^\alpha} \, \mathrm{d}z' - \int_{z}^{+\infty} \frac{\sigma_{\alpha,z}(z') \mathbf{E}(z')}{(z'-z)^\alpha} \, \mathrm{d}z' \right]. \tag{8.37}$$

Thus, unlike the causality constraint for time derivatives, the spatial convolution is free to consider regions to both "forward" and "backward" from z. The second major difference between the proposed spatial convolution and the (Everett, 2009) time–convolution is the leading

derivative with respect to z. However, we point out that the derivative of a convolution is a still a convolution, nonetheless. Thus, our expression still retains the familiar linearity properties of Ohm's law while admitting the non–locality we desire. The first term in Eq (8.37) is recognizable (from above) as the fractional derivative of order α with respect to z. The second term, we find, is the fractional derivative of order α with respect to $-z$ (Baeumer et al., 2009).

Like derivatives of integer order, the Fourier transform of a α–order fractional derivative with respect to z of a function $f(z)$ is simply $(i\nu)^\alpha \bar{f}(\nu)$, whereas the derivative with respect to $-z$ yields Fourier transform $(-i\nu)^\alpha \bar{f}(\nu)$. Consequently, Fourier transform of the sum, as we have in Eq (8.37), has Fourier transform $2\cos\left(\frac{1}{2}\alpha\pi\right)|\nu|^\alpha \bar{f}(z)$. We thus define a fractional differential operator $\mathscr{D}_z^\alpha$ with Fourier transform $|\nu|^\alpha$ for the left/right derivatives in Eq (8.37) as

$$\mathscr{D}_z^\alpha = \frac{1}{2\cos\left(\frac{1}{2}\alpha\pi\right)}\left(\frac{\partial^\alpha}{\partial z^\alpha} + \frac{\partial^\alpha}{\partial(-z)^\alpha}\right). \tag{8.38}$$

Notice that as was done previously with σ_β in (Everett, 2009), the connection between the conductivity function $\sigma_{\alpha,z}$ the underlying presumably rough geology σ left undefined. This still remains an outstanding research question, but before too much effort is spent in pursuit of its answer, we argue the such answers fruitless if the governing spatial space–fractional diffusion equation is too burdonsome to solve or yields results inconsistent with observation. It is the latter which defines the focus of the present research.

To do so, we consider the 1D magnetotelluric problem where there is, again, a presumably rough depth–dependent conductivity function $\sigma(z)$ and the electric field is fully represented by its horizontal component, written here as $u(z)$. Under these simplifying assumptions, the combination of Ampère's and Faraday's law, as decribed above through elimination of the magnetic field, yields a simple ordinary differential equation in the ω freqency domain:

$$-\frac{\mathrm{d}^2 u(z)}{\mathrm{d}z^2} = -\mathrm{i}\omega\mu_0 \mathscr{D}_z^\alpha\left[\sigma_{\alpha,z} u(z)\right]. \tag{8.39}$$

Recall and observe above that for dimensional consistency, the function $\sigma_{\alpha,z}$ necessarily has fractional physical units of S/m$^{1-\alpha}$. This awkwardness can avoided by non–diminensionalizing the space coordinate $z \mapsto \zeta = z/z^*$ where $z*$ is taken here to be range of z in our model domain Ω. In doing so, the fractional differential operator is written as $\mathscr{D}_\zeta^\alpha$ to represent its action with respect to the dimensionless variable ζ and the classically–dimensioned conductivity $\sigma_{\alpha,\zeta} = (z^*)^\alpha \sigma_{\alpha,z}$ is introduced such that

$$-\frac{\mathrm{d}^2 u(\zeta)}{\mathrm{d}\zeta^2}\left(\frac{1}{z^*}\right)^2 = -\mathrm{i}\omega\mu_0 \mathscr{D}_z^\alpha\left[\sigma_{\alpha,z} u(z)\right]. \tag{8.40}$$

As pointed out in the discussion preceding Eq (8.38), the Fourier transform of our differential operator $\mathscr{D}_z^\alpha$ is $|\nu|^\alpha$ and the same holds true for $\mathscr{D}_\zeta^\alpha$ under $\zeta \mapsto \nu$. As a consequence, the Fourier transform $\mathscr{F}$ of Eq (8.40) can be written as

$$-|\nu|^2 \mathscr{F}[u] + \mathrm{i}\omega\mu_0 (z^*)^2 |\nu|^\alpha \mathscr{F}\left[\sigma_{\alpha,\zeta} u\right] = 0, \tag{8.41}$$

which invites combining the ν terms to write

$$-|\nu|^{2-\alpha}\mathscr{F}[u]+\mathrm{i}\omega\mu_0(z^*)^2\mathscr{F}\left[\sigma_{\alpha,\zeta}u\right]=0, \tag{8.42}$$

an expression in the ζ domain that reads

$$-\left(\frac{\mathrm{d}^2u(\zeta)}{\mathrm{d}z^2}\right)^s+\mathrm{i}\omega\mu_0(z^*)^2\sigma_{\alpha,\zeta}u(\zeta)=0 \tag{8.43}$$

with $s=1-\frac{1}{2}\alpha$. The three–dimensional analogue of Eq (8.43) follows immediately in the form of a generalized fractional–order Helmholtz equation $(-\Delta)^s u-k^2u=0$, whose fractional Lapacian operator and methods for working with it constitutes the bulk of the algorithic development in the main body of the present work.

9. CLOSING REMARKS

As described in the Introduction, the goals of this project revolved around efficient computation of geophysical response of complex natural materials, and in particular, an assymptotic analysis of the middle ground in length scale where the details of an exquisitely discretized Earth model transition into an acceptable representation through a fractional calculus framework. Each of these endmember states merited independent research in their own right and the reader is directed to the 'Conclusion' sections of Chapters 2 through 8 to see the long list of particular breakthroughs. That said, the main science achievements are twofold: a hierarchical material properties representation for finite elemnet analysis (Chapter 2); and, a novel solution to the fractional Helmholtz equation with supporting magnetotelluric evidence in the USArray database of the United States National Science Foundation's EarthScope program (Chapter 3). While not in the original research plan, the broad class of problems made accessible by the former made it the natural choice as the primary computational approach for all computations requiring specific, detailed discretizations of fine–featured models. As such, proposed $\mathbf{A} - \Phi$ and nested meshing concepts originally proposed were quickly deprecated in favor of the new, hierarchical scheme, and in doing so we investigated problems in oilfield (Chapters 3–5, 7) and near surface (Chapter 6) geophysics that simply weren't previously possible. Similarly, the fractional Helmholtz solution described in Chapter 8 is the first of its kind in the geophysical literature and complements the previous work on fractional calculus in geosciences in two ways. Most notably, its treatment of fractional derivatives in space — rather than previous works which dealt with fractional time derivatives — resulted in a solution method based deeply in functional analysis and branches of mathematics perhaps less familiar to the geophysical community. Thus, we feel we have provided a solution to the problem at hand and made significant progress in translating these mathematical esoterica to practical–minded physical scientists. Secondly, the fractional Helmholtz study was bolstered by newly–found obervational evidence of Earth electromagnetic response that is compatible with fractional calculus worldview. The database of such evidence is small (but growing) and skeptics of the fractional calculus worldview rightly point out the necessary distinction between causality and compatibility. Nonetheless, because the incalculable level of geologic detail presumably captured by the fractional derivatives is simply beyond the resolution limits of geophysical inversion, as well as those in the foreseeable future, analyses such as ours provide the necessary basis for observational hypothesis testing common across the spectrum of the physical sciences. In short, we have a (fractional calculus) theory and a first-ever method for making predictions; the next step is data collection and analysis to see if the theory holds up under observational and theoretical scrutiny.

REFERENCES

Andersson, J., and B. Dverstorp, 1987, Conditional simulations of fluid flow in three dimensional networks of discrete fractures: Water Resources Research, **23**, 1876–1886.

Andersson, J., A. M. Shapiro, J, and Bear, 1984, A stochastic model of a fractured rock conditioned by measured information: Water Resources Research, **20**, 79–88.

Antil, H., A. Ceretani, and C. N. Rautenberg, 2018a, The fractional Laplacian with spatially variable order. (in prep).

Antil, H., and J. Pfefferer, 2017, A short matlab implementation of fractional poisson equation with nonzero boundary conditions: Technical Report. (`http://math.gmu.edu/~hantil/Tech_Report/HAntil_JPfefferer_2017a.pdf`, accessed Sept 13, 2018).

Antil, H., J. Pfefferer, and S. Rogovs, 2018b, Fractional operators with inhomogeneous boundary conditions: Analysis, control, and discretization: Communications in Mathematical Sciences (CMS), **16**, 1395–1426.

Antil, H., J. Pfefferer, and M. Warma, 2017, A note on semilinear fractional elliptic equation: analysis and discretization: ESAIM. Mathematical Modelling and Numerical Analysis, **51**, 2049–67. (doi:10.1051/m2an/2017023).

Antil, H., and C. N. Rautenberg, 2018, Sobolev spaces with non-muckenhoupt weights, fractional elliptic operators, and applications: arXiv:1803.10350. (`https://arxiv.org/pdf/1803.10350.pdf`, accessed Sept 27, 2018).

Antil, H., and M. Warma, 2019, Optimal control of fractional semilinear pdes: To appear: ESAIM: Control, Optimisation and Calculus of Variations (ESAIM: COCV).

Avdeev, D. B., A. V. Kuvshinov, O. V. Pankratov, and G. A. Newman, 1997, Three–dimensional induction logging problems, Part I: An integral equation solution and model comparisons: Journal of Geomagnetism and Geoelectricity, **49**, 1519–1539.

———, 2002, Three–dimensional induction logging problems, Part I: An integral equation solution and model comparisons: Geophysics, **67**, 413–426. (doi:10.1190/1.1468601).

Baeumer, M., M. M. Meerschaert, and E. Nane, 2009, Space–time duality for fractional diffusion: Journal of Applied Probability, **46**, 1100–1115.

Bahr, K., M. Smirnov, E. Steveling, and the BEAR Working Group, 2002, A gelation analogy of crustal formation derived from fractal conductive structures: Journal of Geophysical Resarch: B, **107**, 2314. (doi:10.1029.2001JB000506).

Bear, J., C. F. Tsang, and G. D. Marsily, 2012, Flow and contaminant transport in fractured rock: Academic Press.

Benson, D. A., S. W. Wheatcraft, and M. M. Meerschaert, 2000, The fractional-order governing equations of Lévy motion: Water Resources Research, **36**, 1413–1423.

Berger, M. J., and J. Oliger, 1984, Adaptive mesh refinement for hyperbolic partial differential equations: Journal of Computational Physics, **53**, 484–512.

Berggren, M., 2004, Approximations of very weak solutions to boundary–value problems: SIAM Journal of Numerical Analysis, **42**, 860–77.

Berkowitz, B., and H. Scher, 2005, Quantification of non—Fickian transport in fractured formations, *in* Dynamics of Fluids and Transport in Fractured Rock, AGU Geophysical Monograph 162: American Geophysical Union, 23—31.

Beskardes, G. D., W. A. McAliley, M. Ahmadian, D. T. Chapman, C. J. Weiss, and J. E. Heath, 2019, Power density distribution in subsurface fractures due to an energized steel well-casing source: Journal of Environmental & Engineering Geophysics, **24**, 285–297.

Beskardes, G. D., and C. J. Weiss, 2018, Modelling dc responses of 3-d complex fracture networks: Geophysical Journal International, **214**, 1901–1912.

Beskardes, G. D., C. J. Weiss, and M. E. Everett, 2016, Estimating the power law distribution of Earth electrical conductivity from low-frequency, controlled-source electromagnetic responses: Geophysical Journal International, **214**, 639–651.

Bogdanov, I. I., V. V. Mourzenko, J. F. Thovert, and P. M. Adler, 2003, Effective permeability of fractured porous media in steady state flow: Water Resources Research, **39**, 1023. (doi:10.1029/2001WR000756).

Bonito, A., and J. Pasciak, 2017, Numerical approximation of the fractional powers of regularly accretive operators: IMA Journal of Numerical Analysis, **37**, 1245–73.

Bonito, A., and J. E. Pasciak, 2015, Numerical approximation of fractional powers of elliptic operators: Mathematics of Computation, **84**, 2083–2110. (doi:10.1090/S0025-5718-2015-02937-8).

Bonnet, E., O. Bour, N. E. Odling, P. Davy, I. Main, P. Cowie, and B. Berkowitz, 2001, Scaling of fracture systems in geological media: Reviews of Geophysics, **39**, 347–383.

Busby, J. P., 2000, The effectiveness of azimuthal apparent resistivity measurements as a method for determining fracture strike orientations: Geophysical Prospecting, **48**, 677–695.

Caballero-Sanz, V., D. Roubinet, S. Demirel, and J. Irving, 2017, 2.5-D discrete-dual-porosity model for simulating geoelectrical experiments in fractured rock: Geophysical Journal International, **209**, 1099–1110.

Cacas, M. C., E. Ledoux, G. D. Marsily, B. Tillie, A. Barbreau, E. Durand, B. Feuga, and P. Peaudecerf, 1990, Modeling fracture flow with a stochastic discrete fracture network: calibration and validation: 1. the flow model: Water Resources Research, **26**, 479–489.

Caffarelli, L. A., and P. R. Stinga, 2016, Fractional elliptic equations, Caccioppoli estimates and regularity: Annales de l'Institut Henri Poincaré. Analyse Non Linéaire, **33**, 767–807. (doi10.1016/j.anihpc.2015.01.004).

Caputo, M., 2000, Models of fluids in porous media with memory: Water Resources Research, **36**, 693–705.

Chave, A. D., and A. G. Jones, 2012, The magnetotelluric method: Theory and practice: Cambridge University Press.

Christensen, N. B., 1996, Electromagnetic subsurface imaging. a case for an adaptive Born approximation: Surveys in Geophysics, **18**, 488–510.

Commer, M., G. M. Hoversten, and E. S. Um, 2015, Transient–electromagentic finite–difference time–domain earth modeling over steel infrastructure: Geophysics, **80**, E147–E162. (doi: 10.1190/GEO2014-0324.1).

Couchman, M. J., and M. E. Everett, 2017, Controlled source electromagnetic monitoring of hydraulic fracturing: Wellbore and fluid effects: Annual Meeting of the American Geophysical

Union, GP32A–01.
Daily, W., A. Ramirez, R. L. Newmark, and K. Masica, 2004, Low–cost reservoir tomographs of electrical resistivity: The Leading Edge, **23**, 472–480. (doi: 10.1190/1.1756837).
Davy, P., 1993, On the frequency length distribution of the San Andreas fault system: Journal of Geophysical Research: Solid Earth, **98**, 12141–12151. (doi:10.1029/93JB00372).
de Dreuzy, J. R., P. Davy, and OBour, 2001, Hydraulic properties of two–dimensional random fracture networks following a power law length distribution 2. Permeability of networks based on lognormal distribution of apertures: Water Resources Research, **37**, 2079–2095. (doi:10.1029/2001WR900010).
de Dreuzy, J.-R., G. Pichot, B. Poirriezn, and J. Erhel, 2013, Synthetic benchmark for modeling flow in 3D fractured media: Computers & Geosciences, **50**, 59–71. (doi:10.1016/j.cageo.2012.07.025).
Deseri, L., and M. Zingales, 2015, A mechanical picture of frational-order Darcy equation: Communications in Nonlinear Science and Numerical Simulation, **20**, 940–949.
Elser, J., V. A. Podolskiy, I. Salakhutdinov, and I. Avrutsky, 2007, Nonlocal effects in effective–medium response of nanolayered metamaterials: Applied Physics Letters, **90**, 191109. (doi:10.1063/1.2737935).
Everett, M. E., 2009, Transient electromagnetic response of a loop source over a rough geological medium: Geophysical Journal International, **177**, 421–429. (doi: 10.1111/j.1365-246X.2008.04011.x).
Everett, M. E., E. A. Badea, L. Shen, G. Merchant, and C. J. Weiss, 2001, 3–D finite element analysis of induction logging in a dipping formation: IEEE Transactions on Geoscience and Remote Sensing, **39**, 2244–52. (doi: 10.1109/36.957287).
Everett, M. E., and C. J. Weiss, 2002a, Geological noise in near-surface electromagnetic induction data: Geophysical Research Letters, **29**, 1010. (doi:10.1029/2001GL014049).
———, 2002b, Geological noise in near-surface electromagnetic induction data: Geophysical Research Letters, **29**, 1010. (doi:10.1029/2001GL014049).
Fitterman, D. V., 1989, What pipes can do to your transient EM interpretation: SEG Technical Program Expanded Abstracts, 219–221. (doi: 10.1190/1.1889587).
Fitterman, D. V., F. C. Frischknecht, A. T. Mazzella, and W. L. Anderson, 1990, Example of transient electromagnetic soundings in the presence of oil field pipes: Geotechnical and Environmental Geophysics, Society of Exploration Geophysicists, 79–88.
Ge, J., M. E. Everett, and C. J. Weiss, 2012, Fractional diffusion analysis of the electromagnetic field in fractured media Part I: 2D approach: Geophysics, **77**, WB213–WB218.
———, 2015, Fractional diffusion analysis of the electromagnetic field in fractured media – Part 2: 3D approach: Geophysics, **80**, E175–E185. (doi:10.1190/geo2014-0333.1).
Gong, J., and W. R. Rossen, 2017, Modeling flow in naturally fractured reservoirs: effect of fracture aperture distribution on dominant sub-network for flow: Petroleum Science, **14**, 138–154.
Gutierrez, M., and D. J. Youn, 2015, Effects of fracture distribution and length scale on the equivalent continuum elastic compliance of fractured rock masses: Journal of Rock Mechanics and Geotechnical Engineering, **7**, 626–637.
Habashy, T. M., R. W. Groom, and B. R. Spies, 1993, Beyond Born and Rytov approximations: a nonlinear approach to electromagnetic scattering: Journal of Geophysical Research, **98**, 1759–1775.

Haber, E., D. W. Oldenburg, and R. Shekhtman, 2007, Inversion of time domain three-dimensional electromagnetic data: Geophysical Journal International, **171**, 550–564.
Haber, E., C. Schwarzbach, and R. Shekhtman, 2016, Modeling electromagnetic fields in the presence of casing: SEG Technical Program Expanded Abstracts, 959–964. (doi: 10.1190/sebam2016-13965568.1).
Hatton, C. G., I. G. Main, and P. G. Meredith, 1994, Non-universal scaling of fracture length and opening displacement: Nature, **367**, 160–162. (doi:10.1038/367160a0).
Hestenes, M. R., and E. Stiefel, 1952, Methods of conjugate gradients for solving linear systems: Journal of the National Bureau of Standards, 409–436.
Hickey, M. S., S. Trevino, and M. E. Everett, 2017, Monitoring hydraulic fracturing using ground-based controlled source electromagnetics: Annual Meeting of the American Geophysical Union, GP32A–02.
Hohmann, G. W., 1971, Electromagnetic scattering by conductors in the earth near a line source of current: Geophysics, **36**, 101–131. (doi: 10.1190/1.1440150).
Hoversten, G. M., M. Commer, E. Haber, and C. Schwarzbach, 2015, Hydro-frac monitoring using time–domain electromagnetics: Geophysical Prospecting, **63**, 1508–1526. (doi: 10.1111/1365-2478.12300).
Hoversten, G. M., G. A. Newman, H. F. Morrison, E. Gasperikova, and J.-I. Berg, 2001, Reservoir characterization using crosswell electromagnetic inversion: A feasibility study for the Snorre Field, North Sea: Geophysics, **66**, 1177–1189.
Howard, A. Q., 1972, The electromagnetic fields of a subterranean cylindrical inhomogeneity excited by a line source: Geophysics, **37**, 975–984. (doi: 10.1190/1.1440320).
Jackson, J. D., 1975, Classical electrodynamics: Wiley.
Jannin, G., J. Chen, L. E. DePavia, L. Sun, and M. Schwartz, 2017, Deep electrode: A game-changing technology for electromagnetic telemetry: SEG Technical Program Expanded Abstracts, 1059–1063. (doi:10.1190/segam2017-17731164.1).
Johnson, R. H., F. N. Trofimenkoff, and J. W. Haslett, 1987, Resistivity response of a homogeneous earth with a finite–length contained vertical conductor: IEEE Transactions on Geoscience and Remote Sensing, **GE-25**, 414–421. (10.1109/TGRS.1987.289852).
Johnson, T. C., and D. M. Wellman, 2015, Accurate modeling and inversion of electrical resistivity data in the presence of metallic infrastructure with known location and dimension: Geophysical Journal International, **202**, 1096–1108. (doi: 10.1093/gji/ggv206).
Kafafy, R., T. Lin, Y. Lin, and J. Wang, 2005, Three dimensional immersed finite element methods for electric field simulation in composite materials: International journal for numerical methods in engineering, **64**, 940–972.
Karato, S.-I., and D. Wang, 2013, Electrical conductivity in rocks and minerals, *in* Physics and Chemistry of the Deep Earth: John Wiley & Sons, Ltd., 5, 145–184. (doi:10.1002/9781118529492.ch5).
Kato, T., 1960, Note on fractional powers of linear operators: Proceedings of the Japan Academy, **36**.
Kaufman, A. A., and W. E. Wightman, 1993, A transmission line model for electrical logging through casing: Geophysics, **58**, 1739–1747.
Kazlauskas, E. M., 2010, Multi-fold tdem experiment design for near surface conductivity mapping: Master's thesis, Virginia Tech, Blacksburg VA.
Koudina, N., R. G. Garcia, J. F. Thovert, and P. M. Adler, 1998, Permeability of

three-dimensional fracture networks: Physical Review E, **57**, 4466–4479.
Lane, J., F. Haeni, and W. Watson, 1995, Use of a square-array direct-current resistivity method to detect fractures in crystalline bedrock in New-Hampshire: Ground Water, **33**, 476–485.
Lee, S. H., M. F. Lough, and C. L. Jensen, 2001, Hierarchical modeling of flow in naturally fractured formations with multiple length scales: Water Resources Research, **37**, 443–456. (doi:10.1029/2000WR900340).
Legarth, B., E. Huenges, and G. Zimmermann, 2005, Hydraulic fracturing in a sedimentary geothermal reservoir: Results and implications: International Journal of Rock Mechanics and Mining Sciences, **42**, 1028–1041.
Lei, Q., J. P. Latham, and C. F. Tsang, 2017, The use of discrete fracture networks for modelling coupled geomechanical and hydrological behaviour of fractured rocks: Computers and Geotechnics, **85**, 151–176.
Lesmes, D. P., and S. P. Friedman, 2005, Relationships between the electrical and hydrogeological properties of rocks and soils: Hydrogeophysics, Water Science and Technology Library, **50**, 87–128.
Li, L., and S. Lee, 2008, Efficient field-scale simulation of black oil in a naturally fractured reservoir through discrete fracture networks and homogenized media: SPE Reservoir Evaluation and Engineering, **11**, 750–758.
Li, Y., and K. Spitzer, 2002, Three-dimensional DC resistivity forward modelling using finite elements in comparison with finite-difference solutions: Geophysical Journal International, **151**, 924–934.
Lions, J. L., and E. Magenes, 1972, Non–homogeneous boundary value problems and applications: Springer–Verlag.
Long, J., and D. M. Billaux, 1987, From field data to fracture network modeling: an example incorporating spatial structure: Water Resources Research, **23**, 1201–1216. (doi:10.1029/WR023i007p01201).
Long, J. C. S., J. S. Remer, C. R. Wilson, and P. A. Witherspoon, 1982, Porous media equivalents for networks of discontinuous fractures: Water Resources Research, **18**, 645–658.
Lowry, T., M. B. Allen, and P. N. Shive, 1989, Singularity removal: A refinement of resistivity modeling techniques: Geophysics, **54**, 766–774. (doi.org/10.1190/1.1442704).
Mandelbrot, B. B., and J. W. V. Ness, 1968, Fractional Brownian motions, fractional noises and applications: SIAM Review, **10**, 422–437.
McGillivray, P. R., D. W. Oldenburg, R. G. Ellis, and T. M. Habashy, 1994, Calculation of sensitivities for the frequency–domain electromagnetic problem: Geophysical Journal International, **116**, 1–4. (doi:10.1111/j.1365-246X.1994.tb02121.x).
Meerschaert, M. M., and A. Sikorskii, 2012, Stochastic models for fractional calculus: Walter de Gruyter GmbH & Co. KG.
Metzler, R., and J. Klafter, 2000, The random walk's guide to anomalous diffusion: a fractional dynamics approach: Physics Reports, **339**, 1–77. (doi:10.1016/S0370-1573(00)00070-3).
Mourzenko, V. V., I. I. Bogdanov, J. F. Thovert, and P. M. Adler, 2011, Three-dimensional numerical simulation of single-phase transient compressible flows and well-tests in fractured formations: Mathematics and Computers in Simulation, **81**, 2270–2281.
Mukherjee, S., and M. E. Everett, 2011, 3–D controlled source electromagnetic edge–based finite element modeling of conductive and permeable heterogeneities: Geophysics, **76**, F215–26. (doi: 10.1190/1.3571045).

Mustapha, H., 2011, Finite element mesh for complex flow simulation: Finite Elements in Analysis and Design, **47**, 434–442.
Newmark, R. L., W. Daily, and A. Ramirez, 1999, Electrical resistance tomography using steel cased borehole as electrodes: SEG Technical Program Expanded Abstracts, 327–330.
Nieuwenhuis, G., D. Yang, K. J. MacLennan, D. Oldenburg, M. Wilt, and V. Ramadoss, 2015, Electrical imaging using a well casing as an antenna, a case study from a CO_2 sequestration site in Montana: Annual Meeting of the American Geophysical Union, GP13A–1273.
Parry, J. R., and S. H. Ward, 1971, Electromagnetic scattering from cylinders of arbitrary cross section in conductive half-space: Geophysics, **36**, 67–100. (doi: 10.1190/1.1440165).
Patzer, C., K. Tietze, and O. Ritter, 2017, Steel–cased wells in 3–D controlled source EM modelling: Geophysical Journal International. (accepted, doi:10.1093/gji/ggx049).
Polak, E., and G. Ribière, 1969, Note sur la convergence des méthodes de directions conjuguées: Revue Française d'Informatique Recherche Opérationnelle, **16**, 35–43.
Pollard, D. D., and P. Segall, 1987, Theoretical displacements and stresses near fractures in rock: with applications to faults, joints, veins, dikes and solution surfaces, *in* Fracture Mechanics of Rock: Academic Press, 277–349.
Qian, W., and D. E. Boerner, 1995, Electromagnetic modelling of buried line conductors using an integral equation: Geophysical Journal International, **121**, 203–214. (doi: 10.1111/j.1365-246X.1995.tb03521.x).
Ramirez, A., W. Daily, A. Binley, D. LaBrecque, and D. Roelant, 1996, Detection of leaks in underground storage tanks using electrical resistance methods: Journal of Environmental & Engineering Geophysics, **1**, 189–203.
Ramirez, A. L., R. L. Newmark, and W. D. Daily, 2003, Monitoring carbon dioxide floods using electrical resistance tomography (ert): Sensitivity studies: Journal of Environmental & Engineering Geophysics, **8**, 187–208.
Revil, A., and P. W. J. Glover, 1998, Nature of surface electrical conductivity in natural sands, sandstones, and clays: Geophysical Research Letters, **25**, 691–694.
Roache, P. J., 1998, Verification of codes and calculations: American Institute of Aeronautics and Astronautics Journal, **36**, 696–702.
Robinson, J., T. Johnson, and L. Slater, 2013, Evaluation of known-boundary and resistivity constraints for improving cross-borehole DC electrical resistivity imaging of discrete fractures: Geophysics, **78**, D115–127.
———, 2015, Challenges and opportunities for fractured rock imaging using 3D cross-borehole electrical resistivity: Geophysics, **80**, E49–E61.
Robinson, P. C., 1983, Connectivity of fracture systems — a percolation theory approach: Journal of Physics A: Mathematical and General, **16**, 605–614. (doi:10.1088/0305-4470/ 16/3/020).
Ronczka, M., C. Rücker, and T. Günther, 2015, Numerical study of long-electrode electric resistivity tomography — Accuracy, sensitivity, and resolution: Geophysics, **80**, E317–E328.
Roubinet, D., and J. Irving, 2014, Discrete-dual-porosity model for electric current flow in fractured rock: Journal of Geophysical Research: Solid Earth, **119**, 767–786.
Rücker, C., and T. Günther, 2011, The simulation of finite ERT electrodes using the complete electrode model: Geophysical Research Letters, **76**, F227–F238.
Rücker, C., T. Günther, and K. Spitzer, 2006, Three-dimensional modelling and inversion of dc resistivity data incorporating topography – I. modelling: Geophysical Journal International, **166**, 495–505. (doi: 10.1111/j.1365-246X.2006.03010.x).

Rucker, D. F., J. B. Fink, and M. H. Loke, 2011, Environmental monitoring of leaks using time-lapsed long electrode electrical resistivity: Journal of Applied Geophysics, **74**, 242–254.
Rucker, D. F., M. H. Loke, M. T. Levitt, and G. E. Noonan, 2010, Electrical-resistivity characterization of an industrial site using long electrodes: Geophysics, **75**, WA95–WA104.
Saad, Y., 2011, Numerical methods for large eigenvalue problems, revised edition: Society for Industrial and Applied Mathematics.
Salar, K., and P. Knupp, 2000, Code verification by the method of manufactured solutions: Technical report, Sandia National Laboratories. (SAND2000-1444).
Schenkel, C. J., and H. F. Morrison, 1990, Effects of well casing on potential field measurements using downhole current sources: Geophysical Prospecting, **38**, 663–686. (doi: 10.1111/j.1365-2478.1990.tb01868.x).
Schwarzbach, C., R.-U. Börner, and K. Spitzer, 2011, Three-dimensional adaptive higher order finite element simulation for geo-electromagnetics-a marine CSEM example: Geophysical Journal International, **187**, 63–74. (doi: 10.1111/j.1365-246X.2011.05127.x).
Seran, E., M. Godefroy, E. Pili, N. Michielsen, and S. Bondiguel, 2017, What we can learn from measurements of air electric conductivity in ^{222}Rn-rich atmosphere: Earth and Space Science, **4**, 91–106. (doi:10.1002/2016EA000241).
Shen, J., B. Su, and N. Guo, 2009, Anisotropic characteristics of electrical responses of fractured reservoir with multiple sets of fractures: Petroleum Science, **6**, 127–138.
Skinner, D., and G. Heinson, 2004, A comparison of electrical and electromagnetic methods for the detection of hydraulic pathways in a fractured rock aquifer, Clare Valley, South Australia: Hydrogeology Journal, **12**, 576–590.
Slater, L., and D. P. Lesmes, 2002, Electrical hydraulic relationships observed for unconsolidated sediments: Water Resources Research, **38**, 31–1.
Snow, D. T., 1970, The frequency and apertures of fractures in rock: International Journal of Rock Mechanics and Mining Sciences, **7**, 23–40. (doi:10.1016/0148- 9062(70)90025-2).
Song, R., and Z. Vondraček, 2008, On the relationship between subordinate killed and killed subordinate processes: Electronic Communications in Probability, **13**, 325–36.
Sun, Q., R. Zhang, Q. Zhan, and Q. H. Liu, 2017, Multiscale hydraulic fracture modeling with discontinuous Galerkin frequency-domain method and impedance transition boundary condition: IEEE Transactions on Geoscience and Remote Sensing, **55**, 6566–6573.
Tang, W., Y. Li, A. Swidinsky, and J. Liu, 2015, Three-dimensional controlled–source electromagnetic modelling with a well casing as a grounded source: a hybrid method of moments and finite element schemeo: Geophysical Prospecting, **63**, 1491–1507. (doi:10.1111/1365-2478.12330).
Tarasov, V., 2005, Electromagnetic field of fractal distribution of charged particles: Physics of Plasmas, **12**, 082106.
———, 2008, Universal electromagnetic waves in dielectric: Journal of Physics of Condensed Matter, **20**, 175223.
Taylor, R. W., and A. HFleming, 1988, Characterizing jointed systems by azimuthal resistivity surveys: Groundwater, **26**, 464–474.
Telford, W. M., L. P. Geldart, and R. E. Sheriff, 1990, Applied geophysics, 2nd edition: Cambridge University Press.
Tsang, C. F., and I. Neretnieks, 1998, Flow channeling in heterogeneous fractured rocks: Reviews of Geophysics, **36**, 275–298.

Tsang, C. F., I. Nernetnieks, and Y. Tsang, 2015, Hydrologic issues associated with nuclear waste repositories: Water Resources Research, **51**, 6923–6972. (doi:10.1002/2015WR017641).

Tsang, Y. W., C. F. T. F. V. Hale, and B. Dverstorp, 1996, Tracer transport in a stochastic continuum model of fractured media: Water Resources Research, **32**, 3077–3092.

Uchida, M., T. Doe, W. Dershowitz, A. Thomas, P. Wallmann, and A. Sawada, 1994, Discrete-fracture modeling of the Aspo LPT-2, large-scale pumping and tracer test, *in* SKB International Cooperation report ICR 94-0: Swedish Nuclear Fuel and waste Management Co.

Um, E. S., C. M. Commer, and G. A. Newman, 2014, A strategy for coupled 3d imaging of large-scale seismic and electromagnetic data sets: Application to subsalt imaging: Geophysics, **79**, ID1–13. (doi:10.1190/GEO2013-0053.1).

Um, E. S., M. Commer, G. A. Newman, and G. M. Hoversten, 2015, Finite element modeling of transient electromagentic fields near steel–cased wells: Geophysical Journal International, **202**, 901–913. (doi: 10.1093/gji/ggv193).

Ushijima, K. H., H. Mizunaga, and T. Tanaka, 1999, Reservoir monitoring by a 4-D electrical technique: The Leading Edge, **18**, 1422–1424.

Vallianatos, F., 2017, Transient electromagnetic method in the Keritis basin (Crete, Greece): Evidence of hierarchy in a complex geological structure in view of Tsallis distribution: Annals of Geophysics, **60**, no. 6, GM675.

———, 2018, A non extensive view of electrical resistivity spatial distribution estimated using inverted Transient Electromagnetic responses in a karstified formation (Keritis basin, Crete, Greece): Physica A, Statistical Mechanics and its Applications, **505**, 171–178.

Vallianatos, F., M. Kouli, and D. Kalisperi, 2018, Evidence of hierarchy in the complex fracture system of Geropotamos (Crete, Greece), as extracted from transient electromagnetic responses: Pure and Applied Geophysics, **175**, 1–4. (doi/10.1007/s00024-018-1835-8).

van der Vorst, H. A., 1992, BI-CGSTAB: A fast and smoothly converging variant of BI-CG for the solution of nonsymmetric linear systems: SIAM Journal of Scientific and Statistical Computing, **13**, 631–644.

von Kameke, A., F. Huhn, G. Fenandez-Garcia, A. Munuzuri, and V. Perez-Munuzuri, 2010, Propagation of a chemical wave front in a quad-two-dimensional superdiffusive flow: Physical Review E, **81**.

Wait, J. R., 1952, Electromagnetic fields of current–carrying wires in a conducting medium: Canadian Journal of Physics, **30**, 512–523. (doi: 10.1139/p52–049).

———, 1957, The effect of a buried conductor on the sub–surface fields for a line source excitation: Radio Science, **7**, 587–591. (doi: 10.1029/RS007i005p00587).

Wait, J. R., and J. T. Williams, 1985, EM and IP response of a steel well casing for a four-electrode surface array: Part I — Theory: Geophysical Prospecting, **33**, 723–735. (doi: 10.1111/j.1365-2478.1985.tb00775.x).

Wang, M. F., F. J. Dickin, and R. Mann, 1999, Electrical resistance tomographic sensing systems for industrial applications: Chemical Engineering Communications, **175**, 49–70.

Wang, W., X. Wu, and K. Spitzer, 2013, Three-dimensional dc anisotropic resistivity modelling using finite elements on unstructured grids: Geophysical Journal International, **193**, 734–746. (doi: 10.1093/gji/ggs124).

Weiss, C. J., 2001, A matrix–free approach to solving the fully 3D electromagnetic induction problem: SEG Technical Program Expanded Abstracts, **20**, 1451–1454. (doi: 10.1190/1.1816377).

———, 2013, Project APhiD: A Lorenz–gauged **A**-Φ decomposition for broadband electromagnetic induction in a fully heterogeneous Earth: Computers & Geosciences, **58**, 40–52. (doi: 10.1016/j.cageo.2013.05.002).
———, 2014, An overset grid method for global geomagnetic induction: Geophysical Journal International, **198**, 8–24. (doi: 10.1093/gji/ggu108).
———, 2017, Finite–element analysis for model parameters distributed on a hierarchy of geometric simplices: Geophysics, **82**, E155–E167. (doi:10.1190/geo2017-0058.1).
Weiss, C. J., D. F. Aldridge, H. A. Knox, K. A. Schramm, and L. C. Bartel, 2016, The direct–current response of electrically conductive fractures excited by a grounded current source: Geophysics, **81**, E201–10. (doi: 10.1190/GEO2015-0262.1).
Weiss, C. J., G. D. Beskardes, and B. G. van Bloemen Waanders, 2018, Hierarchical material property representation in finite element analysis: Convergence behavior and the electrostatic response of vertical fracture sets: SEG Technical Program Expanded Abstracts, 4773–4777. (doi:10.1190/segam2018-2998297.1).
Weiss, C. J., and M. E. Everett, 2007, Anomalous diffusion of electromagnetic eddy currents in geologic formations: Journal of Geophysical Research, **112**, 2006JB004475.
Weiss, C. J., and G. A. Wilson, 2017, Modeling the electrical response of oil field infrastructure: SEG Technical Program Expanded Abstracts, 1064–1069. (doi:0.1190/segam2017-17632610.1).
Weymer, B. A., M. E. Everett, T. S. de Smet, and C. Houser, 2015, Review of electromagnetic induction for mapping barrier island framework geology: Sedimentary Geology, **321**, 11–24.
Williams, J. T., and J. R. Wait, 1985, EM and IP response of a steel well casing for a four-electrode surface array: Part II — Numerical results: Geophysical Prospecting, **33**, 736–745. (doi: 10.1111/j.1365-2478.1985.tb00776.x).
Xu, C., and P. Dowd, 2010, A new computer code for discrete fracture network modelling: Computers & Geosciences, **36**, 292–301.
Yang, D., D. Oldenburg, and L. Heagy, 2016, 3D DC resistivity modeling of steel casing for reservoir monitoring using equivalent resistor network: SEG Technical Program Expanded Abstracts, 932–936. (doi: 10.1190/segam2016-13868475.1).
You, S., and X. D. Liu, 2005, A numerical method for solving variable coefficient elliptic equation with interfaces: Journal of Computational Physics, **202**, 411–445.
Zeng, S., D. Wilton, J. Chen, J. Liu, and W. Hu, 2017, Fast electromagnetic modeling of energized casing for deep subsurface prospecting: SEG Technical Program Expanded Abstracts, 1049–1053. (doi:10.1190/segam2017-17784256.1).
Zhang, J. R., R. L. Mackie, and T. R. Madden, 1995, 3-D resistivity forward modeling and inversion using conjugate gradients: Geophysics, **60**, 1313–1325.
Zhang, P., W. Abdallah, M. Ramadhan, A. Marsala, S. Saif, S. Lyngra, and S. Ma, 2017, Crosswell electromagnetic survey: An effective approach for reservoir-scale saturation mapping: SEG Technical Program Expanded Abstracts, 1054–1058. (doi:10.1190/segam2017-17251684.1).
Zhang, Q.-H., 2015, Finite element generation of arbitrary 3-D fracture networks for flow analysis in complicated discrete fracture networks: Journal of Hydrology, **529**, 890–908.
Zhang, Q.-H., S. Z. Lin, Z. Q. Xie, and H. D. Su, 2016, Fractured porous medium flow analysis using numerical manifold method with independent covers: Journal of Hydrology, **542**, 790–808.

Zhang, Y. Y., D. J. Liu, Q. H. Ai, and M. J. Qin, 2014, 3D modeling and inversion of the electrical resistivity tomography using steel cased boreholes as long electrodes: Journal of Applied Geophysics, **109**, 292–300.

Zhdanov, M. S., and S. Fang, 1996, Quasi-linear approximation in 3–D electromagnetic modeling: Geophysics, **61**, 646–665.

———, 1997, Quasi-linear series in three-dimensional electromagnetic modeling: Radio Science, **32**, 2167–2188.

DISTRIBUTION

Hardcopy—Internal

Number of Copies	Name	Org.	Mailstop
1	Güngör Didem Beşkardeş	08861	0750
1	Kyle R. Jones	08861	0750
1	William M Miller	05900	1218
1	Bart G van Bloemen Waanders	01463	01318
1	Erik K. Webb	08860	0735
1	D. Chavez, LDRD Office	1911	0359

Email—Internal

Name	Org.	Sandia Email Address
Technical Library	01177	libref@sandia.gov

This page intentionally left blank.

Sandia National Laboratories is a multimission laboratory managed and operated by National Technology & Engineering Solutions of Sandia LLC, a wholly owned subsidiary of Honeywell International Inc., for the U.S. Department of Energy's National Nuclear Security Administration under contract DE-NA0003525.